To the Graduate Council:

I am submitting herewith a dissertation written by Boyd McCutchen Evans III entitled "MEMS Capacitive Strain Sensing Elements for Integrated Total Knee Arthroplasty Prosthesis Monitoring." I have examined the final electronic copy of this dissertation for form and content and recommend that it be accepted in partial fulfillment of the requirements for the degree of Doctor of Philosophy, with a major in Biomedical Engineering.

Mohamed R. Mahfouz

Major Professor

We have read this dissertation
and recommend its acceptance.

Richard D. Komistek

William R. Hamel

Syed K. Islam

Ally E. Fathy

Accepted for the Council:

Carolyn R. Hodges

Vice Provost and Dean of the
Graduate School

(Original signatures are on file with official student records.)

MEMS Capacitive Strain Sensing Elements for Integrated Total Knee Arthroplasty Prosthesis Monitoring

A Dissertation

Presented for the

Doctor of Philosophy Degree

The University of Tennessee, Knoxville

Boyd McCutchen Evans III

December 2007

Dedication

This dissertation is dedicated to my family, as each member paid an important role in its completion. I would like to thank my wife, Kathy, for her support and her hard work with all our boys (she is the one always cheering the loudest). I would especially like to thank Ben for helping lead our family during this time and stepping up whenever he was needed. I would like to thank Drew for his cheerful demeanor during all of the times when I needed it, and I would like to thank Boyd IV for his patience and quiet thoughtfulness during this time.

Acknowledgements

First, I would like to thank God for giving me the perseverance, wisdom, and creativity to complete this work. I would like to thank Dr. Mahfouz for his mentorship and the wonderful opportunities that he has given me. I would like to thank Dr. Komistek for his contagious enthusiasm for all things involving biomedical engineering and for introducing me to this program. Dr. Hamel proved to be a true advocate of the student during my program, and I will always value his support. Dr. Fathy's assistance with instrument calibration was appreciated, and Dr. Islam provided great support in the design of circuits for the measurement of the small changes in capacitance. I would also like to thank Dr. Penumadu for his support in the design of test methods for the sensors. Ada Pfohl is greatly appreciated for teaching me how to handle ten number one priorities at the same time.

I was privileged to work with many incredible students along the way. Gary To designs the most artistic circuit boards that I have ever seen. Emily Pritchard served as a sounding board for many ideas and provided excellent feedback plus she always knows when fresh cookies are needed. I would like to thank Preston Kelly and Andrea North for their support in the ORNL clean room, and I am grateful for Gary Alley's support and for providing access to ORNL facilities for portions of this work. I would like to thank Mohammed Haider and Sazia Eliza for their work on the circuits related to this research. I would like to express appreciation to the rest of my colleagues at the University of Tennessee's Center for Musculoskeletal Research especially Brandon Merkl, Michael Kuhn, Joel Outten, Katy Alford, and Joey Bader.

Abstract

Measuring the *in vivo* load state of Total Knee Arthroplasty (TKA) components is required to understand the structural environment and wear characteristics of the devices. The ability to acquire this information gives tremendous insight into the mechanics of the joint replacement prosthesis. Data corresponding to normal loads, in-plane loads, shear loads, load center, contact area, and the rate of loading is needed to fully understand the kinematics and kinetics of the orthopedic implant. In this research, a novel sensing system has been developed which is capable of fully characterizing three-dimensional strain and stress at a single location.

Capacitance-based sensors were chosen to avoid the power loss and drift characteristics typical of resistive elements due to resistive heating effects. A design and optimization methodology has been developed by combining conformal mapping electrostatic analysis techniques with methods from micromechanics of composite materials. Results of the design and optimization technique are used to understand the behavior of the sensing system. Simulation of these systems was performed using multiphysics finite element analysis, and novel methods for fabricating the sensors were adapted from techniques for fabricating microelectromechanical systems (MEMS) using biocompatible materials.

An array of six sensors was fabricated with a critical dimension of 2.25 micrometers. This array consisted of a parallel plate capacitor for measuring normal strain, two differential elements for sensing shear strain normal to the plane of the array, and three interdigitated transducer (IDT) elements for characterizing strain in the plane of

the sensor. The normal strain sensor exhibited a sensitivity of 1.54×10^{-3} picofarads per megapascal, and the shear sensor had a sensitivity of 4.77×10^{-5} picofarads per megapascal. Testing results showed that all sensors had linear response to loading and insignificant drift. Multiaxial testing results illustrated the ability of the differential sensors to determine loading direction.

A multiaxial, MEMS sensor array has been developed for use in orthopedic, load-measuring conditions. This system has been optimized for use in soft materials such as ultra-high molecular weight polyethylene (UHMWPE). In the future, arrays of sensors will be embedded in orthopedic components to determine the total state of stress at local positions within the component.

Table of Contents

Chapter 1 Introduction and Previous Work 1

1.1 Introduction 1

1.2 Review of Knee Replacement Procedures and Technology 2

1.2.1 Total Knee Arthroplasty Procedure 2

1.2.2 Biomechanics of the normal and TKA knee 5

1.2.3 Wear of the Total Knee Arthroplasty Prosthesis 8

1.2.4 Contact Area and Stress Measurement 10

1.2.5 Orthopedic Load Determination 11

1.3 Previous Research in MEMS Strain and Pressure Sensors 14

1.3.1 MEMS Pressure Sensors 14

1.3.2 Micromachined Strain Sensors 15

1.3.3 Robotic Tactile Sensors 16

1.3.4 Embedded MEMS Strain Sensors 17

1.3.5 Microfabricated Sensors Summary 18

1.4 Dissertation Objectives and Structure 18

1.5 Dissertation Contributions 21

Chapter 2 Analytical Modeling of Capacitance-based Strain Sensors 24

2.1 Sensor Design and Operation Concepts 24

2.2 Continuum Mechanics Modeling of Parallel Plate Capacitors 30

2.3 Potential and Electric Field Evaluation Using Conformal Mapping 36

2.3.1 Schwarz-Christoffel Mapping 38

2.3.2 Mapping of Parallel Plate Capacitor Fringe Capacitance 42
2.3.3 Mapping of Fringe Capacitance for Parallel Plate Capacitors of Unequal Size 45
2.3.4 Analytical Solution of the Capactiance and Electric Field of Two Thin, Finite, Charged Plates 49
2.3.5 Comparison of Analytical Results with Commercial FEA Software for Electrostatic Solutions 59
2.4 Summary of Analytical Techniques for Capacitance-based Sensors 61
Chapter 3 Analysis of Microscopic Deformation of Electrode Structures and Capacitive Response 63
3.1 Apparent Properties of Non-homogeneous Systems of Materials 64
3.1.1 Equivalent Stress Model for Determining Young's Modulus in Directions Orthogonal to Electrodes 64
3.1.2 Equivalent Strain Model for Determining Young's Modulus in Directions Parallel to Electrode Major Dimensions 66
3.2 Embedded Sensor Response to Normal and Transverse Loading 68
3.3 Response of an Embedded Capacitor to Shear Loading 73
3.4 Analysis of the Response of an Interdigitated Capacitor to Loads Parallel and Orthogonal to the Sensor Electrodes 79
3.4.1 Analysis of Composite Material Properties of the IDT 82
3.4.2 IDT Response Due to x Direction Loading 86
3.4.3 IDT Response Due to y Direction Loading 90
3.4.4 Optimization of IDT Response 91

3.4.5 Summary of Results of IDT Response Analysis and Optimization 101
3.5 Conclusions on Analytical Relationships Between the Deformation of Composite Electrodes and Changes in Capacitance 101
Chapter 4 Multi-physics Finite Element Modeling of Capacitive Sensor Structures 104
4.1 Material Properties and Units for Finite Element Analysis 105
4.2 Strategy for Modeling Embedded Strain Sensors 107
4.3 Finite Element Modelling of Parallel Plate Capacitor Structures 111
4.3.1 Parallel Plate Capacitor FEA Convergence Study 114
4.3.2 Parallel Plate Capacitor FEA Model Details 117
4.3.3 Parallel Plate Capacitor FEA Results 118
4.4 Shear Sensor Finite Element Analysis 126
4.4.1 Shear Sensor Model Boundary Conditions 126
4.4.2 Results of shear sensor finite element modeling 128
4.4.3 Maxwell field modeling of shear sensor geometries 132
4.5 Interdigitated Capacitor Multiphysics Modeling 135
4.5.1 Boundary Conditions for Modeling Interdigitated Strain Sensors 135
4.5.2 Results of x Direction Loading Models 138
4.5.3 Boundary Conditions and Results for y-direction Pressure Modeling 142
4.5.4 IDT Capacitance Results and Multiphysics FEA Parameter Studies 149
4.5.5 IDT Load Response Parameter Study 155
4.5.6 Maxwell Electrostatic Field Analysis for Interdigitated Sensors 157
4.6 Summary of Multiphysics Modeling of MEMS Strain Sensors 158
Chapter 5 Microfabrication of Capacitive Strain Sensors 162

5.1 Fabrication of Prototype Sensors on Silicon Wafer Substrates 163
5.2 Parylene Processing and Etching 169
5.3 Investigation of Lithography on Polyethylene Substrates 174
5.4 Summary of Fabrication Research for MEMS Strain Sensors 176
Chapter 6 Testing Methods and Data for Microfabricated Strain Sensors 178
6.1 Normal Strain Sensor Testing 178
6.2 Shear Sensor Testing and Results 185
6.3 IDT Sensor Test System and Data 192
6.4 Uncertainty Analysis of Testing Methods 194
6.5 Summary of Strain Sensor Testing Methods and Results 197
Chapter 7 Conclusions and Summary of Sensor Research 200
7.1 Conclusions of Microfabricated Strain Sensor Research 200
7.2 Future Research in the Area of Embedded Strain Sensors 204
BIBLIOGRAPHY 206
APPENDIX 218
APPENDIX A US Patent No. 7,097,662 219
APPENDIX B Computational Modeling 237
Vita 252

List of Figures

Figure 1.1: Diagram of total knee arthroplasty prosthesis and anatomy. 3

Figure 1.2: Illustration of femoral rollback and contact point motion..... 6

Figure 1.3: Anatomy of the knee including cruciate ligaments and collateral ligaments... 8

Figure 2.1: Design concept for multi-axial strain sensor array using capacitance detection techniques. 25

Figure 2.2: Multiaxial strain sensor with elements for three normal strains and three shear strains. 26

Figure 2.3: Illustration of capacitance function of the three sensor components. 27

Figure 2.4: Cross section of a parallel plate capacitor showing dipole formation and surface charge distribution when a voltage, V_d, is applied across the plates..... 31

Figure 2.5: Rectangle in upper right quadrant of complex plane, W..... 37

Figure 2.6: Rectangle mapped to exterior of unit circle on upper half of complex plane, T, using the transformation $t=e^{w}$. 37

Figure 2.7: Mapping of a polygon in the Z=x+jy domain to the T=t+iτ domain. 40

Figure 2.8: Mapping of semi-infinite parallel plates from the z plane to the T plane. 44

Figure 2.9: Plot of transformation of equipotential and flux lines from W plane to Z plane using Equation (2-29). 46

Figure 2.10: Geometry used for mapping from the T plane to the Z plane for a semi-infinite parallel plate capacitor with plates of unequal length. 47

Figure 2.11: Plot of transformation of equipotential and flux lines from W plane to Z plane for parallel plate capacitor with unequal plate sizing..... 50

Figure 2.12: Geometry used to determine the capacitance and flux between two thin electrodes in the same plane. 51
Figure 2.13: Flux and potential lines mapped from parallel plate capacitor to model the fringe effects of a parallel strip capacitor. 58
Figure 2.14: Geometry from Maxwell electrostatic FEA analysis for result comparison. 60
Figure 3.1: Representative element of parallel plate capacitor under normal strains. 65
Figure 3.2: Representative volume element for determining strains in the parallel plate capacitor for measuring normal strains. 67
Figure 3.3: (a) Simplified view of normal loading of parallel plate using a system of springs in series for visualization purposes. (b) Simplified view of transverse loading of parallel plate using a system of springs in parallel for visualization. These simplified models neglect Poisson's ratio effects and shear stresses between the layers. 69
Figure 3.4: Capacitance change for a 1 MPa load as a function of base capacitance value. 73
Figure 3.5: Representative volume element with applied shear loading showing exaggerated deformations. 74
Figure 3.6: Representative volume element showing the shape of the original geometry in dashed lines, the deformations of the individual layers, and total deformation. 74
Figure 3.7: (a) illustration of three electrode shear sensor with applied shear load for determining capacitance change with shear, and (b) similar differential capacitor geometry to illustrate the electrode function. 77

Figure 3.8: (a) Geometry of undeformed IDT with primary dimensions illustrated, (b) deformed geometry with load applied perpendicular to electrodes (x-direction loading), and (c) deformed geometry with load applied parallel to electrodes (y-direction loading). 81

Figure 3.9 Illustration of representative element used to model the displacement between electrodes for the interdigitated strain sensor. 83

Figure 3.10: System of springs in both series and parallel used to illustrate deformation of interdigitated strain sensor. 83

Figure 3.11: Change in capacitance and directional sensitivity as a function of electrode length. The electrode length varies from 100 to 1,000 μm, the gap is 2.0 μm, the thickness is 500 nanometers, the electrode width is 5.0 μm, and the number of electrodes is 50. 93

Figure 3.12: Change in capacitance and directional sensitivity as a function of the number of IDT electrodes. The electrode length is 500 μm, gap is 2.0 μm, width is 5.0 μm, and the number of electrodes is 50. 94

Figure 3.13: Change in capacitance and directional sensitivity as a function in-plane stress subjected to the IDT electrodes. The electrode length is 500 μm, thickness is 0.5 μm, gap between electrodes is 2.0 μm, and the number of electrodes is 50. 96

Figure 3.14: Change in capacitance and directional sensitivity as a function of the width of the gap between the IDT electrodes. The electrode length is 500 μm, thickness is 0.5 μm, the width is 5.0 μm, and the number of electrodes is 50. 97

Figure 3.15: Change in capacitance and directional sensitivity as a function of the width of the IDT electrodes. The electrode length is 250 μm, thickness is 0.5 μm, gap between electrodes is 2.0 μm, and the number of electrodes is 50. 99

Figure 3.16 Change in capacitance and directional sensitivity as a function of the thickness of the IDT electrodes. The electrode length is 250 μm, width is 5 μm, gap between electrodes is 2.0 μm, and the number of electrodes is 50. 100

Figure 4.1: Typical finite element mesh from Coventor for multi-physics modeling of electrode structures. Symmetry in the yz plane has been used to simplify the analysis and allow for a finer mesh in the analysis region. Upper parylene and polyethylene layers are hidden for clarity. 109

Figure 4.2: Upper and lower view of parallel plate finite element model for 5 pF sensor with mechanical boundary conditions annotated for normal loading. 112

Figure 4.3: Parallel plate FEA model with upper polyethylene layer and parylene dielectric layers displayed as transparent. One-fourth symmetry used in model. 113

Figure 4.4: Parallel plate convergence results based on capacitance..... 115

Figure 4.5: Parallel plate convergence results based on displacement results..... 115

Figure 4.6: Finite element analysis results for embedded normal strain sensor. Capacitor is embedded in the center of figure shown. 119

Figure 4.7: Displacement magnitude results from parallel plate strain sensor with upper embedding layer hidden. 119

Figure 4.8: z direction stress for normal strain sensor with upper encapsulation layer hidden. 120

Figure 4.9: Strain in the z direction for normal strain sensor. The upper encapsulating layer is hidden. 121
Figure 4.10: Principal stress results for normal strain sensor. 121
Figure 4.11: Finite element results for z direction loading and orthogonal loading for five different geometries of normal strain sensors. 123
Figure 4.12: Sensitivity analysis results for loads ranging from 0.02 MPa to 20 MPa and base capacitance values of 1, 2.5, 5, 7.5, and 10 picoFarads. 125
Figure 4.13: Geometry and boundary conditions for evaluating the shear stress sensor.128
Figure 4.14: xz strain results for three electrode sensor showing good strain uniformity. 129
Figure 4.15: xz stress results indicate the boundary conditions result in uniform loading. 130
Figure 4.16: Deformed geometry of shear representative element showing classic deformation from shear strain 130
Figure 4.17: x displacement results indicate positive displacement of lower surface and negative displacement of upper surface. 131
Figure 4.18: Results of load and array electrode parameter study and math model. 132
Figure 4.19: Electric field results from Maxwell two-dimensional model. 134
Figure 4.20: Electric field density magnitude from Maxwell two-dimensional model. . 134
Figure 4.21: Boundary conditions for interdigitated capacitor and x direction load. 137
Figure 4.22: Perspective view of boundary conditions for in-plane strain sensor. 138
Figure 4.23: Displacement magnitude results for embedded IDT with x direction loading. 139

Figure 4.24: Midplane x displacement results for embedded IDT in polyethylene with x direction load. 139
Figure 4.25: Midplane x component of stress results for x direction loading. 141
Figure 4.26: Midplane x direction strain results for x direction loading. 141
Figure 4.27: Top view of boundary conditions for y direction loading of embedded IDT. Upper polyethylene layer is transparent such that IDT is visible. 143
Figure 4.28: Perspective view of boundary conditions for y direction loading. 143
Figure 4.29: Cut away view of displacement magnitude results for y direction stress. . 144
Figure 4.30: Cut away view of y displacement results for loading parallel to IDT electrodes (y direction stress)..... 145
Figure 4.31: y direction stress results for y direction loading. Upper level polyethylene layer is hidden. 146
Figure 4.32: Results of y direction strain for loading parallel to IDT electrodes. 147
Figure 4.33: x direction stress resulting from y direction loading. 148
Figure 4.34: x direction strain resulting from y direction loading, an example of Poisson's ratio effects..... 148
Figure 4.35: Results of parameter study based on the number of IDT electrodes. 150
Figure 4.36: Results of IDT digit length parameter study. 152
Figure 4.37: Base capacitance as a function of electrode thickness. 153
Figure 4.38: Results of IDT thickness parameter study showing x direction or lateral loading results, y direction (longitudinal load) results as well as directional sensitivity. 154
Figure 4.39: Response of IDT to loads ranging from 0.02 MPa to 20 MPa. 156

Figure 4.40: Maxwell results for the electric field of interdigitated strain sensor at the tip of the electrodes. 159
Figure 4.41: Electric field results showing fringing field in the xz plane for the interdigitated capacitor..... 160
Figure 5.1: Silicon wafer substrate after contact printing and image reversal process. Photoresist appears dark reddish-brown in this image. 164
Figure 5.2: Microscopic view of Figure 5.1 showing a 2 micrometer spaced sensor after image reversal process. Photoresist edges are translucent due to undercutting..... 164
Figure 5.3: Generic process flow for depositing one layer of material on silicon, polyethylene, or other substrate using image reversal process. 165
Figure 5.4: Images of 2 micrometer spacing interdigitated electrode at 50X magnification. Structures fabricated on silicon wafers. 169
Figure 5.5: Chemical structure of four most common types of parylene. 170
Figure 5.6: Parameters for parylene polymerization and coating process. 171
Figure 5.7: Images of silicon wafer with SiO_2 release/dielectric layer and parylene layer with interdigitated electrodes after lift-off. Right image is micrograph at 200X of 5 μm electrodes with 2 μm gaps between electrode digits. 171
Figure 5.8: Device wafers during oxygen plasma processing in PT-72. 173
Figure 5.9: Substrates following etching of vias in parylene layer with PT-72 and removal of photoresist layer used for patterning. 173
Figure 5.10: Optical profilometry of plasma-treated polymer surfaces..... 175

Figure 5.11: Upper image shows sensing array fabricated using parylene on Silicon substrate. Lower image is an interdigitated capacitor with 2 micrometer gaps between 5 micrometer legs fabricated on high-density polyethylene sheet material..... 177
Figure 6.1: Array of parallel plate sensor mounted on printed circuit board for testing. 179
Figure 6.2: Experimental setup for load testing the capacitive sensor array. 180
Figure 6.3: Load profile for capacitance array test for chip B, element 2-2, 5 pF..... 183
Figure 6.4: Change in capacitance with load from 1, 5, and 10 pF capacitive sensors. . 183
Figure 6.5: Comparison of sensor testing results with FEA and math model. 184
Figure 6.6: Illustration of testing scenario for shear sensors. 187
Figure 6.7: Upper left is illustration of transfer of shear load to epoxy connecting polycarbonate and FR-4 material. Upper right is image of test sample in MTS machine, and lower image is of sample used for shear testing. 188
Figure 6.8: Results of shear sensor testing for 0.344, 0.689, and 1.034 MPa shear loads. 190
Figure 6.9: Comparison of experimental results and results predicted by analytical techniques and finite element analysis. 191
Figure 6.10 Loading and mounting diagram for testing of IDT in plane strain sensors. 193
Figure 6.11: Image of PC board with sensor array mounted for cantilver testing. 193
Figure 6.12: Raw data from in strain sensor test. 195
Figure 6.13: Data from constant loading averaged and plotted with linear least squares fit. 195
Figure 6.14: Enlarged view of MTS load data and capacitance data for 222.4 N (50 pound) load. 198

List of Tables

Table 2-1: Comparison of analytical calculations with commercial FEA software.....62

Table 3-1: Results of analytical model for a 1 MPa load and different value capacitors..72

Table 4-1: Properties of materials and units used for the finite element study.....106

Table 4-2: Summary of parallel plate convergence results.....116

Table 4-3: Capacitance sensitivity for five normal strain sensors.....124

Table 4-4: Capacitance results for IDT electrode number parameter study.....150

Table 4-5: Data from electrode thickness parameter study.....152

Table 6-1: Comparison of predicted sensitivity of sensors and test results.....184

Table 6-2: Comparison of predicted sensitivity of the shear sensor and test results.....188

List of Symbols and Abbreviations

A	area
Au	gold
C	Capacitance, Centigrade
CNF	Cornell Nanofabrication Facility
E	electric field, elastic modulus
F	Farad, force
FR-4	a type of flame retardant printed circuit board
HMDS	hexmethyldisilazane, $C_6H_{19}NSi_2$
HP-IB	Hewlett-Packard instrumentation bus
HTG	Hybrid Technology Group
IDT	interdigitated transducer
j	imaginary number representing the square root of -1
K	complete elliptic integral
K’	complete elliptic integral of complementary modulus
k	modulus
k’	complementary modulus
kPa	kilopascals
l	length
LCR	inductance, capacitance, and resistance
m	meter
μm	micrometer, 1×10^{-6} m

min	minutes
mm	millimeters
MPa	megapascals
n	number of electrode digits
N	Newtons, Nitrogen
PE	polyethylene
pF	picofarad 1×10^{-12} Farads
psi	pounds per square inch
P	polarization
PT-72	Plasma Therm model 72 reactive ion etcher
q	charge
RAM	random access memory
RIE	reactive ion etch
RMS	root mean squared
RSA	Roentgen stereophotogrammatic analysis
s	strain
s	seconds
Si	Silicon
SF_6	sulfur hexafluoride
SiO_2	silicon dioxide
SMB	sub-miniature B
TKA	Total Knee Arthroplasty
TMAH	tetramethylammonium hydroxide

UHMW	ultrahigh molecular weight
YES	Yield Engineering Systems
w	transformation coordinate
χ_e	electric susceptibility
δ	offset amount
ε	permittivity
ε_0	permittivity of free space
ε_r	relative permittivity
σ	stress
ψ	field
φ	flux
γ	shear strain
ν	Poisson's ratio
ρ_v	charge density
Δ	difference, change
∇	gradient

Chapter 1
Introduction and Previous Work

1.1 Introduction

The procedure of replacing patient's knee joints affected by osteoarthritis and other disease originated in the early 1970's. Although the maturity of this procedure evolved tremendously in the following decades, there is still the need to improve the biomechanical and wear characteristics of the knee prosthesis. An underlying goal for joint replacement prosthesis should be that regardless of the age of the patient, any prosthesis should be expected to last a lifetime and have similar function or performance to the normal knee. Presently, this state of maturity has not been reached in the orthopedics industry. Much of the problem in designing a knee replacement for the total knee arthroplasty (TKA) procedure lies in the fact that there is very little *in vivo* data on the load conditions available.

The goal of this research is to advance the state-of-the-art in miniature sensor systems for measuring the internal strain and pressure in prosthetic devices. The ability to measure the strain in the prosthesis will allow greater understanding of the internal stresses, contact forces, wear, relative motions, and overall performance of the knee implant. The ability to obtain *in vivo* data on implant performance on a patient-specific basis will allow for treatment methodologies and follow-up procedures to be tailored to

help the individual patient receive the longest lifetime and best performance from his or her implant. Research performed using this system will help future patients by improving the overall understanding of the factors that affect implant wear and function.

This section will give an overview of the challenges associated with the replacing the human knee and review important concepts with regard to total joint replacement procedure, biomechanics, wear, and load. The review of these concepts establishes the motivation and functional aspects of this research. Also, the objectives, structure, and contributions of this dissertation are presented in this chapter.

1.2 Review of Knee Replacement Procedures and Technology

1.2.1 Total Knee Arthroplasty Procedure

The total knee arthroplasty (TKA) or knee replacement procedure comprises resecting the diseased bearing surfaces of the femur and tibia and replacing them with metal or plastic components. Figure 1.1 illustrates the components and anatomy used commonly in the total knee replacement. Metal components are commonly made from titanium or cobalt-chrome with a plastic spacer between the femoral and tibial components fabricated from ultrahigh molecular weight polyethylene (UHMWPE). Advances in the knee replacement implant occurred rapidly in the 1970's as surgeons Insall, Walker, and Ranawat in New York competed to perfect the dual condylar knee replacement. The race was on as they competed with Coventry and Turner's geometric knee, Townley's anatomic knee, and in England, Freeman's posterior stabilized knee [1].

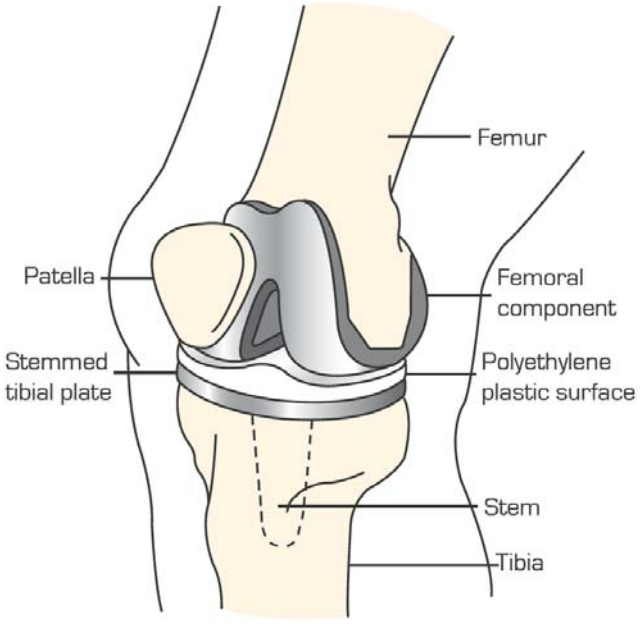

Figure 1.1: Diagram of total knee arthroplasty prosthesis and anatomy.

Knee replacement procedures research also took advantage of advances in hip replacement procedures in the 1960's by Sir John Charnley and others [2].

Based on the National Inpatient Survey (NIS) of medical procedures database, the number of annual knee arthroplasty procedures in the United States is reported to be 326,000 nationwide [3]. The proportion of revisions (surgeries to replace a failed knee replacement joint) to primary procedures (first joint replacement) is reported to be 8-15% of total procedures, and the longevity of these implants varies significantly in published literature, from 8-20 years [4,5,6,7,8]. Also, revision surgeries are significantly more complicated for both patient and surgeon than primary arthroplasty procedures and generally have poorer outcomes [9]. In the past decade, patients have been receiving

TKA procedures at a younger age, and they are expecting to have an even higher rate of revision surgery in the future due to implant wear, aseptic loosening, or other failure mechanisms due to their more active lifestyles [10]. Revision surgeries are generally much more invasive than primary arthroplasty procedures due to the requirement of removal of the failed implant including the requirement that more bone has to be resected to prepare for the new implant [11]. Also, recipients of knee replacements are advised not to participate in high impact activities (running, skiing, aerobics, vigorous walking, or tennis) [12].

Failure mechanisms of TKA prosthetics have been studied by several researchers. In a 2002 review of all (212) revisions at one institution between 1997 and 2000, Sharkey et al. attributed early failures to infection (25.4%), loosening (16.9%), instability (21.2%), extensor mechanism deficiency (6.6%), avascular necrosis of the patella (4.2%), and isolated patella resurfacing (0.9%). The prevalent causes of overall failure were polyethylene wear (25%), aseptic loosening (24.1%), instability (21.2%), infection (17.5%), arthrofibrosis (14.6%), malalignment (11.8%), extensor mechanism deficiency (6.6%), patella necrosis (4.2%), periprosthetic fracture (2.8%), and the need to resurface the patella (0.9%) [13]. Fehring, et al, in a survey of 440 patients, found similar results [14], as well as a 2006 study of 318 patients requiring revision by Mulhall [15].

Better instrumentation in the orthopedics community could be used for computer assisted surgical alignment, the detection of infectious organisms or the body's response, and the measurement of vibrations, component loading and wear *in vivo*. Ideally, the knee replacement prosthesis should be expected to last the lifetime of the recipient, and allow

the recipient to return to a broader range of activity. Significant improvement in existing knee replacement components and procedures will be required for knee replacement components to be expected to last the lifetime of the patient and for patients to be expected to participate in a wider range of activities.

1.2.2 Biomechanics of the normal and TKA knee

It is tempting to assume the motion of the knee is similar to a simple hinge, and an early knee replacement prosthesis studied by Waldius [16,17] used a hinge in place of articulating surfaces. Several iterations of hinged designs followed, but none were successful because the stresses placed on both device and its attachment to bone caused loosening in almost all cases. These stresses occurred because the simple hinged devices neglected the importance of the other planes of motion in the human knee.

The human knee is a complex system of muscles, ligaments, and bones (femur, tibia, and patella) produce the flexion and extension of a knee. Extension of the knee occurs due to contraction of the quadriceps muscles with assistance from the tensor fasciae latae. Flexion is due primarily to the action of the hamstrings, and secondarily the gracilis and the sartorius. Medial and lateral motions of the femur with respect to the tibia are constrained by the medial and lateral collateral ligaments, the cruciate ligaments, and by the interaction between the femoral condyles and the tibial intercondyler eminence. Anterior motion of the tibia relative to the femur is constrained by the anterior cruciate ligament (ACL) and posterior motion by the posterior cruciate ligament (PCL) [18,19].

Three important concepts with regard to the biomechanics of the knee are rollback, axial rotation of the femur with respect to the tibia, and lift-off. Figure 1.2

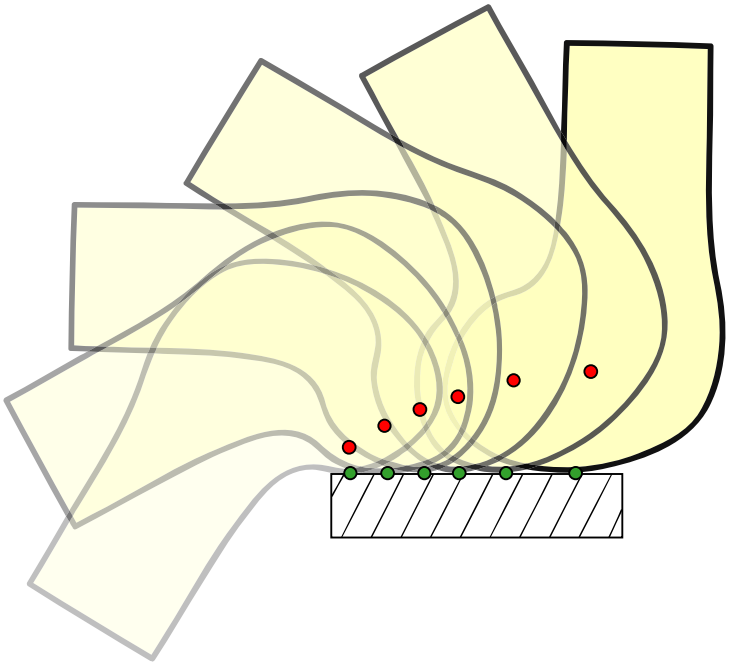

Figure 1.2: Illustration of femoral rollback and contact point motion.

illustrates femoral roll back with flexion from 0 to 150 degrees. Motion of the contact point is shown with a green dot, and position of the radius of curvature of the surface at that contact point is illustrated with a red dot. Researchers have used cadaver studies [20,21,22], video gait analysis [23,24,25], Roentgen stereophotogrammatic analysis (RSA) [26,27], and *in vivo* fluoroscopy [28,29,42] to study the biomechanics of the normal and implanted knee. Rollback is the posterior translation of the femur with respect to the tibia with increased flexion. In a 2003 study of five subjects with non-implanted knees by Komistek, Dennis, and Mahfouz [29], the rollback (posterior translation being negative) of the medial and lateral condyles during gate was measured to be -4.3 mm (range of -1.9 – -10.3 mm) and 0.9 mm (range +3.4 – -5.8mm); respectively, using video fluoroscopy. In the same study, during deep flexion, subjects averaged -12.7 mm (range

1.4 – -29.8 mm) and -2.9 mm (range +3.0 – -9.0 mm). The difference between the translation of the medial and lateral condyles is evidence of axial rotation of the femur with respect to the tibia for these subjects. In this study, the average rotation was an external rotation of the femur with respect to the tibia of more than 13° for deep flexion and less than 5° for gait. External rotation and posterior translation of the femur with respect to the tibia is considered normal.

Rotation of the femur with respect to the tibia in the frontal plane is often described as "lift-off". The term lift-off refers on one of the condyles lifting off of the tibial insert. The transmission of forces during stance is generally 70–75% through the medial condyle and 25–30% through the lateral condyle. Lift-off results in all of the tibio-femoral contact forces being transmitted through a single condyle and can occur in either condyle. It can also result in edge loading of the femur against the tibial components in TKA yielding eccentric wear patterns and increased wear [30].

The biomechanics behind the complicated motions of the knee are a subject of significant debate. It is generally assumed that the external axial rotation of the femur with respect to the tibia during flexion and internal axial rotation during extension are the result of the both the geometry of condyles and the cruciate ligament attachments. The condyles of the knee decrease in radius in the sagittal plane from the anterior to the posterior direction, somewhat like the shape of a spiral. This results in the axis of rotation moving in both the posterior and inferior directions with flexion. The geometries of the contact surfaces of the femur and tibia contribute to the complicated structure and motion of the knee. The size and radius of the both condyles is not the same with the lateral

condyle being slightly smaller than the medial condyle. Each of these factors contributes the rotation of the femur with respect to the tibia during flexion and rotation of the femur about its long axis during flexion [31]. Figure 1.3 illustrates the anatomy of the knee.

1.2.3 Wear of the Total Knee Arthroplasty Prosthesis

As shown in the previous section, recent studies on TKA failure have shown that wear of the polyethylene insert continues to contribute to 25% of the revisions of TKA implants. Several studies by Peter Walker and others have demonstrated that the contact stresses in condylar total knee replacements can often exceed the yield stress of polyethylene (21 MPa) and have shown that cyclic sliding motion as opposed to rolling

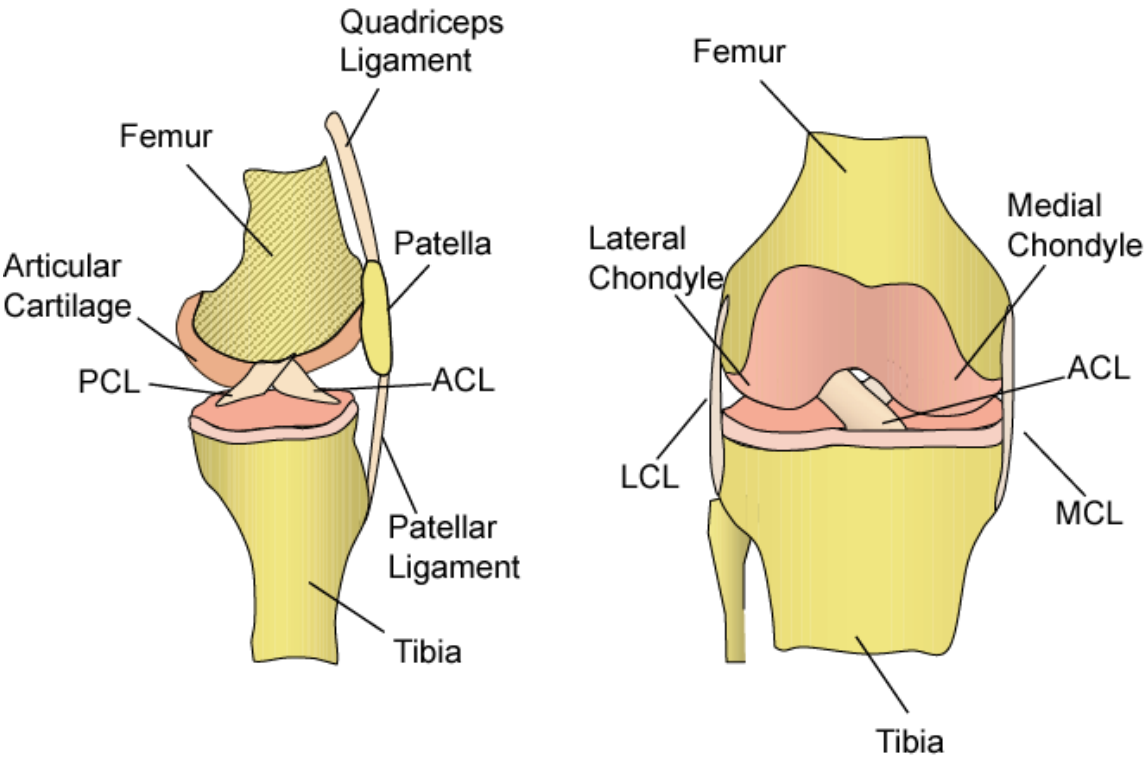

Figure 1.3: Anatomy of the knee including cruciate ligaments and collateral ligaments.

motions contribute to the greatest wear of the polyethylene insert [32,33,34,35,36]. Polyethylene wear in the TKA knee is also a function of surgical technique, implant kinematic patterns, sterilization techniques, material properties, design conformity, and contact area [37]. *In vivo* kinematic studies using video fluoroscopy give tremendous insight into the joint motions that may lead to increased wear. These motions include anterior as opposed to posterior femoral translation during deep flexion [38,39], internal as opposed to the normal external rotation during gait [40,41], femoral condylar lift-off [42,43,44,45], edge loading, and multidirectional sliding or shear forces [46,47]. Previous methods of studying wear include retrieval analysis [48,49], tribological wear simulators [50,51,52], computational simulation [53], static x-ray analysis [54,55], RSA [56,57,58], and video fluoroscopy [37,53,59,60].

Excessive implant wear may contribute to other failure mechanisms such as osteolysis, which may lead to implant loosening and failure or breaking of the bone supporting the implant [61]. Osteolysis occurs when exposure to wear debris stimulates an inflammatory response from macrophages and osteoclasts resulting in bone absorption around the implant. In a 2000 cell culture study, Hirashima demonstrated that incubating macrophages with 5 micrometer (μm) diameter particles simulating wear debris elicited the macrophages to release the inflammatory cytokines tumor necrosis factor-alpha (TNA-α) and interleukin-6 (IL-6). This study also showed that macrophages exposed to polyethylene particles did not have to come in contact with bone marrow cells to induce bone-absorbing osteoclast formation and resorption of the bone matrix [62,63].

Excessive wear may also be an indicator of other problems with the implant or implantation procedure. In Mulhall's recent study of failure modes in TKA revisions, 318 patients from multiple centers were assessed to determine the factors causing implant failure [15]. In this study, allowances were made for multiple causes pertaining to failure of the implant, and 64% of patients in this study had interrelated causes of failure. Similar to Sharkey's [8] findings, 24.5% of the participants in this study were primarily due to polyethylene wear. Of the subjects with excessive wear, 44% had coexisting instability, and 9.6% were subject to malalignment. 29% of patients with instability had loosening as a coexisting condition, and of those patients over half had coexisting osteolysis.

1.2.4 Contact Area and Stress Measurement

The contact stresses and pressures in the knee have been measured using a variety of technologies including cadaver studies with Fuji pressure-sensitive film, contact finite element studies, and Tekscan electronic pressure sensing film. It should be noted that the elastic limit of the polyethylene insert found in the patellar and femoral components ranges from 15 MPa-21 MPa. Jin, Stewart, and Auger, et al. evaluated the use of Hertzian contact stress theory on the contact stresses in the condyles. Using a loading of 1.5 times body weight on each condyle (1.5 kN load on each condyle), they correlated the major and minor condylar radii and insert thickness with the contact pressures and showed that it was common for the pressure to exceed the elastic limit of the insert by a factor of two or more if the radii of these components were not designed carefully [64,65]. A finite element study by D'Lima, Chen, and Colwell showed that contact stresses may range from 17-26 MPa for low conformity tibiofemoral implants and from 9.6-35.1 MPa for

high conformity implants [66]. Other studies found the contact stresses between the tibial and femoral components to be on the order of the yield stress of the polyethylene and exceed this stress under certain conditions [67]. A study on contact stress in patella replacements by Buechel, Pappas, and Makris showed that most patellar implants had line contact with the femoral components, and these had contact stresses greater ranging from 10-40 MPa for gait, 34 to greater than 60 MPa for stair ascent, and 45 to greater than 60MPa for deep flexion activities. The patella study found that the highly conforming DePuy, LCS patella had contact stress of approximately 3 MPa for all activities [68]. The findings of wear and contact studies for patella and tibial components are troublesome when the exponential relationship between contact stress and wear rate are considered [69], as well as the combined effects of wear particles, osteolysis, and component loosening.

1.2.5 Orthopedic Load Determination

The ability to determine *in vivo* forces and torques is necessary in order to predict the performance of new orthopedic implant designs, to determine the effects of orthopedic procedures and surgical parameters, and to understand the effects of load on the fundamental processes of bone growth and absorption and degenerative joint disease. Studies employing instrumented prosthetics and incorporating data telemetry produce the most direct method of determining implant loads. In the past, these devices have been expensive and not approved for use in a wide range of subjects [70].

Most research using instrumented implants has been performed using hip replacement prosthesis. Initial research was performed on the instrumented hip by Rydell

in 1966 using strain gages and leads passing through the skin [71]. The first use of telemetry to measure hip forces was by English and Kilvington, who measured peak loads of 2.56 times body weight during gate, but they did not publish their work extensively [72]. Another pioneer of *in vivo* force sensing using telemetry was German researcher Georg Bergmann. Bergmann has published research on hip loading using forces measured using strain gages. His instrumented prosthesis is powered using an inductive coil, and the measurements are sent to a personal computer using an RF telemetry system [73,74,75,76]. The power for this system is transmitted inside the limb using an inductive coil worn around the patient's leg during testing. Bergmann reported loads from two patients. His data showed that joint loads range from 2.8 to 4.8 times body weight depending on walking speeds. These loads increased to 5.5 times body weight with jogging, and stumbling caused hip loads to go as high as 7.2 times body weight [77,78]. Similar research on hip implants has been performed by Davy and Kotzar, and they implanted a similar hip prosthesis in two patients. Davy and Kotzar measured peak loads of 2.1-2.8 times body weight during gait and a maximum value of 5.5 times body weight during periods of instability during single leg stance [79,80].

The earliest work on measuring femoral loads was an extrapolation of the work performed on hip implants using massive femoral implants. Bassey, Littlewood, and Taylor instrumented a titanium implant which replaced the hip and the proximal half of the tibia. This implant used four foil strain gages bonded to a proximal internal cavity in two half-bridge configurations and a distal, intramedulary (inside the bone canal) extension to the prosthesis. The distal-femoral, intramedulary extension was the earliest

attempt to measure loading near the knee joint. This implant was powered using inductive coupling and allowed for the axial strain in the femoral prosthesis to be measured. Implant forces were measured at 2.5–4 times body weight during for jumping activities, 1.2 times body weight for treadmill gait activities, and 1.36–1.37 times body weight for stair climbing and descending activities [81,82]. Taylor performed a following study using an instrumented massive distal femoral replacement and found similar results [83,84].

Darryl D'Lima, MD and Clifford Colwell MD of the Scripps Clinic Center for Orthopeaedic Research and Education have recently published information regarding a tibial prosthesis instrumented with strain gages and telemetry. This was a ten-year project performed in collaboration with DePuy, Johnson and Johnson; Microstrain, Inc.; and NK Biotechnical. For this project, a tibial tray was modified by DePuy and instrumented by Microstrain, Inc. and Kenton Kaufman of NK Biotechnical [85]. The portion of the tibial tray comprising the tibial plateau was modified to function as a load cell. The tray was separated into upper and lower halves connected by four short rods. Material was removed from areas in the lower portion of the tray to form four diaphragms, and strain gages were attached to these areas, which resemble four load cells at the anteriomedial, anteriolateral, posteriomedial, and posteriolateral corners of the implant. The hollow portion of the stem of the tibial tray enclosed the electronics for this system. This system was powered using inductive coupling, and power was transmitted using a coil worn around the leg of the subject. This device appears to have been fabricated using off-the-shelf surface-mount electronic components [86,87].

Doctors D'Lima and Colwell implanted the instrumented tibial tray in an 80 year old male patient weighing 148 pounds. Six weeks following the implantation procedure, peak forces during gate averaged 2.2 times body weight. Stair climbing averaged 1.9 times body weight six days following the procedure and increased to 2.5 times body weight six weeks following the initial procedure [88].

1.3 Previous Research in MEMS Strain and Pressure Sensors

Previous work in the area of sensors for the measurement of strain and pressure have consisted primarily of piezoresistive, bulk-micromachined diaphragms, on-chip sensors for the measurement of process-induced surface stresses, and tactile sensors for robotic grippers. Fluid shear stress sensors have been investigated by researchers and aerodynamicists investigating flow measurement [89,90,91,92]. The Navy has investigated embedded strain sensors to determine the stress in composite materials [93,94,95,96]. There is also interest in measuring the pressure between amputated limbs and the socket of prosthetics [97]. This section reviews the recent research in this area.

1.3.1 MEMS Pressure Sensors

The literature contains several references to the application of microelectrical systems to the measurement of strain and pressure. Much of the early development on bulk micromachined silicon, diaphragm-based, sensors was performed at Motorola in the nineteen eighties by David Monk, John Gagg, Gordon Bitko, Andrew McNeil, and others [98,99,100]. These were silicon diaphragm-based MEMS pressure sensors for the

sensing of gas and liquid pressures. These devices consist of single sensors and are primarily designed to measure the air pressure in automobile tires or the pressure in a compressed gas cylinder or lines. They may have piezoresistive strain gages implanted in the membranes or measure the capacitance between the diaphragm and the surface below. Recently, MEMS pressure sensors are approaching maturity for some applications for example: automotive tire pressure sensing, manifold absolute pressure sensing, and barometric pressure sensing [101], as well as the recent applications in avionics [102,103,104,105].

1.3.2 Micromachined Strain Sensors

Microfabricated systems consisting of layers of thin films of various materials deposited under a variety of thermal conditions are subject to distortion due to coefficient of thermal expansion (CTE) mismatch effects. Residual strain existing in the thin films affects the device performances and is one of the most common properties to be characterized. Damage to microdevices may be caused by unacceptably high residual strains by buckling or warping, or other damage. A measurement device to monitor and characterize residual strain during microfabrication is crucial for sensitive applications. A Vernier mechanical-amplifier approach has been developed by Lin and Pisano from Berkeley whereby surface residual stress cause movement in a surface micromachined lever [106]. This concept for measuring chip surface strain in air was extended by the Berkley researchers using a double ended tuning fork resonant technique capable of resolving 33 nanostrain [107]. Gianchandani and Najafi optimized bent-beam sensors for the measurement of surface strain and achieved 60 microstrain resolution at 10 MPa

[108]. The University of Wisconsin has designed and fabricated a micromachined strain sensor with a series of capacitive tines that are connected at the ends to a deformable beam. Surface stresses induce an outward flexing motion in the beams supporting the tines, and the relative motion between opposing plates/tines results in capacitance changes [109].

1.3.3 Robotic Tactile Sensors

Researchers in the field of robotics have been interested in developing tactile sensor arrays to determine the forces exerted by robotic grippers, tele-operational manipulators, and haptic interfaces. A group of researchers at Stanford lead by Gregory Kovacs has developed a tactile sensing array for such an application. The 64 by 64 element array is capable of characterizing three components (normal pressure and out of plane shear) of the three-dimensional stress profile with a sensitivity range of 0.23-35 kPa for normal stress and 1.0-60 kPa for x and y direction shear. This array was fabricated on a silicon wafer using CMOS-compatible fabrication processes, uses four piezoelectric sensors per array element, and includes digital control circuitry fabricated in conjunction with the sensor elements [110]. Researchers at the University of Illinois have developed a polyimide-based, flexible sensor array with nickel-chrome resistors capable of measuring normal displacements [111]. An early three-axis, capacitance-based, tactile sensor was proposed by Chu, Sarro, and Middelhoek of Deft University, however their prototype had a force range of 0.01 N [112]. Recently, the University of Tokyo has developed a single-axis, flexible, pressure-sensing array based on organic field-effect transistors for artificial skin applications [113,114].

1.3.4 Embedded MEMS Strain Sensors

The US Office of Naval Research has funded recent research at the University of Minnesota to develop an embedded MEMS strain-rosette sensor to determine the structural integrity of composite materials in the hulls of submarines. This sensor is embedded 6 mm below the surface of a graphite composite plate. Since it is in the rosette configuration it can determine the maximum shear and principle strains in the plane of the sheet of material. Other requirements of the sensor were that it had to be powered externally (indefinite lifetime), have an insignificant effect on the structural integrity of the material in which it is embedded (less than 0.150 mm thick and an area less than 625 mm^2), a means to correlate the measured effects with the true effects in the structure, and the sensor package must withstand the fabrication process.

For this project, three sensor designs were explored. These included using a piezoresistive filament fabricated on the wafer surface and two capacitive cantilever designs including a rectangular cantilever and a curved cantilever beam. The sensor did not appear to be finalized before the project funding ended, and it seemed that several difficulties were left unresolved. These problems include strain shielding by the silicon substrate due to the high modulus of elasticity of the silicon as compared to the matrix material in the composite and a general insensitivity to compressive loads due to cantilever buckling and out of plane motion. This sensor system uses an RFID-based transponder and reader transmitting at 64 kHz and 128 kHz, respectively to power the sensor, transmit data, and receive data [93,94,95,96,115].

1.3.5 Microfabricated Sensors Summary

Previous researchers investigating miniaturized sensors for the measurement of strain, pressure, and displacement have performed excellent work. However, a sensing rosette capable of fully characterizing loads in three dimensions has yet to be developed. Previous traction sensors provide some ability to measure multi-axial loads, but suffer from crosstalk and hysteresis affects. The measurement range of previous sensors has been several orders of magnitude smaller than those required for the measurement of orthopedic loads. These effects are likely increased with the application of true three dimensional loading conditions. Previous work has not provided a pathway to low-power biocompatible implantable sensors of measuring the dynamic loads in orthopedic components.

1.4 Dissertation Objectives and Structure

The goal of this dissertation is to investigate capacitance-based sensing techniques which may be incorporated in the total knee arthroplasty prosthesis. These devices will help researchers understand the loads, contact areas, wear characteristics, and overall dynamics of the human knee. Implemented on a commercial scale, these sensors can be used to help patients achieve greater longevity from their knee implants, because interventions such as orthotics and physical therapy may be used to achieve optimum biomechanics and minimal wear.

Sensors embedded in orthopedic components have a challenging set of requirements to meet. They must sustain stresses of greater then 20 MPa, use biocompatible fabrication techniques, and have low power requirements. The compliance of the sensor should match the compliance of the material in which it is embedded or it will have lower response and contribute to stress concentrations in the device itself. Materials should be biocompatible and a strategy should be followed to allow for future FDA approval. Arrays of individually addressable sensors are required in order to understand contact areas and stresses, as well as the motions between components. These devices must be easily interfaced with signal conditioning and telemetry. The goal of this research is to investigate sensors which provide the pathway to meet these goals.

Chapter 1 of this dissertation introduces the challenges facing engineers and clinicians in duplicating the motion of the human knee. This chapter discusses the joint replacement components and procedures, mechanics, loading methods, and background on current measurement techniques. This information establishes the needs of the targeted application for this research. Chapter 1 proceeds to review previous research in the area of microfabricated sensors for the measurement of pressure and strain, Chapter 1 concludes with an overview of the dissertation structure and contributions.

Chapter 2, Analytical Modeling and Constitutive Equations for Capacitive Strain Sensors, discusses gives an overview of the proposed measurement method of these sensors. This chapter also examines analytical techniques for modeling the flux and potential of capacitance-based sensors. Finally, an analytical approach is used to determine the capacitance of an interdigitated sensor.

Chapter 3 examines the response of the capacitive strain sensor using the methods of micromechanics of composite materials. Analytical methods are used to couple the deformation response of the sensors to load with the results of the capacitance analysis in Chapter 2. Closed form solutions to the change in capacitance with applied load are developed in this section. The results are used to examine the sensitivity to applied load direction.

Chapter 4 uses numerical techniques to examine the response of the sensors discusses the results of the finite element design studies, the fabrication experiments, and testing of the devices. Parameter studies are conducted to determine the sensitivity of sensors to the various design parameters, and the sensitivity of load quantity and direction are evaluated. Results are discussed in the context of analytical solutions presented in Chapter 3.

Chapter 5 discusses the microfabrication approach to constructing the sensors discussed in this research. An emphasis is made on the use of currently accepted biocompatible materials. Contributions in the areas of fully biocompatible material fabrication are discussed.

In Chapter 6, the development of testing techniques for each of the three sensors is presented. The mechanical approach of the testing to produce the desired loading is discussed as well as the instrumentation for each test. Calibration curves for the sensors are shown, and the associated results are discussed.

Chapter 7 summarizes the work accomplished in this dissertation. Data from the analytical, numerical, and experimental results is presented together where possible. The next steps for research in this area are outlined.

1.5 Dissertation Contributions

A new class of sensors has been investigated which can be incorporated in a wide variety of devices to yield truly smart structures. Original contributions from this research have been made in the areas of microfabrication, analysis of capacitive structures, capacitance-based sensing, and multi-dimensional strain measurement. Several fields have the need for embedded sensors for the measurement of strain. In this research, a strain sensor has been investigated that is capable of fully characterizing the strain in three dimensions. Current commercial sensors are only capable of fully characterizing strain in two dimensions. This research has established fabrication techniques for embedding these microsensors in polyethylene materials through a plasma-based microtexturing process. This research has lead to greater understanding of the function of interdigitated capacitive structures and smart structures.

The design of three capacitance-based strain sensor elements was investigated including a parallel plate capacitive sensor for normal strain, a differential parallel plate capacitor for shear strain, and an interdigitated capacitor for in-plane strains. These three sensors when used together in an array are capable of determining the three-dimensional state of strain in the bulk material. An invention disclosure was written on early research in this area was submitted to the U.S. Patent Office. This invention disclosure was

awarded U.S. Patent Number 7,097,662 titled, “In-vivo orthopedic implant diagnostic device for sensing load, wear, and infection.”

An analytical solution for the fringing field of two offset parallel plate electrodes has been developed as part of this research. Also, a mathematical model has been developed to predict the micromechanics of high modulus of elasticity sensors embedded in lower modulus materials. A coupled mathematical model that relates the sensor micromechanics to changes in capacitance was developed for the three types of sensors, and sensitivity analysis of sensor geometries using the coupled mathematical model has been performed in order to optimize the device sensitivity. Also, the evaluation of embedded capacitive sensors for strain measurement in three orthogonal directions using multiphysics finite element analysis is presented in this dissertation.

Original contributions have been made in the area of MEMS fabrication techniques as part of this work. Techniques for patterning the biocompatible material parylene were developed using plasma etching. These techniques were used for the investigation and testing of capacitive sensors with a parylene polymer dielectric. Sensor fabrication using biocompatible materials was investigated, and a plasma-based microtexturing process for improved adhesion to biomedical-grade polyethylene was demonstrated. In this work, sensor electrodes were fabricated directly on the measurement polyethylene substrate material of interest as compared to fabricating sensors on intermediate materials. Features with 2.0 micrometer critical dimensions were patterned on polyethylene substrates as part of this work.

Testing methods for the evaluation of fundamental prototypes of the capacitive multiaxial strain sensors were also investigated. Methods were developed for applying

normal, in-plane, and multiaxial loads to the sensors for calibration purposes. The ability of the differential shear sensor to distinguish between out of plane shear and normal strain was demonstrated.

Chapter 2
Analytical Modeling of Capacitance-based Strain Sensors

2.1 Sensor Design and Operation Concepts

A multiaxial, capacitance-base, strain sensor has been investigated to aid in the understanding of the loads in orthopedic components. This chapter discusses the design of an array of capacitance-based sensors for the multi-axial characterization of strain. In this chapter, the sensor design and the general effects of strain on the capacitance of the sensor are discussed. Analytical techniques are used to develop relationships for determining the changes in capacitance with strain.

The sensing technique has been optimized for fabrication by the two dimensional lithography techniques used in microfabrication. Capacitance-based sensors were chosen for this project due to their lack of resistive heating, low power consumption, and the ability to fabricate the electrodes using biocompatible materials. Figure 2.1 shows the design concept for this project using parallel plate capacitors oriented in three orthogonal planes. Strain in the sensor results in capacitance change by varying the distance between the plates. The final sensors are fully encapsulated inside the component.

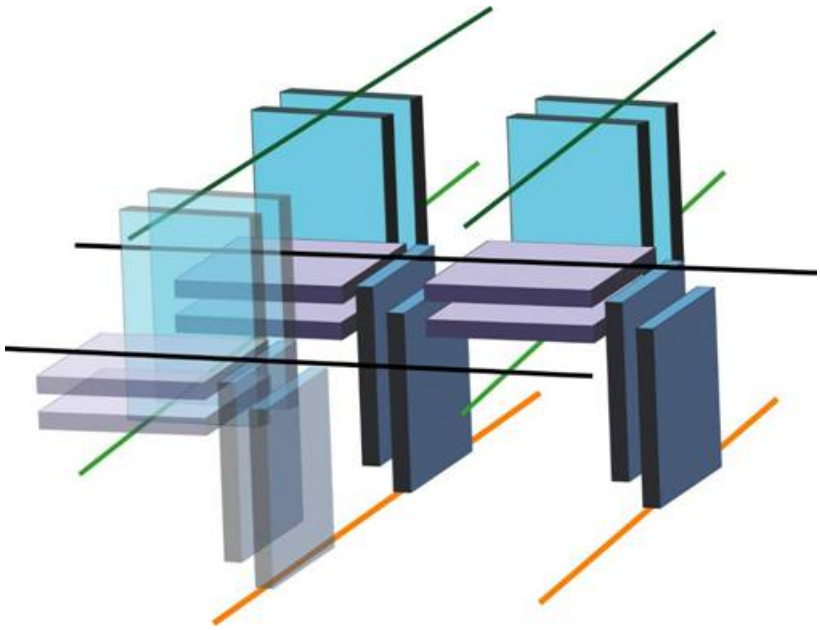

Figure 2.1: Design concept for multi-axial strain sensor array using capacitance detection techniques.

Analytical and numerical modeling techniques were used in this research to investigate the capacitance of the microfabricated electrodes. These techniques were also used to estimate the changes in capacitance from applied loading conditions. Two different methods were used for analytical modeling, these were the methods of continuum mechanics and conformal mapping methods.

For the concept shown in Figure 2.1, changes in capacitance may be measured as the distance between the electrodes changes as a result of induced strain. Several limitations exist in this concept. Three-dimensional microfabrication techniques have not reached sufficient maturity to fabricate the system shown. Also, to fully characterize the strain tensor in three dimensions, six sensors are required to solve for the three normal

strains and three shear strains, and shear strains are not measured in this configuration. We have investigated the use of three different sensors to solve for the normal, in-plane, and shear forces.

Figure 2.2 shows how the concept illustrated in Figure 2.1 may be collapsed into a plane such that it can be fabricated using MEMS techniques, and more detail about the function of these sensors is shown in Figure 2.3. A parallel plate capacitor is used to determine the strain normal to the plane of the sensors, s_{zz}. Two differential translating capacitors indicate the shear components out of the sensor plane, s_{zx} and s_{zy}. Three interdigitated capacitors function to determine the strains, s_{xx}, s_{yy}, and τ_{xy}.

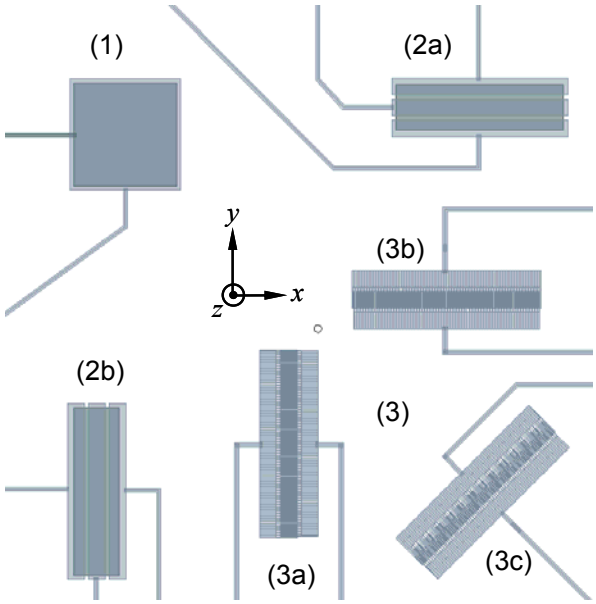

Figure 2.2: Multiaxial strain sensor with elements for three normal strains and three shear strains.

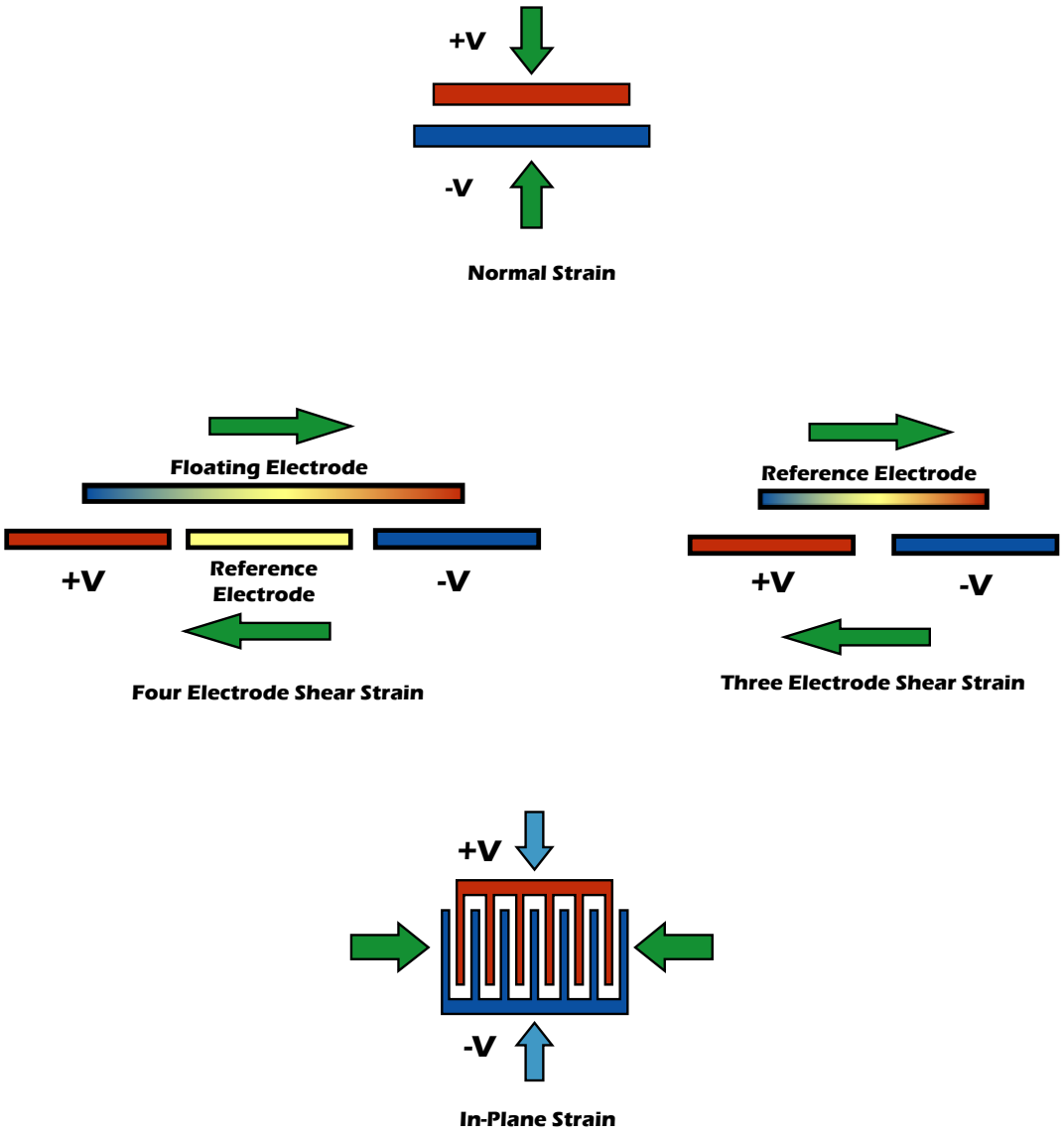

Figure 2.3: Illustration of capacitance function of the three sensor components.

As shown in Figure 2.3, normal strains are indicated by changes in capacitance as the distance between the electrodes in the parallel plate sensor changes. For this sensor, the lower plate is fabricated slightly larger than the upper plate to make this element insensitive to changes in the active area due to shear. An additional effect in this sensor is an increase in the size of the plates as a normal force is applied due to transverse strain.

Two configurations of the shear strain sensor are shown in Figure 2.3. There are advantages and disadvantages to both of these electrode configurations. The differential geometry used for the shear sensor has the ability to cancel out the effects of other strains and noise. For the four electrode shear sensor, a voltage is applied between the two outer electrodes labeled +V and -V, or potentially two out of phase sine waves. The upper electrode is electrically floating, and the center electrode, V_{ref}, indicates the measurement. Shear strains result in displacement of the upper electrode with respect to the lower electrodes, and causes a decrease in impedance on one side of the sensor and an increase in the other side. If the phase of the input signals is known, this difference can be used to indicate the measurement. This arrangement has no signal when it is balanced and motion of the upper plate relative to the lower ones yields a signal which has a sign indicating the direction of motion. Strains other than shear strains result in the same motion of the upper electrode with respect to the lower electrodes. The four electrode configuration has the advantage that all traces are in the lower plane and vias are not required. It also has lower effects from stray capacitance, however the four electrode shear sensor has a larger area than the three electrode configuration.

The three electrode shear sensor is shown in Figure 2.3 operates in a similar manner as the four electrode version and has the advantage of a more compact geometry.

This configuration has the advantage that multiple sets of electrodes in this configuration may be easily connected in parallel to amplify the change in capacitance. Vias may be required if all traces on the sensor are required to be in the same plane for connections and may result in inaccuracies in the measurement.

Sensor element three of Figure 2.3 is an interdigitated capacitor design. This design is used to approximate the vertical capacitors in Figure 2.1. As this element experiences strain, several effects may be present. If the stiffness of the electrodes is similar to the embedding media or the size of the features is small with respect to the embedding geometry, the size of the electrodes will change in relation to the strain placed on that media. This sensor geometry is sensitive to changes in strain in multiple directions. When strain occurs parallel to the direction of the interdigitated electrodes, the length of the electrodes increases or decreases causing changes in the capacitance of the sensor, and the transverse strain which is smaller then the normal strain by a factor of the Poisson's ratio causes changes in the gap between the electrodes. Strain in the direction perpendicular to the electrode digits results in a change in the gap between the electrodes and Poisson's ratio effects cause a change in the length of the electrodes. In these sensors, a significant fringe capacitance exists out of the plane of the sensor, as well as the primary capacitance between the sensor digits. Fringe effects are significant with these sensors and must be taken into consideration in any calculations or modeling. Optimization of this sensor is necessary to ensure that the sensitivity is preferential to the measuring direction, and to take into account the effects of stray capacitance and electrode dimensions.

2.2 Continuum Mechanics Modeling of Parallel Plate Capacitors

Continuum mechanics methods have been used previously to determine the capacitance between parallel conductors with an applied potential. Dielectric effects will be the primary factor in determining the performance of the capacitive sensor. Insulators or dielectrics differ from conductors due to the absence of free charges available for conduction. Dielectric materials do have fixed charges that determine the characteristics of the field with the material. The effect of applying an external field causes the electron clouds of the atoms of the material to shift causing the formation and alignment of electric dipoles within the material. The dipoles consist of a positive charge at the center of the nucleus separated by a negative charge at the center of the shifted electron cloud. The effect of the formation and alignment of dipoles within the material is referred to as polarization [116,117]. The degree and direction of alignment is given by the polarization vector, ***P***. These effects are illustrated in Figure 2.4. In Equation (2-1), the polarization vector is expressed in terms of ***E***, the electric field, and χ_e, the electric susceptibility.

$$\vec{P} = \chi_e \varepsilon_0 \vec{E} \tag{2-1}$$

Polarization causes an opposing electric field within the material and the sum of the applied field and the opposing field results in a net reduction in the electric field. This is similar to the double-layer effect in microfluidics. The flux lines in this system are not

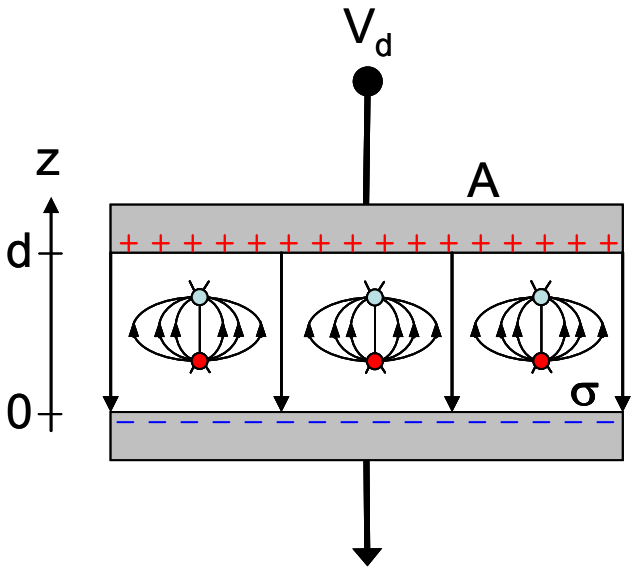

Figure 2.4: Cross section of a parallel plate capacitor showing dipole formation and surface charge distribution when a voltage, V_d, is applied across the plates.

changed, however. The effect of the dielectric material polarization on the flux density, ***D***, can be seen in the following relation:

$$\vec{D} = \varepsilon_0 \vec{E} + \vec{P} \tag{2-2}$$

The susceptibility and polarization are fundamental to understanding the influence of the dielectric material on the field. Equations (2-1) and Equation (2-2) can be combined into Equation (2-3).

$$\vec{D} = \varepsilon_0 (1 + \chi_e) \vec{E} = \varepsilon_r \varepsilon_0 \vec{E} = \varepsilon \vec{E} \tag{2-3}$$

ε is the permittivity of the material and is related to the free space permittivity by the factor ε_r. The relative permittivity is related to electric susceptibility by Equation (2-4).

$$\varepsilon_r = 1 + \chi_e \tag{2-4}$$

The boundary conditions applied to the structures determine the electric fields existing within the device. In our case, the voltage applied between multiple structures will be the primary known boundary conditions. These structures will be separated by a known dielectric material. Poisson's equation and Laplace's equation can be used to determine the potential function when the conditions at the boundary are known.

The divergence expression is given in Equation (2-5) below where ρ_v is the charge density in the volume containing the dielectric material.

$$\nabla \cdot \vec{D} = \rho_v \tag{2-5}$$

Given that $\boldsymbol{D}=\varepsilon \boldsymbol{E}$, Equation (2-6) can be written as shown below.

$$\nabla \cdot \vec{E} = \frac{\rho_v}{\varepsilon} \tag{2-6}$$

It is also known that the electric field is a function of the potential field by the gradient expression.

$$\vec{E} = -\nabla V \tag{2-7}$$

Equation (2-7) can be inserted into Equation (2-6) to give Poisson's equation shown in Equation (2-8).

$$\nabla \cdot \nabla V = \nabla^2 V = \frac{-\rho_v}{\varepsilon} \tag{2-8}$$

The total charge in the medium will be zero (ρ_v=0), and Equation (2-8) results in Laplace's equation shown below.

$$\nabla^2 V = 0 \tag{2-9}$$

The Laplacian operator can be expanded into Cartesian coordinates by the following:

$$\nabla^2 V = \frac{\partial^2 V}{\partial x^2} + \frac{\partial^2 V}{\partial y^2} + \frac{\partial^2 V}{\partial z^2} \tag{2-10}$$

Using the parallel plate geometry shown in Figure 2.4**,** Equation (2-10) reduces to:

$$\frac{\partial^2 V(z)}{\partial z^2} = 0 \tag{2-11}$$

Integrating Equation (2-11) once, yields Equation (2-12).

$$\int \frac{\partial^2 V(z)}{\partial z^2} = \frac{\partial V(z)}{\partial z} = C_1 \tag{2-12}$$

A second integration is shown below.

$$\int \frac{\partial V(z)}{\partial z} = V(z) = C_1 z + C_2 \tag{2-13}$$

The constants of integration, C_1 and C_2, can be determined by employing the boundary conditions. $V(d)=V_d$, and $V(0)=0$. Applying $V(0)=0$ gives a value of 0 for C_2, and $V(d)=V_d$ gives a value of V_d/d for C_1. For the following equations, d represents the distance between the plates.

$$V(z) = \frac{V_d z}{d} \tag{2-14}$$

The electric field intensity can be determined by the gradient equation,

$$\vec{E} = -\nabla V = -\frac{\partial}{\partial z}\left(\frac{V_d}{d} z\right)\vec{k} = -\left(\frac{V_d}{d}\right)\vec{k} \tag{2-15}$$

The electric flux density can then be determined:

$$\vec{D} = \varepsilon\vec{E} = -\varepsilon_r\varepsilon_0\left(\frac{V_d}{d}\right)\vec{k} \tag{2-16}$$

For parallel plate case, the flux density and the surface charge density are equal resulting in Equation (2-17).

$$\rho_s = \varepsilon_r\varepsilon_0\left(\frac{V_d}{d}\right) \tag{2-17}$$

The total charge on an individual conductor can be found by multiplying the surface charge density by the area, *A*.

$$Q = \frac{\varepsilon_r\varepsilon_0 V_d}{d} \tag{2-18}$$

The capacitance is the ratio of the charge on one of the plates to the voltage applied, between the plates, however the capacitance, *C*, is a constant for fixed electrode and dielectric geometries.

$$C = \frac{Q}{V} \tag{2-19}$$

$$C = \frac{\varepsilon_r\varepsilon_0 V_d A}{dV_d} = \frac{\varepsilon_r\varepsilon_0 A}{d} \tag{2-20}$$

2.3 Potential and Electric Field Evaluation Using Conformal Mapping

Conformal mapping is a robust technique that allows one to map Laplacian fields from areas that are readily solved to more complicated regions and geometries where a solution is desired. In complex analysis, a conformal map is a transformation function in which angles and the relative proportions of neighboring small line segments are preserved as a function is mapped from one region to another. Conformal mapping techniques are an extension of the Riemann mapping theory of complex analysis which states that any non-empty, open, simply connected subset of the complex plane there exists a one-to-one mapping from the subset to the unit disk. Mapping functions must be analytic functions (single-valued and differentiable) in the reason of interest, or at least single-valued on a Riemann surface [118].

Bernhard Riemann developed the Riemann mapping theorem for his doctoral dissertation in 1851. Since this time, high-speed computers and finite element analysis have become common engineering tools and have gained wide acceptance for solving both structural and electrostatic problems. In this research, techniques are investigated which yield an analytical solution to the problem of changing capacitance with strain. An analytical solution to these problems allows one to very rapidly estimate the capacitance conditions for a large variety of electrode geometries and materials. Analytical solutions also give insight into the numerical algorithms that will be required to interpret the results from these sensors upon implementation. Figures 2.5 and 2.6 illustrate the mapping of the W plane to the T plane using the complex mapping function, $t=e^{w}$, where $w=u+jv$. In the W plane, complex values range from 0 to pi and real values range from 0 to 1.

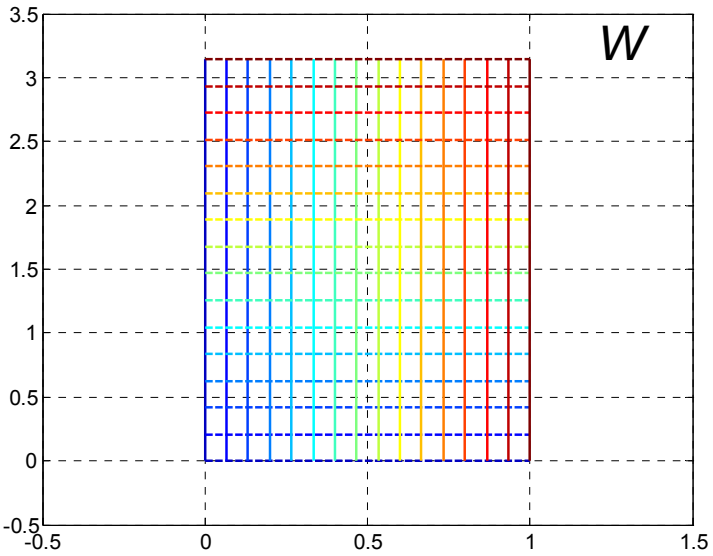

Figure 2.5: Rectangle in upper right quadrant of complex plane, *W*.

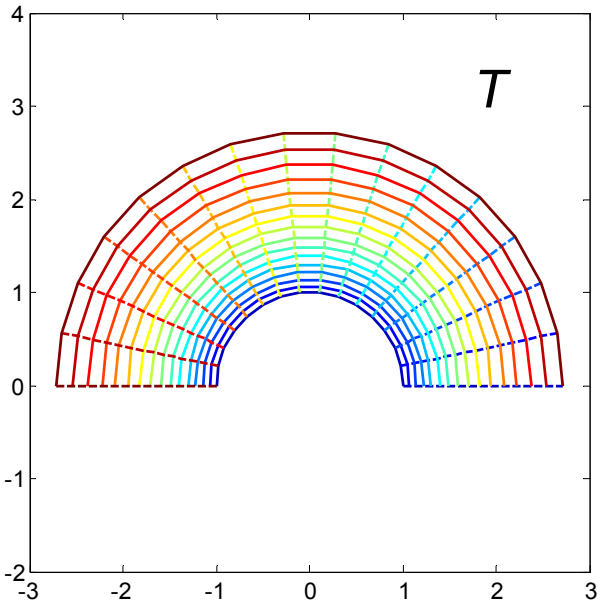

Figure 2.6: Rectangle mapped to exterior of unit circle on upper half of complex plane, *T*, using the transformation $t=e^{w}$.

In Figures 2.5 and 2.6, the colored solid and dashed lines are preserved between planes to indicate the mapping of regions from W plane to the T plane. This equation was plotted using Matlab programming software (The MathWorks, Inc. Natick, Massachusetts). The Matlab codes used in this research are presented in the Appendix.

More complicated functions may be required to solve for the fields encountered in common problems. The difficulty then lies in deriving the equations for the mapping functions which allows one to relate a given field to another field for which the solution is known. It is not always possible to find a single equation that directly maps the field of interest to one which is readily solved, and is sometimes required to map these fields through intermediate planes, geometry shapes, and variables. In this work, the W plane is used to refer to a plane which is readily solved, the T plane is used to represent an intermediate plane, and the Z plane is used to represent the plane of the desired solution.

2.3.1 Schwarz-Christoffel Mapping

Many fields are commonly encountered which are bounded by straight line segments or which may be treated as being bounded by straight line segments, even if these segments "meet" at infinity. For these types of geometries, a method was developed independently by both Schwarz [119] and Christoffel [120] for determining the differential equations describing the field transformation to an intermediate plane. These equations must then be integrated and constants of integration and a scaling factor inherent in the technique must be solved for using the boundary conditions of the problem. Using the methods developed by Schwarz and Christoffel, the differential

equation can be determined for most fields within polygonal boundaries, however integrating these equations may not be possible by analytical means.

A brief description of the Schwarz-Christoffel transformation will be given followed by application to specific problems of interest to this research in the following sections. Mapping of an arbitrary polygon from the Z plane to the t axis of the T plane is shown below in Figure 2.7. This transform is followed by mapping from the T plane to the W plane. Most effort is required determining the transformation from the Z plane to the T plane and an exponential transformation as previously shown is generally used between the T plane and the W plane. It is important that the relative proportions of neighboring small line segments and the angles of intersecting line segments be preserved during transformation. These dimensions and angles are determined by the integration parameters and by the choice of intermediate mapping points.

The general form for the differential equation for mapping the interior of a polygon using the Schwarz-Christoffel mapping technique is given by Equation (2-21). Solution of this differential equation is shown in Equation (2-22). For the geometry of Figure 2.7 and similar geometries, the vertices of the polygon are labeled and the corresponding exterior angles of the vertices are determined while traversing the geometry in the counter clockwise direction. Arbitrary locations for the mapping of these vertices may be selected on the t axis for problems with up to three vertices, and analytical solutions can often be derived for these problems. However, the selection of the values of the T plane points determines how difficult it may be to integrate the resulting equations. The values $-\infty$, -1, 0, 1, and ∞ are used frequently for the transformation values of T plane points or parameters. The scaling issues resulting from

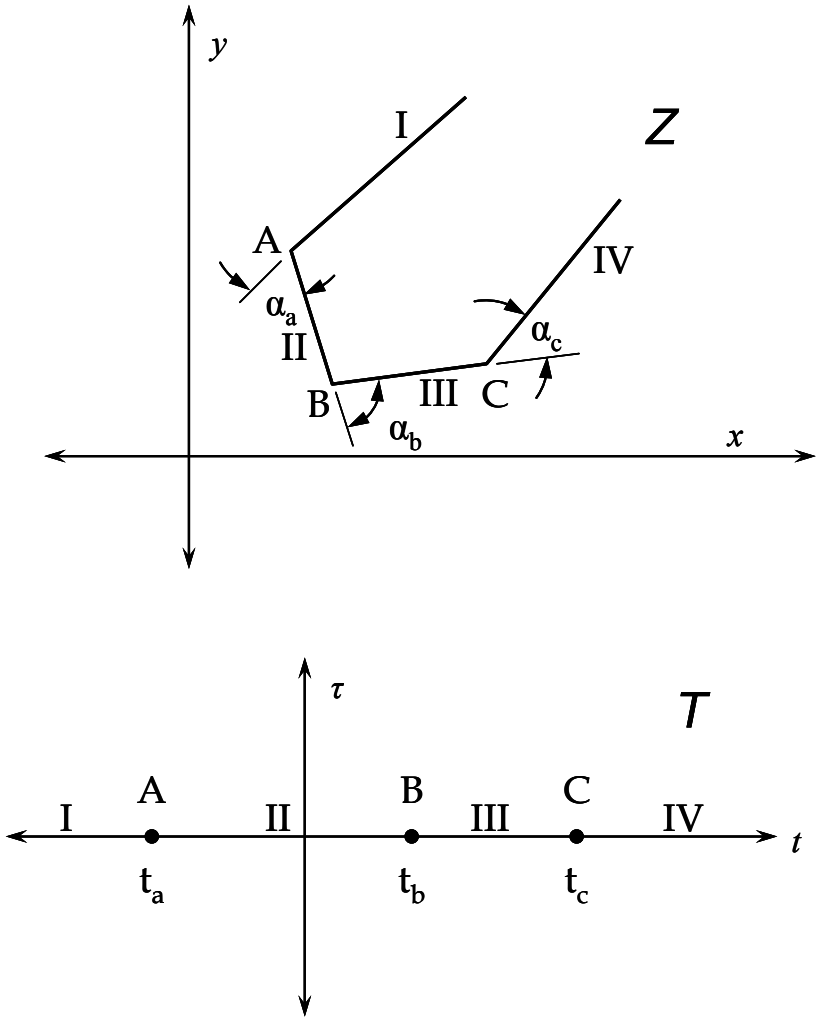

Figure 2.7: Mapping of a polygon in the Z=x+jy domain to the T=t+iτ domain.

these choices are taken into consideration when the scaling and integration constants are determined. The selection of a value of infinity on the t axis for mapping vertices causes the terms associated with this point to reach a value of 1 as t_k approaches infinity and these terms may be neglected. Mapping of the geometry shown in Figure 2.7 is given by Equations (2-23) and (2-24).

$$\frac{dz}{dt} = C_0 \prod_{k=1}^{n} (t - t_k)^{\frac{-\alpha_k}{\pi}} \tag{2-21}$$

$$z(t) = C_0 \int_{t_0}^{t} \prod_{k=1}^{n} (t - t_k)^{\frac{-\alpha_k}{\pi}} + C_1 \tag{2-22}$$

$$\frac{dz}{dt} = C_0 (t - t_a)^{\frac{-\alpha_a}{\pi}} (t - t_b)^{\frac{-\alpha_b}{\pi}} (t - t_c)^{\frac{-\alpha_c}{\pi}} \tag{2-23}$$

$$z(t) = C_0 \int_{t_0}^{t} (t - t_a)^{\frac{-\alpha_a}{\pi}} (t - t_b)^{\frac{-\alpha_b}{\pi}} (t - t_c)^{\frac{-\alpha_c}{\pi}} dt + C_1 \tag{2-24}$$

For mapping polygons containing more than three vertices, only three of the T plane points or parameters may be chosen arbitrarily. Other points must be chosen using iterative techniques and the complexity of this approach increases significantly. Integrals with singularities must often be integrated numerically as part of parameter solution

problem, and the process must be repeated for any change in geometry. Once parameters are determined, the resulting integrals are not capable of solution and involve both variables in the complex plane or planes. The derivation of these mapping techniques has been the topic of several references and dissertations. More detailed treatments of this approach can be found in these references [121,122,123].

2.3.2 Mapping of Parallel Plate Capacitor Fringe Capacitance

Conformal mapping techniques can be used to solve for the fringe capacitance of a parallel plate capacitor. Maxwell explored alternate analytical solutions to this problem in his Treatise on Electricity and Magnetism [124]. This problem is a common example of a practical application of Schwarz-Christoffel mapping, and the solution may be compared to Maxwell's analytical version. However in most previous work, symmetry is used between the upper and lower plates to further simplify the problem. For this research, the field above and below both plates is analyzed such that the result may be extended to non-symmetric cases in which the plates are of different sizes. This problem may be fully solved using the Schwarz-Christoffel mapping technique due to the ability to use three points to represent the geometry. The use of thin, semi-infinite plates allows this problem to be represented using techniques reserved for polygons with three sides. A single point is used to represent the inner point at minus infinity of the inner and outer sides of the plates, points A and C in Figure 2.8. In the T plane, point A is assigned to $\pm\infty$, B is assigned to -1, C is assigned to the origin in the T plane, and D is assigned to 1. The angles for these vertices in Z plane are 2π for vertex A, $-\pi$ for B and D, and π for C.

The geometry shown in Figure 2.8 was used for the transformation. These values may be substituted into Equation (2-22) to give Equations (2-25) through (2-26).

$$\frac{dz}{dt} = C_0(t+1)^{\frac{\pi}{\pi}}(t-1)^{\frac{\pi}{\pi}}(t-0)^{\frac{-\pi}{\pi}} \tag{2-25}$$

$$z(t) = C_0\int_{t_0}^{t}\frac{(t^2-1)}{t}dt + C_1 \tag{2-26}$$

Integrating Equation (2-26) leads to Equation (2-27), below.

$$z(t) = C_0\left(\frac{1}{2}t^2 + \ln(t)\right) + C_1 \tag{2-27}$$

For the geometry shown in Figure 2.8, the constant C_0 can be solved by integrating between the points B and D. C_1 can be moved inside the parenthesis and solved by substitution to give Equation (2-28). The equation for transformation from the Z to the T plane is given by:

$$z(t) = \frac{d}{\pi}\left(\frac{1}{2}t^2 + \ln(t) + \left(\frac{j\pi}{2} - \frac{1}{2}\right)\right) \tag{2-28}$$

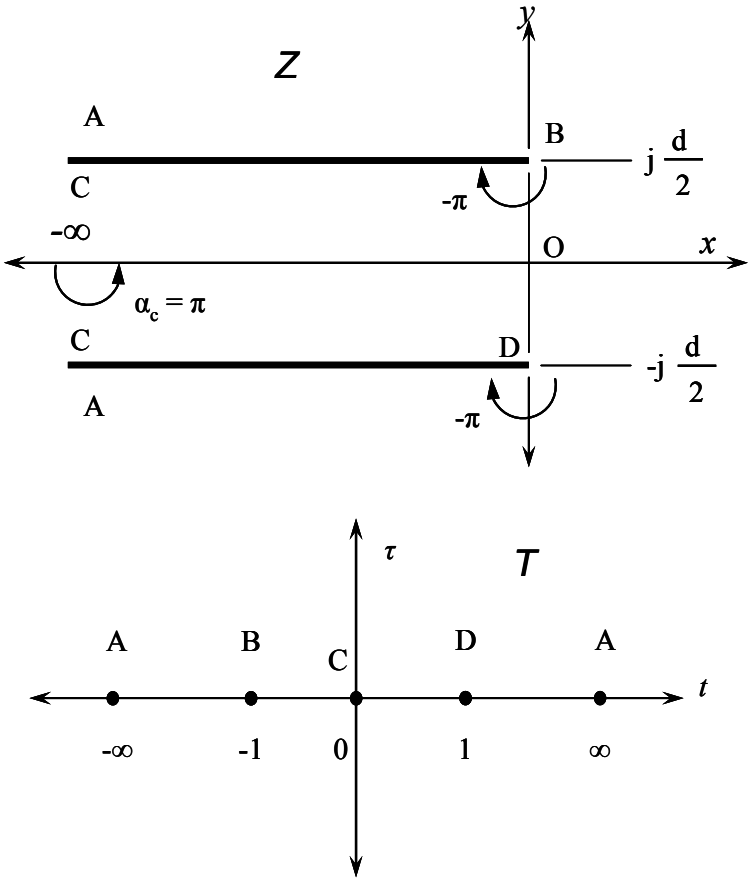

Figure 2.8: Mapping of semi-infinite parallel plates from the z plane to the T plane.

A second transformation is required from the T to W plane. This is accomplished using the exponential transformation, $t=e^{w}$, shown Figure 2.6. This gives the final transformation equation from the Z plane to the W plane as shown in Equation (2-29).

$$z(w)=\frac{d}{\pi}\left(\frac{1}{2}e^{2w}+w+\left(\frac{j\pi}{2}-\frac{1}{2}\right)\right) \tag{2-29}$$

This equation is plotted in Figure 2.9. Plots for equations in this section were performed in Matlab. Simple algorithms were used to create the grids shown in the following illustrations. Complex notation was used for all coordinates in the original plane. The original grid was transformed using the derived transformation equation and plotted again using the same coloring and dashed or solid lines as in the original plane.

2.3.3 Mapping of Fringe Capacitance for Parallel Plate Capacitors of Unequal Size

For the embedded strain sensor, it may be advantageous to make one of the plates in the parallel plate capacitor slightly larger than the other plate. This would have the advantage of eliminating the effects of shear which might cause one plate to shift slightly with respect to the other plate. In this section, we examine modeling the fringe capacitance of the parallel plate capacitor with offset plates by conformal mapping techniques. This is accomplished using the techniques presented in previous sections, however the loss of symmetry in the problem results in an added complexity. The geometry for this mapping is shown in Figure 2.10.

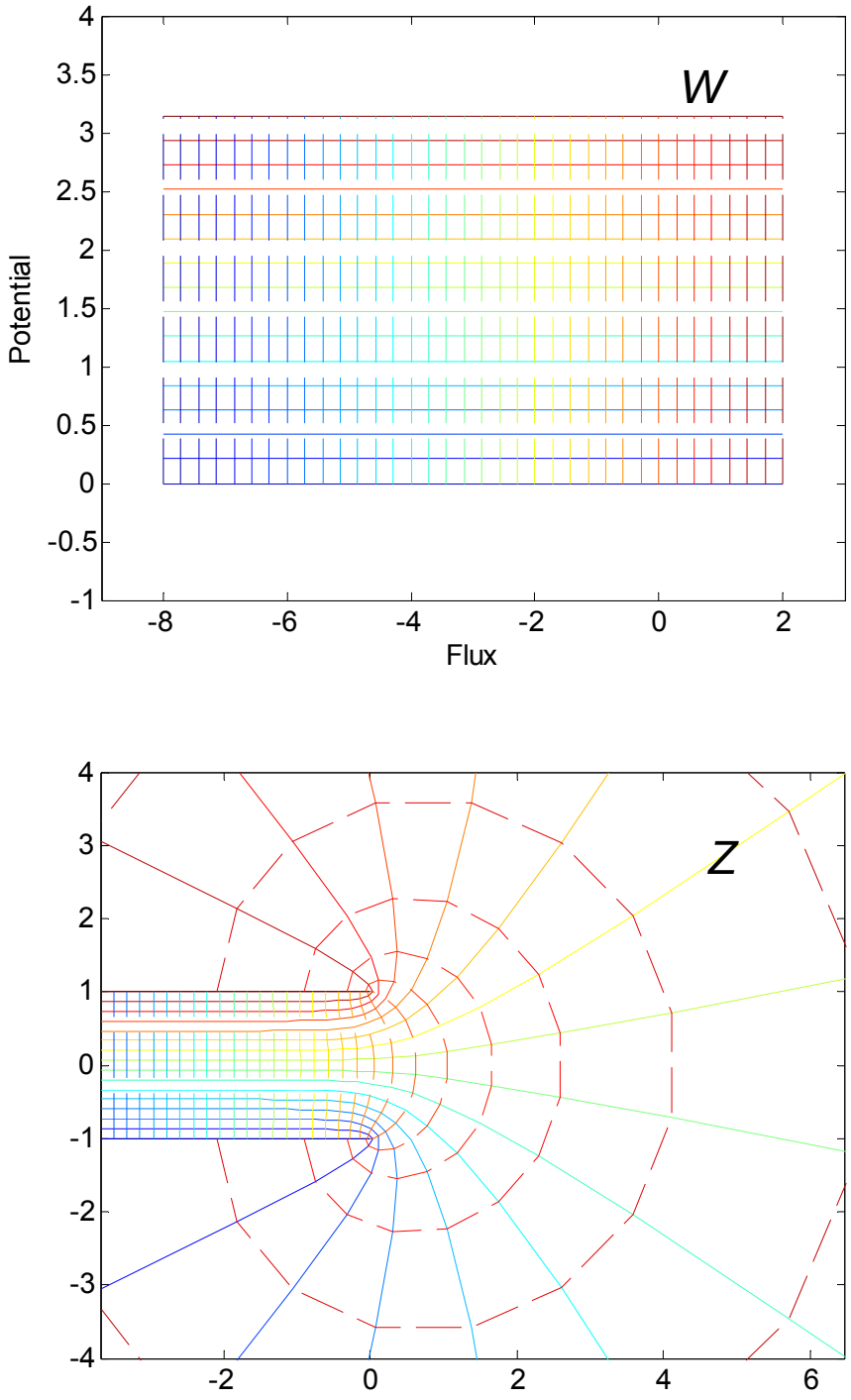

Figure 2.9: Plot of transformation of equipotential and flux lines from *W* plane to *Z* plane using Equation (2-29).

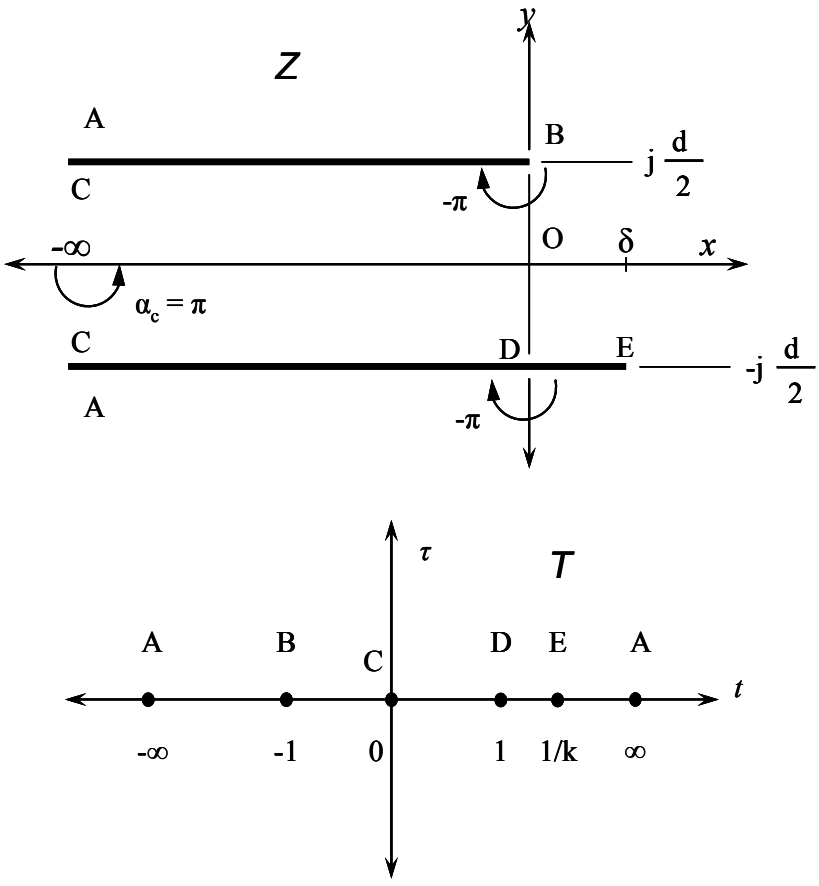

Figure 2.10: Geometry used for mapping from the T plane to the Z plane for a semi-infinite parallel plate capacitor with plates of unequal length.

For this geometry, the resulting differential equation is shown below in Equation (2-30). This differential equation may be solved by integration as previously shown, however this results in three unknown constants, C_0, C_1, and k, which must be determined. These may be determined by solving a system of nonlinear equations using points B, D, and E to determine the values. In this case, C_0 and C_1 may be determined in terms of k. Iterative techniques are used to determine the final parameters including k.

$$z(t) = C_0 \int \frac{(t+1)(t-1/k)}{t} dt + C_1 \tag{2-30}$$

$$z(t) = \frac{d}{\pi}\left(\frac{1}{2}t^2 + \left(1 - \frac{1}{k}\right)t - \frac{1}{k}\ln(t) + C_1\right) \tag{2-31}$$

C_0 and C_1 may be determined in terms of k. The final value of k is then determined iteratively. Equations (2-32) and (2-33) represent C_0 and C_1 in terms of k, the plate spacing, d, and the lower plate offset δ.

$$C_0 = \frac{jd - \delta}{\frac{1}{2k^2} + \frac{1}{k}\ln(k) - \frac{j\pi}{k} - \frac{1}{2}} \tag{2-32}$$

$$C_1 = \frac{jd}{2} - C_0\left(\frac{1}{k} - \frac{j\pi}{k} - \frac{1}{2}\right) \tag{2-33}$$

A second transformation is required from the T plane to the W plane using the exponential transformation, $t=e^{w}$. This yields the transformation equation from the Z plane to the W plane as shown below in Equation (2-34) and is plotted in Figure 2.11.

$$z(w)=\frac{d}{\pi}\left(\frac{1}{2}e^{2w}+\left(1-\frac{1}{k}\right)e^{w}-\frac{1}{k}w+C_1\right) \tag{2-34}$$

2.3.4 Analytical Solution of the Capacitance and Electric Field of Two Thin, Finite, Charged Plates

An analytical solution for the capacitance between two thin, finite, charged plates can be determined using similar methods to those discussed in the previous section. This is the two-dimensional representation of two thin, parallel conductors lying in the same plane. The traditional notation and methods used by Maxwell, Binns, and Schinzinger are used in this section and expand upon these previous works [124,118,121,125]. This geometry may be solved with a single transformation of the idealized field between two parallel plates with no fringing to that of two finite conductors lying in the same plane. The geometry used for this analysis is shown in Figure 2.12. The flux, φ_0, will be regarded as an unknown that will be solved for using the geometry and boundary conditions in the transformation plane, which will ultimately lead to an analytical solution for the capacitance. To determine the capacitance the initial transformation will be inverted using Jacobian elliptical functions. In the Z plane, the x and y axes may also

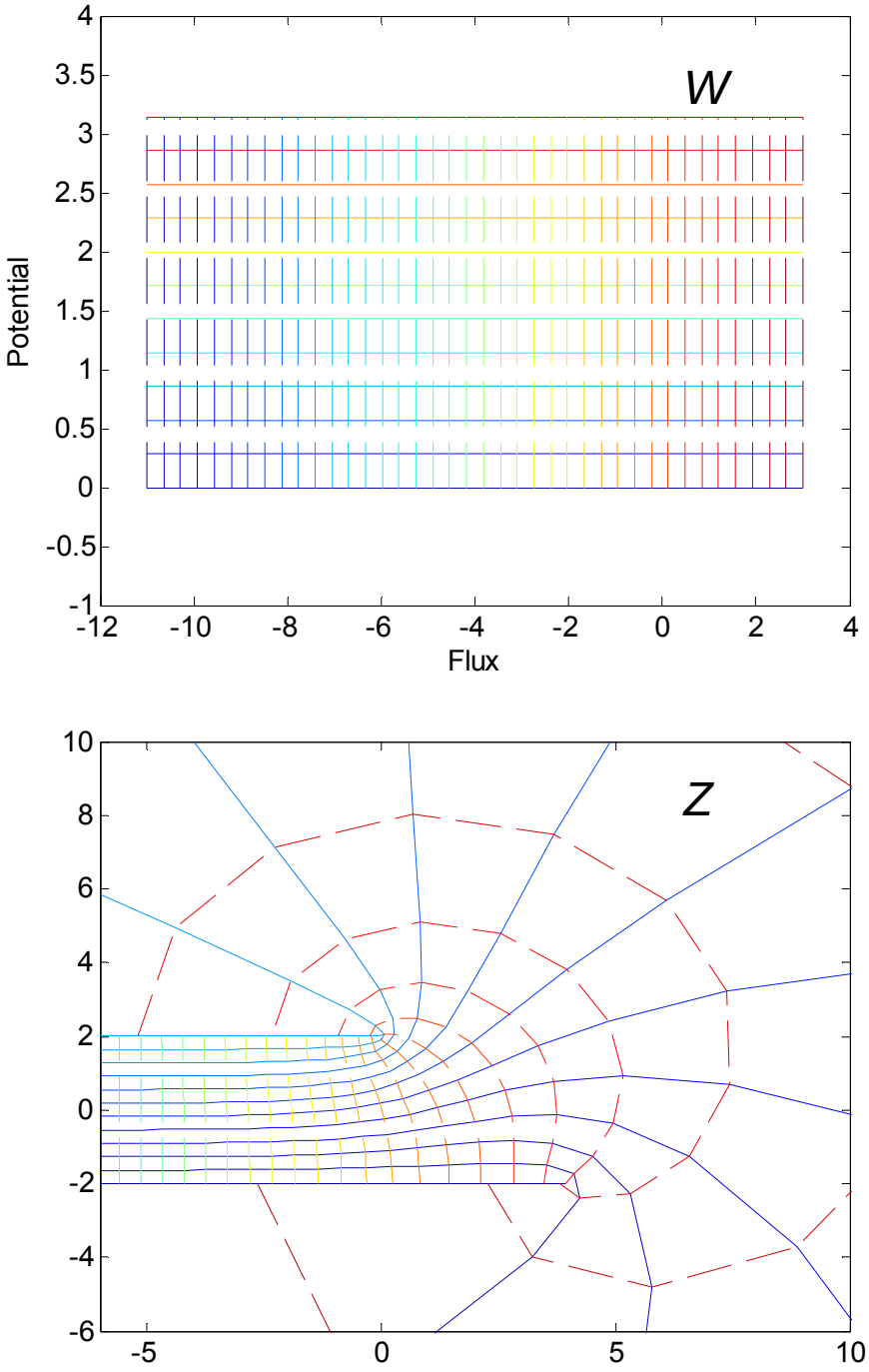

Figure 2.11: Plot of transformation of equipotential and flux lines from *W* plane to *Z* plane for parallel plate capacitor with unequal plate sizing.

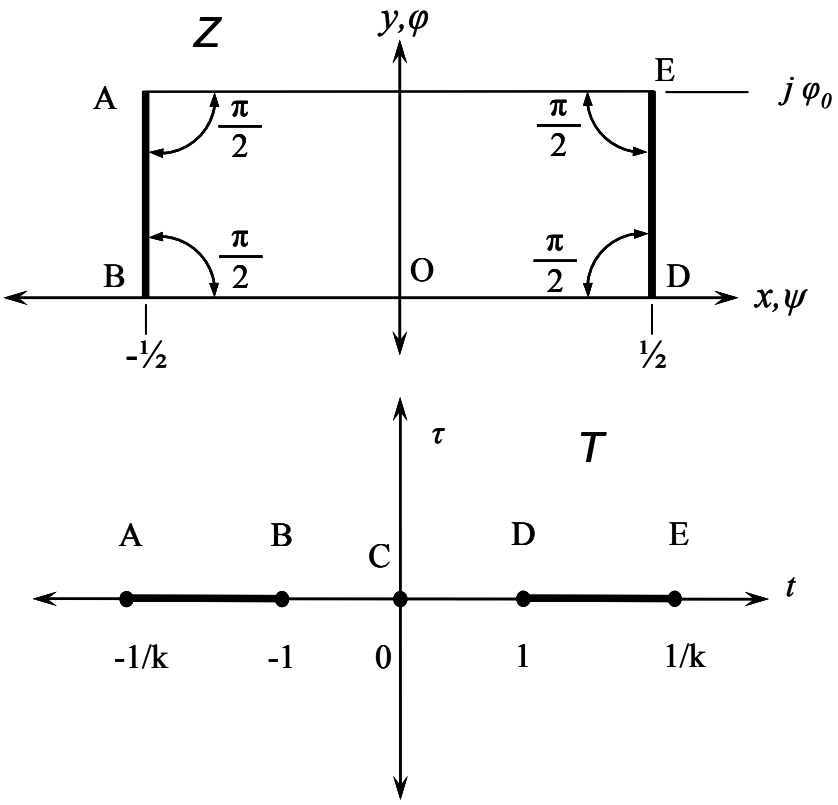

Figure 2.12: Geometry used to determine the capacitance and flux between two thin electrodes in the same plane.

be envisioned as representing the potential and the flux of the system. For this system, the potential between the plates will be set at 1.

The differential equation resulting from this configuration is shown below in Equation (2-35). Simplification of Equation (2-35) yields Equation (2-36). Multiplying by *k/k* and substituting *B* for kC_0 yields the typical form of the elliptical integral of the first kind as studied by Legendre and Jacobi as shown in Equation (2-37).

$$\frac{dw}{dt} = C_0\left(t + 1/k\right)^{\frac{-\pi/2}{\pi}}(t+1)^{\frac{-\pi/2}{\pi}}(t-1)^{\frac{-\pi/2}{\pi}}\left(t - 1/k\right)^{\frac{-\pi/2}{\pi}} \tag{2-35}$$

$$w(t) = C_0\int \frac{1}{\sqrt{\left(t^2-1\right)\left(t^2-1/k^2\right)}}dt + C_1 \tag{2-36}$$

$$w(t) = B\int_0^t \frac{1}{\sqrt{\left(1-t^2\right)\left(1-k^2t^2\right)}}dt \tag{2-37}$$

Elliptic functions were first encountered in the calculation of the length of the arc of an ellipse. The use of $\pm 1/k$ for the position of B and D in the T plane leads to the commonly used Jacobian form of this equation, whereby *k* is the modulus of the ellipse and found from a relationship between the lengths of the major and minor axes of the ellipse.

For a general upper limit, this integral is often referred to as incomplete, whereas an upper limit of 1 corresponds to the complete elliptical integral of the first kind. This integral may be used to determine the entire arc length of an ellipse. The value of the complete elliptical integral of the first kind is often referred to as *K* or *K(k)*, as shown in Equation (2-38).

$$K = C_0 \int_0^1 \frac{1}{\sqrt{\left(1-t^2\right)\left(1-k^2t^2\right)}}\,dt \tag{2-38}$$

The complementary modulus, k', is also useful in analytical solutions and can be determined from the modulus as shown in Equation (2-39).

$$k' = \sqrt{1-k^2} \tag{2-39}$$

The complete integral to the complementary modulus, k', can be found by two different methods as shown below. This constant is useful when determining the transformation constants.

$$K' = \int_0^1 \frac{1}{\sqrt{\left(1-t^2\right)\left(1-k'^2t^2\right)}}\,dt \tag{2-40}$$

$$K' = \int_1^{1/k} \frac{1}{j\sqrt{\left(1-t^2\right)\left(1-k^2t^2\right)}}\,dt \tag{2-41}$$

$$K + jK' = \int_0^{1/k} \frac{1}{\sqrt{\left(1 - t^2\right)\left(1 - k^2 t^2\right)}} dt \tag{2-42}$$

Jacobi observed that elliptical integrals could be beneficial in analytical work, but that also the inverse functions could be beneficial as well. He derived a series of elliptical functions based on the inverse of the elliptical integrals. Jacobi defined a new function, sn, (pronounced "ess-en") to be a function of the inverse of the elliptical integral of the first kind. Values of this function may be determined through tabulated values or from series expansions. Therefore if *w* is a function of the elliptical integral of t and k as shown in Equation (2-36), t is an elliptical function of *w* and *k* as shown in Equation (2-43).

$$t = sn\left(w, k\right) \tag{2-43}$$

For this application, we need to find the inverse transformation from z to t, and this is possible using the Jacobian elliptic functions. Applying the relation in Equation (2-43) to Equation (2-36) results in the following:

$$t = sn\left(\frac{w}{B}\right). \tag{2-44}$$

The Jacobian elliptic function can now be applied to find the inverse of Equation (2-42).

$$sn(K + jK') = \frac{1}{k} \tag{2-45}$$

Equation (2-44) can be used to solve for B, by substituting $1/k$ for t using the boundary conditions in Figure 2.12 which show that point E or $1/k$ in the T plane maps to $½+j\varphi_0$ in the Z plane. Therefore, when $t=1/k$, $w=½+j\varphi_0$, leads to Equations (2-46) through (2-48).

$$1/k = sn\left(\frac{1/2 + j\varphi_0}{B}\right) \tag{2-46}$$

$$sn(K + jK') = sn\left(\frac{1/2 + j\varphi_0}{B}\right) \tag{2-47}$$

$$K + jK' = \frac{1/2 + j\varphi_0}{B} \tag{2-48}$$

The unknown constant, B, may be determined by equating the real and imaginary parts of Equation (2-48) resulting in Equations (2-49) and Equation (2-51). The total flux for the system can be solved for in terms of K' and K.

$$B = \frac{1}{2K} \tag{2-49}$$

$$\frac{\varphi_0}{B} = K' \tag{2-50}$$

$$\varphi_0 = \frac{K'}{2K} \tag{2-51}$$

Since φ_0 is found using the complete elliptic integrals it represents the total flux of the surface of the electrode. Gauss's law can be applied to determine the charge of the system followed by the capacitance.

$$q = \varepsilon_r \varepsilon_0 \varphi_0 \tag{2-52}$$

Because $q=CV$ and the difference in potential was defined as one, the capacitance per unit length of the system is determined by:

$$C = \varepsilon_r \varepsilon_0 \frac{K'}{2K} \tag{2-53}$$

For this problem, it was assumed that plates were "thin". It is possible to develop a relationship that includes the effects of thick, three-dimensional electrodes by summing the sidewall capacitance and the fringe capacitance as shown below. L represents the electrode length, t the thickness, and d the separation. A factor of two is added to this relationship to account for the flux and charge on both sides of the electrodes.

$$C = \varepsilon_r \varepsilon_0 \left(\frac{K'}{K} + \frac{t}{d} \right) L \tag{2-54}$$

For interdigitated electrodes, this relationship may be multiplied by the number of legs, n, to form a relationship for the total capacitance of interdigitated system. Such a relationship is beneficial for determining the approximate capacitance of interdigitated structures quickly and conveniently without having to result to finite element methods. To determine the fringe field of the parallel plates with gap distances different from the basic solution, a non-dimensional approach is used to determine *k* as shown in Equation (2-55), where *w* is the width of the electrodes.

$$k = \frac{d}{d + w} \tag{2-55}$$

The final relationship is shown below in Equation (2-56). The notation *K(k)* is used to emphasize the variability of this term as a function of *k*.

$$C = n \varepsilon_r \varepsilon_0 \left(\frac{K'(k)}{K(k)} + \frac{t}{d} \right) L \tag{2-56}$$

Equations (2-44) can be plotted to illustrate the flux and potential lines of the parallel conductors as shown in Figure 2.13.

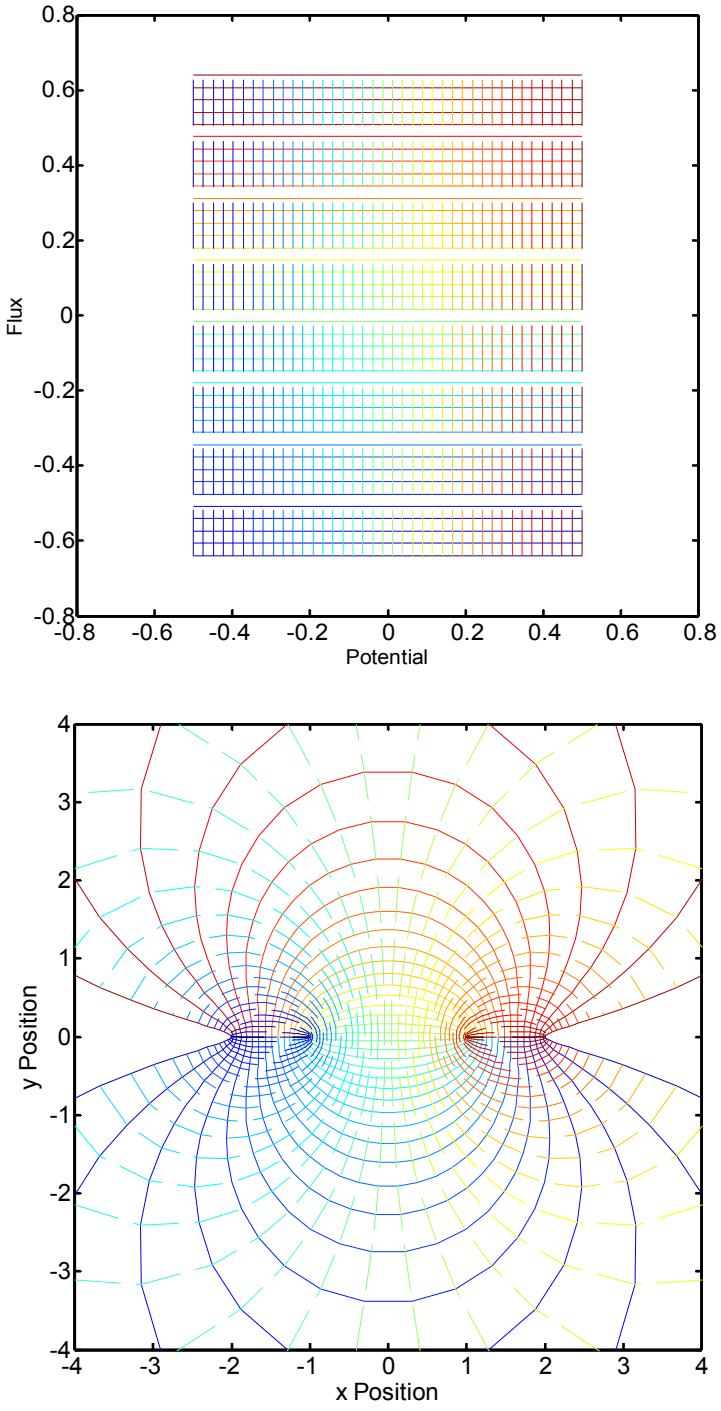

Figure 2.13: Flux and potential lines mapped from parallel plate capacitor to model the fringe effects of a parallel strip capacitor.

2.3.5 Comparison of Analytical Results with Commercial FEA Software for Electrostatic Solutions

In order to examine the accuracy of Equation (2-56), finite element analysis of an interdigitated electrode geometry was compared with the results from the analytical solution. The test problem consisted of geometry similar to that under investigation for this research. The test problem consisted of a series of an interdigitated structure consisting of 4.75 micrometer digits, 2.25 micrometer gaps, and 1.0 micrometer thick electrodes. This structure consisted of a top electrode with 15 digits and a bottom electrode with 14 digits and a total of 28 gaps between the digits. The electrodes were on top of a layer polyethylene (ε_r=2.25), and had a layer of parylene (ε_r=3.0) between the electrodes and over the electrodes for 2.0 micrometers. The upper layer of parylene was embedded in polyethylene. The geometry used for comparing finite element and mathematical modeling results is shown in Figure 2.14.

To account for the contributions from the different layers of dielectric materials, Equation (2-57) has three terms inside the parenthesis based on the dielectric constant of the material. These terms consider the polyethylene below the electrodes and parylene between and above the electrodes. It is assumed that the primary contribution to the flux above the electrodes is from the parylene dielectric.

$$C = n\varepsilon_0 L\left(\varepsilon_{PE} \frac{K'(k)}{2K(k)} + \varepsilon_{Parylene} \frac{K'(k)}{2K(k)} + \varepsilon_{Parylene} \frac{t}{d} \right) \tag{2-57}$$

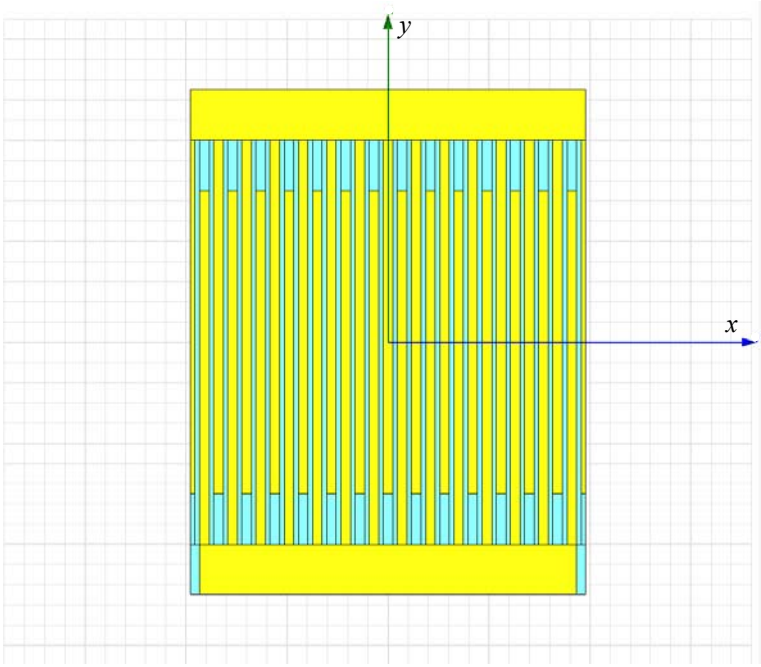

Figure 2.14: Geometry from Maxwell electrostatic FEA analysis for result comparison.

Determining *K(k)* can be performed by taking the binomial expansion of the integrand followed by a term by term integration. Equation (2-59) shows one such series expansion. Tabularized values of *K(k)* are also available, as well as arithmetico-geometric scale procedures [118]. Methods for determining values for the incomplete elliptic integrals in the complex plane are also available, but are generally more difficult to implement.

$$K(k) = \frac{\pi}{2}\left(1 + \frac{1}{4}k^2 + \frac{9}{64}k^4 + \frac{25}{256}k^6 + \frac{1225}{16384}k^8 + \ldots\right) = \frac{\pi}{2}\sum_{n=0}^{\infty}\left[\left(\frac{1}{2}\right)_m k^m\right]^2 \qquad (2\text{-}58)$$

$(½)_m$ denotes products of the form (½) (½+1) (½+2) …

Results of the comparison of the mathematical model with finite element methods are shown in Table 2-1. The results of the Maxwell electrostatic analysis gave 0.1964 pF as the capacitance between the two electrodes. The analytical solution gave a result of 0.1972 pF for the capacitance between the two electrodes. This differed from the Maxwell solution by 0.0008 pF or 0.4%. The same model was also run using the Coventor MemElectro finite element software which predicted that the capacitance between the two electrodes would be 0.1951 pF and differed from Maxwell by 0.67%. Results from all three methods agree with good consistency.

2.4 Summary of Analytical Techniques for Capacitance-based Sensors

Analytical techniques based on the Riemann mapping theorem have been used to examine the fields produced by pairs of electrodes. These techniques have been used to develop relationships between electrode geometry and the capacitance between electrodes. The analytical models developed in this section as well as the graphical results of those models and the validation of the analytical models using finite element analysis represent contributions of this research. The limitations of this approach are that it only considers only the two dimensional geometry formed by the electrode digits and gap between, it treats the fringe field above and below the electrodes non-continuously from the capacitance between the electrode digits, and the capacitance contribution from the sides of the electrode digits is handled using the idealized parallel plate formula. In the next chapter, these relationships will be coupled with theory from mechanics of composite materials to develop relationships coupling strain and changes in capacitance.

Table 2-1: Comparison of analytical calculations with commercial FEA software.

Method	Result (pF)	Difference (pF)	% Difference
Maxwell Solution	0.1964		
Analytical Solution	0.1972	0.0008	0.41
Coventor Solution	0.1951	0.0013	0.67

Chapter 3
Analysis of Microscopic Deformation of Electrode Structures and Capacitive Response

The fabrication of integrated sensors involves the use of multiple materials with differing properties. Previous work in the area of embedded sensors has shown that it is very important to match material properties as closely as possible [93,94,95,96,115]. It is not always possible to exactly match material properties, and differences in material properties will alter the behavior of the structure on a microscopic level and potentially on the macroscopic level. In this section, methods from mechanics of composite materials are used to develop analytical approximations for sensor response. These solutions are coupled with expressions for capacitance developed in Chapter 2 to give approximate solutions for the coupled change in capacitance with stress.

Analytical approximations for the behavior of the sensors on a microscopic scale were developed in the process of performing the finite element analysis models in the following chapter. These models were developed as a way of describing the response of the sensors to stress, and as a means of validating that understanding of the micromechanics of the sensor by comparing results to finite element results. Analytical approximations are also beneficial in interpreting the results of the sensing system once

physically implemented. Also, the equations in this section were developed to illustrate mathematically the role of the design parameters on the function of the system, and in that respect they aid in optimizing the geometry of the sensor system.

3.1 Apparent Properties of Non-homogeneous Systems of Materials

To develop solutions for the micromechanical behavior of sensor structures, mechanics of materials approaches will be used to develop approximations for the sensor deformation, which can be coupled with solutions for capacitance from Chapter 2 to obtain expressions for the change in capacitance with applied strain or load. Researchers in the field of composite materials are typically concerned with macroscopic or bulk strains and deformations. The solution of microscopic strains and material interactions is an evolving field. In this approach, a series of simplifying assumptions will be made in order to develop first approximations for the change in capacitance with deformation.

3.1.1 Equivalent Stress Model for Determining Young's Modulus in Directions Orthogonal to Electrodes

Figure 3.1 illustrates the parallel plate capacitor sensor for determining normal strains with an applied normal stress. This diagram will be used to illustrate the representative volume element of the system. The representative volume element corresponds to the smallest region of the structure over which stresses and strains might be considered macroscopically uniform. The stresses and strains are not uniform on the microscopic scale due to the non-homogenous structure of the material.

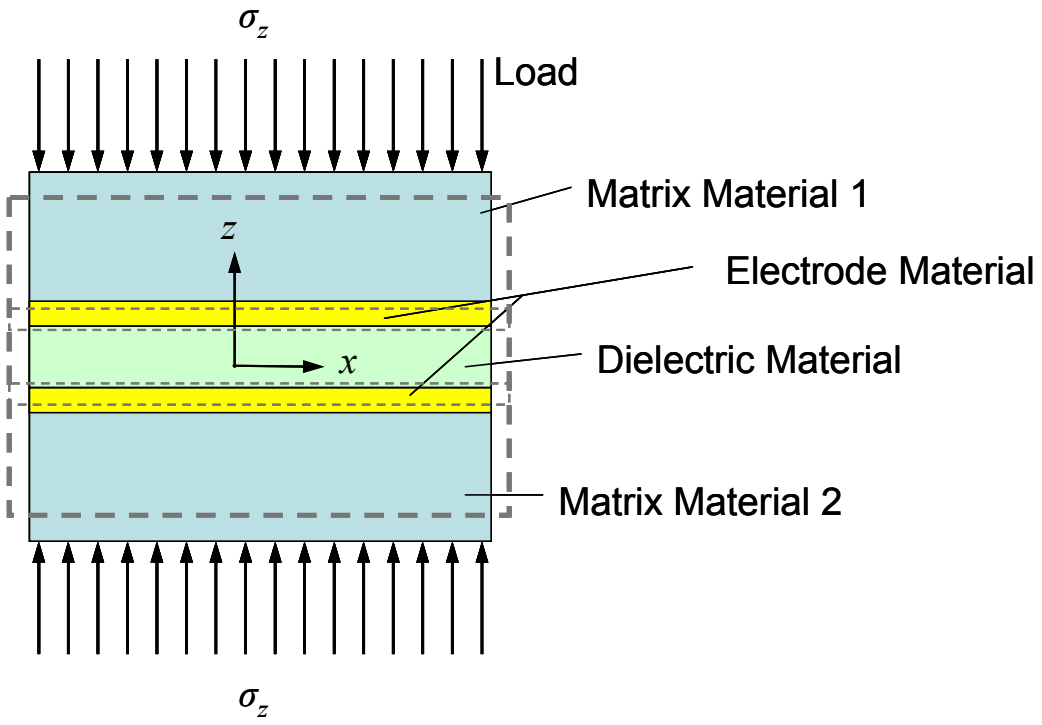

Figure 3.1: Representative element of parallel plate capacitor under normal strains.

For any composite system of materials, one of the first problems that must be solved is determining materials properties. In order to determine the change in capacitance with stress in the normal direction, the primary concern is with the strain in the dielectric material in the normal direction. However, the presence of materials of widely varying elastic modulus significantly affects the stiffness of the entire system. The Maxwell-Reuss model applies to systems similar to that shown in Figure 3.1. For the z-direction loading condition shown, the primary assumption in this model is that the same stress is applied to all of the layers of material and that the overall strain in the representative volume shown is the sum of the strains of the individual components of the

element. Also, the characteristic volumes of the material must be determined empirically or estimated using finite element analysis.

The compliance of the material in the normal direction may be approximated by the Maxwell-Reuss model as shown in Equation (3-1), where E represents Young's modulus and V represents the Volume of material contained in the representative element.

$$E_z = \frac{V_{Total}}{\frac{V_1}{E_1} + \frac{V_2}{E_2} + \frac{V_3}{E_3} + \ldots} \tag{3-1}$$

3.1.2 Equivalent Strain Model for Determining Young's Modulus in Directions Parallel to Electrode Major Dimensions

Different material behavior is observed when loading composite materials in the plane parallel to the stiffening material. Figure 3.2 illustrates this loading condition. The primary assumption used to determine material properties in this case is that all layers of materials undergo the same strain. The Kelvin-Voight model, or rule of mixtures, is commonly used to find the material properties in this direction.

$$E_x = E_1 \frac{V_1}{V_{Total}} + E_2 \frac{V_2}{V_{Total}} + E_3 \frac{V_3}{V_{Total}} + \ldots \tag{3-2}$$

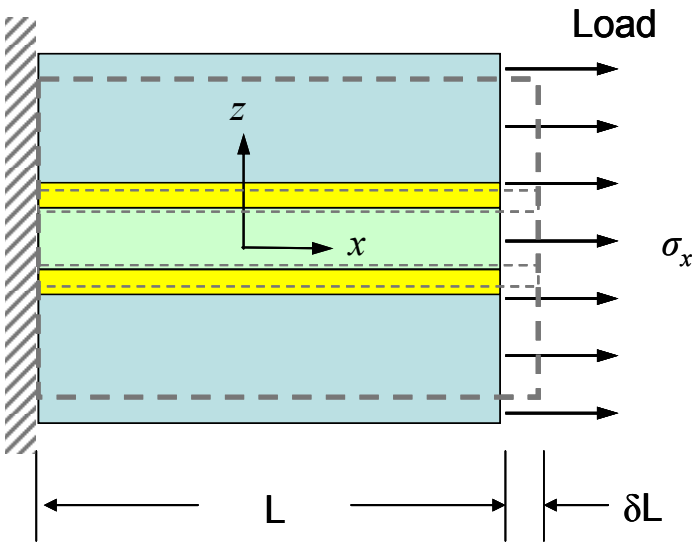

Figure 3.2: Representative volume element for determining strains in the parallel plate capacitor for measuring normal strains.

In a similar manner, the Poisson's ratio, ν, for the composite material may be determined as shown in Equation (3-3).

$$\nu_{xz} = \nu_1 \frac{V_1}{V_{Total}} + \nu_2 \frac{V_2}{V_{Total}} + \nu_3 \frac{V_3}{V_{Total}} + \ldots \tag{3-3}$$

The expressions developed thus far pertain to primarily homogeneous combinations of materials. The problem of embedded sensors does not fit this model very well, as the matrix material exists in far greater quantities than the sensor materials. Applying these equations strictly would result in most material properties approaching that of the embedding material for the sensor problem. On a macroscopic scale, this is an

accurate approximation and part of the motivation for embedding thin films of materials inside the matrix material. These small quantities of materials have little effect on the properties of the system on a global scale. However, when developing analytical solutions for the sensor response on a microscopic scale. These equations must be adjusted to allow for the microscopic effects of the sensor elements. For this research, a representative volume will be used for calculating the sensor response. It will be assumed that beyond some characteristic length, the influence of the bulk of the matrix material on the sensor response is insignificant. This characteristic length will be discussed further where these equations are applied and is an interesting topic for further research.

3.2 Embedded Sensor Response to Normal and Transverse Loading

The concepts of the previous section will be applied to developing an analytical solution for the change in capacitance of a parallel plate capacitor encapsulated within another material. A first order approximation of the deformation of the composite system of materials would be to approximate the sensor as a system of elastic members or springs in series or parallel as shown in Figure 3.3. The limitation of this approximation is that it neglects the shear interactions between the layers of materials. This concept helps in visualizing the deformation of the system and the contribution of the different layers of materials, but neglects transverse deformation which occur due to Poisson's ratio effects. The effects of transverse strain are included in all analytical models formulated in this research.

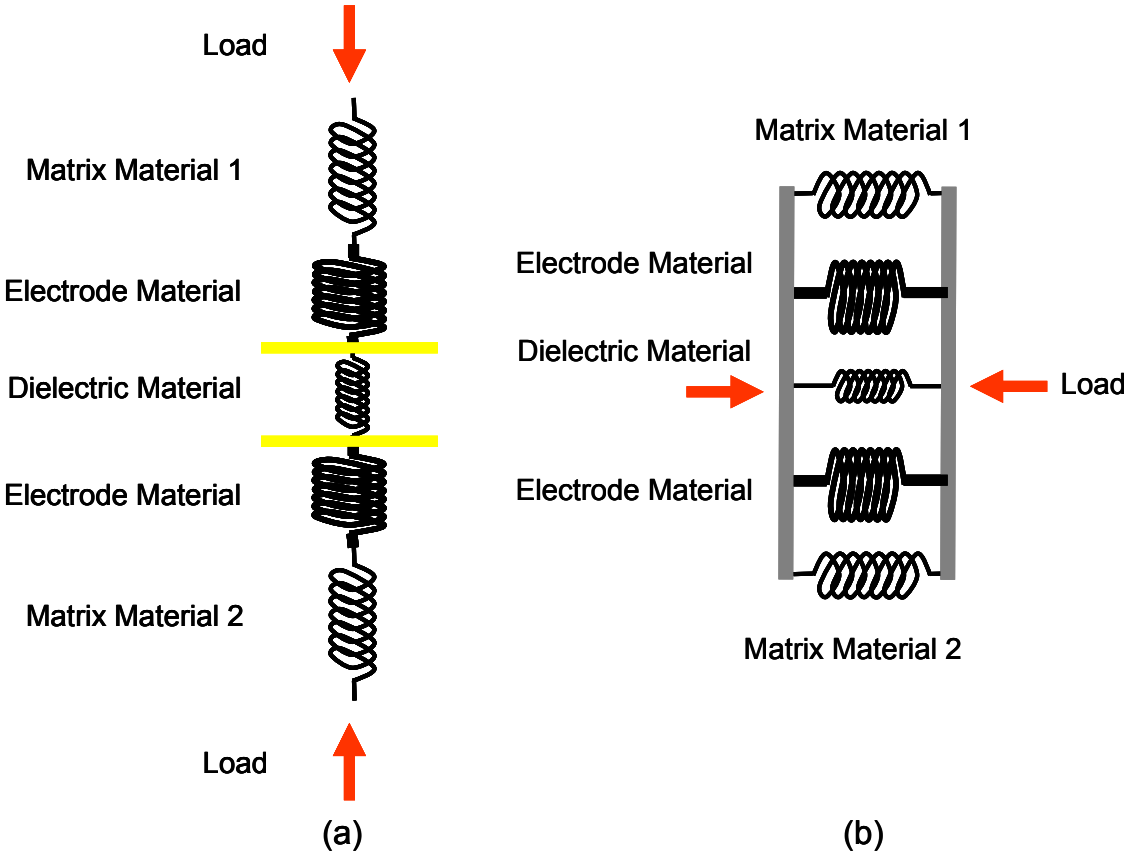

Figure 3.3: (a) Simplified view of normal loading of parallel plate using a system of springs in series for visualization purposes. (b) Simplified view of transverse loading of parallel plate using a system of springs in parallel for visualization. These simplified models neglect Poisson's ratio effects and shear stresses between the layers.

As shown in Figure 3.1 when loading is applied normal to the plates of a parallel plate capacitor embedded in an encapsulating material, two effects are apparent. The first and most obvious effect is that the plates are driven closer together due to compression of the dielectric material. The second effect is that the area of the plates increases due to the tendency of the volume to remain nearly constant during this process. This effect will be referred to as the transverse strain or Poisson's ratio effect in this research. The expression for the capacitance of a parallel plate capacitor with rectangular plates in and unstressed state is shown in Equation (3-4). *l* and *w* represent the length and width of the plates respectively, and *d* represents the plate separation.

$$C_{Unstressed} = \frac{\varepsilon_0 \varepsilon_r lw}{d} \tag{3-4}$$

The capacitance after the application of normal loading to this system can be determined by calculating the change in geometry due to loading. This calculation is made more complicated by the combination of Poisson's ratio effects and the anisotropic nature of the materials. Equation (3-5) represents the capacitance in the parallel plate system upon application of load. In this equation, s_x, s_y, and s_z are used to represent the strain in the materials in the *x* and *y* directions. s_z represents the strain perpendicular to the xy plane and is assumed to equal s_x in this case. In order to determine the change in capacitance, these strains must be determined from the applied loading conditions using the composite material properties derived in section 3.1. s_x for the normal loading case may be found by multiplying the Poisson's ratio of the system by the applied stress,

divided by the directional modulus of elasticity as shown in Equation (3-6), and the total change in capacitance is given by Equation (3-7).

$$C_{\sigma_z} = \frac{\varepsilon_0 \varepsilon_r \left(l + s_y l\right)\left(w + s_x w\right)}{\left(d + s_z d\right)} \tag{3-5}$$

$$C_{\sigma_z} = \frac{\varepsilon_0 \varepsilon_r \left(l + \nu_{xz} \frac{\sigma_y}{E_x} l\right)\left(w + \nu_{xz} \frac{\sigma_y}{E_x} w\right)}{\left(d + \frac{\sigma_y}{E_z} d\right)} \tag{3-6}$$

$$\Delta C_{\sigma_z} = \varepsilon_0 \varepsilon_r \left[\frac{\left(l + \nu_{xz} \frac{\sigma_y}{E_x} l\right)\left(w + \nu_{xz} \frac{\sigma_y}{E_x} w\right)}{\left(d + \frac{\sigma_y}{E_z} d\right)} - \frac{lw}{d} \right] \tag{3-7}$$

The relationship of capacitance to loading in the transverse direction is similar to the one for normal loading. Equation (3-7) illustrates the expected change in capacitance when the normal shear sensor is loaded in the transverse direction. The primary effect of transverse loading is a change in the length of the capacitor electrode. A secondary effect is the change in the width of the electrodes and a change in the gap between the electrodes due to the transverse strain which is a function of Poisson's ratio.

$$\Delta C_{\sigma_y} = \varepsilon_0 \varepsilon_r \left[\frac{\left(l + \frac{\sigma_x}{E_x} l \right)\left(w + \nu_{xy} \frac{\sigma_x}{E_x} w \right)}{\left(d + \nu_{xy} \frac{\sigma_x}{E_y} d \right)} - \frac{lw}{d} \right] \tag{3-8}$$

Analytical solutions were used to predict the sensitivity of the normal strain sensor to changes in electrode area and load direction. For this study, 300 nm gold electrodes embedded in UHMW PE were investigated. The properties of parylene were used to simulate a 2.0 μm thick dielectric layer. Square capacitor geometries were used with 274, 434, 614, 751, and 868 μm wide electrodes representing 1, 2.5, 5, 7.5, and 10 pF value capacitors, respectively. Results of this analysis predicted response ranging from 2.18×10^{-3} pF for the 1 pF capacitor to 20.8×10^{-3} pF for the 10 pF capacitor for the 1 MPa stress. The response to transverse loading indicated good sensitivity to load direction. Results are summarized in Table 3-1 and illustrated in Figure 3.4.

Table 3-1: Results of analytical model for a 1 MPa load and different value capacitors.

Electrode Length/Width (μm)	Base Capacitance (pF)	Delta C Normal 1 MPa Stress (pF)	Delta C Transverse 1 MPa Stress (pF)
274	1.0	0.00218	0.000942
434	2.5	0.00521	0.00235
614	5.0	0.0104	0.00471
751	7.5	0.0156	0.00706
868	10	0.0208	0.00941

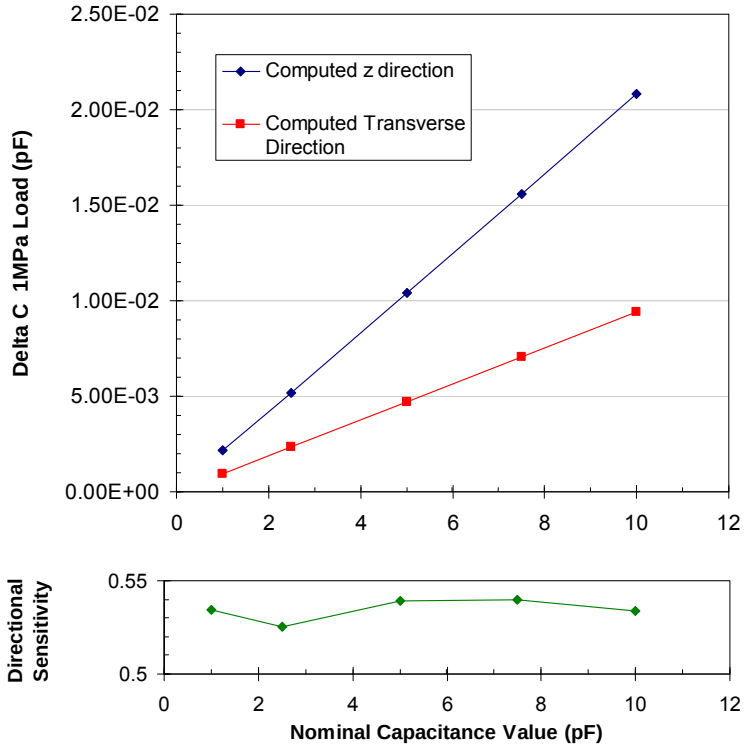

Figure 3.4: Capacitance change for a 1 MPa load as a function of base capacitance value.

3.3 Response of an Embedded Capacitor to Shear Loading

It is important to determine an expression for the in-plane shear modulus of the capacitive structure in order to develop and expression for the change in capacitance with shear loading. Figure 3.5 and Figure 3.6 illustrate a representative volume element of the sensor structure with applied shear loading. In order to determine an expression for the shear modulus for this structure using a mechanics of materials approach, it is assumed that all layers of the material are subjected to the same shear stress. However, each layer exhibits a unique deformation response to the applied stress. This is a similar approach to that used for the normal strains in section 3.1.

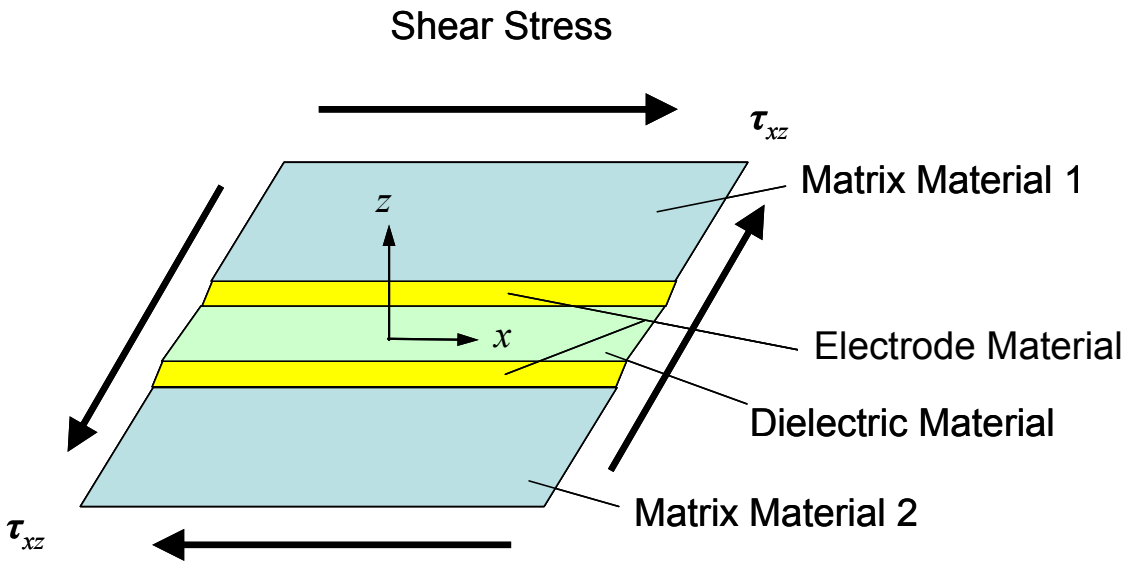

Figure 3.5: Representative volume element with applied shear loading showing exaggerated deformations.

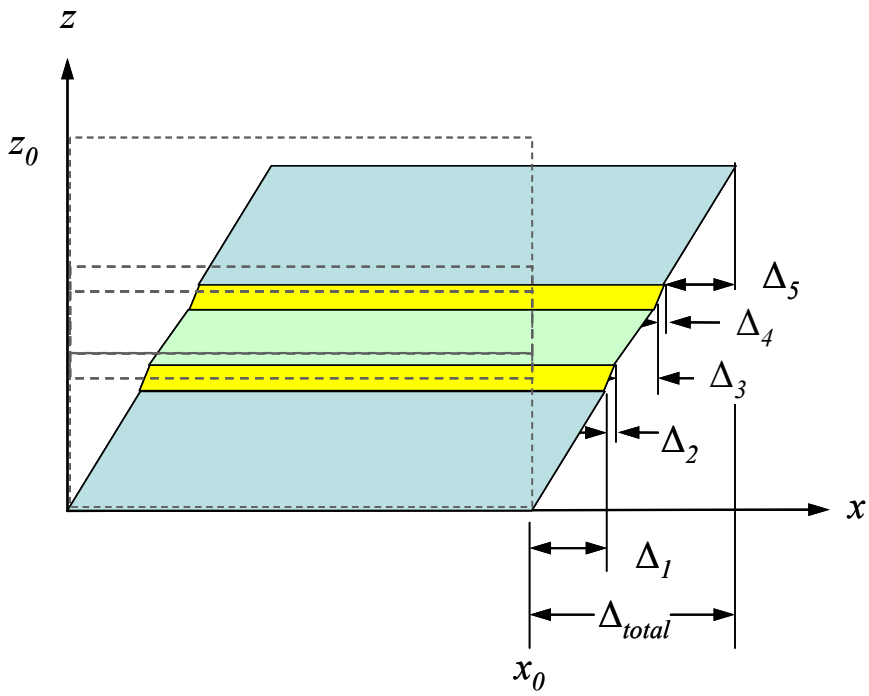

Figure 3.6: Representative volume element showing the shape of the original geometry in dashed lines, the deformations of the individual layers, and total deformation.

The geometry of Figure 3.5 will be used to help visualize the relationship for shear modulus. Figure 3.6 is a simplified diagram of the deformation from a pure shear stress which neglects the rotation of the element which is equal to the strain. The apparent shear modulus of the representative element is determined by the original height, z_0, of the element divided by the perpendicular deformation, Δ_{total}, as shown in Equation (3-9). The shear modulus, G, is defined as the shear stress, τ, divided by the shear strain, γ_{xz} as shown in Equation (3-10). The deformation, Δ_{total}, of the representative element in this case is the sum of the deformations of the constituent layers. Therefore the shear modulus of the representative volume can be defined by the rule of mixtures or the sum of the shear modulus of the constitutive materials multiplied by the volume fraction as shown in Equation (3-11).

$$\gamma_{xz} = \frac{\Delta_{total}}{z_0} \tag{3-9}$$

$$G = \frac{\tau_{xz}}{\gamma_{xz}} \tag{3-10}$$

$$G = G_1 \frac{V_1}{V_{Total}} + G_2 \frac{V_2}{V_{Total}} + G_3 \frac{V_3}{V_{Total}} + \ldots \tag{3-11}$$

Relationships between stress, strain, and capacitance can be developed using the previous figures and relations in this section along with Figure 3.7a. Since the signal from one leg of the sensor is subtracted from the other, the differential geometry used for the

shear sensor has the ability to cancel out any electrical noise received due to common mode rejection. This is similar to the case of two parallel plate capacitors in series as shown in Figure 3.7b, where the yellow electrode in the center is the reference electrode used for reading the measurement. Displacement of the upper electrode in any direction other than in the sensing direction results in no signal, because the effect is seen equally by both capacitors and subtracted out as well.

Equation (3-12) gives is the expression for the nominal capacitance between the upper plate of the capacitor and one of the lower plates. The change in capacitance is caused by a lateral shift in the upper electrode as shown in Figure 3.5 and expressed in Equation (3-13). Subtracting the unstressed capacitance from the sensor capacitance under shear stress results in Equation (3-14) and Equation (3-15).

$$C_{Unstressed} = \frac{\varepsilon_0 \varepsilon_r l_1 l_2}{d} \tag{3-12}$$

$$C_{Shear} = \frac{\varepsilon_0 \varepsilon_r (l_1 + \Delta l_1) l_2}{d} \tag{3-13}$$

$$\Delta C = C_{Shear} - C_{Unstressed} = \frac{\varepsilon_0 \varepsilon_r l_2 [(l_1 + \Delta l_1) - l_1]}{d} \tag{3-14}$$

$$\Delta C = C_{Shear} - C_{Unstressed} = \frac{\varepsilon_0 \varepsilon_r l_2 \Delta l_1}{d} \tag{3-15}$$

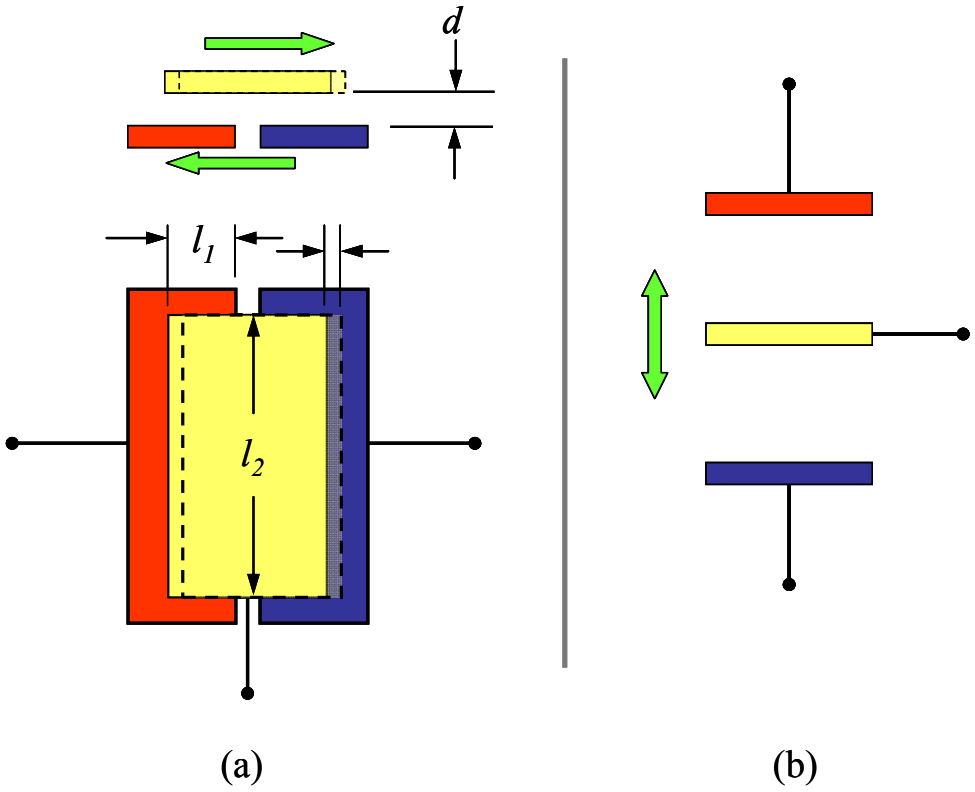

Figure 3.7: (a) illustration of three electrode shear sensor with applied shear load for determining capacitance change with shear, and (b) similar differential capacitor geometry to illustrate the electrode function.

The amount of translation in the upper electrode is determined by the shear strain and the vertical distance between the upper and lower electrodes. This is substituted into Equation (3-15) to yield Equation (3-16). Cancelling the distance term in both the numerator and the denominator yields Equation (3-17).

$$\Delta C = \frac{\varepsilon_0 \varepsilon_r l_2 (\gamma d)}{d} \tag{3-16}$$

$$\Delta C = \varepsilon_0 \varepsilon_r l_2 \gamma \tag{3-17}$$

If the change in capacitance is desired in terms of the shear stress, this can be determined by solving Equation (3-10) for the shear stress and substituting into Equation (3-17). The result is Equation (3-18) shown below. Furthermore, this result can be solved for a simple relationship between the shear stress as a function of the change in capacitance as shown in Equation (3-19). A similar expression relating the change in capacitance to the shear strain is shown in Equation (3-20).

$$\Delta C = \varepsilon_0 \varepsilon_r l_2 \frac{\tau}{G} \tag{3-18}$$

$$\tau = \frac{\Delta C \varepsilon_0 \varepsilon_r l_2}{G} \tag{3-19}$$

$$\gamma = \Delta C \varepsilon_0 \varepsilon_r l_2 \tag{3-20}$$

These results represent the changes in capacitance for two parallel electrodes with an applied shear stress or strain. For the case of the three-electrode, differential, capacitive sensor, change in capacitance between the upper electrode and one of the lower electrodes will increase by the amount given in the expressions above while the other will decrease by the same amount. If a circuit is used that automatically subtracts the signals, the change in capacitance will be twice what is shown in these relationships.

3.4 Analysis of the Response of an Interdigitated Capacitor to Loads Parallel and Orthogonal to the Sensor Electrodes

This investigation examines the use of an interdigitated transducer (IDT) for the measurement of in-plane stress and strain. Interdigitated capacitors represent a more complex analysis situation than parallel plate capacitors because the interdigitated capacitors have significant stray capacitance effects which may not be neglected. Furthermore, IDTs are sensitive to strains in multiple directions, and therefore the IDT geometry must be optimized in order for it respond preferentially to stress or strain in a given direction.

Figure 3.8 illustrates the unstressed geometry of the IDT electrodes as well as exaggerated deformations under applied loading conditions. The two primary geometric changes which occur as the IDT experiences changes in loading are a change in the length of the electrodes due to strain in the y direction and a change in the gap between electrodes due to strain in the x direction. This section is focused on the difficult case of high modulus, metallic electrode materials embedded in lower modulus dielectric and embedding materials. In this configuration, less-pronounced changes in the width and thickness also occur.

The interdigitated electrode geometry experiences changes in capacitance as a result of stress in both the direction parallel to the electrodes and in the direction perpendicular to the electrodes as illustrated in Figure 3.8. Depending on the design parameters of the IDT (electrode thickness, electrode width, gap spacing, electrode length, and number of electrodes), the sensitivity of the sensor may range from equal sensitivity with applied load regardless of direction to greater sensitivity to loading in either direction. The variation in the sensitivity to load direction with design parameters necessitates that a sensitivity analysis to the various design parameters be performed on the interdigitated sensor in order to optimize its performance and directional sensitivity. To perform this optimization study by multiphysics finite element analysis would be both physically and computationally time consuming. For this optimization, it would be beneficial to develop a mathematical model capable of quickly simulating the change in capacitance with applied loading and sensitivity of the parameters of interest using computational algorithms and programming methods such as C, Fortran, or Matlab.

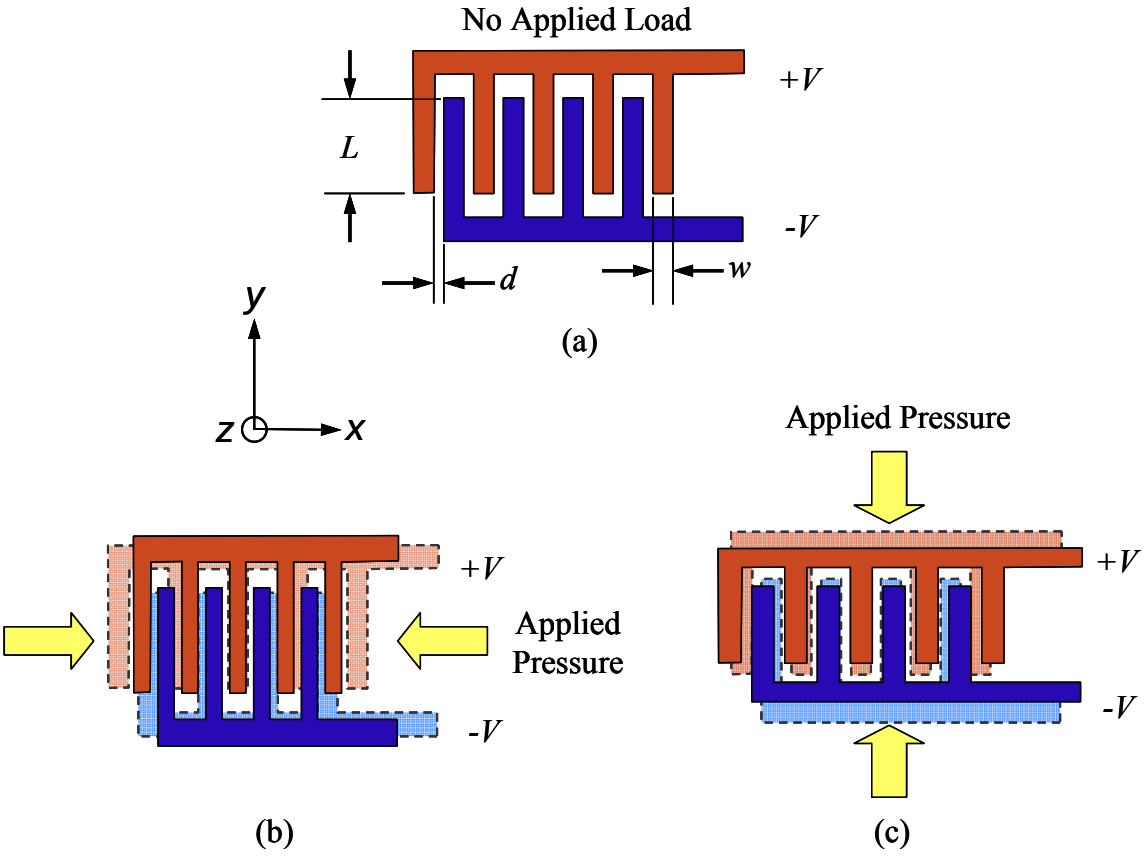

Figure 3.8: (a) Geometry of undeformed IDT with primary dimensions illustrated, (b) deformed geometry with load applied perpendicular to electrodes (x-direction loading), and (c) deformed geometry with load applied parallel to electrodes (y-direction loading).

A similar process to that used to determine the composite material properties for the parallel plate capacitor was used to determine composite material properties for the interdigitated sensor. The layers of the sensor are: 1) upper encapsulation layer, 2) dielectric overburden, 3) combined electrode-dielectric layer, and 4) substrate layer. The representative geometry is shown in Figure 3.9. This structure possesses an additional order of complexity because not only must the interactions between layers be taken into account, but also the micromechanical interactions between the legs of the electrodes and the dielectric materials. A very significant measure of interest is the change in the gap between the electrodes in this structure.

3.4.1 Analysis of Composite Material Properties of the IDT

In the analysis of the parallel plate capacitors, a simplified way of viewing the response of the sensor to transverse or "in-plane" stress is that of a system of springs or elastic elements acting in parallel with each other. In a similar fashion, a simplification of the response of the IDT is that of a system of elastic elements acting in parallel, however an additional layer or elastic element must be added consisting of the behavior of the combined dielectric material and electrode. The combined electrode-dielectric material layer may be approximated as two elastic elements in series with each other, the combination of which are in parallel with the other materials. This behavior may be visualized by the system of springs in Figure 3.10.

In this system, it is assumed that each of the elastic layers experiences equal deformation. Since the elastic modulus or stiffness of each layer is different, each layer contributes a different force and has a different amount of stress in it although the strain

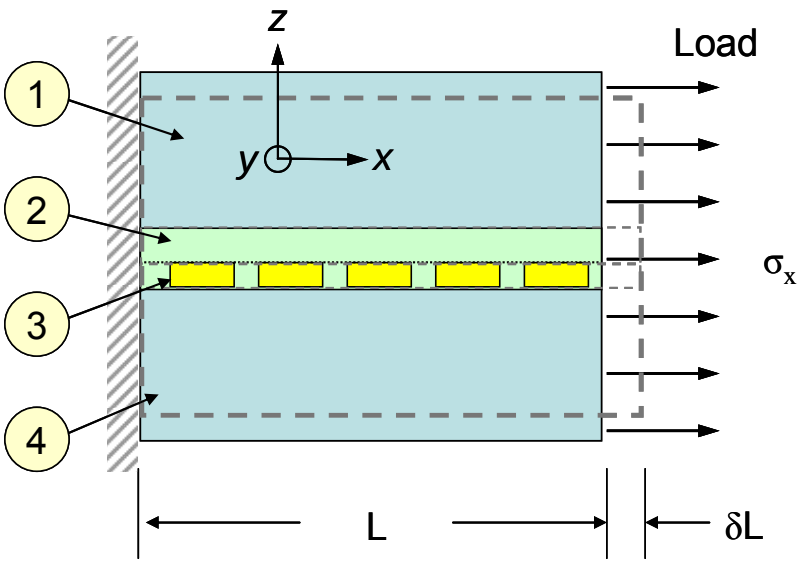

Figure 3.9 Illustration of representative element used to model the displacement between electrodes for the interdigitated strain sensor.

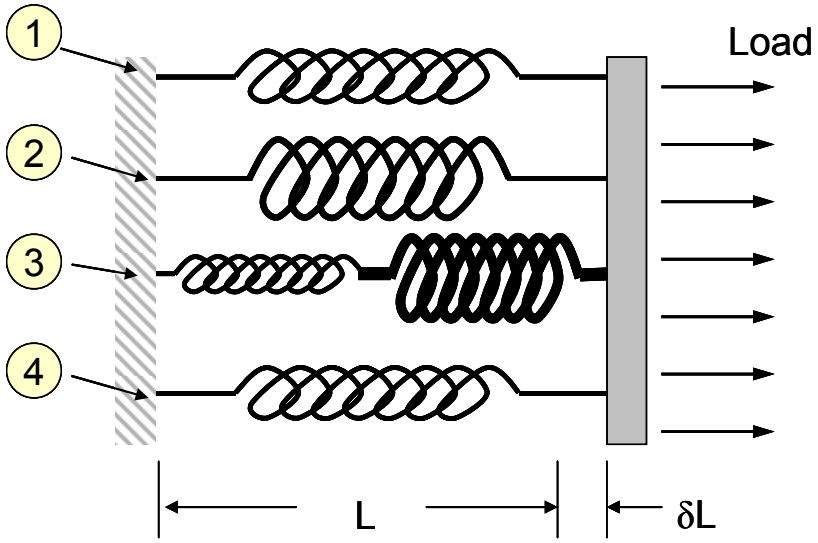

Figure 3.10: System of springs in both series and parallel used to illustrate deformation of interdigitated strain sensor.

is nearly equal between the layers. In the third layer, which is illustrated by the strong spring and the weak spring in series in Figure 3.10, the two springs in that layer experience the same total displacement as the others. However, the two springs within the layer are subject to the same forces or stress, but different strains or displacements. A similar analogy could be made to a set of capacitors in parallel, with one of the sets of parallel capacitors consisting of two capacitors in series. The layers of material store elastic energy similar to the way the capacitors store charge. This model will be used to develop a set of expressions for approximating the change in capacitance of the IDT with loading. Transverse strains due to Poisson's ratio effects will be considered.

When stresses normal to the IDT electrodes are present, it is assumed that each of the layers experiences the same total displacement or "bulk" strain. This is expressed in Equation (3-21). The bulk stress and effective elastic modulus for the layer is illustrated in Equation (3-22). The amount of stress applied to an area is determined by dividing the total load by the area over which it is applied. Conversely, the total force acting on a surface may be determined by multiplying the stress by the area over which it is applied as expressed in Equation (3-23), where s is the strain.

$$s_1 = s_2 = s_3 = s_4 = s_x \tag{3-21}$$

$$\sigma_{1x} = E_1 s_x, \quad \sigma_2 = E_2 s_x, \quad \sigma_3 = E_3 s_x, \quad \sigma_4 = E_4 s_x \tag{3-22}$$

$$F = \sigma A_{Total} = \sigma_1 A_1 + \sigma_2 A_2 + \sigma_3 A_3 + \sigma_4 A_4 \tag{3-23}$$

The most commonly used definition of strain is the change in length of an element divided by its original length, and the elastic modulus is defined as the ratio of the applied stress to its resulting strain or $s=\delta L/L$ and $E=\sigma/s$. For the composite structure of Figure 3.9, the effective elastic modulus may be determined by the Kelvin-Voight model as shown in Equation (3-24). The added complexity occurs in determining the effective modulus for the third layer, as it is comprised of materials of different modulus. The modulus of this layer may be determined by the Reuss model where the materials of this layer are in series rather than parallel as expressed in Equation (3-25). In this Equation, the "*e*" subscript represents the electrode material and the "*d*" subscript represents the dielectric material.

$$E_x = E_1 \frac{V_1}{V_{Total}} + E_2 \frac{V_2}{V_{Total}} + E_{3x} \frac{V_3}{V_{Total}} + E_4 \frac{V_4}{V_{Total}} \tag{3-24}$$

$$E_{3x} = \frac{E_e E_d}{E_e \dfrac{V_d}{V_{Layer3}} + E_d \dfrac{V_e}{V_{Layer3}}} \tag{3-25}$$

In the z direction, the modulus of elasticity for layer 3 is found using the Kelvin-Voight model as shown in Equation (3-26). The modulus for the representative volume element may then be found using the Reuss model as shown in Equation (3-27).

$$E_{3z} = \left(E_e \frac{V_e}{V_{Layer3}} + E_d \frac{V_d}{V_{Layer3}} \right) \tag{3-26}$$

$$E_z = \frac{V_{Total}}{\frac{V_1}{E_{1\,4}} + \frac{V_2}{E_2} + \frac{V_3}{E_{3z}} + \frac{V_4}{E_4}} \tag{3-27}$$

In the y direction, the effective modulus of the volume element may be determined by a single application of the Reuss model for composite elasticity.

$$E_y = E_1 \frac{V_1}{V_{Total}} + E_2 \frac{V_2}{V_{Total}} + E_e \frac{V_e}{V_{Total}} + E_m \frac{V_m}{V_{Total}} + E_4 \frac{V_4}{V_{Total}} \tag{3-28}$$

3.4.2 IDT Response Due to x Direction Loading

As illustrated in Figure 3.8b, when the IDT experiences stress in the x direction (orthogonal to the IDT electrodes) a series of deformations occur. The primary result is that the gap between the legs is reduced due to compression as well as the width of the legs themselves. The secondary result is the increase in the length of the legs due to Poisson's ratio effects. The thickness of the legs out of the plane of the page also increases slightly due to Poisson's ratio effects. As illustrated in the previous equations, the layers of the material may be visualized as having the same total deformation; however the forces and stresses in each layer are not unequal. In order to estimate the

electrode displacement, the total strain can be calculated using the applied stress and the effective modulus of the representative element followed by determining the stress in each of the layers. Finally, the layer stress can be solved for the displacement in the electrode and the dielectric material between the electrodes. Poisson's ratio effects are primarily demonstrated by a change in the length of the electrodes.

In order to determine the change in capacitance of the IDT due to a given stress, the changes in electrode height, length, width, and gap spacing must be computed. Several steps must be taken to determine these effects. To determine the effects of in-plane stress acting normal to the IDT electrodes the bulk strain on the system must first be determined. The effective modulus for the representative element was given in Equation (3-24). The average strain in the layer may be determined by Equation (3-29).

$$s_x = \left(\frac{P_x}{E_x} \right) \tag{3-29}$$

Using Equation (3-22), the stress in the individual layers may be determined. Note that the stress for the electrode layer in the x direction is determined by Equation (3-30).

$$\sigma_{3x} = \left(\frac{P_x}{E_x} \right) \left(\frac{E_e E_d}{E_e \frac{V_d}{V_{Layer3}} + E_d \frac{V_e}{V_{Layer3}}} \right) \tag{3-30}$$

By assuming that the stress is uniform in the electrode layer, the strain and deformation in the electrode and the dielectric material may be approximated.

$$s_e = \frac{\sigma_{3x}}{E_e}, \; s_d = \frac{\sigma_{3x}}{E_d} \tag{3-31}$$

The mechanical properties of the IDT have been developed sufficiently that a computational model may be developed to demonstrate the response of the sensor. The key equations necessary for electrical simulation were developed in Chapter 2 as Equation (2-55) and Equation (2-57). These equations are repeated below for clarity where Equation (3-35) is the geometrical modulus, a non-dimensional parameter representing the aspect ratio of the electrode system. Equation (3-36) determines the capacitance of the electrodes as a function of the number of digits, relative permittivity of the substrate dielectric, gap dielectric, and encapsulation dielectric. This capacitance is the sum of the fringe capacitance in the substrate, the fringe capacitance in the encapsulation material, and the capacitance between the sidewalls of the electrodes. The *K(k)* and *K'(k)* terms represent the complete elliptic integral with respect to the modulus and complementary modulus, respectively.

$$k = \frac{d}{d + w} \tag{3-32}$$

$$C = n\varepsilon_0 L\left(\varepsilon_{PE}\frac{K'(k)}{2K(k)} + \varepsilon_{Parylene}\frac{K'(k)}{2K(k)} + \varepsilon_{Parylene}\frac{t}{d}\right) \tag{3-33}$$

Similarly to the parallel plate capacitor problem, it is necessary to determine the response of the IDT to two orthogonal loading conditions. These two loading conditions consist of stress parallel to the digits of the capacitor and stress perpendicular to the digits of the capacitor. These conditions will be modeled using Matlab computational software, and the basis for the Matlab algorithms will be presented. A new function, C_IDT, based on Equation (3-33) may be defined in Matlab representing the capacitance of the electrode system as seen in Equation (3-34).

$$C_{Original} = C_IDT(n, \varepsilon_1, \varepsilon_2, \varepsilon_3, L, t, d, w) \tag{3-34}$$

Equation (3-34) can be used to determine the changes in capacitance due to application of in-plane stress in the x direction, which may also be viewed as in-plane stress normal to the direction of the electrodes. The function C_IDT is valid for both tension and compression using the sign convention that compressive forces are negative and tensile stresses are positive in Equation (3-32).

$$C_{\sigma_x} = C_IDT\left(n, \varepsilon_1, \varepsilon_2, \varepsilon_3, \left(L - \nu L\frac{P_x}{E_x}\right), \left(t - \nu t\frac{\sigma_{3x}}{E_e}\right), \left(d + d\frac{\sigma_{3x}}{E_m}\right), \left(w + w\frac{\sigma_{3x}}{E_e}\right)\right) \tag{3-35}$$

This equation illustrates that as a stress is applied in the *x* direction, the electrode width and the gap between electrodes changes as a function of the stress in the layer. The thickness of the electrodes changes due as a function of Poisson's ratio and the layer stress. Also, the length changes as a function of the total stress and the Poisson's ratio.

3.4.3 IDT Response Due to y Direction Loading

As displayed in Figure 3.8c when a stress, P_y, is applied parallel to the IDT electrode direction, a different set of effects is observed. In this case, the primary result is that the length of the legs is reduced due to compression. The secondary result is that the width of the legs and the gap between the legs increases to Poisson's ratio effects. The thickness of the legs out of the plane of the page also increases slightly under compression due to Poisson's ratio effects. To determine these changes the stress in the x direction in the electrode layer must be calculated which results from the y direction loading. We can modify Equation (3-33) to illustrate the changes in dimensions due to this type of loading condition. Substituting Equation (3-33) into Equation (3-34) leads to Equation (3-37) for the overall change in capacitance.

$$\left(\sigma_{3x}\right)_{\sigma_y} = \left(\nu \frac{P_y}{E_y}\right)\left(\frac{E_e E_d}{E_e \frac{V_d}{V_{Layer3}} + E_d \frac{V_e}{V_{Layer3}}}\right) \tag{3-36}$$

$$C_{\sigma_y} = C_IDT\left(n, \varepsilon_1, \varepsilon_2, \varepsilon_3, \left(L + L\frac{P_y}{E_y}\right), \left(t - \nu t \frac{\sigma_{3x}}{E_e}\right), \left(d - d\frac{\sigma_{3x}}{E_m}\right), \left(w - w\frac{\sigma_{3x}}{E_e}\right)\right) \tag{3-37}$$

3.4.4 Optimization of IDT Response

The expressions that were developed for changes in capacitance in the IDT resulting from loading were used to examine the effects of changes in geometry on the predicted sensitivity of the IDT sensor. A base geometry of a 50 digit IDT with an digit width of 5 micrometers (μm), gaps between digits of 2 μm, a thickness of 500 nm, and an electrode length of 500 μm was used for this study. From this base geometry, each of the parameters was varied to determine the effects of each on the sensitivity to direction of applied load and the change in capacitance due to the applied load.

A Matlab simulation was performed to simulate and plot the results of this study. The simulation varied all of the parameters and plotted the results with a run time of 3.4 seconds on a laptop computer. This includes the time to perform the capacitance calculation using the series solution to the elliptical integrals. The algorithm for this simulation is shown in the Appendix, and the results are plotted in the following figures. These results show the change in capacitance as the parameters change and also the change in directional sensitivity. The directional sensitivity is determined by dividing the response to loading in the x direction by the response to loading in the y direction. The directional sensitivity parameter is an indication of the apparent Poisson's ratio the sensing system perceives from the load and the material, and therefore this parameter should be less than 1.0 and ideally near the value of 0.45 which is approximately the Young's modulus of the composite system.

The effect on IDT sensitivity was investigated by varying the length of the electrodes from 100 μm to 1000 μm and determining the response to two orthogonal 1

MPa loads. Figure 3.11 illustrates the results of this investigation. This figure illustrates the changes in the IDT sensitivity to load as the length of the IDT electrodes is varied. It also shows the change in the directional sensitivity of the IDT as this change occurs. The change in IDT sensitivity is observed to increase linearly from less than 1×10^{-3} pF to almost 8×10^{-3} pF through increasing the length of the electrodes in the IDT using the analytical tools developed in this section. The directional sensitivity does not change with a change in the length of the electrodes by these methods. For the geometry used in this simulation, the directional sensitivity was 0.78, which indicates some sensitivity to load direction. However, the sensitivity to direction is significantly larger then the ideal value of approximately 0.45.

The change in the sensitivity of the IDT strain sensor to stress normal and perpendicular to the IDT electrodes was simulated as the number of digits was varied from 5 electrodes to 100 electrodes. Results of this simulation are shown in Figure 3.12. The results of the analysis indicate that the sensitivity to stress is predicted to directly correlate with the number of IDT digits. The change in capacitance with 5 electrodes is predicted to be less than 1×10^{-3} pF, but approaches 1.6×10^{-2} pF as the number of electrodes approaches 100. The sensitivity to direction does not appear to be a function of the number of electrodes. The directional sensitivity values stayed nearly constant at a value of 0.77, which indicates some sensitivity to direction.

For this study, it is important to examine the change in capacitance to stress in the material surrounding the sensor. Examining the response to stress is important to

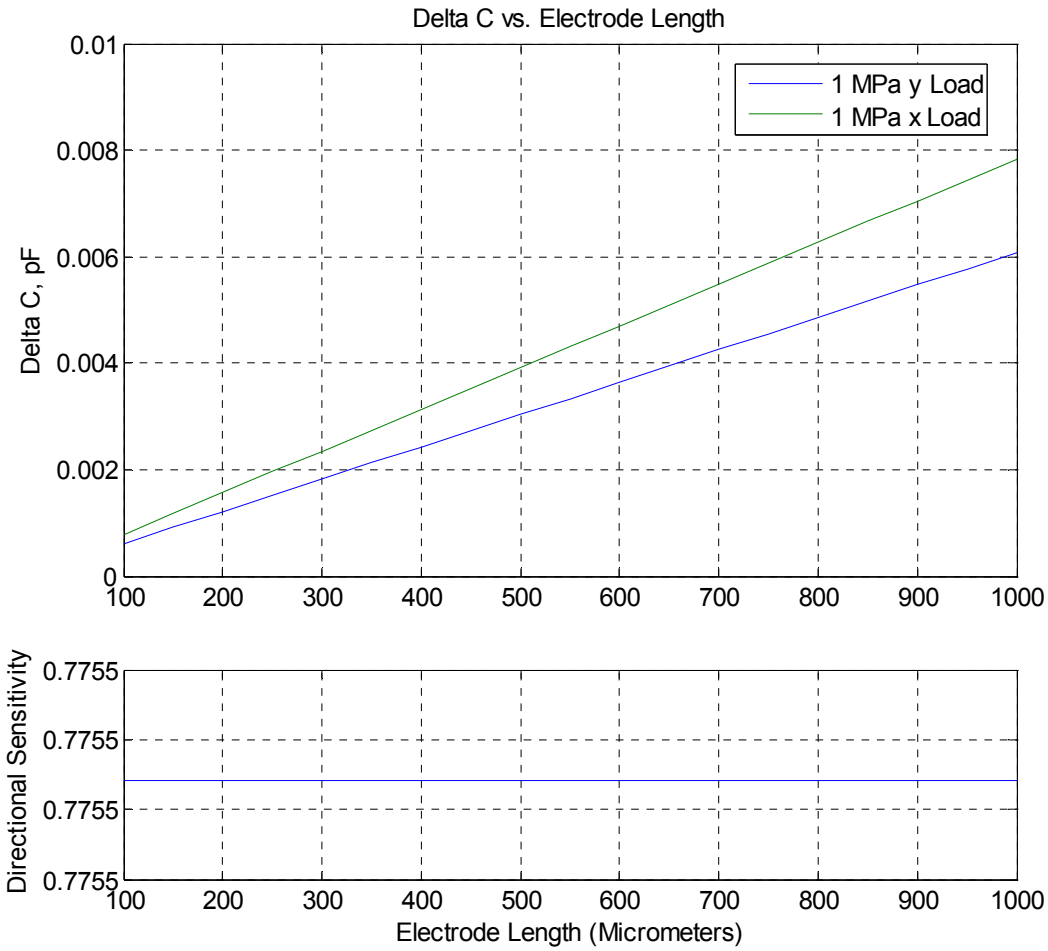

Figure 3.11: Change in capacitance and directional sensitivity as a function of electrode length. The electrode length varies from 100 to 1,000 µm, the gap is 2.0 µm, the thickness is 500 nanometers, the electrode width is 5.0 µm, and the number of electrodes is 50.

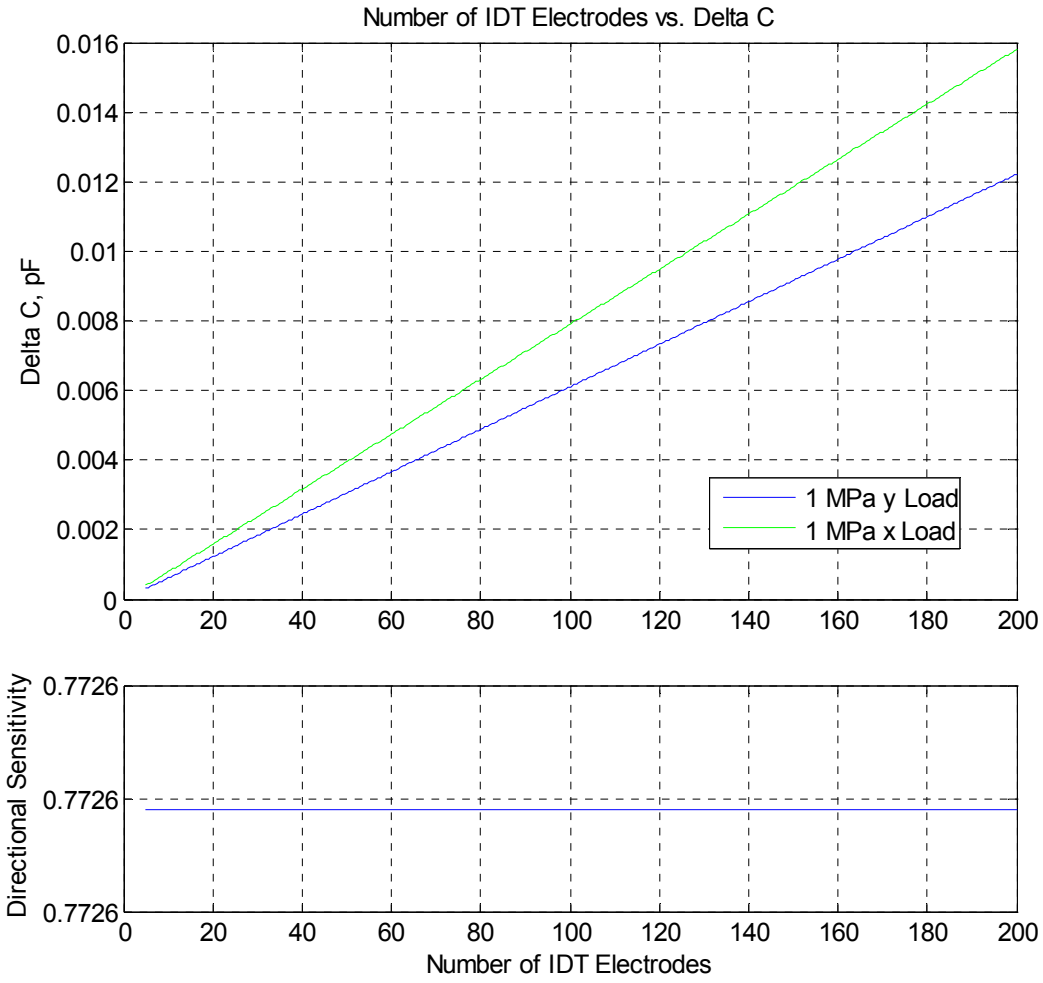

Figure 3.12: Change in capacitance and directional sensitivity as a function of the number of IDT electrodes. The electrode length is 500 µm, gap is 2.0 µm, width is 5.0 µm, and the number of electrodes is 50.

determine if the analytical model predicts a linear or a nonlinear response. In Figure 3.13, the change in capacitance as the sensor is subjected to a range of pressures varying from 0.02 MPa to 20 MPa is examined. This load was applied in both the x and the y directions. The results of this study indicate that the IDT should respond nearly linearly to applied pressures. The change in capacitance for stress in the x direction was 12.6×10^{-6} pF for the 0.02 MPa load and 25×10^{-3} pF for the 20 MPa load. The results of the directional sensitivity analysis predict that this value varies from 0.737 to 0.719 over the range of loading applied. The variation in directional sensitivity is attributed to a small nonlinearity in the response to stress in the x and y directions. This nonlinearity leads to a small variation in the directional sensitivity over the range of loads studied.

Another important factor to be considered is the gap distance between the electrodes. To determine the effect of electrode gap, the gap was varied from 0.25 μm to 8 μm while fixing the width, thickness, length, and number of electrodes. As seen in Figure 3.14, the effect of varying the gap between the electrodes has a large effect on both the sensitivity of the IDT to stress and the directional sensitivity of the sensor. These results indicate that the IDT sensitivity to stress may be improved an order of magnitude by reducing the size of the gap between the electrodes. Also at the smaller gap dimensions, the directional sensitivity of the sensor begins to approach the desired value of 0.45.

The width of the IDT electrodes contributes to the stray capacitance of the IDT electrode system; but even more important, it provides the primary contribution to the stiffness and the micromechanics of IDT electrodes as they are subjected to stress or

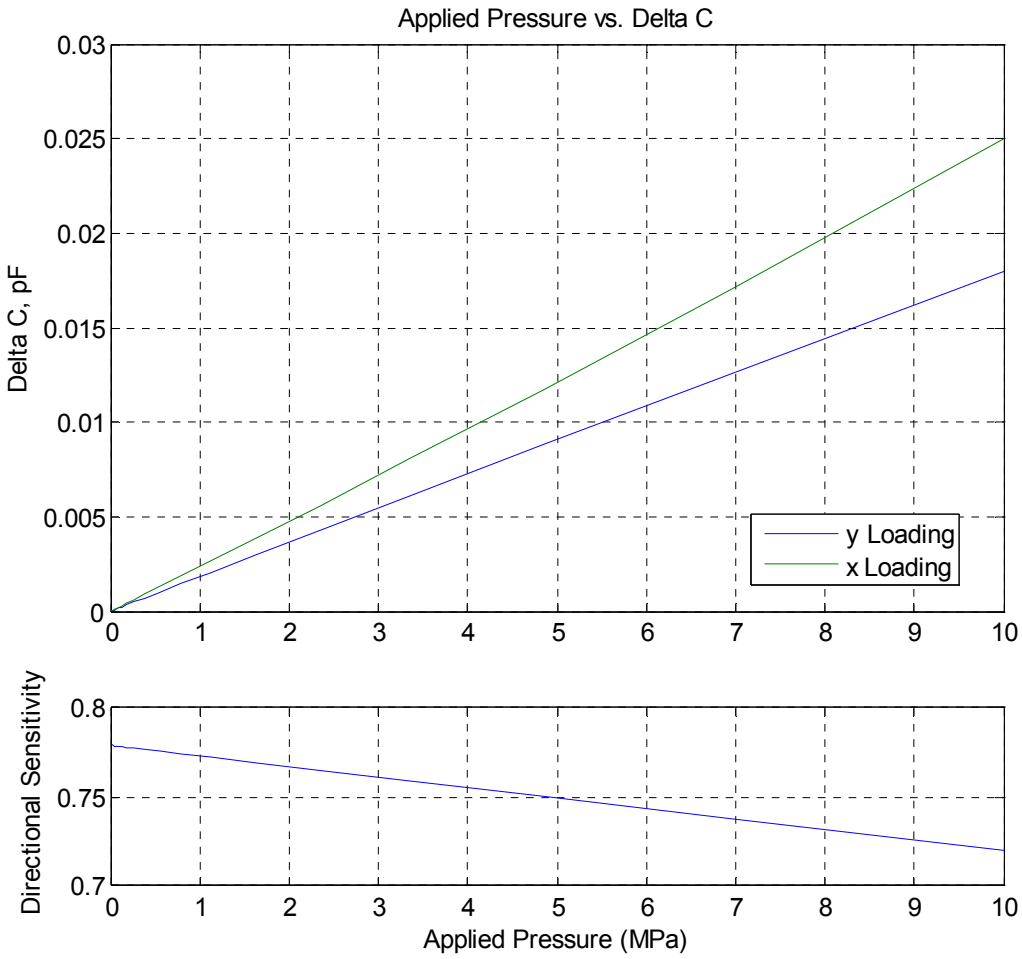

Figure 3.13: Change in capacitance and directional sensitivity as a function in-plane stress subjected to the IDT electrodes. The electrode length is 500 μm, thickness is 0.5 μm, gap between electrodes is 2.0 μm, and the number of electrodes is 50.

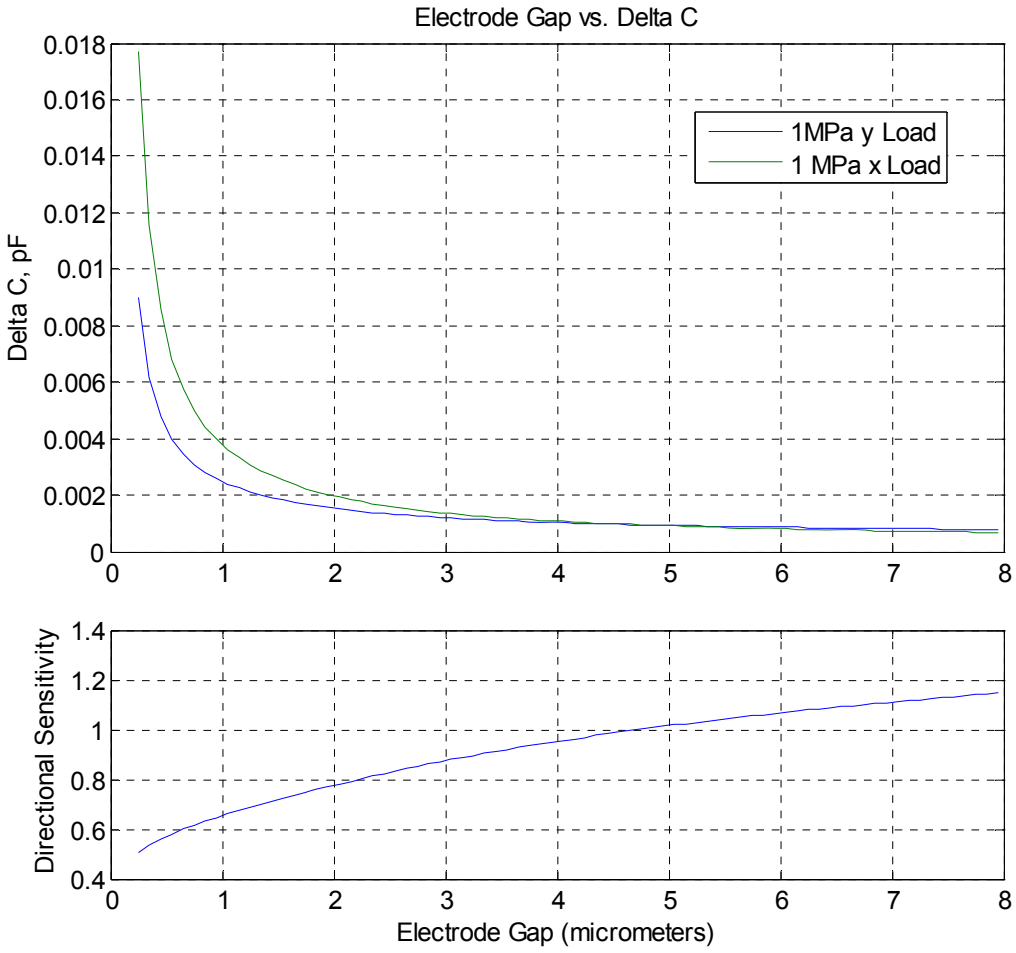

Figure 3.14: Change in capacitance and directional sensitivity as a function of the width of the gap between the IDT electrodes. The electrode length is 500 µm, thickness is 0.5 µm, the width is 5.0 µm, and the number of electrodes is 50.

strain. This contribution to the compliance of the overall electrode has a large affect on the response of the sensor, because the combined dielectric and electrode should have a similar change in dimensions as the embedding material. This forces the more compliant dielectric material to have larger strain causing a greater change in capacitance. As seen in Figure 3.15, this effect has a large influence on the sensitivity of the sensor to strain and an even larger influence on the directional sensitivity of the system. At very narrow electrode widths as compared to the gap between the electrodes, the sensor is more sensitive to pressure in the direction parallel to the electrodes. At a certain width, the sensitivity becomes the same, and then the IDT becomes more sensitive to pressure normal to the direction of the electrode.

The aspect ratio of the electrode determines the amount of capacitance between the faces of the electrodes as compared to fringe capacitance out of the plane of the electrodes. The thickness of the electrode also influences its stiffness and therefore the micromechanics of the electrodes. The thickness of the electrode was varied from 0.1 to 6 μm to observe the effects of very thick and very thin electrodes. As can be seen from Figure 3.16, the electrode thickness appears to have the most significant effect on the directional sensitivity and overall response of the sensor. The sensitivity of the IDT to the 1 MPa load was 3 femptofarads with a thickness of 0.1 μm, but this value increased to over 22 femptofarads as the thickness was increased to 6 μm. Moreover, changing the thickness of the IDT has the most significant effect on the directional sensitivity of the IDT to in-plane stress normal and orthogonal to the IDT electrodes. As the thickness was

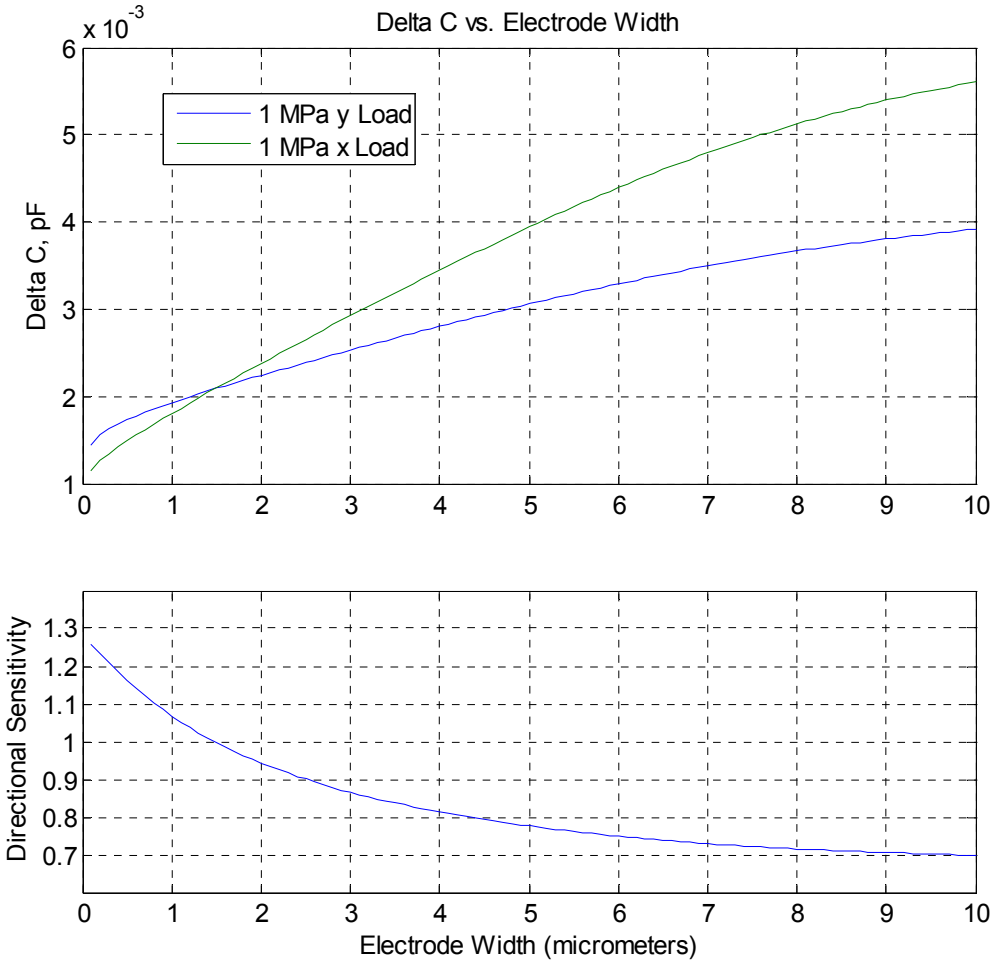

Figure 3.15: Change in capacitance and directional sensitivity as a function of the width of the IDT electrodes. The electrode length is 250 µm, thickness is 0.5 µm, gap between electrodes is 2.0 µm, and the number of electrodes is 50.

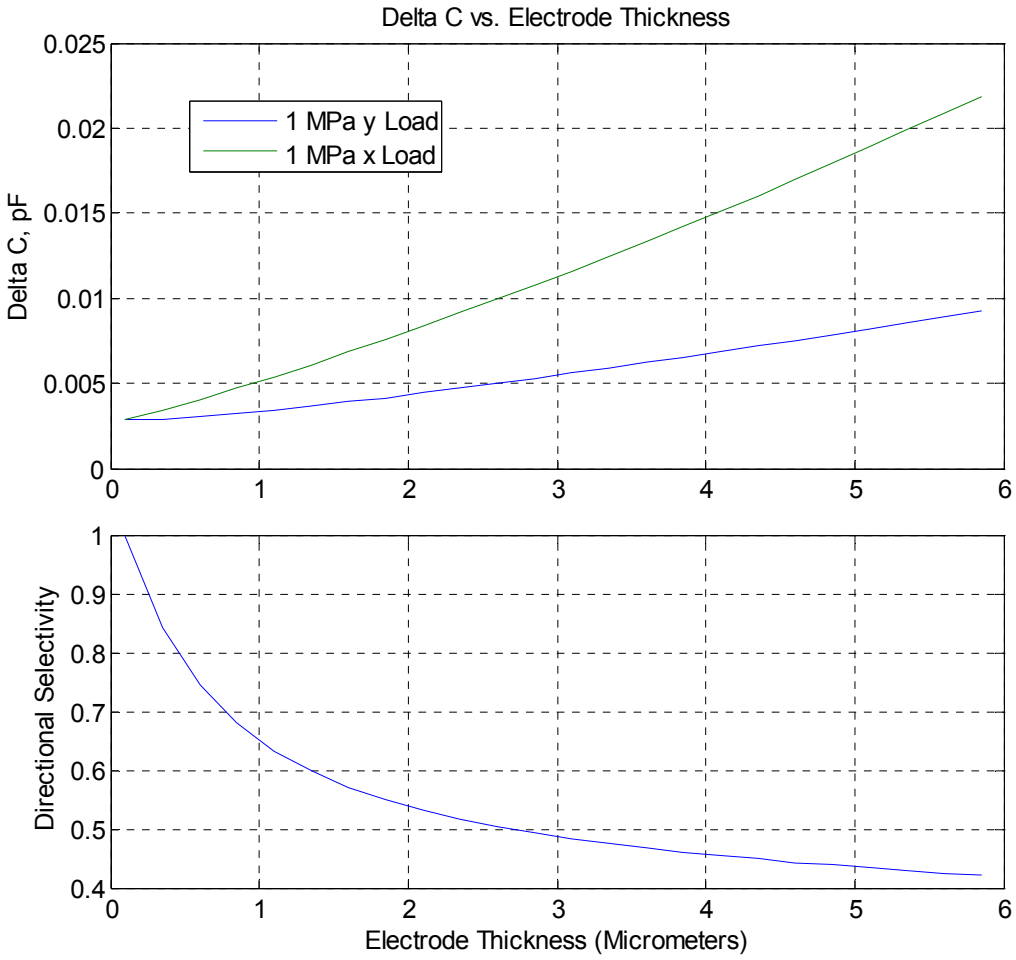

Figure 3.16 Change in capacitance and directional sensitivity as a function of the thickness of the IDT electrodes. The electrode length is 250 μm, width is 5 μm, gap between electrodes is 2.0 μm, and the number of electrodes is 50.

increased, the directional sensitivity value rapidly approached the ideal value of approximately 0.45.

3.4.5 Summary of Results of IDT Response Analysis and Optimization

A mathematical model has been developed to quickly predict the response of the interdigitated transducer of higher elastic modulus embedded in a matrix of dielectric material of lower elastic modulus. The effects of varying the electrode length, the amount of pressure the electrodes are subjected, the number of electrodes, the electrode gap distances, as well as the electrode thickness and width have been examined using this technique. It should be noted that in this analysis the effects of shear stresses between layers of materials has been neglected, and a simplified model of material interaction has been utilized. The analytical techniques developed appear to be a convenient way to quickly examine many variations in geometry. The results of this study showed that IDT has a nearly linear response to the application of stress, and that the response can be improved in a linear manner by increasing the length or the number of electrodes. Finally, it was shown that the electrode thickness, width, and gap distance can be used to optimize the directional sensitivity of the IDT strain sensor to load.

3.5 Conclusions on Analytical Relationships Between the Deformation of Composite Electrodes and Changes in Capacitance

In this chapter, a model for the change in capacitance with applied stress has been developed for the composite material properties of the sensor elements by adapting techniques from mechanics of composite materials methods. Using these methods,

relationships between the change in capacitance and applied normal and transverse loading conditions have been developed for the parallel plate capacitor. Similarly, a model has been developed to simulate the response of the differential shear sensor to shear stress. Finally, this modeling technique was extended to the change in capacitance in an interdigitated capacitor for pressure loads applied both in parallel and orthogonal to the digits of the electrodes.

Limitations to this technique are that it neglects the shear forces that exist between layers of materials, and that it requires input from other results such as experimental results or finite element results to determine characteristic volume parameters. Another limitation is the understanding of material property values for the materials used in this research due to differences in properties of materials when deposited as thin films as compared to bulk materials. The benefit of this technique is that once these parameters are determined, the response of the system may be approximated quickly and a range of parameters examined.

Parameter studies carried out in this research predict that the parallel plate sensor sensitivity increases as the area of the electrodes increases and as the electrode gap decreases. The primary design parameter for the shear sensor is the width of the sensor electrodes, and the sensitivity increases linearly with the width of the electrodes. The interdigitated strain sensor has increasing directional and overall sensitivity with decreasing digit gap spacing and with increasing electrode thickness. Overall IDT sensitivity may also be increased by increasing electrode length and number.

The relationships developed in this chapter aid in the understanding of sensor response which is ultimately required in order to interpret results from embedded sensors. They also allow for the optimization of sensor geometry in a rapid manner. The relationships developed in this section and the results of the parameter studies are one of the contributions of this research.

Chapter 4
Multi-physics Finite Element Modeling of Capacitive Sensor Structures

Understanding the loads on orthopedic components has been a primary concern of those involved in implant research and design. The relative implant kinematics, contact areas, and contact stresses are important to the performance and wear of any prosthesis. This chapter discusses the design of an array of capacitance-based sensors for the multi-axial characterization of strain and the results of finite element analysis for the optimization of the sensors. These devices are designed such that they may be fabricated by two dimensional lithography techniques. Capacitance-based sensors were chosen for this project due to their lack of resistive heating, low power consumption, and the ability to fabricate the electrodes using biocompatible materials.

The overall design concept for these sensors was introduced in Chapter 2. Multiphysics modeling in this research combines the simulation of mechanical effects and electrostatic effects. In this chapter, particular attention is given to the mechanical response the sensor geometry, because understanding the mechanical response gives insight as to the changes in capacitance due to stress and the sensors sensitivity to a particular load or stress condition. It is anticipated that during use of these sensors, they will be fully encapsulated inside the relatively soft polyethylene bearing material.

Boundary conditions applied during these studies are intended to reflect the microscopic state of stress and strain in the polyethylene as a result of macroscopic loading. The boundary conditions and loading are presented for each of the sensor geometries in this chapter and the stress, strain, and capacitance results of the models are presented.

4.1 Material Properties and Units for Finite Element Analysis

Finite element analysis requires the use of consistent units. For many finite element packages, it is the researcher's responsibility to choose units and ensure that the material properties are consistent. MEMS structures present a particular challenge to the area of units and materials properties. The length scales used in MEMS are significantly smaller than those used in typical engineering analysis problems. If the designer were to use conventional sets units for length and properties, the amount of leading zeros in many dimensions can lead to large round-off errors. Therefore, the primary unit system for analysis must be scaled with the problem while ensuring that the secondary units of density, acceleration, and pressure as well as any other secondary units required for multiphysics analysis are consistent.

For this analysis; the units of length are chosen to be the micrometer, the unit of force is the micronewton, and the unit of mass is the kilogram. Units of density are kilograms per cubic micrometer ($kg/\mu m^3$). The unit of pressure is micronewtons per micrometers squared ($\mu N/\mu m^2$) which conveniently yields the same number values as megapascals (MPa).

Only a small number of materials have been approved for biocompatible applications by the Food and Drug Administration (FDA). Material properties of biocompatible and MEMS materials must be chosen carefully because they have a significant effect on the response of the capacitance-based sensors. The ability of an embedded sensor to respond to the loads is reduced when the sensor materials have higher stiffness than the embedding materials. Material properties and dimensions should be optimized to give the best sensor response and reduce the sensors influence on the stress and strain in the device. Table 4-1 summarizes the units and material properties used in this investigation.

Table 4-1: Properties of materials and units used for the finite element study.

Material	**CoCr**	**UHMWPE**	**Au**	**Parylene C**	**PMMA**	**Polyimide**	**Units**
Young's Modulus	2.2 (10^5)	6.9 (10^2)	5.7 (10^4)	2.8(10^3)	2.5 (10^3)	2.9 (10^3)	$\mu N/\mu m^2$ (MPa)
Poisson's Ratio	0.32	0.46	0.35	0.4	0.4		
Density	8.3(10^{-15})	9.3(10^{-16})	1.9(10^{-14})	1.29(10^{-15})	9.3(10^{-16})	1.39(10^{-15})	$Kg/\mu m^3$
Relative Permittivity		2.3		2.95 (1 MHz)	2.9		
Load							μN
Pressure							$\mu N/\mu m^2$ (MPa)
Displacement							μm

4.2 Strategy for Modeling Embedded Strain Sensors

The design strategy for the embedded sensors capable of characterizing strain in three dimensions was discussed at the beginning of Chapter 2. The geometry for these designs is illustrated in Figure 2.1, Figure 2.2, and Figure 2.3. Three different sensor geometries are necessary to determine the normal strain, in-plane strain, and shear strain. A parallel plate capacitor is used to determine the strain normal to the plane of the sensors, s_{zz}. Two differential translating capacitors indicate the components shear strain normal to the sensor plane, s_{zx} and s_{zy}, and three interdigitated capacitors function to determine s_{xx}, s_{yy}, and s_{xy}. Multiphysics finite element analysis has been used to predict sensor response to loading and to determine the effects of the various design parameters on their response.

For this investigation, high density meshes of non-linear parabolic elements were used to model the structure of the device. Mesh density convergence studies were conducted to ensure that sufficient mesh density was incorporated. Simplifications, such as removing small edges were made to reduce numbers of high aspect ratio elements which increase simulation time. Models were analyzed on computer servers utilizing the Windows® (Microsoft Corp. Redmond, WA) operating system. In most models, the mesh density and model detail were dictated by a 2.0 gigabyte limit on random access memory (RAM) imposed by the combination of Windows® and Coventor. Models were scaled such that a high density mesh could be incorporated to accurately model the small stresses and displacements. Symmetry was used to reduce the model size in the case of the parallel plate sensor. In the case of the shear sensor, the width of the sensor was

reduced by a factor of five. For the interdigitated capacitor, sensors with shorter electrode digits and fewer numbers of electrodes were employed than what is anticipated for the final implementation of these devices. Models were analyzed to examine the effects of scaling, and some of these results are presented. The mathematical models presented in Chapter 3 were developed in conjunction with the finite element models, and the effects of scaling were incorporated in these models.

A combination of analysis tools have been used in the design of this system. The MEMS design software Coventor (Coventor, Inc. Cary, NC) was used extensively in this project. Coventor is capable of 3D simulation of MEMS geometry, process simulation, and multi-physics finite element analysis. Multiphysics finite element analysis allows capacitance to be solved for the mechanical analysis results. Coventor can also export the GDSII files required to create masks for photolithography. A typical Coventor geometry and mesh is shown in Figure 4.1 for the interdigitated electrode.

The effects of stray capacitance play an important role in this project and Maxwell (Ansoft, Inc. Pittsburgh, PA) was chosen for the investigation of fringe field. Electrostatic field analysis allows visualization of the field in the dielectric. This tool may be used to examine fringing fields and determine if the capacitance effects are occurring between the intended geometric elements.. Each sensor was modeled with a 2 volt potential applied to the electrodes for electrostatic simulations. A two-dimensional model was used for the shear sensor two visualize the function of this sensor and the effects of stray capacitance. A three-dimensional model was used for the IDT to investigate the effects both above the electrodes and at the end of the electrodes.

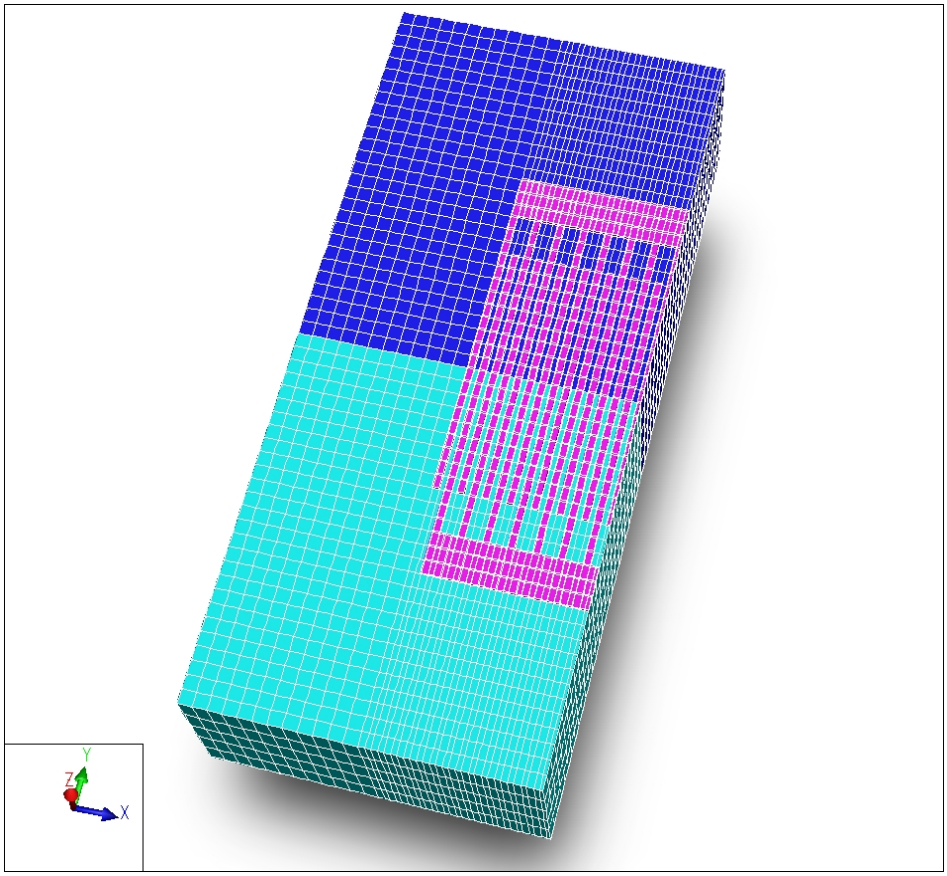

Figure 4.1: Typical finite element mesh from Coventor for multi-physics modeling of electrode structures. Symmetry in the yz plane has been used to simplify the analysis and allow for a finer mesh in the analysis region. Upper parylene and polyethylene layers are hidden for clarity.

Parabolic Manhattan brick elements were used for all Coventor models, which are 27 node quadratic elements with three nodes per edge. Coventor uses the solver from Abaqus (Abaqus, Inc. Providence, RI) finite element software for solving mechanical simulations. Linear elastic behavior was assumed for all materials in this investigation. Loads resulting in 1 MPa stress were applied which should not violate the linear elastic assumption; however, in the actual prosthesis previous research has shown that loads may approach the yield stress of the material. [69,126,127] A typical mesh is shown in Figure 4.1. The material properties of gold were used for all electrodes, and all electrodes were covered in a 2 μm layer of parylene and embedded in polyethylene.

Coventor uses a boundary element method to solve the Laplace equation in a single-layer for surface charge given an applied voltage. As part of this algorithm, the three-dimensional continuum element mesh is collapsed into a three-dimensional arrangement of shell or boundary elements. The MemElectro electrostatic module of Coventor uses a corrected fast Fourier transform technique to simplify the resulting system matrix. MemElectro solves the Laplace equation iteratively in a single-layer form (Gauss' Law) for the surface charge q, given an applied potential, V. Coventor's primary strength is its ability to perform multiphysics finite element analysis, which in this case was used to solve for the deformed geometry due to an applied loading condition followed by determination of the change in capacitance due to that deformation. Because Coventor does not solve for the field in the dielectric layers, Maxwell was used for the computation and visualization of the three-dimensional fields. [128] However, Maxwell

is not capable of modeling the effects of mechanical stress on the electrode shape or changes in capacitance due to applied loads.

The method for determining the change in capacitance due to the applied loads was to perform the electrostatic analysis on the model geometry in an unstressed state, followed by the mechanical analysis due to a 1 MPa stress in the z or x direction. A second electrostatic analysis was performed using the load induced displacements from the mechanical analysis. The difference between the undeformed and deformed geometry computed capacitance is the reported change in capacitance. Using this approach, convergence studies were performed on initial geometries of each electrode type. The mesh density sufficient for mesh convergence better than 0.25% was determined, and typical models consisted of between 10,000 and 25,000 parabolic elements.

4.3 Finite Element Modeling of Parallel Plate Capacitor Structures

Coventor multiphysics analysis was used to determine the response of the parallel plate capacitor with a parylene dielectric material embedded in a polyethylene matrix. One-fourth symmetry was used to reduce the mesh size of the parallel plate models. Coventor was used to examine the effects of electrode size and loading on the response of the embedded sensor. A convergence study was performed prior to analysis to determine the appropriate mesh density for the study. Results were compared with the analytical models developed in the previous analysis. Typical mesh models are shown in Figure 4.2 and Figure 4.3. Models were examined for sensitivity to normal and transverse loading.

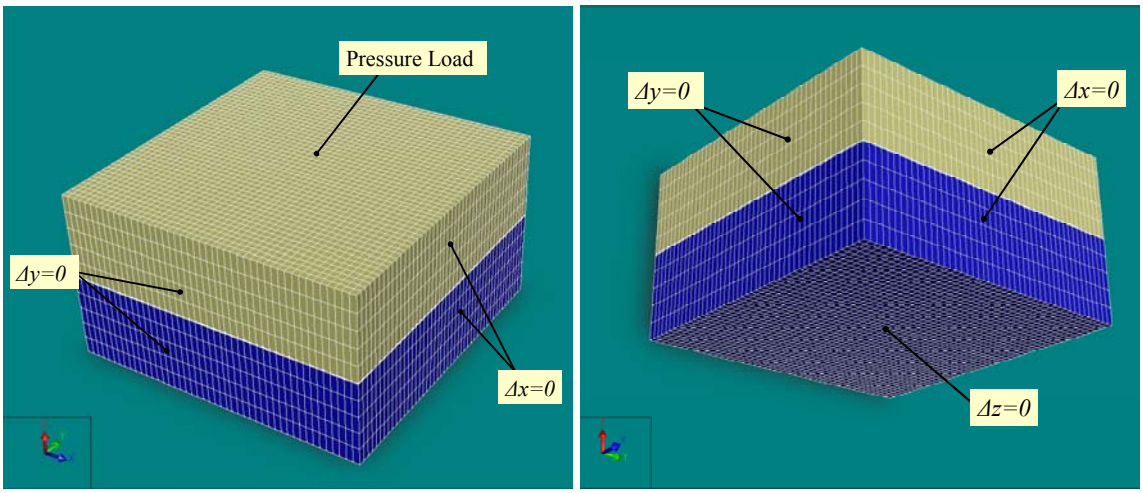

Figure 4.2: Upper and lower view of parallel plate finite element model for 5 pF sensor with mechanical boundary conditions annotated for normal loading.

The effects of electrode size were examined as well as the response to a wide range of loading values.

The electrodes were simulated as having a thickness of 300 nm and the material properties of gold. The dielectric material between the electrodes was given the properties of the biocompatible material parylene. The parylene layer was given a thickness of 2.0 µm. The primary loading condition examined was a 1 MPa load applied in the negative z direction. A 200 µm polyethylene encapsulation layer was applied both above and below the sensing layer. The overall dimensions of the quarter-symmetry model were 700 µm wide by 700 µm long and 402.6 µm tall. Material properties were previously shown in Table 4-1. Figure 4.3 illustrates the normal strain sensor with the upper polyethylene layer displayed as transparent. Boundary conditions are shown, and the electrodes are visible above the lower polyethylene layer.

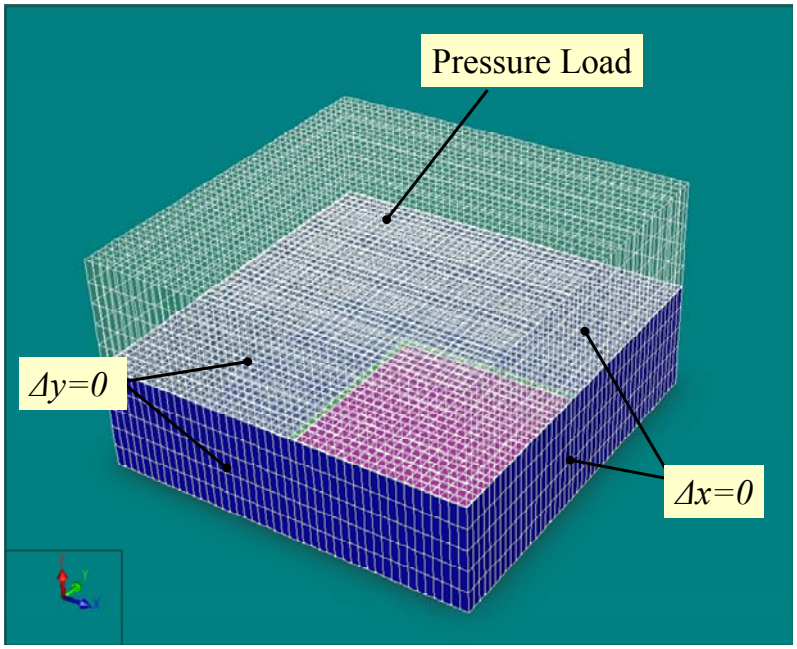

Figure 4.3: Parallel plate FEA model with upper polyethylene layer and parylene dielectric layers displayed as transparent. One-fourth symmetry used in model.

4.3.1 Parallel Plate Capacitor FEA Convergence Study

A convergence study was performed to ensure adequate mesh density for modeling the capacitor structures. Measuring the effects of mesh density is particularly important for this problem due to the interest in modeling the interactions of microscopic and macroscopic structures. 27 node Manhattan brick elements were used for this model and the mesh density was modified by varying the allowable x, y, and z maximum element size. Models varying from course to significantly finer meshes were examined. Models consisting of 567; 2,601; 6,561; 22,188; 41,616; and 55,488 elements were examined for convergence. The 1.0 pF capacitor was used as the base model for convergence studies, then other models with similar mesh densities were analyzed based on these results. Convergence results are illustrated in Figure 4.4 and Figure 4.5. Detailed results showing the mesh settings and analysis results are shown in Table 4-2.

Figure 4.4 illustrates the change capacitance results with the number of elements over the convergence study. This data shows that the capacitance was not significantly affected by the number of elements. Figure 4.5 illustrates that electrode displacement results as a function of the number of model elements. This data shows that the displacement results are more dependent on the number of elements than the capacitance results. For this study there is interest in modeling very small changes in electrode geometry and the resulting changes in capacitance, a very high degree of convergence is desired and models producing better than 0.25% convergence in both displacement and capacitance were used resulting in models with approximately 25,000 elements were used for the following studies.

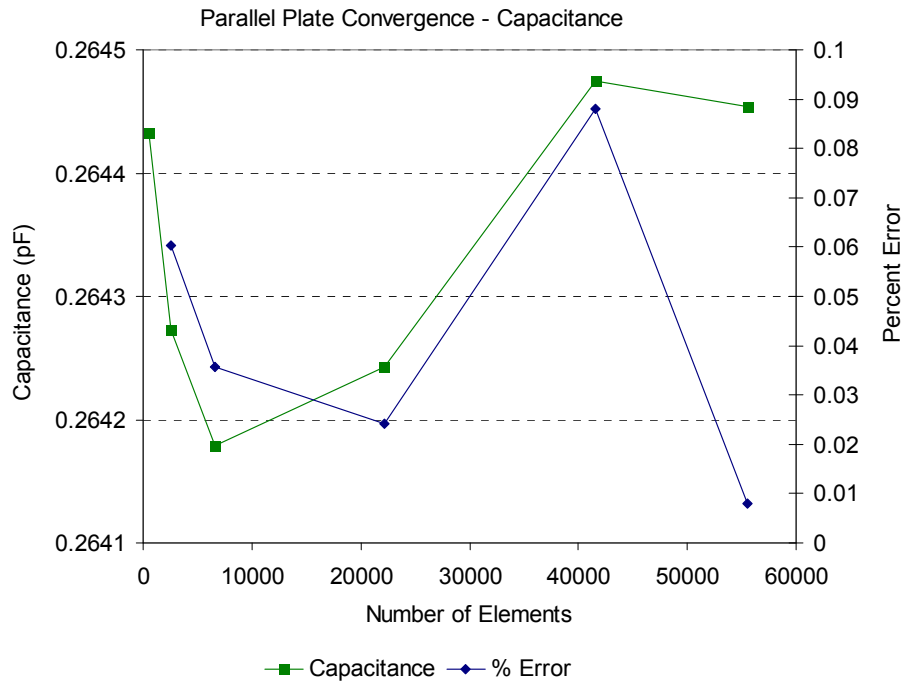

Figure 4.4: Parallel plate convergence results based on capacitance.

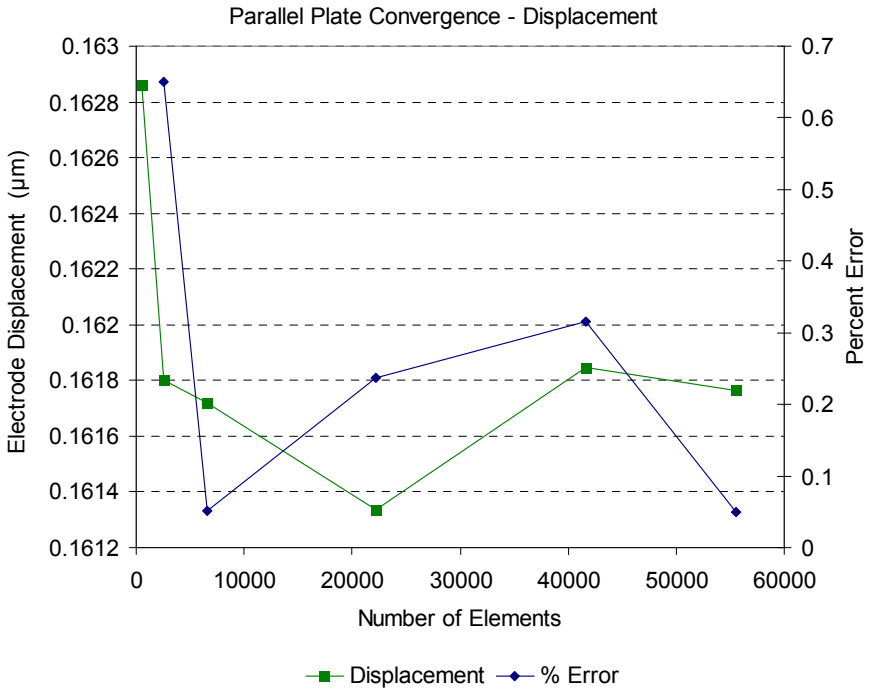

Figure 4.5: Parallel plate convergence results based on displacement results.

Table 4-2: Summary of parallel plate convergence results.

Model	**A**	**B**	**C**	**D**	**E**	**F**
x Element Size (microns)	40	20	12.5	8	5	5
y Element Size (microns)	40	20	12.5	8	5	5
z Element Size (microns)	40	30	30	20	30	20
Total Number of Elements	567	2601	6561	22188	41616	55488
Average Aspect Ratio	35.2417	14.6204	9.95422	5.80001	7.5368	5.6526
Min Aspect Ratio	1.09	1.45741	2.42901	2.44176	2.5413	2.5
Max Aspect Ratio	152.478	76.2389	45.7433	27.3027	26.6667	26.6667
Capacitance	0.26443	0.26427	0.26418	0.26424	0.26447	0.26445
Capacitance % Error		0.06034	0.03560	0.02422	0.08792	0.00809
Node Displacement	0.43138	0.43167	0.43171	0.43188	0.43176	0.43174
Node X Displacement	2.0906E-34	7.4563E-35	4.4766E-35	1.9251E-35	1.6587E-35	2.6341E-35
Node Y Displacement	0.22526	0.22550	0.22552	0.22565	0.22554	0.22553
Node Z Displacement	-2.7269E-35	-1.1467E-35	-4.4798E-36	-1.8123E-36	-7.1509E-37	-1.8153E-36
TOP ELECTRODE Y+ MaxDeflection	0.16286	0.16180	0.16172	0.16134	0.16185	0.16176
TOP ELECTRODE X- MaxDeflection	0.16286	0.16180	0.16172	0.16134	0.16185	0.16176
LWR ELECTRODE Y+ MaxDeflection	0.16952	0.16885	0.16862	0.16823	0.16834	0.16845
LWR ELECTRODE X- MaxDeflection	0.16952	0.16885	0.16862	0.16823	0.16834	0.16845
Electrode Displacement Error		0.65111	0.05127	0.23671	0.31567	0.05007

4.3.2 Parallel Plate Capacitor FEA Model Details

As shown in Figure 4.3, one-quarter symmetry was used to reduce the number of elements in the finite element models. In the x-z plane of symmetry, the model was constrained to have zero displacement in the x direction. Similarly in the y-z plane of symmetry, the parallel plate model was constrained to have no displacement in the y direction. The lower surface of the model was constrained in the z direction. A 1 MPa stress was applied to the top surface of the model in the -z direction to determine the response to normal stress.

A similar modeling approach was used to determine the response to in-plane loading, however the 1 MPa stress in the x direction was applied to the -x surface of the model. This case was examined to determine the response to loading in the transverse direction. This case is used to determine the sensitivity of the sensor to loading direction and the effects of transverse strain.

A parameter study was performed to determine the effects of electrode size or nominal capacitance. A square shaped electrode was used in each case, and the lower electrode was designed to be 25 μm larger than the upper electrode such that shear stresses or strains would not result in a change in the area of the sensors. The nominal capacitance of each electrode configuration studied was 1, 2.5, 5, 7.5, and 10 picofarads. The width of one side of the square, upper electrode was 274, 434, 614, 751, and 867 μm respectively.

The sensitivity of these sensors to a range of loading conditions was also examined. The change in capacitance for loads ranging from 0.02 MPa to 20 MPa was

investigated in ten logarithmic steps for all five sensor geometries. This loading allows the response to be plotted logarithmically, and will allow the final sensor geometry to be selected based on the sensitivity of the read-out circuit and the expected load.

4.3.3 Parallel Plate Capacitor FEA Results

In this section, the results of finite element modeling to determine the response of the sensor to a 1 MPa load in the z and x directions are presented. The application of the transverse load in the x direction was used to investigate the response to loading conditions which might result in cross-talk and to determine the ability to measure transverse strain. Results of the load sensitivity analysis and nominal capacitance sensitivity analysis are also presented in this section.

The goal of using high-stiffness material to measure strain while embedded in a softer materials presents several challenges. The effects of embedding small amounts of electrode materials in softer mediums is shown in the results of the finite element analysis. Results for the 5 pF sensor are illustrated in the following figures. Figure 4.6 illustrates the displacement magnitude for the entire model subjected to a 1 MPa load. In Figure 4.7, the upper polyethylene layer is hidden to allow the plane of the upper electrode to be visible. In these figures, it should be noted that the 300 nm thick gold electrodes and the 2 micrometer thick dielectric layer cause no significant discontinuity in the overall displacement of the representative volume of material. These images show that the electrode and dielectric materials tend to have the same displacement as the bulk materials with little effect on the displacements of the embedding material.

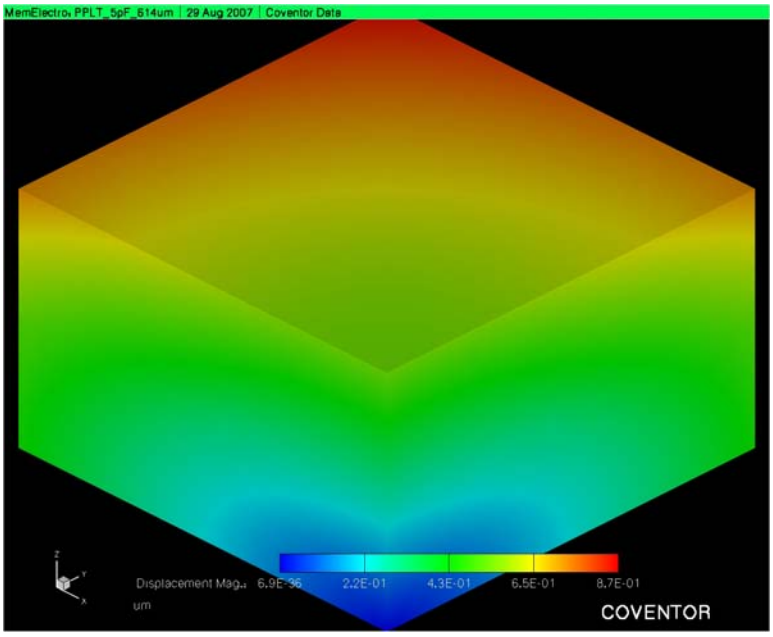

Figure 4.6: Finite element analysis results for embedded normal strain sensor. Capacitor is embedded in the center of figure shown.

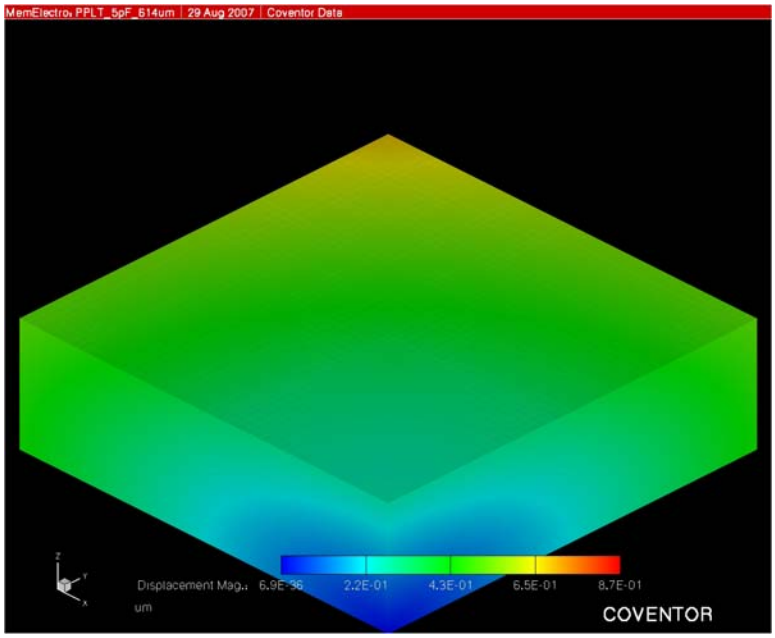

Figure 4.7: Displacement magnitude results from parallel plate strain sensor with upper embedding layer hidden.

When deriving analytical solutions for the parallel plate sensor response using the Maxwell-Reus model, it was assumed that the geometry and loading conditions result in a state of nearly equal stress in the z direction, but not equal strain. The z direction stress results for the 1 MPa z direction load are illustrated in Figure 4.8 and show that the stress is nearly equal through the thickness of the model. The z direction strain results are illustrated in Figure 4.9. These results show that the strain is higher in the softer matrix material and less in the stiffer dielectric and electrode materials. These results agree with the assumptions used to derive the analytical relations for the normal strain sensor response in Chapter 3 and give further insight into the behavior of these sensing systems. Principal stress results are illustrated in Figure 4.10.

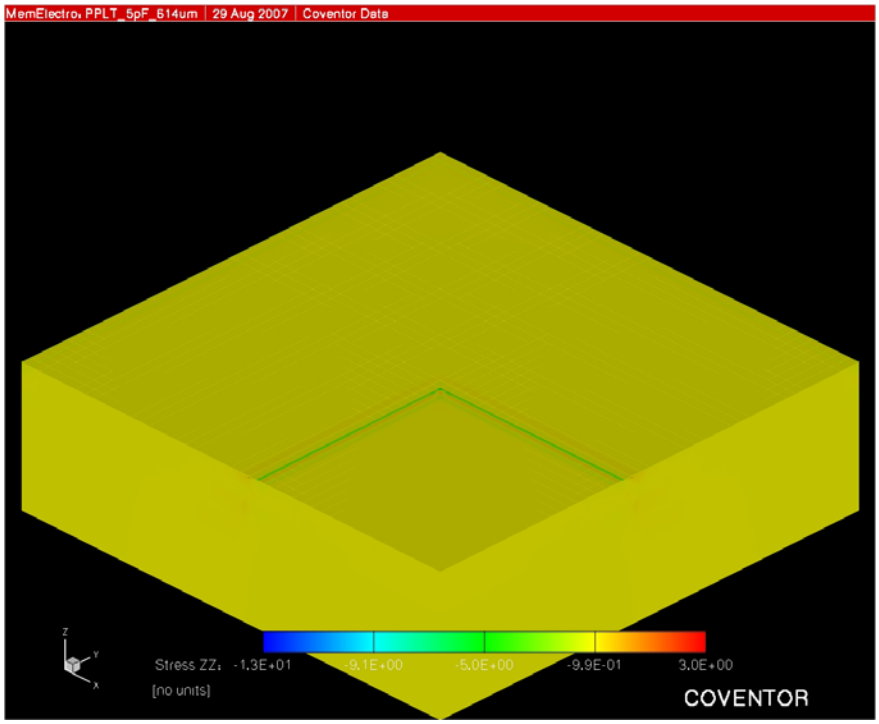

Figure 4.8: z direction stress for normal strain sensor with upper encapsulation layer hidden.

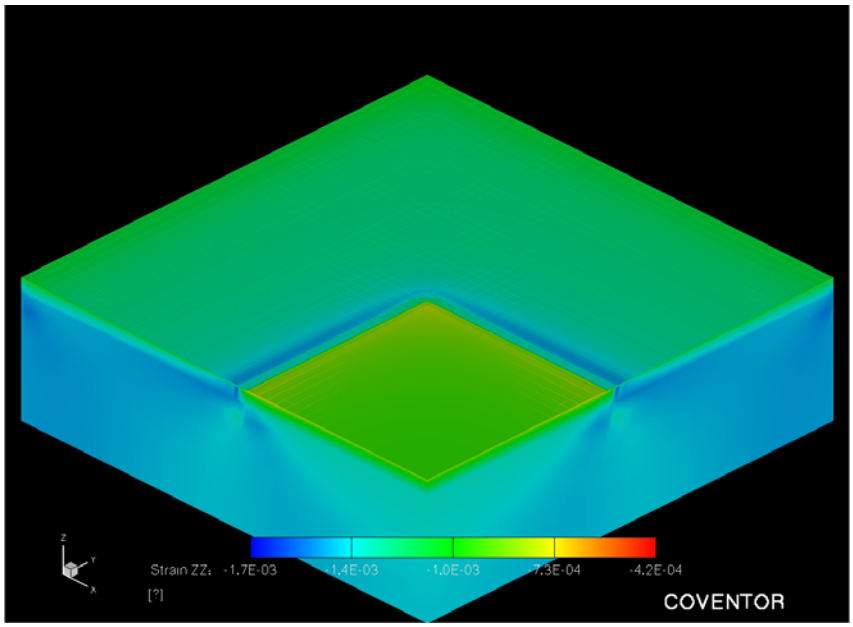

Figure 4.9: Strain in the z direction for normal strain sensor. The upper encapsulating layer is hidden.

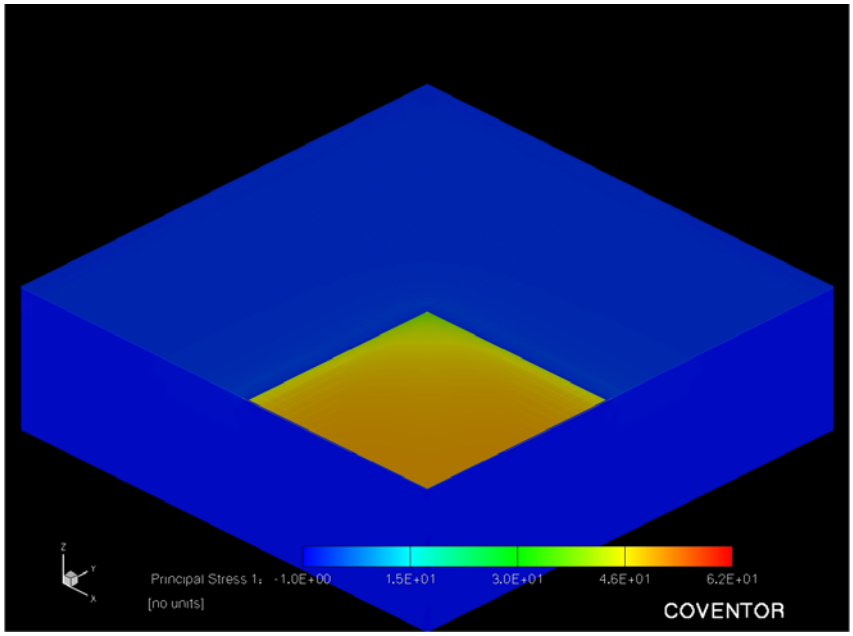

Figure 4.10: Principal stress results for normal strain sensor.

The principal stress results for the embedded sensor subjected to a 1 MPa pressure load in the z direction are illustrated in Figure 4.10. These results show that the principal stress is over an order of magnitude higher in the electrode materials than in the embedding materials. Compressive stress is negative in this figure. This is because the thin but stiff electrode materials are forced to have the same displacement as the matrix materials. Much of this stress results from the transverse strain due to the normal load. As the polyethylene material is compressed the height of the block of material is reduced; however the length and width of the block increase as the total volume is nearly preserved. As the x and y dimensions of the polyethylene increase, the electrode is stretched as well with a nearly equal strain. Since the stress is equal to the strain multiplied by the Young's modulus, regions of higher modulus materials have higher stress values.

Results of the geometry sensitivity analysis are summarized in Figure 4.11, and include the predicted response from the mathematical model. This graph plots the capacitance results of both the normal, z, direction and transverse. x or y, direction with 1 MPa loading conditions for five different sizes of electrode geometry. The ratio of the transverse loading results to the normal load results indicates the sensors sensitivity to direction and is also illustrated. The response of the sensor to transverse loading is expected due to strain orthogonal to the loading direction. This strain is equal to the product of the elastic modulus and its Poisson's ratio divided by the applied stress. If the response in the x or y direction by the sensor response in the z direction, the result should roughly correspond to the Poisson's ratio of the sensing element.

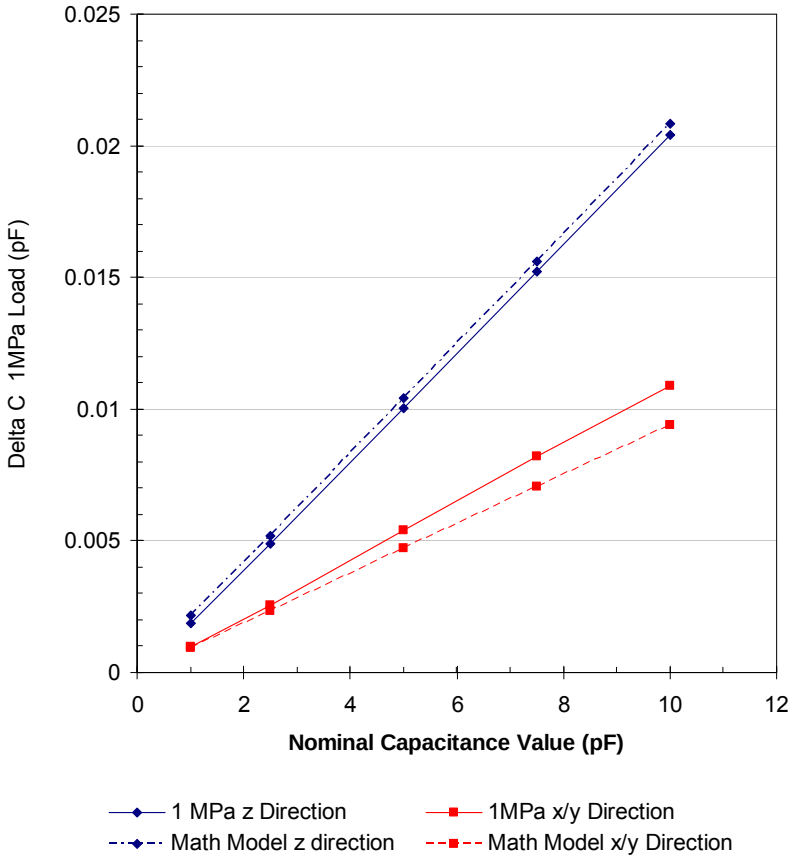

Figure 4.11: Finite element results for z direction loading and orthogonal loading for five different geometries of normal strain sensors.

Finite element modeling of the parallel plate geometry predicts a change in capacitance with a 1 MPa compressive load of 1.85×10^{-3} pF for the 1 pF sensor, 4.87×10^{-3} pF for the 2.5 picofarad sensor, 10.0×10^{-3} pF for the 5 picofarad capacitor, and 20.4×10^{-3} pF for the 10 picofarad sensor. As shown in Figure 4.11, the normal strain sensor has good sensitivity to stress direction with change in capacitance. The ratio of the transverse load direction response to the normal load direction response is 0.53, as compared to the Poisson's ratio of the UHMWPE of 0.46, a difference of 15 percent. The results of the normal strain sensor predict that this sensor has acceptable sensitivity to normal strains and exhibits the desired directional sensitivity.

A sensitivity analysis was performed on the parallel plate geometry using the following series of loads: 0.02 MPa, 0.062 MPa, 0.2 MPa, 0.62MPa, 1.0 MPa, 2.0 MPa, 6.2 MPa, and 20 MPa. This series of loads was applied to a series of geometries with base capacitance values of 1 pF, 2.5 pF, 5 pF, 7.5 pF, and 10 pF. Sensitivity values for this study are shown in Table 4-3. A log-log scale plot of the result of this analysis is shown in Figure 4.12. Results from this study can be used to select the match the response of the capacitive sensor to the signal conditioning circuit.

Table 4-3: Capacitance sensitivity for five normal strain sensors.

Base Capacitance	Sensitivity (pF/MPa)
1	0.001851663
2.5	0.004892504
5	0.010094404
7.5	0.015345666
10	0.020629266

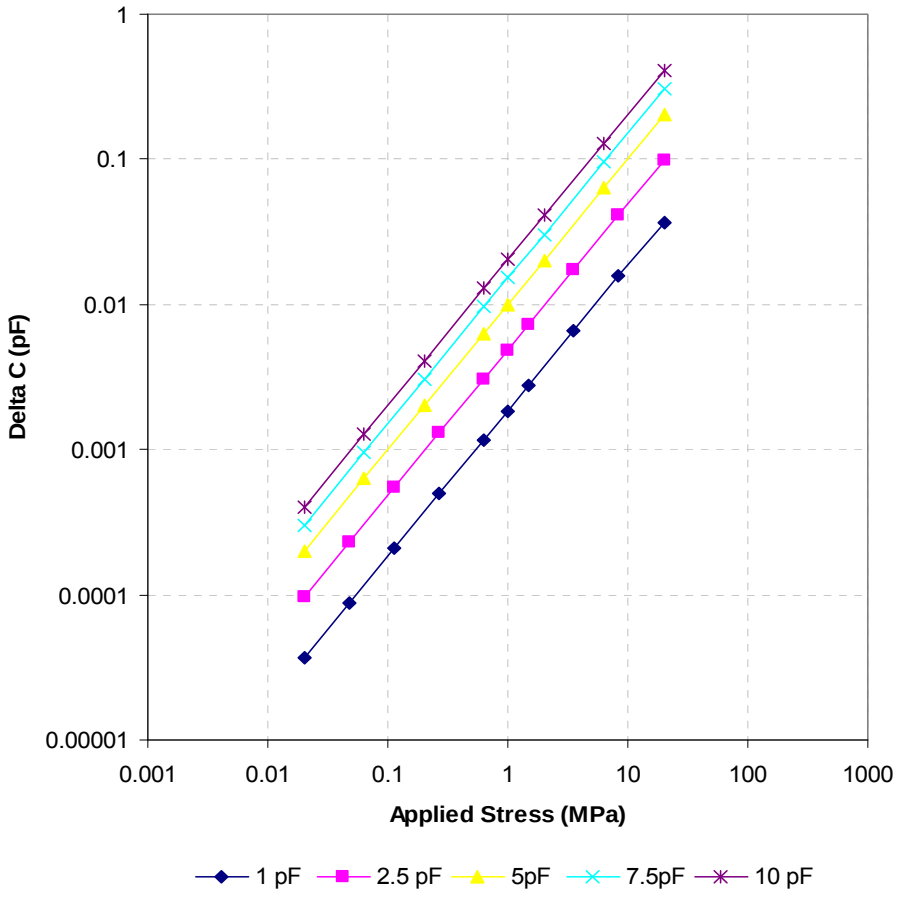

Figure 4.12: Sensitivity analysis results for loads ranging from 0.02 MPa to 20 MPa and base capacitance values of 1, 2.5, 5, 7.5, and 10 picofarads.

4.4 Shear Sensor Finite Element Analysis

Multiphysics finite element analysis was performed on several different configurations of the shear sensor. These geometries include the four electrode geometry, the three electrode geometry, and two configurations of the compact shear sensor which consists of several of the three-electrode sensors connected in parallel. A parametric analysis was run to investigate the response to different amounts of shear loading over four orders of magnitude.

The electrostatic fields around the shear sensor were investigated using the electrostatic solver Maxwell. Two-dimensional Maxwell simulations were analyzed on the three and four electrode configurations of the shear sensors. The results of these models allow visualization of the electric field, allow for better understanding of sensor function and the effects of fringing fields on this device.

4.4.1 Shear Sensor Model Boundary Conditions

Boundary conditions were applied to these models to closely approximate a pure shear loading situation. The boundary conditions given to these structures are intended to accurately represent the state of stress on a microscopic scale due to macroscopic loading of the sensor embedded in a bulk polyethylene structure. Figure 4.13 shows the boundary conditions used for the shear sensor. The boundary conditions for simulation of the shear sensor were chosen to ensure an even shear loading condition over the electrodes without the presence of other stress conditions. The loading condition consisted of a z displacement constraint on the lower surface, a zero y displacement constraint for the

mid-plane separating the front and back halves of the representative element in Figure 4.13, and a zero x displacement constraint for line at the intersection of the bottom surface and the y+ normal surface which is highlighted in red in Figure 4.13.

The representative volume of material used to analyze the shear sensor is 600 x 300 x 200 μm. For the three electrode shear sensor, the lower electrodes were 10 μm wide by 200 μm long with 4 μm between electrodes. The upper electrode was 20 μm wide by 200 μm long. In the case of the four electrode shear sensor, the lower electrodes were 10 μm wide by 200 μm long with the upper electrode being 30 μm wide by 200 μm long. The thickness of the electrodes was 0.5 μm in the Coventor models. In the actual sensor, the lower electrodes would be slightly longer than the upper electrode to prevent signal from the orthogonal shear, however this was not included in the model in order to prevent an area of small, high-aspect-ratio elements.

To represent the effects of macroscopic shear loading of the material in this small element, careful placement of boundary constraints and loads is required. The loading condition required to simulate the application of shear on the small element is for loads to be placed on four surfaces as shown in Figure 4.13. A vector stress equal to the area of the top surface of the model in MPa was applied in +x direction to the top of the model and in the –x direction on the bottom surface of the model, this results in a 1 MPa traction load on the surface of the model. On the x+ and x- surfaces on the right and left of the model, the same 1 MPa load consisting of a vector load equal to the surface area of the face was applied in the +z and -z directions respectively. This loading condition results in a uniform state of shear stress in the model.

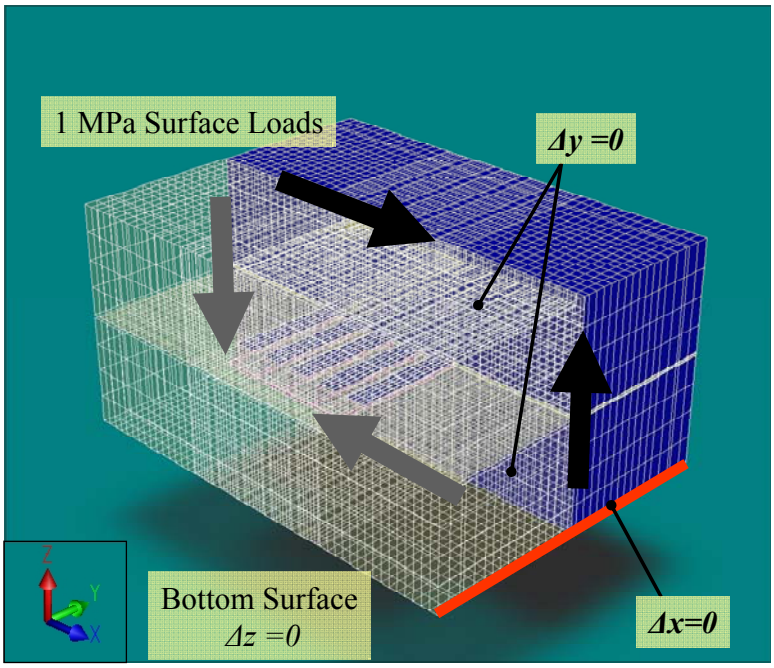

Figure 4.13: Geometry and boundary conditions for evaluating the shear stress sensor.

In the case of the three electrode sensor, the electrostatic boundary conditions were as follows: 1 volts was applied to the lower left electrode, -1 volts was applied to the lower right electrode, and a 0 volt condition was applied to the upper readout electrode. For the four electrode shear sensor, 1.0 volts was applied to the lower left electrode, -1.0 volts to the lower right electrode, and 0 volts was applied to the lower middle electrode. The upper electrode was given a "float" boundary condition which constrains the total charge on the upper electrode to 0 Coulombs total charge.

4.4.2 Results of shear sensor finite element modeling

Shear strain results in the xz direction indicate that the boundary conditions result in uniform shear strain in the bulk material. Some attenuation of strain occurs around the

electrodes due to an increased shear modulus in the area surrounding the electrodes. Values in the area surrounding the electrodes are 0.4 microstrain, and strain values in the bulk material are approximately 3.0 microstrain. Results are shown in Figure 4.14.

Shear stress results in Figure 4.15 indicate a uniform 1 MPa state of stress throughout the model with only small amounts of non-uniformity around discontinuities in material properties. Displacement magnitude results shown in Figure 4.16 indicate that the maximum displacement over the sensor approaches 1 micrometer. This Figure has exaggerated deformations which show uniform displacement over the model in the classic trapezoidal shape resulting from shear.

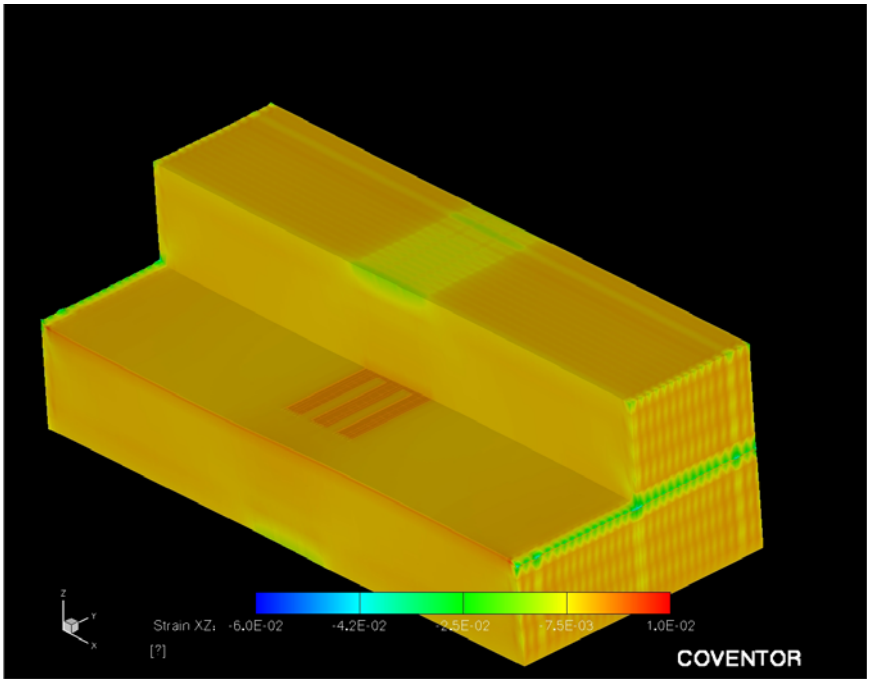

Figure 4.14: xz strain results for three electrode sensor showing good strain uniformity.

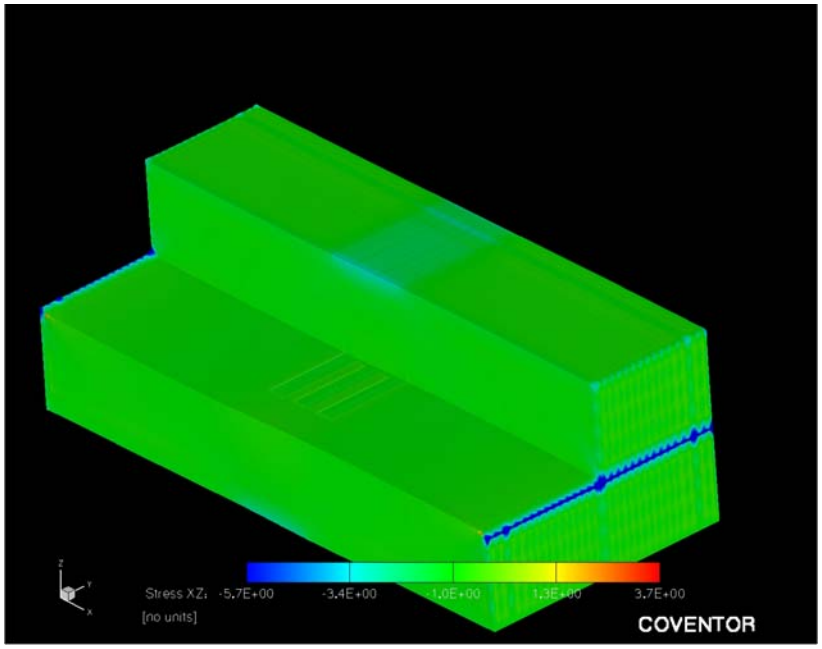

Figure 4.15: xz stress results indicate the boundary conditions result in uniform loading.

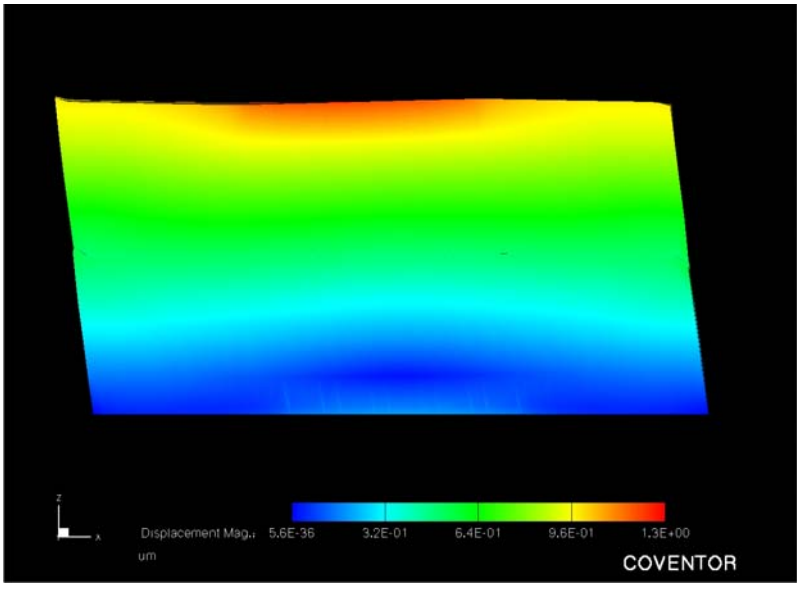

Figure 4.16: Deformed geometry of shear representative element showing classic deformation from shear strain

The displacement in the x direction is shown in Figure 4.17. The x displacement results indicate that the upper surface displaces in the positive x direction and the lower surface displaces in the negative x direction as expected. These results show no significant discontinuity in displacement near the embedded electrodes.

The results of the shear sensor to the logarithmic series of load conditions are shown in Figure 4.18 with the same results for the 4 electrode shear sensor and with the math model results for the single 3 electrode sensor. A smaller area of the model was analyzed in order that a higher density mesh could be used. A 200 μm section of the sensor was modeled, and results were scaled by a factor of five to simulate a 1000 μm long sensor. Load conditions applied consisted of a 0.062, 0.2, 0.62, 2.0, 6.2, and 20 MPa loads. For this load range the results of the single electrode sensor varied from 1.079×10^{-6}

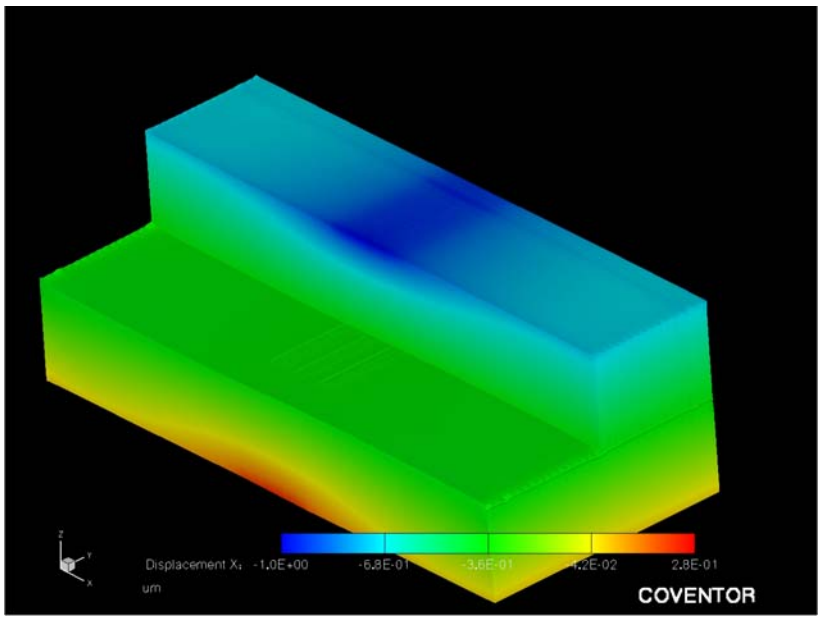

Figure 4.17: x displacement results indicate positive displacement of lower surface and negative displacement of upper surface.

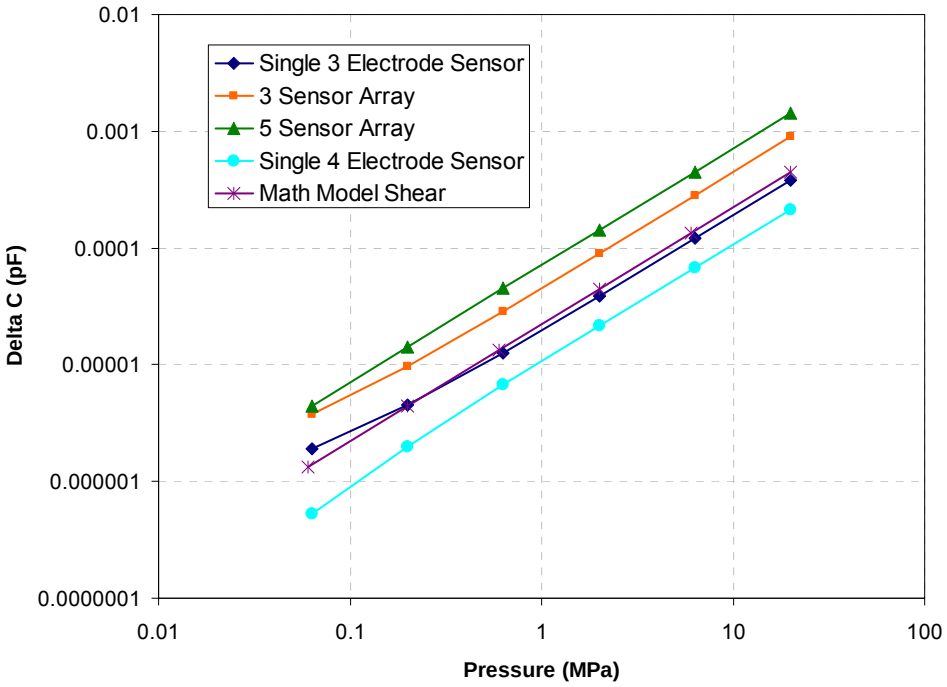

Figure 4.18: Results of load and array electrode parameter study and math model.

pF to 3.810×10^{-4} pF, results of the three electrode sensor varied from 3.790×10^{-6} pF to 8.999×10^{-4} pF, and the results of the five electrode sensor varied from 4.453×10^{-6} pF to 1.438×10^{-6} pF for the range of loads analyzed. Math modeling results corresponded with the FEA results of the single electrode sensor, and the four electrode sensor had significantly lower response than the three electrode sensor as shown below.

4.4.3 Maxwell field modeling of shear sensor geometries

For two-dimensional models, Maxwell uses triangular elements to calculate the field inside the dielectric material. An adaptive meshing approach automatically refines the mesh until the results converge within the desired criteria. 0.1% convergence based

on the total energy was used for this investigation. Typical models contained between 10,000 and 11,000 triangular elements and solved within a few minutes.

The electrostatic boundary conditions of the three electrode shear sensor consisted of a 1.0 volt constraint on the lower left electrode, a -1.0 volt constraint on the lower right electrode, and a 0 volt constraint on the upper electrode. In the case of the four electrode sensor analysis, the middle electrode in the lower layer was given the 0 volt boundary condition and the upper floating electrode was constrained to 0 Coulombs total charge.

Electric field results for the three electrode version of the shear sensor are shown in the combined vector and magnitude plot in Figure 4.19. The intensity is represented logarithmically by the vector color. The model predicts a 2.0×10^5 V/m field between the lower electrodes and the upper electrode. Fringing effects result in a field intensity between the two lower plates ranging from 5.3×10^5 V/m to 2.0×10^5 V/m. These results indicate that the fringing effects would be reduced by placing a ground plane below the two lower electrode, and reducing the fringe effects between the two energized electrodes would likely improve sensitivity.

Electric field results for the four electrode shear sensor are shown in the combined vector and magnitude plot in Figure 4.20. The intensity is represented logarithmically by the vector color. The model predicts a 2.4×10^5 V/m field between the lower electrodes and the upper electrode. Fringing effects result in a field intensity between the two lower plates ranging from 1.1×10^4 V/m to 5.1×10^4 V/m. Similarly to the three-electrode version of the shear sensor, a significant fringing field exists below the sensor which indicates that a ground plane under this area should increase sensitivity by reducing the nominal capacitance of the system.

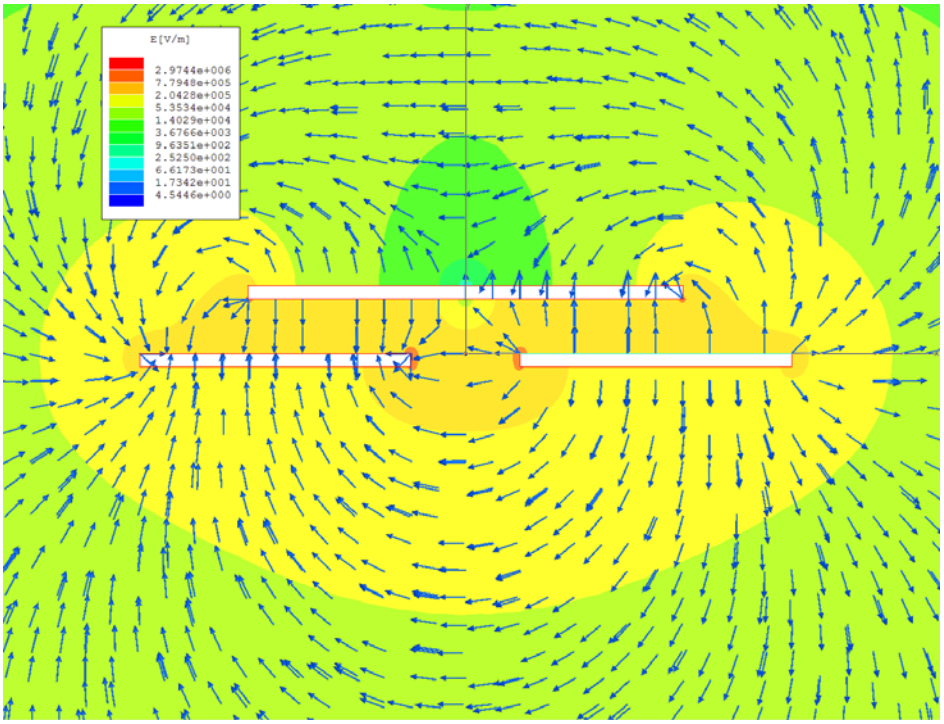

Figure 4.19: Electric field results from Maxwell two-dimensional model.

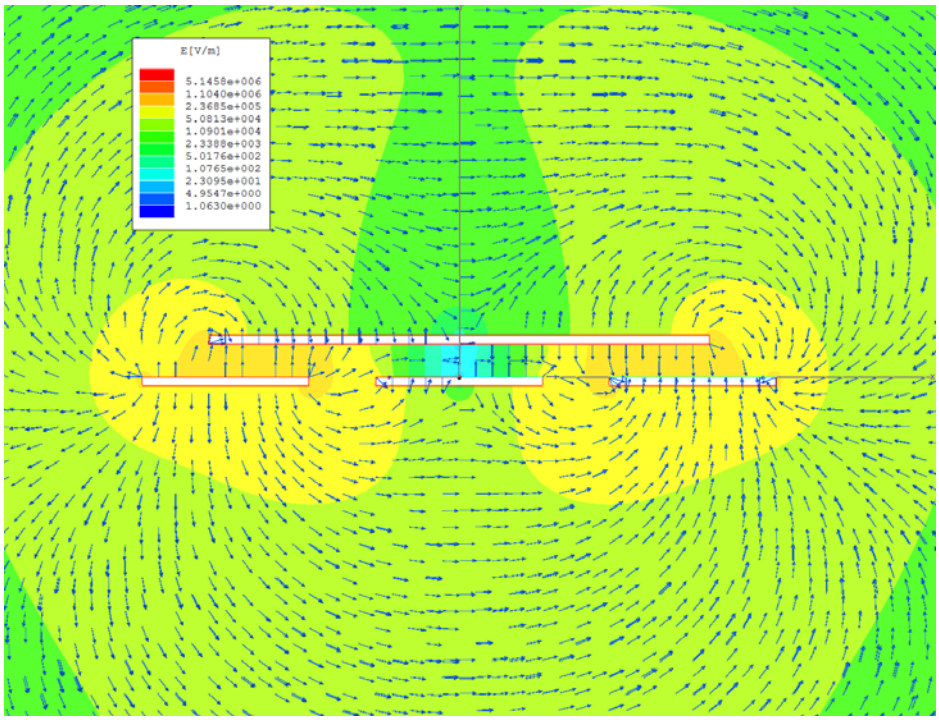

Figure 4.20: Electric field density magnitude from Maxwell two-dimensional model.

4.5 Interdigitated Capacitor Multiphysics Modeling

The interdigitated strain sensor has significantly more design parameters than the normal strain and shear strain sensors discussed previously. These parameters include electrode length, electrode thickness, gap width, electrode width, and the number of electrode digits. Due to the geometry of the interdigitated electrode, it has a response from capacitance between the vertical faces (yz plane faces) of the electrodes as well as a response from the fringe capacitance between the horizontal (xy plane) faces of the electrodes. Moreover, initial FEA analysis indicates that changes in the capacitance between the vertical, yz plane faces of the electrode occur primarily with changes in pressure in the x direction while changes in the fringe capacitance occur primarily with y direction loading. In this section, the boundary conditions for modeling the interdigitated strain sensors are presented as well as the results of overall finite element analysis and parameter studies on the electrode geometry. Finally, field modeling results from Maxwell are discussed. Particular attention is given to the mechanical response the sensor geometry, because knowledge of the mechanical response allows understanding of the change in capacitance resulting from loading and sensitivity to load direction.

4.5.1 Boundary Conditions for Modeling Interdigitated Strain Sensors

The boundary conditions for modeling the embedded structures are intended to represent the state of stress on a microscopic scale resulting from macroscopic loading. The overall dimensions of these models are less than one millimeter in all cases due to the desire to determine the electrode displacement with sufficient accuracy to determine the small changes in capacitance. Two cases were simulated for the interdigitated

capacitor, these were the case of applying stress in the direction orthogonal to the IDT electrodes (x direction) and the case of applying stress parallel to the IDT electrodes (y direction). Both cases used similar constraints on the model and used symmetry to reduce the number of elements by one-half.

Figure 4.21 and Figure 4.22 illustrate the restraint and loading condition for the x direction loading condition. The model is constrained for 0 displacement in the x direction along the plane of symmetry, an x normal plane separating half of the IDT. A 1 MPa stress in the x direction is applied opposite of this surface. A single point in the center of the plane of symmetry is used to constrain the displacement of the model in the y or z directions.

Several different geometries were examined in these simulations and parameter studies were performed. The graphical results of a single geometry are presented in this section. For this example, the IDT had 15 electrode digits on one electrode and 14 electrode digits on the other electrode. The electrode digits were 4.75 μm wide and had 2.25 μm spaces. The overlapping electrode length was 150 μm with a total length of 175 μm. This allowed a 25 μm gap separating the tip of the electrode and the area connecting electrodes of opposite potential. The total thickness of the models was 202.3 μm consisting of a 100 μm lower polyethylene layer, a 100 μm upper polyethylene layer, and 300 nm thick gold electrodes embedded in 2 μm of parylene. The length of the models varied as dimensions changed for parameter studies. A constant amount of embedding material was used for all models and 100 μm of embedding material was included outside the sensor geometry in the x, y, and z directions.

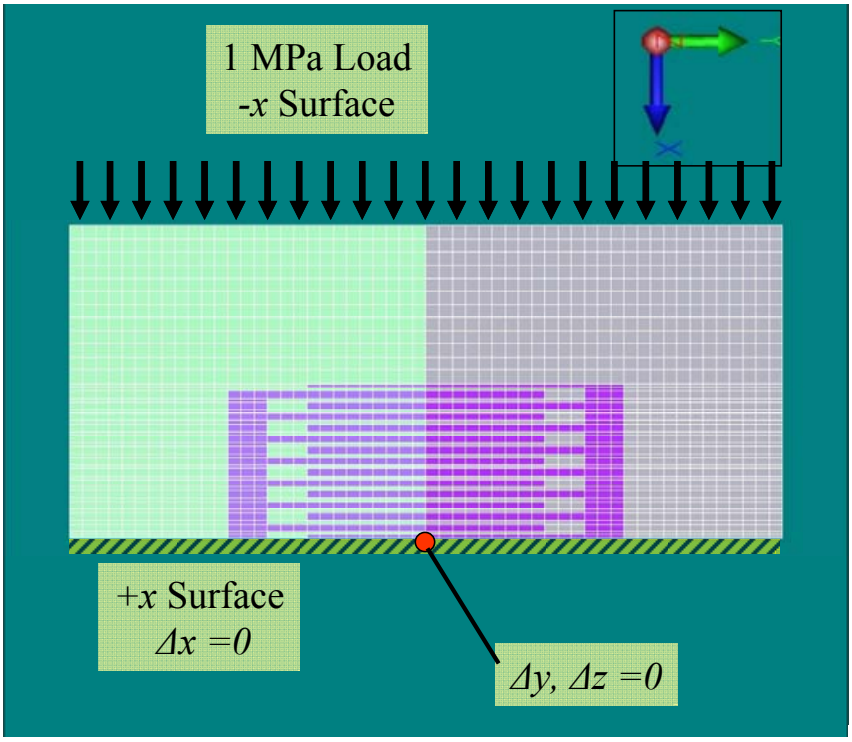

Figure 4.21: Boundary conditions for interdigitated capacitor and x direction load.

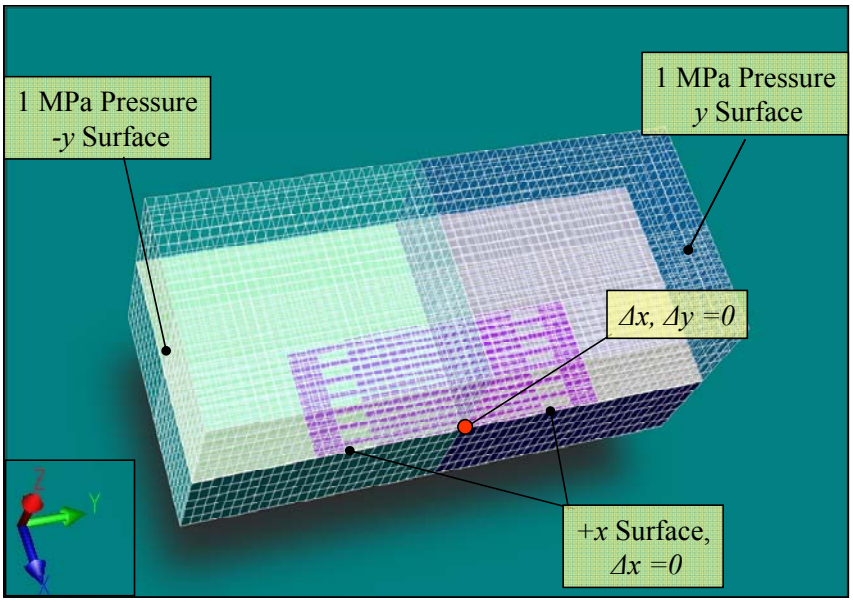

Figure 4.22: Perspective view of boundary conditions for in-plane strain sensor.

4.5.2 Results of x Direction Loading Models

Displacement results graphically illustrate the effect of the boundary conditions and allow visualization of any discontinuities in displacement due to the electrode structure. The displacement magnitude results of the finite element analysis are shown in Figure 4.23. These results show a smooth, symmetric displacement with the magnitude increasing away from the central y and z restraint point. The x component of displacement results are shown in Figure 4.34. As expected, these results show a linearly increasing x displacement away from the plane of symmetry. Although not shown, the y and z displacement results also smoothly increase linearly away from the central y and z constraint point due to the transverse strain resulting from the pressure applied in the x direction. Therefore, the displacement appears to increase radially from the central constraint point in Figure 4.23. Most importantly, large discontinuities in displacement between the sensor and the embedding material are not observed in either of these results.

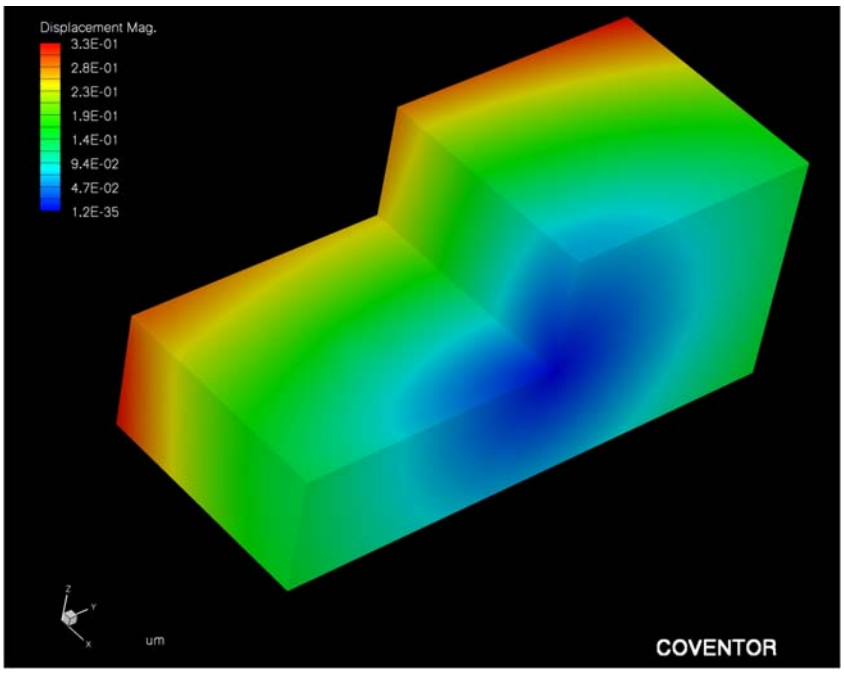

Figure 4.23: Displacement magnitude results for embedded IDT with x direction loading.

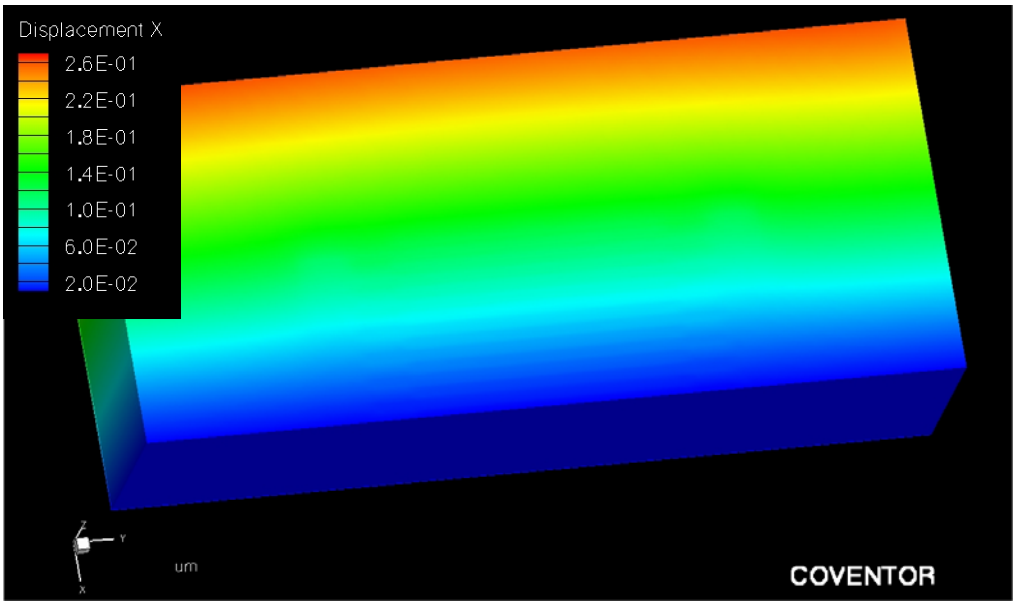

Figure 4.24: Midplane x displacement results for embedded IDT in polyethylene with x direction load.

Stress results are important for verifying the boundary conditions of the model and for understanding the effects of the applied load. The stress results in the x direction are illustrated in Figure 4.25 with the upper embedding layer hidden. Results show that 1 MPa stress is evenly distributed through the embedding polyethylene and the parylene dielectric material. However, a significant discontinuity in stress exists in the electrode materials. As shown in the displacement results, the electrodes have approximately the same displacement as the polyethylene. However, the elastic modulus of the gold electrodes is nearly two orders of magnitude greater than that of the polyethylene; 57,000 MPa for gold as compared to 690 MPa for UHMWPE. Since the stress is proportional to the strain multiplied by Young's modulus, one might expect the stress to be nearly two orders of magnitude greater. The FEA results show that that the stress is 40-50 times greater in the electrodes, and 50 to 70 times greater in the areas of bulk gold.

The x direction strain results shown in Figure 4.26 tell the rest of the story with respect to the state of stress and strain in the material. As expected the strain results for the bulk of the material are uniform and correspond with the ratio of the applied stress divided by the elastic modulus of polyethylene, or 1.45×10^{-3} μm/μm or 1.45 microstrain. Some discontinuity in strain occurs at the junction between the larger areas of gold electrode and the softer materials. However, the most important thing to notice in these results is that the lowest level of strain occurs in the gold electrodes, whereas the highest level of strain occurs in the parylene dielectric between the electrodes. The strain in the parylene between IDT digits is higher than that in the bulk material, and allows the displacement and apparent strain to be nearly equal in the sensor and bulk material.

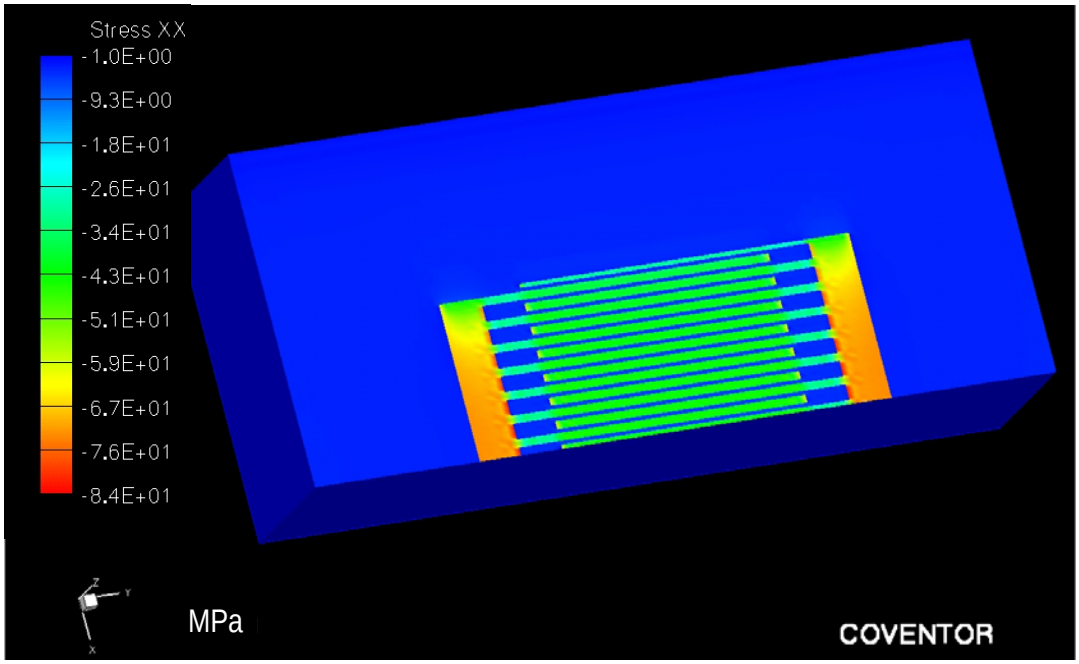

Figure 4.25: Midplane x component of stress results for x direction loading.

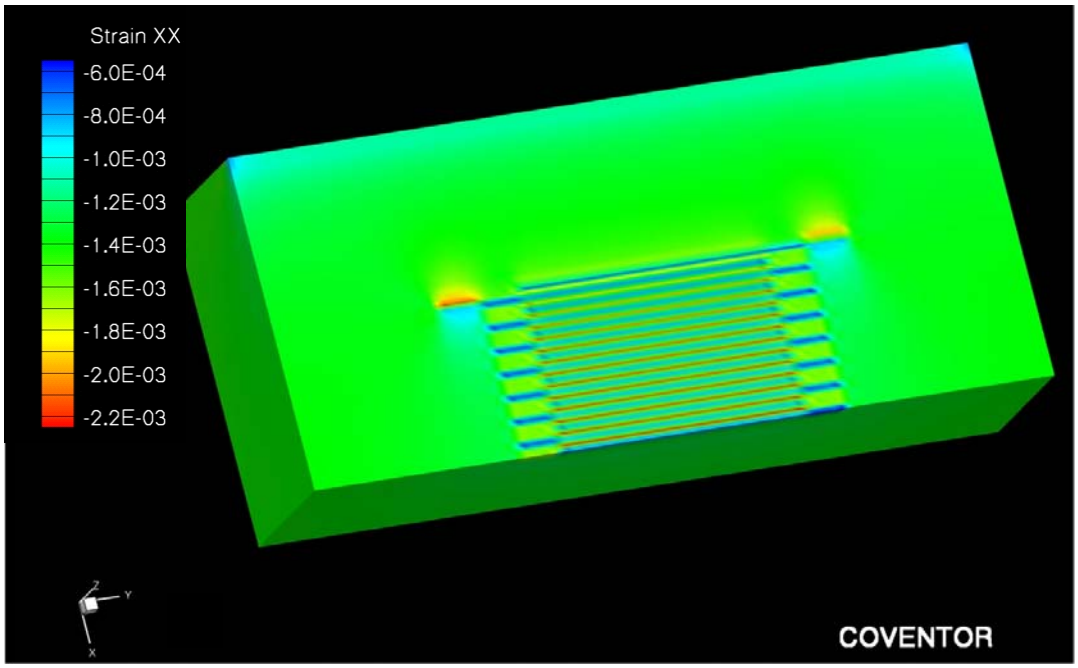

Figure 4.26: Midplane x direction strain results for x direction loading.

According to the x-direction displacement results in Figure 4.24, the electrode digit material and the surrounding dielectric material have almost exactly the same displacement as the bulk embedding material. However, the majority of the strain and displacement occurs in the parylene dielectric material. These results reflect the assumptions made by combining the Voight and Maxwell models for the analytical solution to this problem in Chapter 3. Under loading in the x direction, all of the elastic members act in parallel and have the same bulk displacement. The gold electrode material and the parylene dielectric material act together as a single elastic element which is mechanically in parallel with the other materials. Inside this combined elastic element the parylene and gold materials act in series with each other; with the bulk of the displacement occurring in the softer parylene material. This is represented in Chapter 3 in Figure 3.9 and Figure 3.10.

4.5.3 Boundary Conditions and Results for y-direction Pressure Modeling

The boundary conditions for modeling the embedded IDT structures with y-direction loading were very similar to those for x-direction loading. A symmetry plane with a +x normal was defined splitting the IDT in half along the longitudinal direction. The models were constrained in the x direction in the plane of symmetry, and the model was constrained in the y and z directions at a single central point. For these boundary conditions, a compressive 1 MPa stress was applied on opposite ends of the model to result in symmetric loading and deformation of the system. Figure 4.27 and Figure 4.28 show the boundary conditions of the IDT for applying the 1 MPa compressive stress in the y direction.

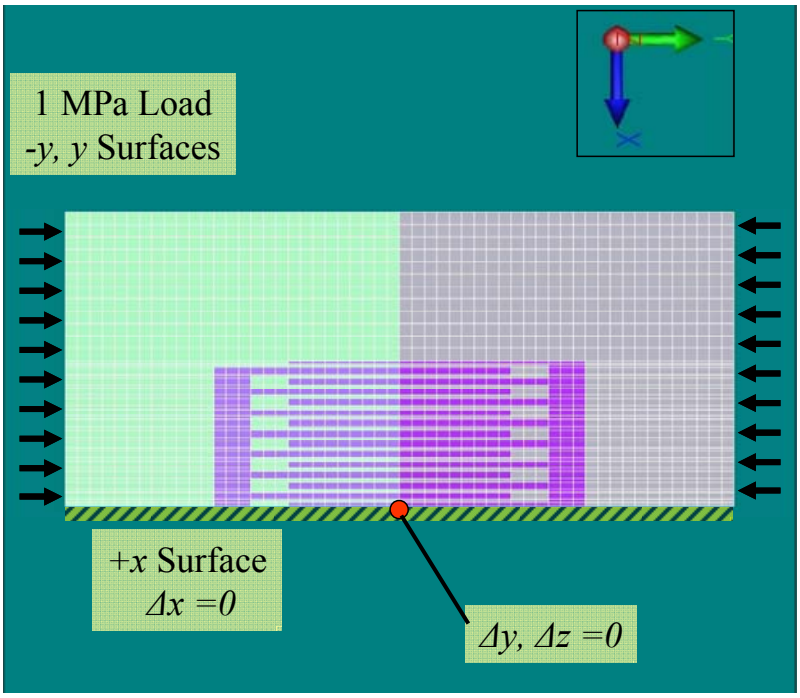

Figure 4.27: Top view of boundary conditions for y direction loading of embedded IDT. Upper polyethylene layer is transparent such that IDT is visible.

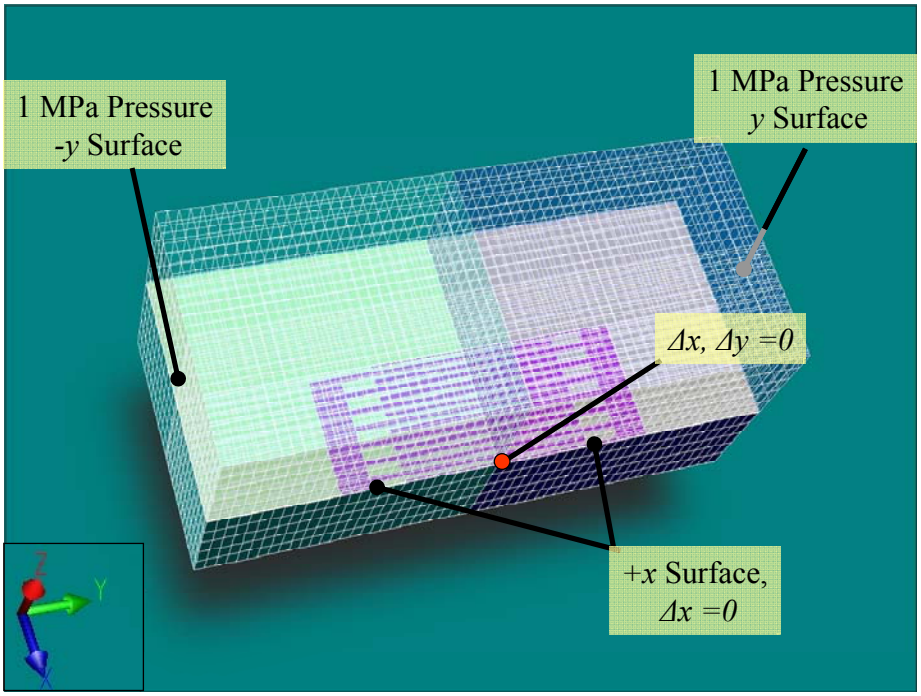

Figure 4.28: Perspective view of boundary conditions for y direction loading.

The displacement magnitude results are presented in Figure 4.29 and the y direction displacement results are shown in Figure 4.30. A cut away view is used for these results to display the results in the sensor plane and through the thickness of the model. The displacement magnitude results show continuous displacement of all materials in a radial pattern from the constraint point. The y displacement results show good uniformity in the y displacement throughout the model. Also, these results appear very linear in the y direction with no obvious discontinuities. Similar to the x loading response of this structure, the most important thing to note is that discontinuities in displacement do not occur near the gold electrodes.

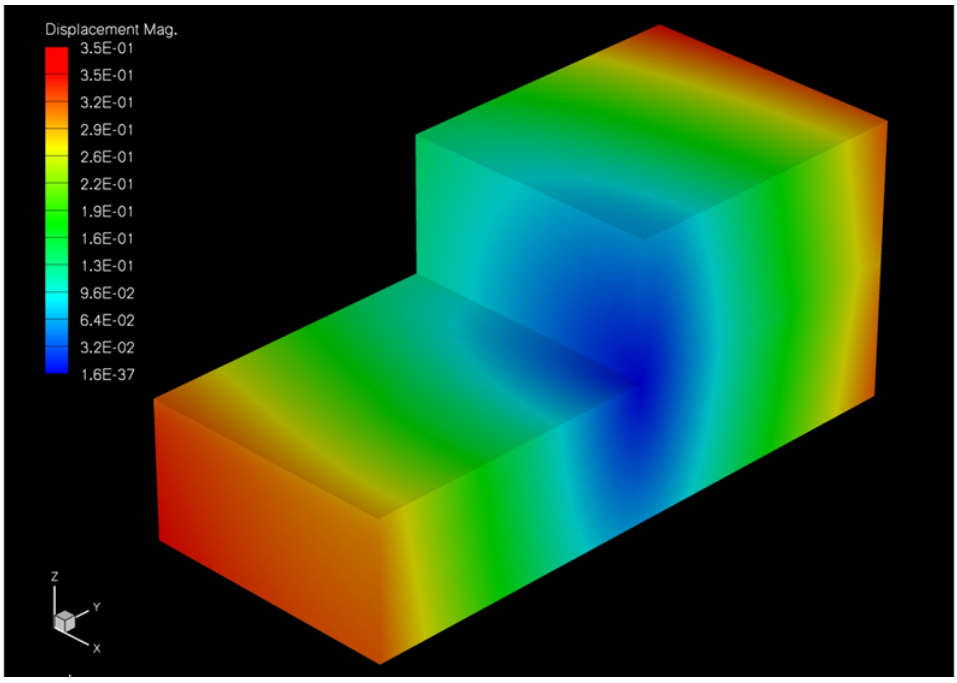

Figure 4.29: Cut away view of displacement magnitude results for y direction stress.

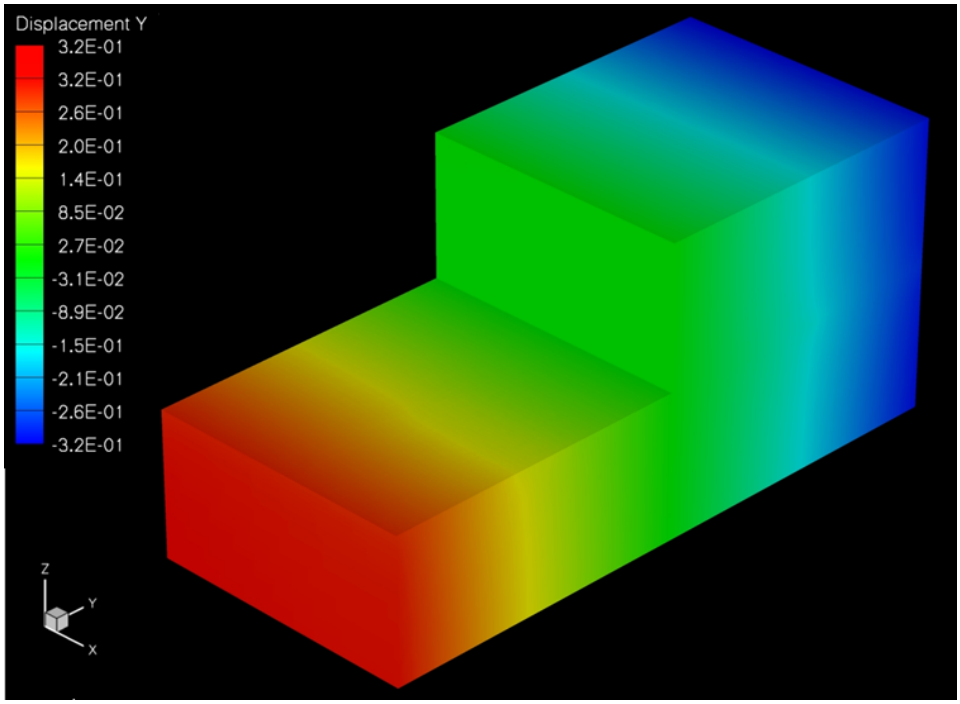

Figure 4.30: Cut away view of y displacement results for loading parallel to IDT electrodes (y direction stress).

Stress and strain results for this loading direction give tremendous insight into the capacitive response of the structure to stress and strain in the y direction. A stress loading in the y direction results in two effects. One is the increase in the length of the IDT electrodes due to the applied stress, and the other effect is a strain orthogonal to the direction of loading due to the Poisson ratio effects.

The 1 MPa y direction loading results in a uniform 1 MPa stress in the y direction as shown in Figure 4.31. Similarly to the x direction loading results, the stress in the electrode materials is over an order of magnitude higher, ranging from 44-80 MPa depending on the strain in the electrodes. Also, the stress in the parylene material is nearly the same value as in the bulk polyethylene material.

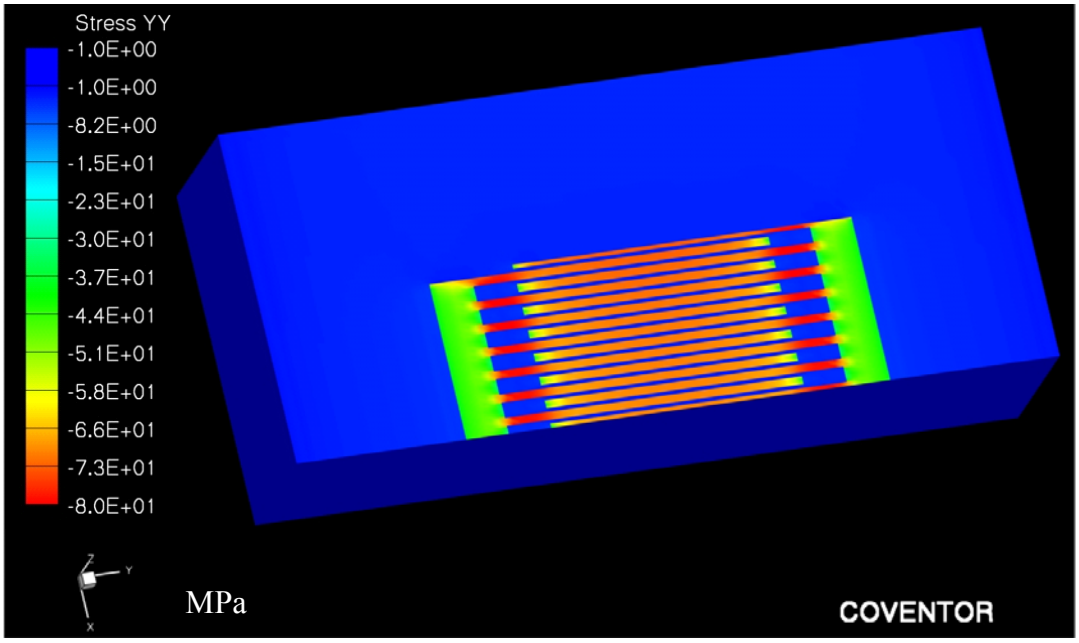

Figure 4.31: y direction stress results for y direction loading. Upper level polyethylene layer is hidden.

Results for the strain in the y direction are illustrated in Figure 4.32. For this case the strain in the bulk material is nearly equal to the ratio of the applied pressure to the elastic modulus of the polyethylene material or 1.45 MPa. These results differ from the previous case in that the strain in the interdigitated electrodes and the parylene dielectric material between the electrodes is nearly equal due to the change in stress direction. The scale in Figure 4.32 is narrow ranging only from 0.8-1.8 microstrain through the entire figure. The strain in the overall electrode structure is slightly less than that in the bulk material. Expectedly, small discontinuities in the strain can be seen at the transitions from the stiffer gold areas to softer polyethylene areas. These results are in agreement with the Kelvin-Voight model used for developing analytical results for this system.

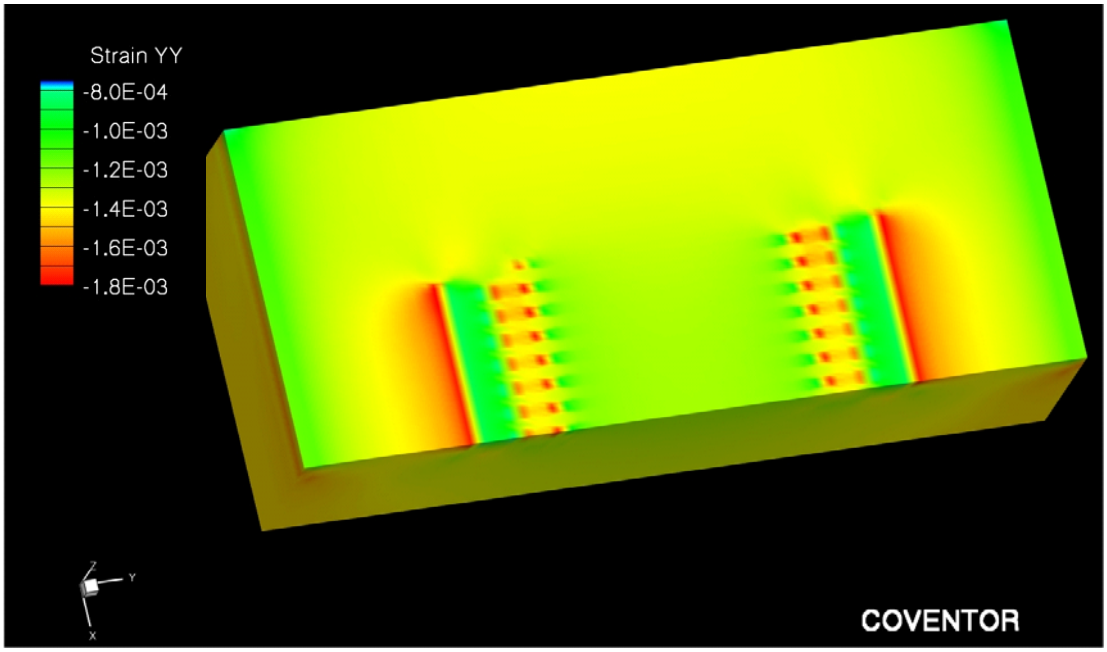

Figure 4.32: Results of y direction strain for loading parallel to IDT electrodes.

The results of the orthogonal sensing direction stresses and strains are presented in Figure 4.33 and Figure 4.34. These results are presented to show how the electrode responds to the transverse strain from Poisson's ratio effects. The first thing that should be noted is that as anticipated there is no x direction stress in the bulk material for this loading condition, however a strain of 0.67 microstrain results in the x direction. This is equal to the Poisson's ratio of 0.46 multiplied by the y direction strain of 1.45 microstrain results in the x direction. As in previous results, the stress in the electrodes is significantly greater than that in the bulk material.

The strain results illustrate that the effect of transverse strain in this direction is very similar to the basic loading condition in the x direction. The least amount of strain in

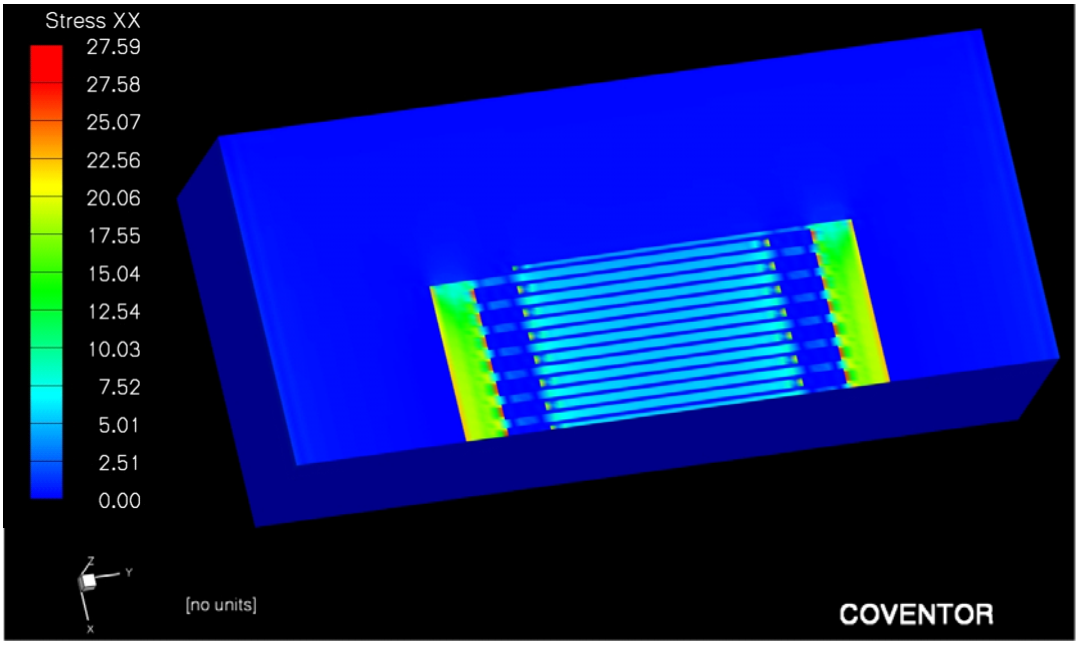

Figure 4.33: x direction stress resulting from y direction loading.

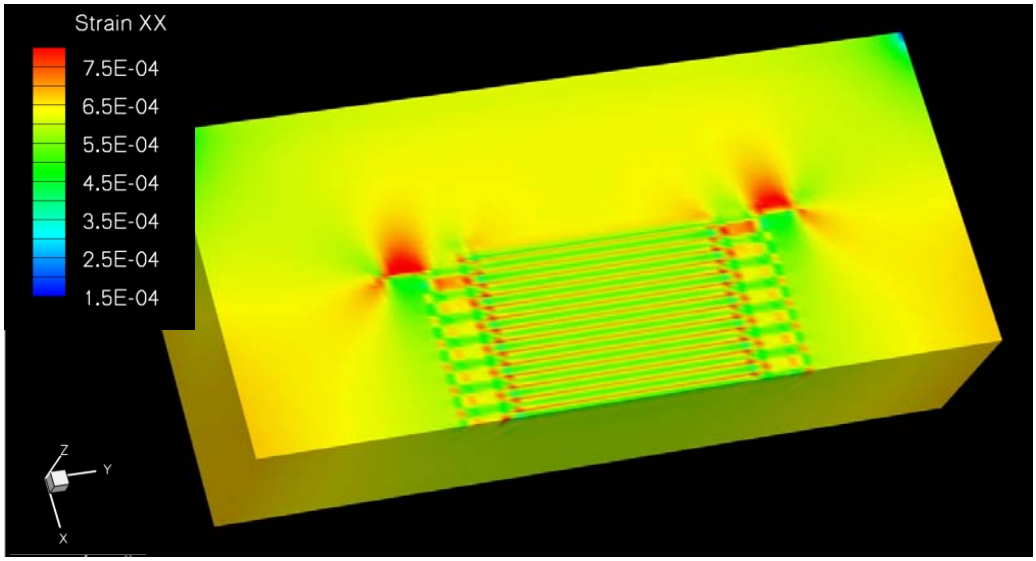

Figure 4.34: x direction strain resulting from y direction loading, an example of Poisson's ratio effects.

the electrode system occurs in the gold electrodes while the greatest occurs in the parylene electrodes. Previously developed analytical models reflect these effects.

4.5.4 IDT Capacitance Results and Multiphysics FEA Parameter Studies

Parameter studies were performed to determine the effects of the different geometric parameters on the change in capacitance and directional sensitivity to load. For these studies, the nominal capacitance was determined using Coventor's MemElectro module followed by mechanical analysis using the MemMech. Electrostatic analysis was then performed on the displaced geometry from the MemMech to determine the change in capacitance. Parameter studies were performed with regard to the number of electrodes, the length of the electrodes, and the amount of load applied to the model.

The parameter study on the number of IDT digits was performed using models with containing 5, 9, 13, 17, 21, 25, and 29 total electrodes. Symmetry was used to model half of the electrode pair. The thickness of these electrodes was 300 nanometers, and the length simulated was 150 nanometers of electrode overlap. The electrode width was 4.75 μm and the gap between electrodes was 2.25 μm. Actual devices would have more electrodes of greater length. The scaled-down geometries used in these studies were to ensure good mesh resolution and accurate modeling of capacitance changes.

Results of the electrode number parameter study are summarized in Table 4-4 and plotted in Figure 4.35. The results of this study showed that the capacitance of these sensors before loading ranged from 1.23×10^{-2} pF to 7.83×10^{-2} pF. The change in capacitance for x direction stress ranged from 3.09×10^{-5} pF for 5 electrodes to 1.90×10^{-4} pF for 29 electrodes, and in the y direction ranged from $2.44(10^{-5})$ pF for 5 electrode

Table 4-4: Capacitance results for IDT electrode number parameter study.

Number of Electrodes	$C_{Initial}$ (pF)	Delta C y Direction stress (pF)	Delta C x direction stress (pF)
5	2.46 (10^{-2})	6.19 (10^{-5})	4.88 (10^{-5})
9	4.68 (10^{-2})	1.17 (10^{-4})	9.75 (10^{-5})
13	6.89 (10^{-2})	1.70 (10^{-4})	1.47 (10^{-4})
17	9.09 (10^{-2})	2.23 (10^{-4})	1.97 (10^{-4})
21	1.13 (10^{-1})	2.76 (10^{-4})	2.47 (10^{-4})
25	1.35 (10^{-1})	3.28 (10^{-4})	2.97 (10^{-4})
29	1.57 (10^{-1})	3.81 (10^{-4})	3.48 (10^{-4})

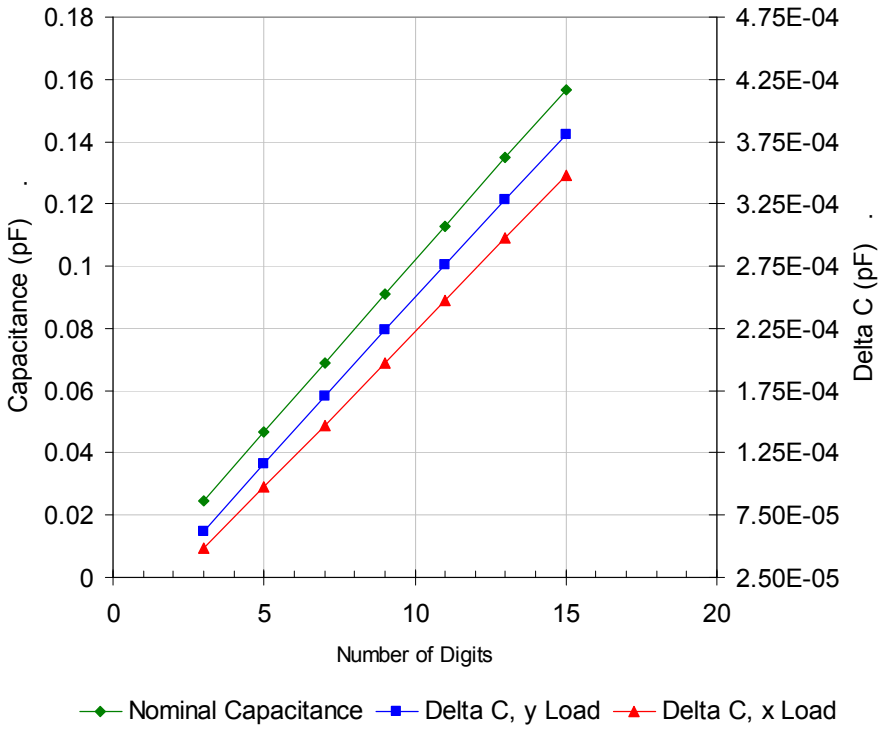

Figure 4.35: Results of parameter study based on the number of IDT electrodes.

geometry to 1.49(10^{-4}) pF for the 29 electrodes. These results indicate that the initial capacitance and the capacitance load response scale linearly with electrode number.

A similar study was performed using the electrode length as the parameter of interest. This study was used to evaluate the 300 nanometer thick, 29 electrode geometry of the previous study at electrode lengths of 100, 150, 200, and 250 micrometer lengths. Results of this study showed that the unloaded capacitance varied from 0.109 pF for the 100 long micrometer electrode sensors to 0.255 pF for the 250 micrometer long electrode sensors. The change in capacitance was 1.15×10^{-4} pF with 1 MPa x direction loading for the 100 micrometer sensors and 2.98×10^{-4} pF for the 250 micrometer sensors. For y direction loading, the change in capacitance ranged from 1.24×10^{-4} pF for the 100 micrometer sensors to 3.29×10^{-4} pF for the 250 micrometer electrode sensors. Results are plotted in Figure 4.36.

The effect of increasing the thickness of the electrodes was examined as part of this analysis. The 29 electrode geometry with 150 micrometer long electrodes was used as the base geometry for this study. The thickness of the electrodes simulated was 0.3, 0.6, 1, 1.5, 2, 3, and 4 μm. The initial capacitance of the 0.3 μm electrode structure was 0.158 pF and increased to 0.349 pF for the 4 micrometer thick structure. This is a linear increase with an offset due to the fringing effects which remain equivalent for each structure. Full results of this parameter study are listed in Table 4-5. Base capacitance values are plotted in Figure 4.37. The change in capacitance with x and y direction loading are illustrated in Figure 4.38. The directional sensitivity values are also shown in Figure 4.38.

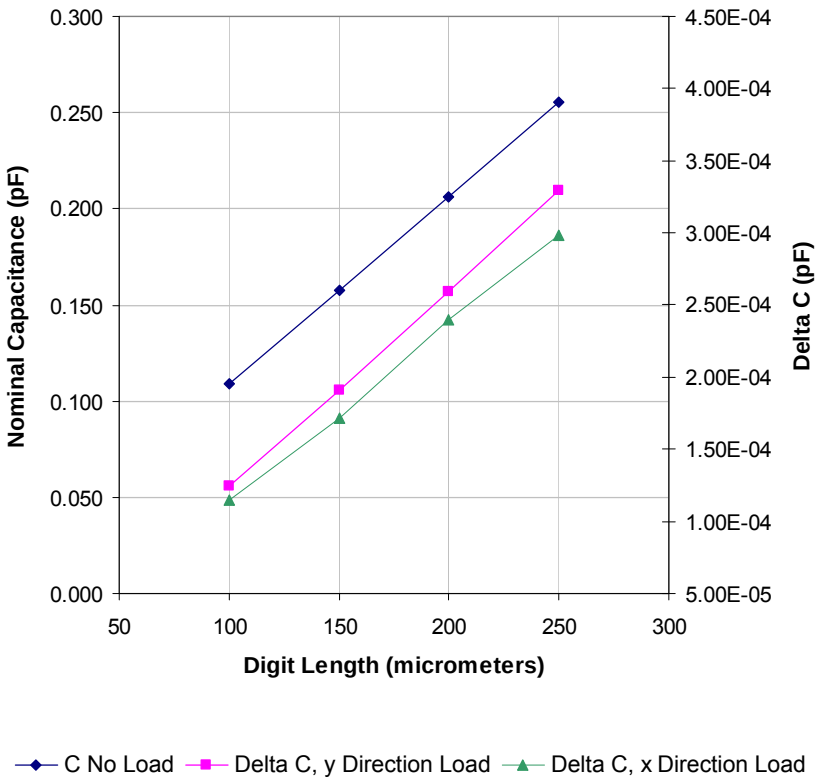

Figure 4.36: Results of IDT digit length parameter study.

Table 4-5: Data from electrode thickness parameter study.

Electrode Thickness	$C_{Initial}$ (pF)	Delta C x Direction Load	Delta C y Direction Load	Directional Sensitivity
0.3	0.158	1.71E-04	1.91E-04	1.114
0.6	0.174	2.23E-04	1.97E-04	0.880
1	0.195	2.77E-04	2.03E-04	0.733
1.5	0.221	3.29E-04	2.10E-04	0.637
2	0.246	3.73E-04	2.16E-04	0.580
3	0.298	4.41E-04	2.25E-04	0.512
4	0.349	4.93E-04	2.33E-04	0.473

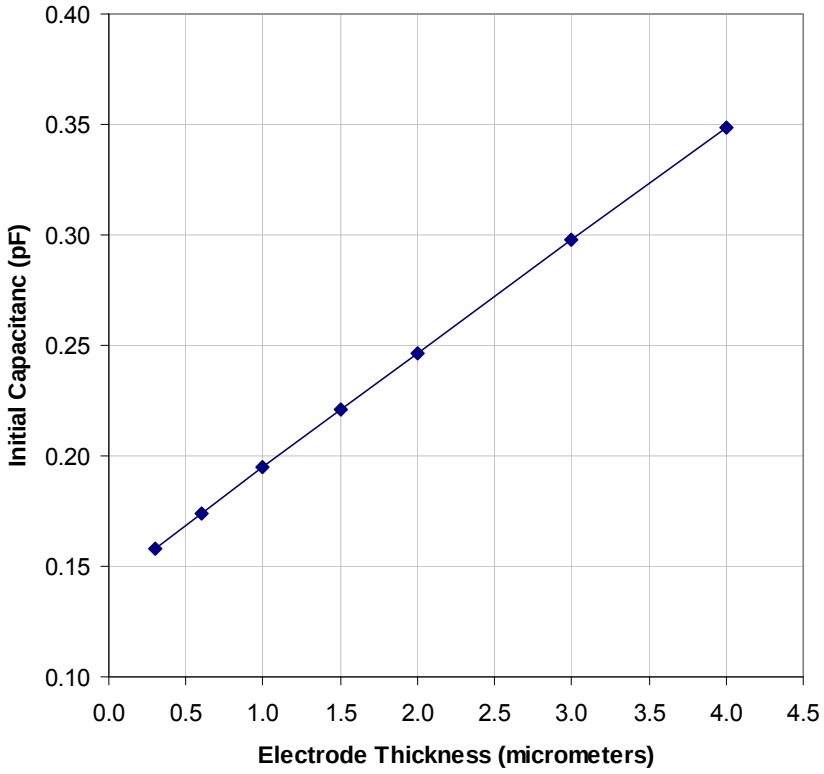

Figure 4.37: Base capacitance as a function of electrode thickness.

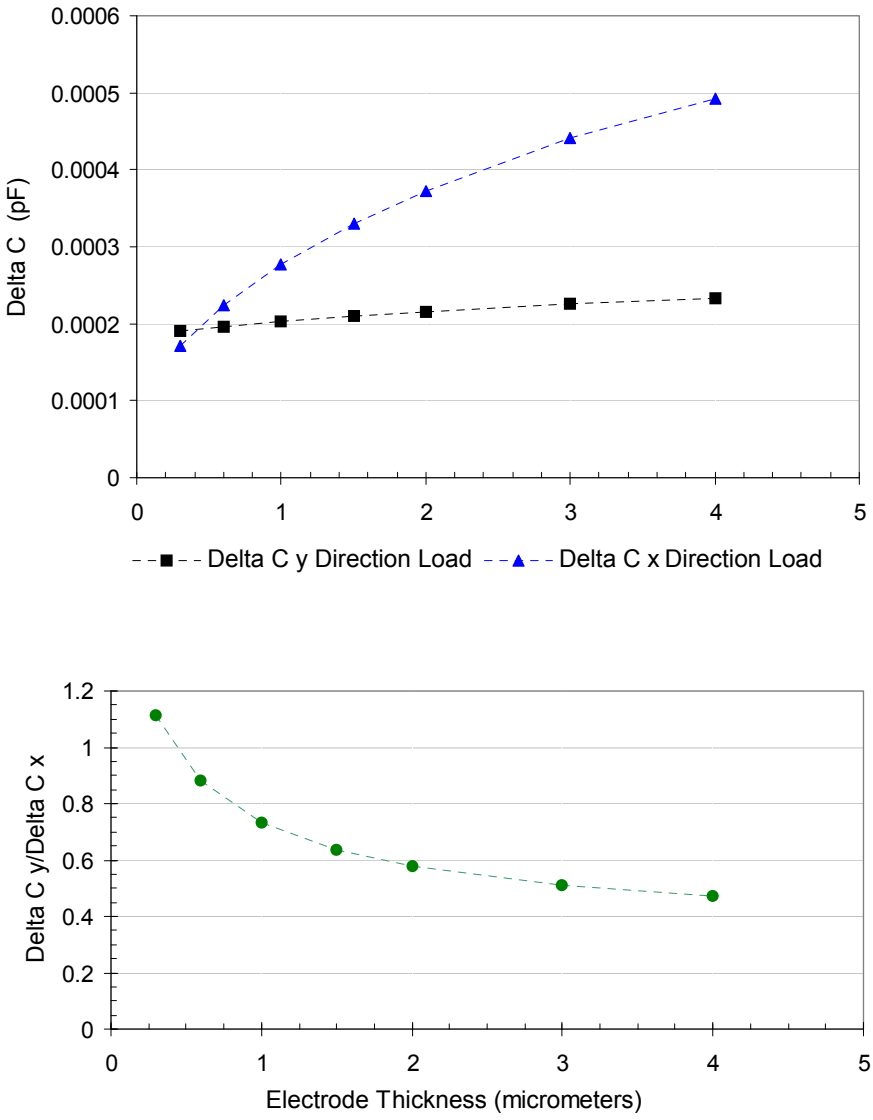

Figure 4.38: Results of IDT thickness parameter study showing x direction or lateral loading results, y direction (longitudinal load) results as well as directional sensitivity.

The results of this study indicated that the thickness plays a key role in the directional sensitivity of the device. The change in capacitance with x direction load ranged from 1.71×10^{-3} pF to 4.93×10^{-3} pF as the thickness increased from 0.3 to 4 μm, and the change in capacitance with y direction stress ranged from 1.91×10^{-3} pF to 2.33×10^{-3} pF as the thickness increased from 0.3 to 4 μm. The 0.3 micrometer thick electrodes had poor sensitivity to direction with a sensitivity parameter of 1.114, however this value quickly approached the value of the Poisson's ratio of the material (approximately 0.46) as the electrode thickness increased. The results plotted in Figure 4.38 show significant improvements in directional and overall sensitivity with electrode thickness, however fabricating the thicker electrodes shown would present a challenge.

4.5.5 *IDT Load Response Parameter Study*

A parameter study was performed on the interdigitated strain sensor to determine if the response of the sensor to applied loading was linear. The base geometry used for this study was the 29 electrode geometry with 150 micrometer long electrode digits. The thickness of the electrodes simulated was 1.5 μm. A logarithmic series of loads spanning four orders of magnitude was applied for this study consisting of 0.02, 0.06, 0.20, 0.60, 2.00, 6.00, and 20.0 MPa. x direction response ranged from 6.70×10^{-6} pF to 6.85×10^{-3} pF, and the y direction response ranged from 4.17×10^{-6} pF to 4.19×10^{-3} pF. The results of the multiphysics analysis for x and y direction loading are plotted in Figure 4.39, and predict that the change in capacitance should vary linearly with applied load. The results of the mathematical model are plotted in dashed lines along with the finite element simulation results.

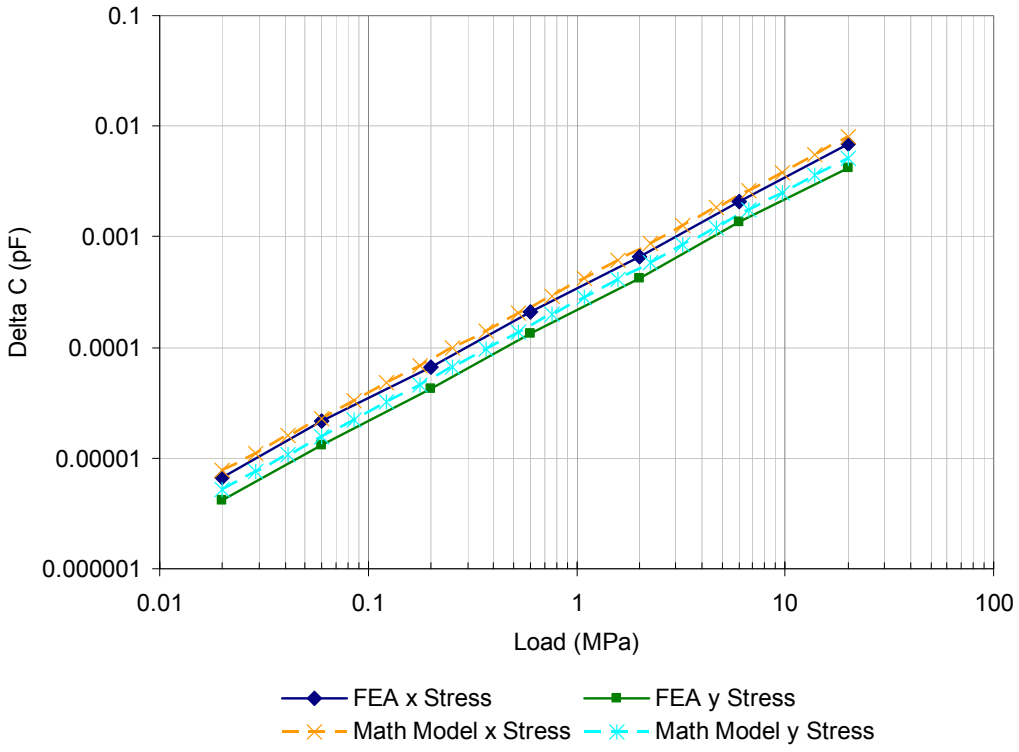

Figure 4.39: Response of IDT to loads ranging from 0.02 MPa to 20 MPa.

4.5.6 Maxwell Electrostatic Field Analysis for Interdigitated Sensors

Three-dimensional Maxwell electrostatic modeling was used to visualize the field surrounding the interdigitated electrodes. The geometry shown in Figure 2.14 was used to visualize the field around the electrodes. This sensor has 15 digits on the upper electrode and 14 digits on the lower electrode for a total of 29 electrodes. The width of the digits was 4.75 μm with a 2.25 μm gap between digits. The digit overlap length was 150 μm. The thickness of the electrodes was 1.0 μm. The substrate material was polyethylene, and the dielectric material between the electrode digits was parylene. Polyethylene was used as the background material for the Maxwell simulation.

Initially there was some concern regarding capacitive interactions between the end of one series of electrode digits and the base of the opposing series. 25 μm of extra space was left between these two areas. Results of the Maxwell three-dimensional analysis show that the electric field in this area is nearly two orders of magnitude lower than the field between the electrode digits. These results are illustrated in Figure 4.40, and indicate that interactions between the end of the electrodes and the material at the base of the electrodes should be minimal. Also, Coventor modeling has shown that at these dimensions the changes in these effects are small compared to the capacitance between the sides of the electrode digits and the xz plane fringing fields.

The fringing effects of the interdigitated structure were examined from a three-dimensional model. Figure 4.41 shows the electric field in the xz plane and the substantial fringing effects for these devices. Although the magnitude of this field drops off quickly in the z direction, its effects over the large area of the electrodes is significant.

The expected capacitance from this geometry without fringing effects was 0.101 pF, however the Maxwell electrostatic simulation predicts that the total capacitance for this system is 0.19279 pF. For this geometry, the capacitance due to fringing effects is nearly equal to the capacitance in the gap between the electrodes.

4.6 Summary of Multiphysics Modeling of MEMS Strain Sensors

In this research, three strain sensors have been studied that when combined have the potential fully characterize the strain in three dimensions. The challenge of embedding electrodes with significantly larger modulus of elasticity for the measurement of strain in softer materials is a significant challenge. The micromechanics of these sensors have been studied using multiphysics finite element analysis and the sensitivity of the design parameters of these structures has been determined.

Simplifications in the model geometry were required to ensure good mesh density and low numbers of elements with high aspect ratios. This was a challenge with the 300 nm coating layers included in the model. Linear elastic properties were used for all materials in this investigation. Only a small volume of material was modeled, and assumptions were made to transfer the state of stress resulting from macroscopic forces to the microscopic features in the model.. The accuracy of the results presented is directly dependent on the quality of the material property data. Elasticity values for thin film deposited materials may very from those of bulk materials and residual stresses may be present.

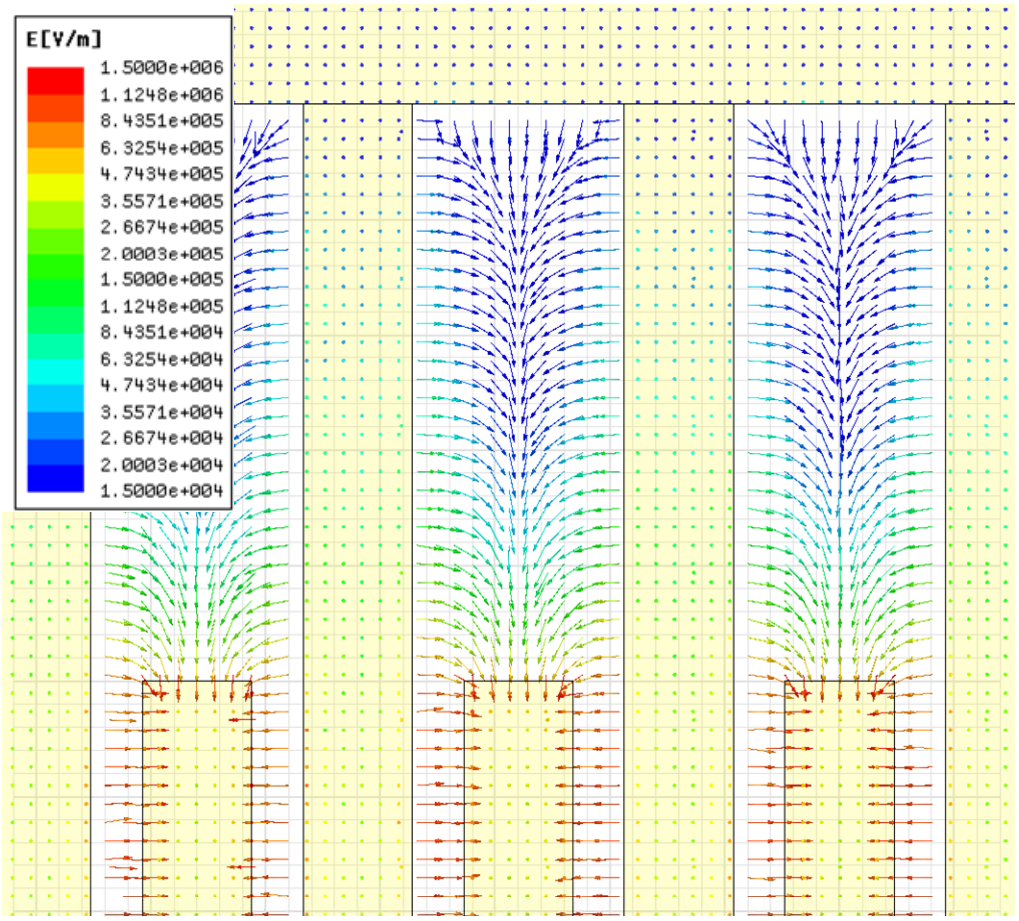

Figure 4.40: Maxwell results for the electric field of interdigitated strain sensor at the tip of the electrodes.

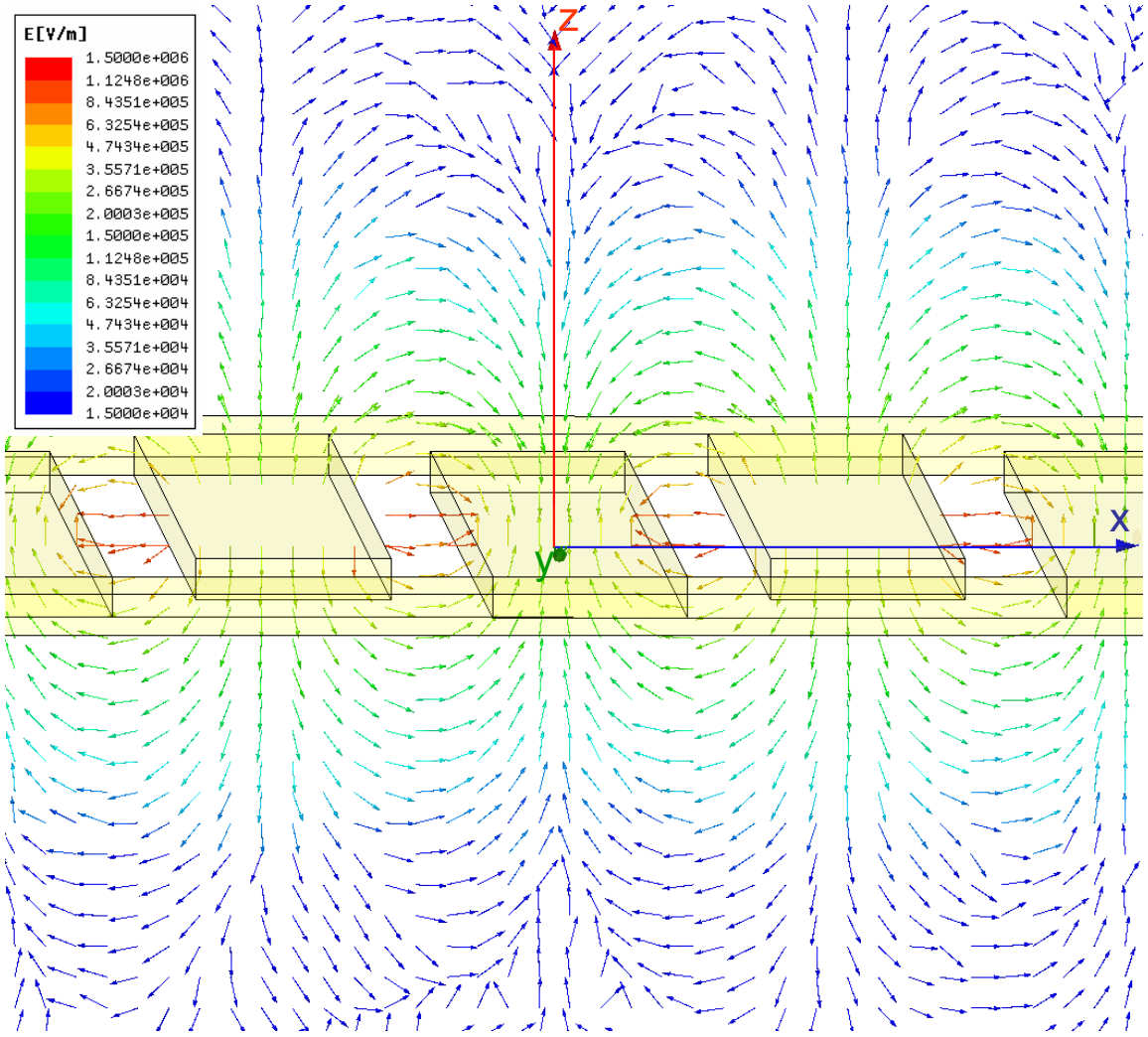

Figure 4.41: Electric field results showing fringing field in the xz plane for the interdigitated capacitor.

FEA modeling results illustrated that the response of the strain sensors may be optimized through careful choice of design parameters. The parallel plate capacitor is sensitive to the area of the sensor, and the shear sensors response may be improved by increasing the width or adding more devices acting in parallel. The response of the IDT may be improved by increasing the number, length, and thickness of the electrode digits.

Chapter 5
Microfabrication of Capacitive Strain Sensors

An investigation of fabrication techniques for the capacitive sensors was performed as part of this research. This investigation was performed using two primary tracks. The first was fabrication of prototype sensors using biocompatible materials deposited lithographically on silicon wafers for proof of concept testing, and the second was the investigation of new techniques for producing these sensors on polyethylene substrates

MEMS fabrication techniques traditionally use silicon wafers as the base substrate for sensor fabrication. One possible method for fabricating a sensor array embedded in a polyethylene tibial spacer would be to fabricate the sensor array directly on the polyethylene spacer or on a polyethylene substrate that can be molded into the tibial insert at a later time. Polyethylene, a low surface energy or hydrophobic material, presents challenges as a fabrication substrate due to the difficulty of adhering higher surface energy materials on lower surface energy substrates.

As part of the investigation of fabrication techniques, the capability to fabricate electrodes on polyethylene substrates containing 2 and 5 micrometer features has been demonstrated. Sensor electrode arrays have also been fabricated on thin parylene C films. Parylene C has been used in several FDA-approved devices including pacemaker electronics and coronary stents. Images of electrodes fabricated on parylene coated

substrates are shown later in this chapter. Facilities at the Cornell Nanofabrication Facility, Oak Ridge National Laboratory's Nanoscale Science and Technology Laboratory, and the University of Tennessee clean room facility in the Science and Engineering Research Facility were used for sensor fabrication. Oxygen plasma reactive ion etching techniques were used as a surface treatment to enable the gold electrodes to adhere to the polyethylene surfaces. Examples of sensor electrodes fabricated on a polyethylene base and on a silicon/parylene base are also illustrated later in this chapter.

Fabrication experiments were performed on a total five different substrate materials. These substrate materials examined were medical-grade UHMW polyethylene bar material, high density polyethylene sheet material, silicon wafers, silicon wafers with 5-10 μm of thermally grown SiO_2, and parylene coated silicon wafers. The basic process for each of these substrates was similar; however each had its own fabrication challenges which required deviation from the basic procedure.

5.1 Fabrication of Prototype Sensors on Silicon Wafer Substrates

An initial procedure for microstructure fabrication was developed using silicon wafers as the substrate material. This process was subsequently expanded upon for use with the other materials. An image reversal based lift-off process was used to leave undercut areas at the edge of the photoresist which yields precise, sharp lines in the deposited material. Figure 5.1 and Figure 5.2 show samples prepared using the image reversal process. Figure 5.3 illustrates the steps in the process of depositing one layer of material.

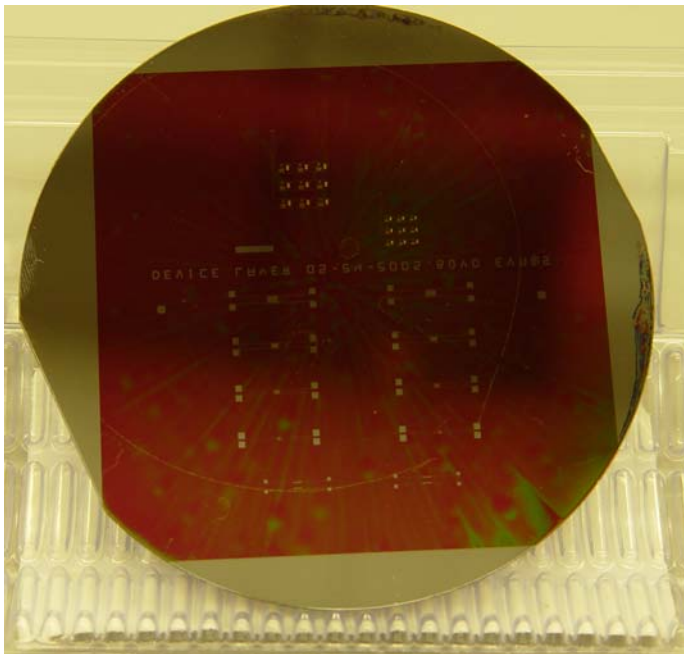

Figure 5.1: Silicon wafer substrate after contact printing and image reversal process. Photoresist appears dark reddish-brown in this image.

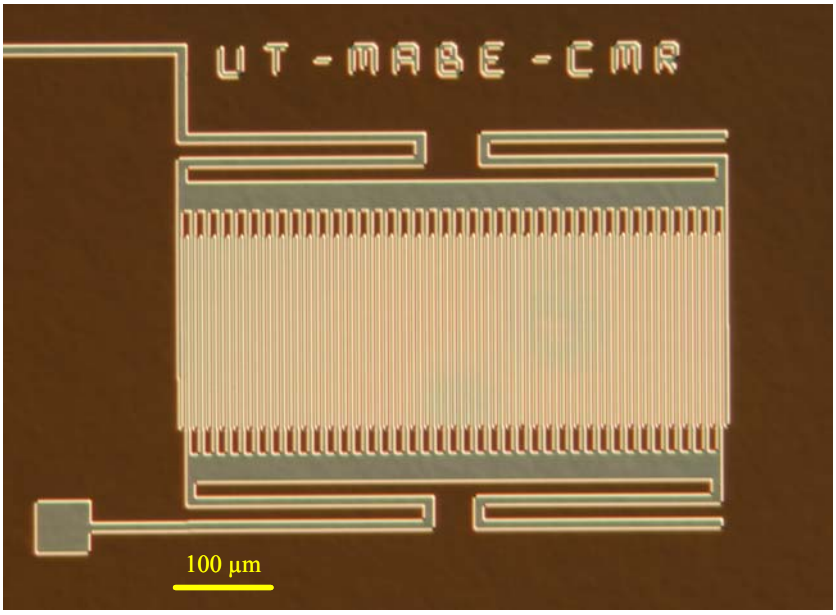

Figure 5.2: Microscopic view of Figure 5.1 showing a 2 micrometer spaced sensor after image reversal process. Photoresist edges are translucent due to undercutting.

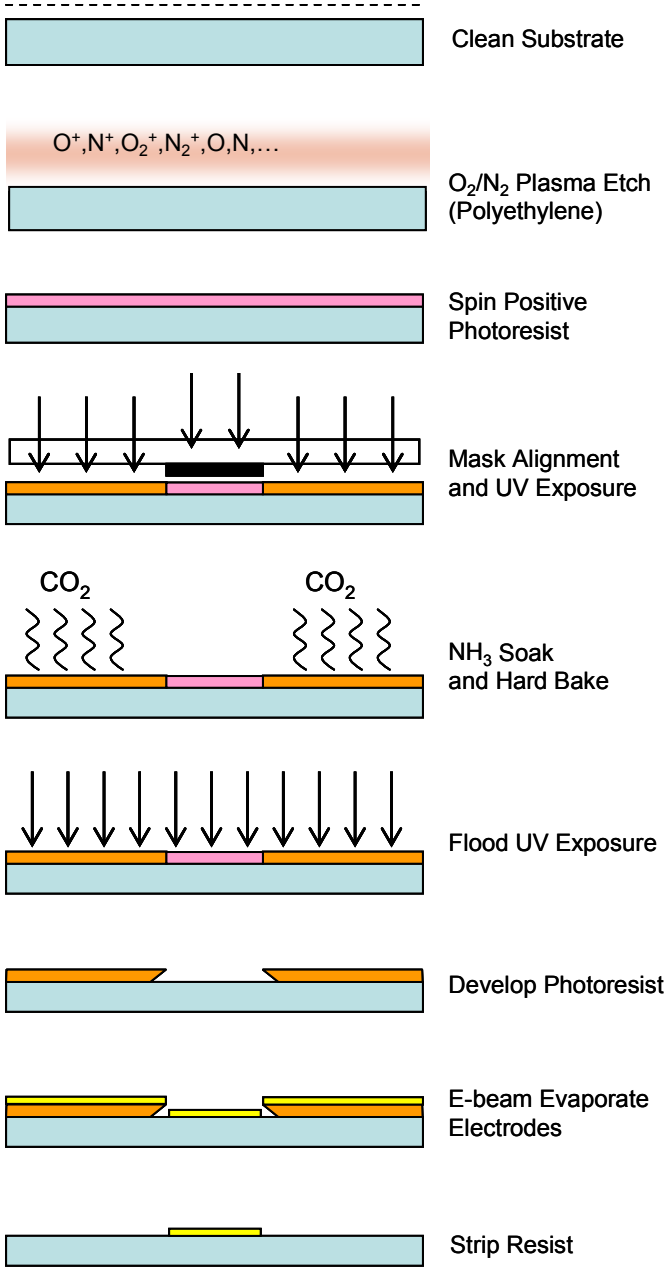

Figure 5.3: Generic process flow for depositing one layer of material on silicon, polyethylene, or other substrate using image reversal process.

Most commercially available silicon wafers are of sufficient conductivity that a dielectric layer is required on top of the silicon substrate to ensure good capacitance and low parasitic resistance between electrodes deposited on the substrate layer. This was achieved by growing a 10 micrometer layer of thermal oxide on the surface of the wafer. Thermal oxide is grown by exposing the silicon wafers to molecular oxygen or water vapor at 800-1200 C. Wafers for this study were either purchased with oxide layers already applied or oxidized in the MRL Cyclone furnace at Cornell. The MRL Cyclone furnace at the Cornell CNF uses a wet oxidation process. This process occurs at a pressure of 760 Torr, a temperature 1100 C, and uses steam with 2.5% HCl which removes any metal ions that form the oxide layer. The growth rate of this process is 85 angstroms per minute. Wafers were processed for 20 hours to yield the 10 micrometer thick layer of oxide.

Wafers were cleaned using the piranha process, a 5:1 ratio of H_2SO_4 to H_2O_2 at 120 C. The silicon wafers were then primed with a monolayer of hexmethyldisilazane (HMDS). The chemical formula for HMDS is $C_6H_{19}NSi_2$, and its structure contains a nitrogen molecule linking two silicon molecules. The two silicon molecules are each attached to three methyl groups. During the HMDS vapor priming step the HN groups break off from the Si molecules to leave the Si molecules free to attach to the surface. The CH_3 groups then form a bridge to the photoresist polymer molecules. The priming procedure consists of cycles of vacuum heating (150 C) and dry nitrogen purge steps to remove moisture from the substrate, followed by exposure to HMDS vapors. HMDS contains functional groups that bind the photoresist molecules to the wafer surface.

Shipley S1818 photoresist was spin cast on the surface of the substrates. For this process, approximately 10 milliliters of photoresist was puddled in the center of the wafer followed by ramping up to 3,000 RPM at 500 RPM per second and holding at 3,000 RPM for 30 seconds to evenly distribute the photoresist on the surface of the wafer. A 60 second softbake at 90 C was used for wafers without oxide layers and a 180 second soft bake at 90 C was used for wafers containing oxide layers. The purpose of the soft bake is to remove the casting solvents in the photoresist prior to exposure. Failure to remove all casting solvents results in bubbles in the exposed resist. Following photoresist coating, the wafers were exposed for 8 seconds using a Hybrid Technology Group (HTG) contact mask aligner.

The exposed wafers were then baked for 80 minutes at 90 C in ammonia gas in a YES 58-SM (Yield Engineering Systems, Livermore, CA) image reversal oven to yield convert the image exposed from the photomask from a positive image to a negative image. Positive photoresist is comprised of a novalac resin combined with casting solvents and the dissolution inhibitor diazoketone. During exposure to light, the diazokeytone is converted to carboxylic acid which promotes dissolving of the novolac resin by a tetramethylammonium hydroxide (TMAH) based developer.

During the bake process in the image reversal oven the carboxylic acid species is neutralized through exposure to the basic vapors of ammonia gas which diffuses into the exposed areas. The neutralized photoresist becomes resistant to further change by exposure to light and less sensitive to further developing, but the ammonia vapors do not affect the previously unexposed areas of the resist. The previously unexposed areas of

resist may be exposed using flood exposure from a UV source and developed using a 0.24 N TMAH developer for best resolution. The substrates for this research were flood exposed under the HTG contact alignment tool for 30 seconds. Figure 5.1 and Figure 5.2 show images of the wafers following image reversal flood exposure and development.

The substrate was then spray developed in Shipley MF-321 developer for 60 seconds. A 30 second oxygen plasma descum was then used to ensure that all photoresist was removed from the substrate in the developed areas. Subsequently, 100 angstroms of titanium was deposited by electron beam evaporation on the substrates as an adhesion layer followed by 1500 angstroms of gold. The preferred rate of evaporation is 1-2 Å per second for smooth coatings. The evaporation process covers the entire surface of the substrates.

The underlying photoresist was subsequently dissolved by an overnight soak in Shipley 1165 photoresist solvent containing N-methyl-2-pyrrolidone (NMP), causing gold in undesired areas to be released from the substrate. The substrates were then cleaned in methanol, followed by running water. Each layer of photolithography requires this process be repeated. The current process requires three layers of photolithography and includes a parylene dielectric coating step followed by photolithography patterning of vias and via etching in oxygen plasma, then photolithography of the top electrode and trace layer. Figure 5.4 shows a set of gold IDT electrodes following the gold evaporation and lift-off process. The electrodes contain 5 μm wide digits and 2 μm gaps. The electrode length is

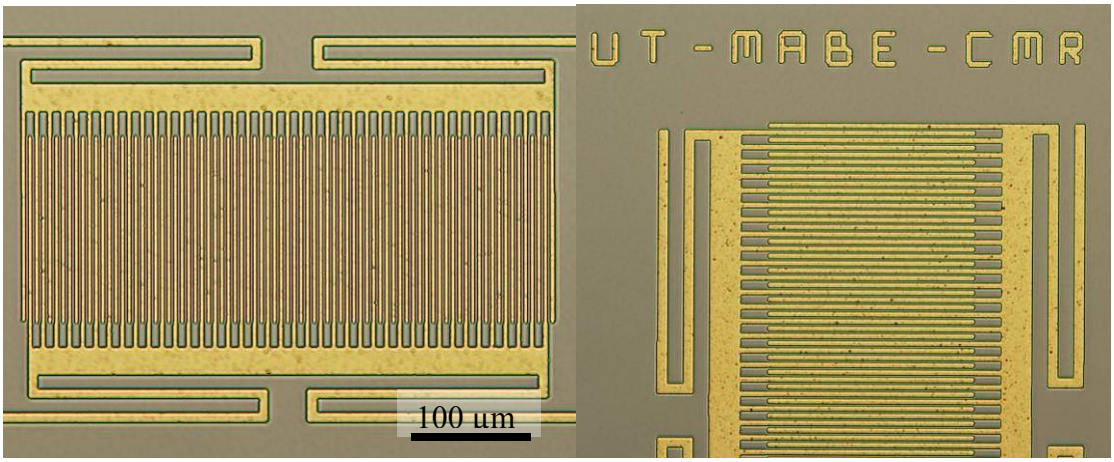

Figure 5.4: Images of 2 micrometer spacing interdigitated electrode at 50X magnification. Structures fabricated on silicon wafers.

5.2 Parylene Processing and Etching

The parylene polymerization process was discovered in 1947 by Michael Mojzesz Szwarc, who was investigating the strength of individual chemical bonds, discovered that when para-xylene was heated to pyrolysis it formed a thin, tan-colored, tube-shaped mass resembling the "skin of a small snake" in the glassware he was using for his experiment. Szwarc noted the new polymer's exceptional physical and chemical inertness. Parylene was further developed by the Union Carbide Corporation and released as a commercial process in 1965. Union Carbide investigated 20 forms of parylene, but only deemed three commercially viable. Specialty Coatings Systems has recently released a high-temperature, fluorinated version of parylene, Parylene HT. The chemical structure of the four most common types of parylene is shown in Figure 5.5 [129].

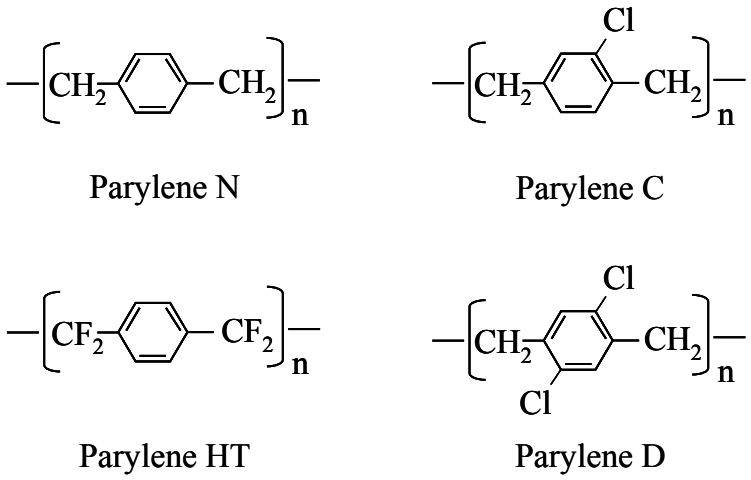

Figure 5.5: Chemical structure of four most common types of parylene.

For the parylene deposition process, the feedstock is a dimer of the parylene molecule of interest, or di-para-xylylene. Pressure in the deposition system is less than below 1 mTorr as controlled by the vacuum system. The sample is placed in a disposable foil container and placed in a tube furnace where it is heated to 150 C which causes the dimer to vaporize. The dimer vapors are drawn into a second furnace at a higher temperature, 680 C, which causes the dimer to pyrolize or split from dimer form to monomer form. The monomer vapors are drawn into the deposition chamber by the vacuum system which is at a temperature of 25 C. The vapors condense on the cooler surfaces of the deposition chamber and crosslink to form a polymer with a high molecular weight of approximately 500,000. Figure 5.6 illustrates the parylene polymerization and coating process. Figure 5.7 illustrates wafers with parylene as the insulating layer between the wafer and the device layer with electrodes fabricated on top of the parylene surface.

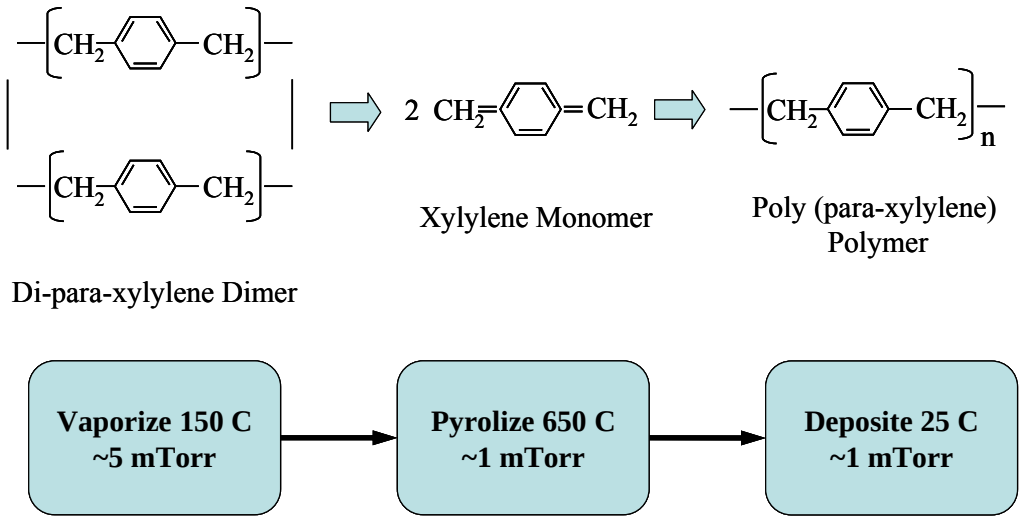

Figure 5.6: Parameters for parylene polymerization and coating process.

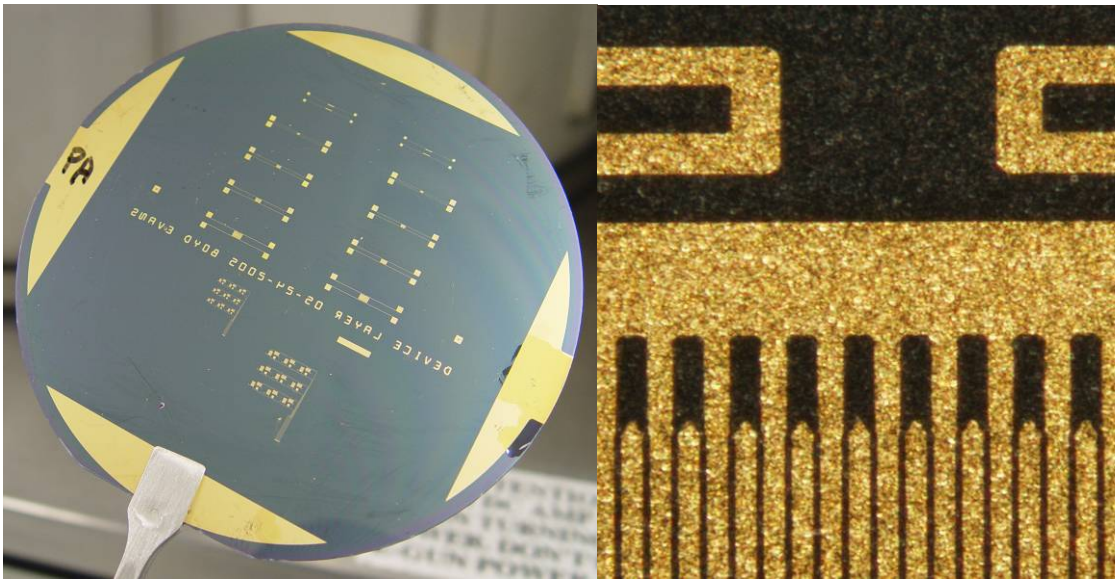

Figure 5.7: Images of silicon wafer with SiO_2 release/dielectric layer and parylene layer with interdigitated electrodes after lift-off. Right image is micrograph at 200X of 5 µm electrodes with 2 µm gaps between electrode digits.

The deposition rate of the parylene polymer was measured in order to deposit the correct thicknesses of material. Parylene C was used in all experiments in this investigation. Parylene coatings were made using a Specialty Coatings Systems (Indianapolis, IN) PDS 2010 Labcoater. The coating thickness is controlled by the amount of dimer placed in a foil boat in the evaporation chamber. In order to determine the amount of parylene required for 2 micrometer thick coatings, several test coatings were performed. Portions of these coatings were peeled off of the test substrate and the thickness of the remaining material was measured with a KLA Tencor P-10 surface profiler. The deposition rate was determined to be 0.608 grams/μm on the Cornell unit.

The etch rate of the parylene polymer using oxygen plasma was characterized to etch via openings in deposited parylene for electrical connections between layers. The precise etch time is required to prevent sputtering of the underlying gold. The etch rate was determined by depositing layers of parylene on silicon substrates. Openings were patterned in the parylene using the via layer mask used in the device fabrication. Samples were exposed to oxygen plasma using a PlasmaTherm PT 72 plasma etching system shown in Figure 5.8. These were etched using 40 standard cubic centimeters per minute (sccm) oxygen flow at a pressure of 40 mTorr. The RF plasma generator was set for 195 Watts at 13.56 MHz. Following etching, the remaining photoresist was stripped and the amount of parylene etched was measured using the Tencor P-10 profilometer. Five scans each of three samples were measured and the etch rate was determined to be 156.2 nanometers per minute. A time of 13.0 minutes was chosen to etch vias in the 2 micrometer thick parylene layers. Plasma etched openings are shown in and Figure 5.9.



Figure 5.8: Device wafers during oxygen plasma processing in PT-72.

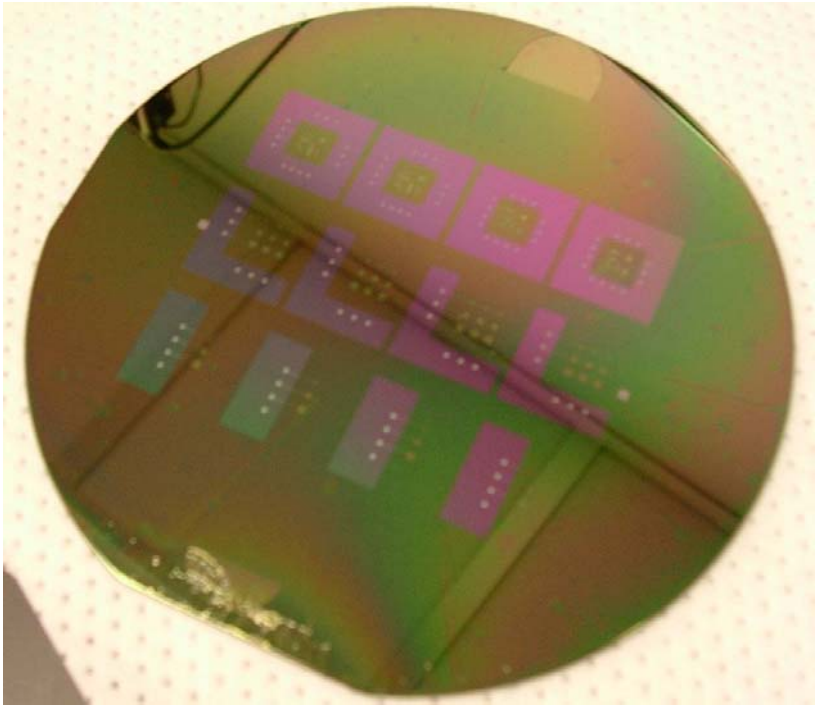

Figure 5.9: Substrates following etching of vias in parylene layer with PT-72 and removal of photoresist layer used for patterning.

5.3 Investigation of Lithography on Polyethylene Substrates

A similar photolithography, image-reversal, electron beam evaporation, and lift-off process was used for research on the use of polyethylene substrates. Early attempts to perform gold lift-off techniques on polyethylene surfaces had very poor results. An extensive cleaning and surface preparation technique was developed for the polyethylene samples. This method consisted of cleaning with a liquinox liquid soap solution, followed by an acetone rinse, a methanol rinse, and an isopropyl alcohol rinse.

The effects of O_2, N_2, SF_6, and combined O_2/N_2 plasma etching were investigated to find a method to activate the surface for deposition of gold. The results of these studies are shown in Figure 5.10. The surface of the polyethylene samples was activated by exposure to an oxygen plasma with a lesser amount of nitrogen supplied to the plasma. This step was performed in an Oxford Instruments (Oxfordshire, UK) Plasmalab 80. The samples were processed for 20 seconds with 50 standard cubic centimeters per minute (sccm) of O_2 and 4 sccm of N_2 using a 13.56 MHz RF plasma at 150 Watts. This step served to micro roughen the surface and increases the energy of the surface by breaking some of the polymer chains on the surface. Optical interferometric profilometry data of the surfaces following plasma treatment is shown in Figure 5.10. Notice the fine topography in the O_2/N_2 plasma treated surface. The surfaces of the polyethylene wafers were not flat enough to allow vacuum mounting in the photoresist spin casting system. Polyethylene wafers coated with photoresist by attaching them to silicon substrates with adhesive. Following photoresist spinning, polymer substrates were soft-baked in an oven for 30 minutes at 90 degrees C to remove excess solvent. The polyethylene samples were

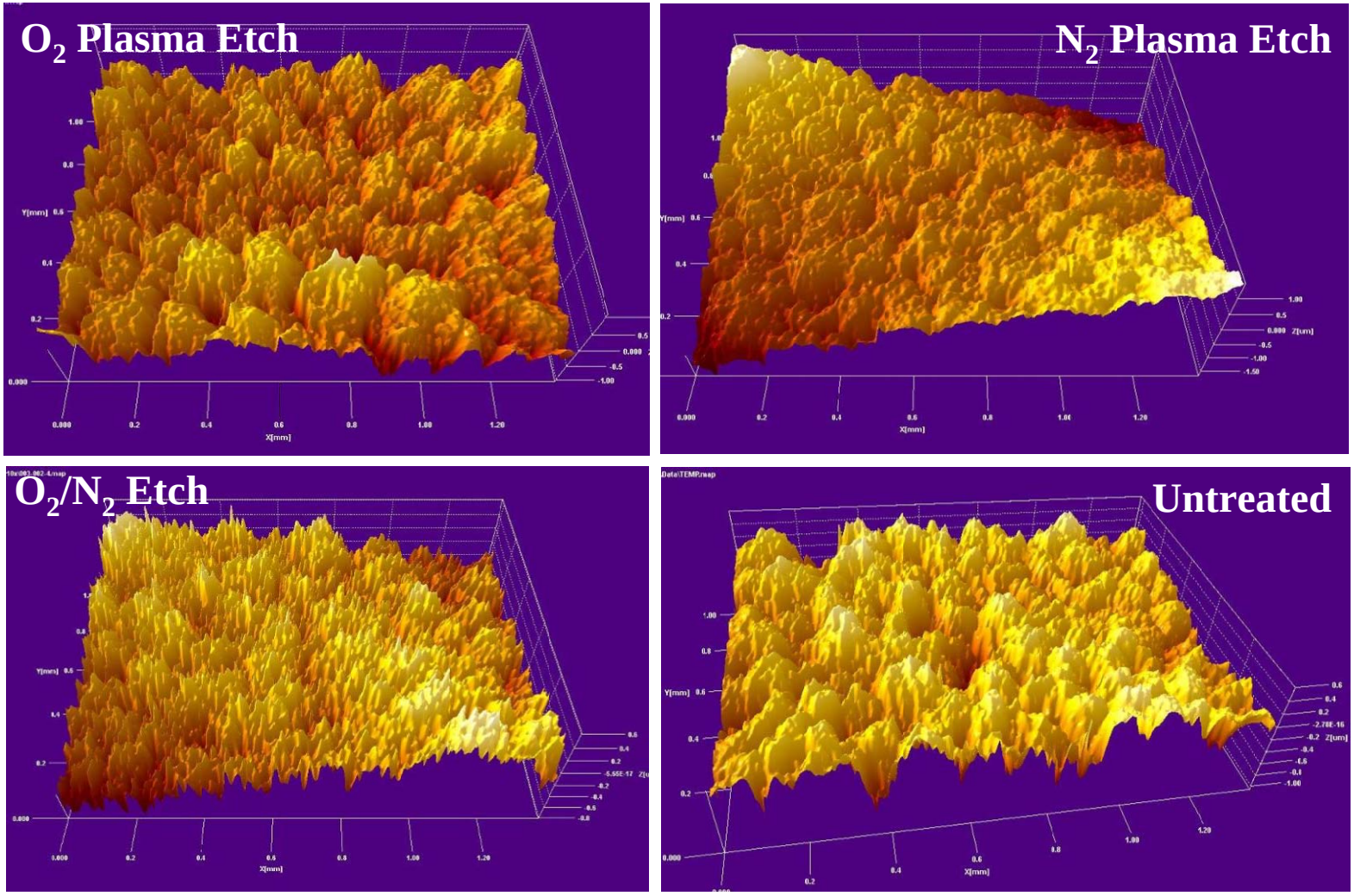

Figure 5.10: Optical profilometry of plasma-treated polymer surfaces.

exposed for 8.5 seconds. Following the image reversal process the polymer samples were descummed using O_2 plasma for 30 seconds followed by a second treatment of the O_2/N_2 plasma for 15 seconds. Metal layers were applied using electron beam evaporation, followed by lift-off in Shipley 1165. Figure 5.11 shows the results of the polyethylene fabrication experiments.

5.4 Summary of Fabrication Research for MEMS Strain Sensors

Photolithography techniques have been developed for fabricating MEMS strain sensors. The critical dimension of these sensors was 2.0 μm. The fabrication process begins with a cleaning process to ensure that they are free from particles or films that would prevent adhesion of electrode layers. The electrodes require the use of a non-conducting substrate or depositing a dielectric layer onto a conducting or semiconducting substrate. The lower dielectric deposition step is followed by using photolithography techniques to deposit the lower gold electrode layer which contains the lower electrode of the parallel plate sensor, the IDT structures and the lower electrodes of the shear sensors. Next, the parylene dielectric layer is deposited on the surface, followed by dry, plasma etching of vias in the parylene. Finally, the upper electrode layers are deposited in the final photolithography step. Novel techniques for the dry etching of parylene and for the microtexturing of polyethylene have been developed during this research and represent fundamental contributions of this work. Improvements in the smoothness of polyethylene substrates will be required for implementation of sensors on polyethylene substrates.

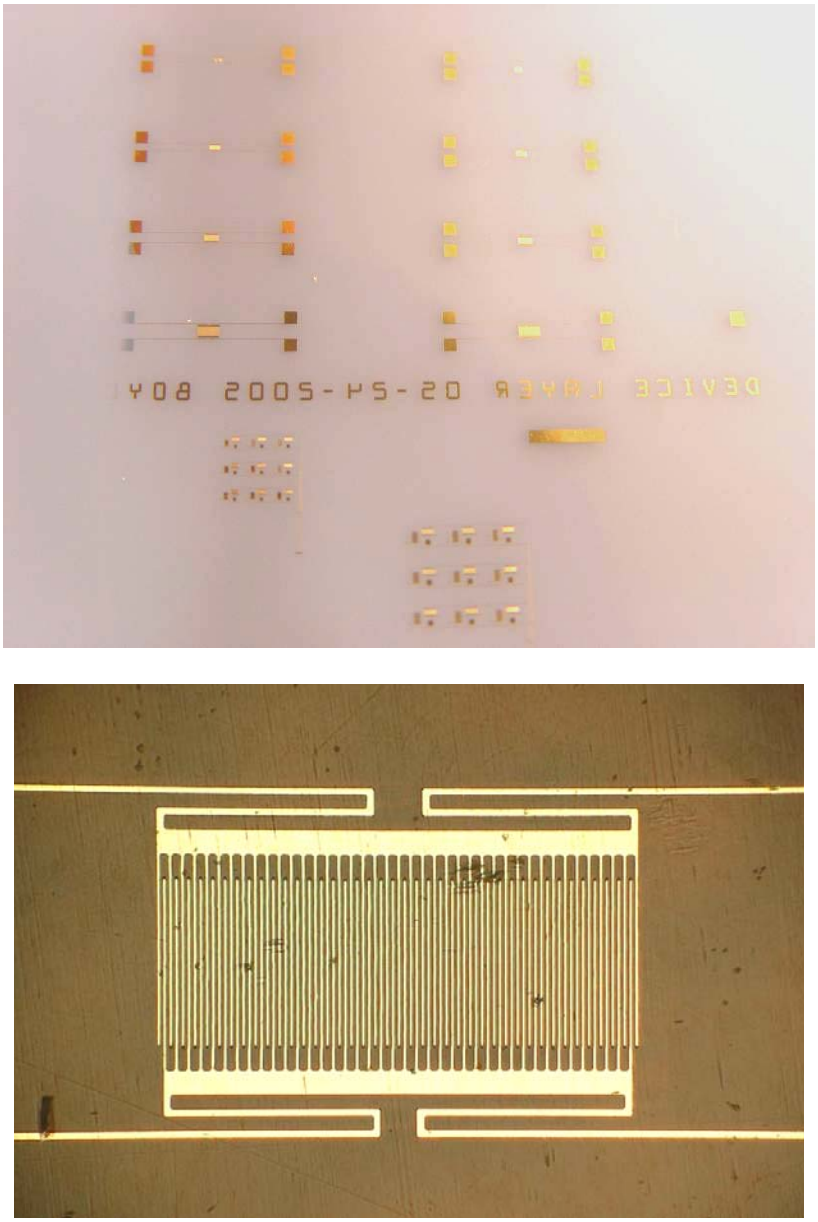

Figure 5.11: Upper image shows sensing array fabricated using parylene on Silicon substrate. Lower image is an interdigitated capacitor with 2 micrometer gaps between 5 micrometer legs fabricated on high-density polyethylene sheet material.

Chapter 6
Testing Methods and Data for Microfabricated Strain Sensors

6.1 Normal Strain Sensor Testing

An array of parallel plate sensors was designed to measure normal forces, and to verify the ability to use a row-column addressing technique to measure the values of individual capacitors. As shown in Figure 6.1, the upper electrodes of the sensors are connected in series by row and the lower electrodes are connected in series by column. Individual sensors are addressed by activating the row and column of the sensor of interest. The sensors were fabricated on a 0.5 mm thick silicon wafer with a 10 μm insulating oxide layer. For testing, they were attached to a printed circuit (PC) board with cyanoacrylate adhesive and electrical connections were made using a wire bonder. Sub-miniature B (SMB) shielded connectors were used to make electrical connections from a precision inductance, capacitance, and resistance (LCR) meter to the PC board. To protect the sensors and wire bonds during testing and handling, they were encapsulated in EP-30 epoxy from Master Bond (Hackensack, NJ). Following the encapsulation process, the surface of the epoxy was machined flat and parallel with the back of the circuit board.

In order to determine the effects of capacitor value on noise and sensitivity, three different values of capacitance were used in the array. The values of the capacitors in the

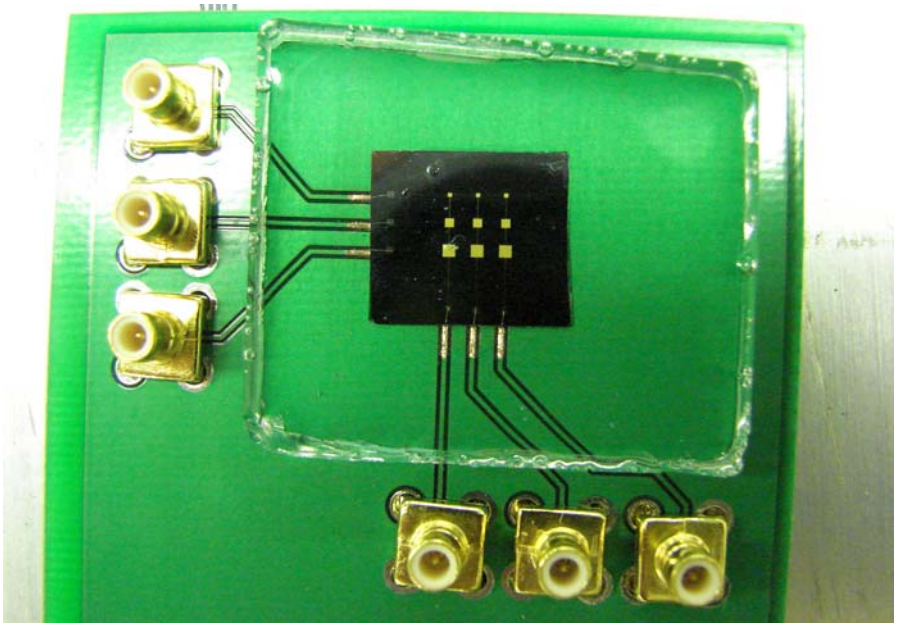

Figure 6.1: Array of parallel plate sensor mounted on printed circuit board for testing.

array are 1 pF, 5 pF, and 10 pF, and the dimensions of these 275 by 275 μm, 614 × 614 μm, and 867 × 867 μm, respectively. The dielectric material is a 2 μm thick layer of parylene. The electrodes consist of a 10 nm titanium adhesion layer and 300 nm of gold.

The experimental setup for applying loads is shown in Figure 6.2. Loads were applied through a 15.87 mm rod fabricated from Delrin® (E. I. duPont de Nemours & Co. Wilmington, DE) polymer material. A maximum load of 444.8 N (100 pounds) was applied to the parallel plate array. Loading through the 15.87 mm diameter rod results in a maximum pressure of 2.247 megapascals (MPa) or 325.9 pounds per square inch (psi). Applied to a homogeneous parylene material, this would result in a strain of 821 parts-per-million or microstrain. Finite element modeling of this structure predicts the strain in



Figure 6.2: Experimental setup for load testing the capacitive sensor array.

the parylene to be approximately 300 microstrain due to stiffening effects from the silicon wafer, silicon dioxide dielectric layer, and gold electrodes.

The array of sensors was tested using a hydraulic MTS (Eden Prairie, MN) 858 Table Top System mechanical testing machine with a 2.5 kilonewton (kN) load cell. The sensors were tested by alternating between no load and a sequentially increasing load. The sequence of loads applied was 0 N, 111.2 N, 0 N, 222.4 N, 0 N, 333.6 N, 0 N, 444.8 N, with a return to 0 N, which corresponds to alternating loads of 0 MPa and 0.562, 1.124, 1.685, and 2.247 MPa. All loads were held for two minutes, and the loading and unloading rate was 11.1 N/m. In English units, this corresponds to loadings of 0, 25, 0, 50, 0, 75, 0, 100, pound loads applied at a loading rate of 2.5 pounds/min. This rigorous testing scheme allowed comparison of static and dynamic loading conditions and allows the repeatability of the sensors to be measured in one test. Also, any drifting of the zero point can be observed. Figure 6.3 shows a plot of the loading profile.

Capacitance was measured with an Agilent 4285A LCR meter. A 1MHz frequency was used at 2 volt peak-to-peak excitation. Foil shielding connected to the LCR meter instrument ground was used to reduce noise. Care was taken to avoid ground loops which cause erratic behavior of the auto balancing impedance bridge circuit in the 4285 LCR meter. The base capacitance of the sensor along with cabling and other fixture or track capacitances was calibrated out, such that the meter recorded the change in capacitance as the load was applied. This allowed for optimization of the output of the meter's six digit display. In order to reduce noise, the average value of 16 samples was taken per measurement and the data recorded every second. The MTS testing machine

recorded data at the same interval. Data from the LCR meter was saved to a laptop computer using a Hewlet-Packard Instrument Bus (HP-IB) to Universal Serial Bus (USB) adaptor and Labview (National Instruments Corp. Austin, TX) software.

Figure 6.3 shows the time series data from the loading test for the 5pF capacitor at array element 2,2. Figure 6.4 shows the capacitance changes for all load cycles plotted with the applied pressure in MPa. The 10 pF capacitor has a response of 2.86×10^{-3} pF/MPa per pound force with a coefficient of determination (r^2) of 0.936. The 5 pF capacitor has a response of 1.54×10^{-3} pF/MPa with a coefficient of determination of 0.986, and the 1 pF capacitor has a response of 4.93×10^{-4} pF/MPa with an r^2 coefficient of 0.936. The sensitivity appears to scale with size for these results. The improved linearity of the 5 pF capacitor is attributed to better load centering over this sensor, due to its position (row 2, column 2) in the center of the array during load testing.

The results of the testing data from several different 5 pF sensors were compared with predictions from the closed form solutions and the finite element analysis results. Finite element modeling results presented in earlier were to investigate sensors embedded in polyethylene; however in order to compare with experimental results, the models were modified to include the properties of the Si, SiO_2, and epoxy materials used to fabricate the prototypes. The change in capacitance with applied load is plotted in Figure 6.5.

The total change in capacitance for the 5 pF sensor was 4.13×10^{-3} pF for the 2.25 MPa stress. Finite element modeling of this geometry predicted a change of 2.12×10^{-3} pF for this load. A least squares technique was used to determine the slope of these results which predicts the sensitivity of the sensor. The sensitivity values are listed in Table 6-1.

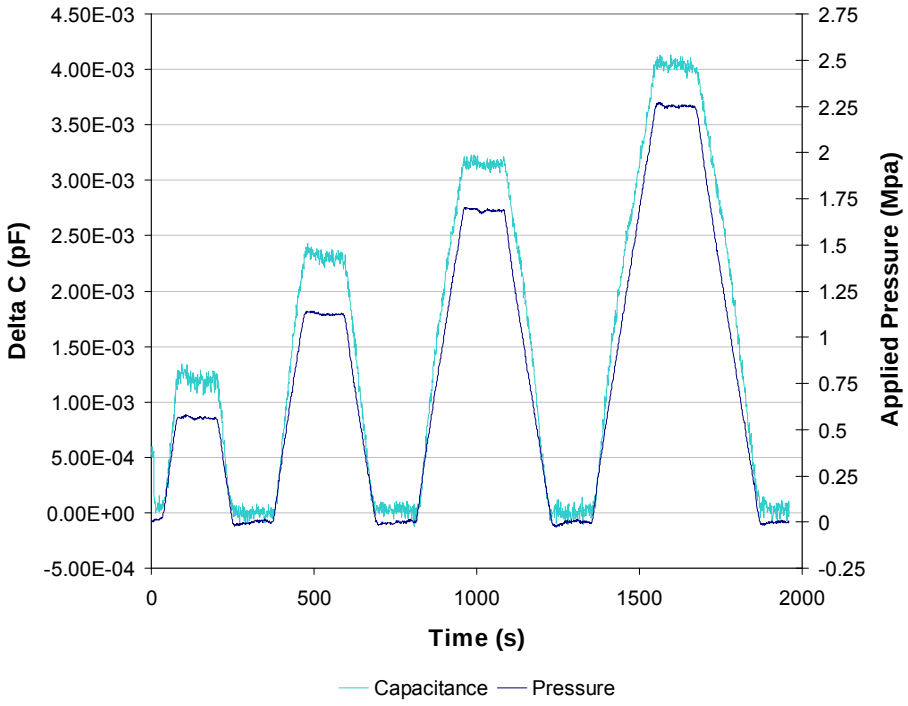

Figure 6.3: Load profile for capacitance array test for chip B, element 2-2, 5 pF.

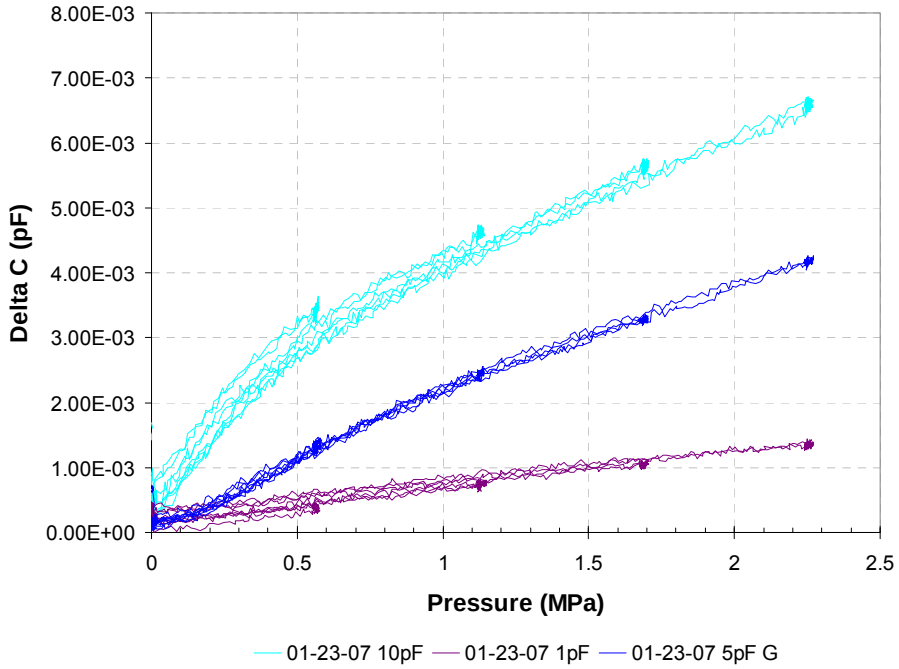

Figure 6.4: Change in capacitance with load from 1, 5, and 10 pF capacitive sensors.

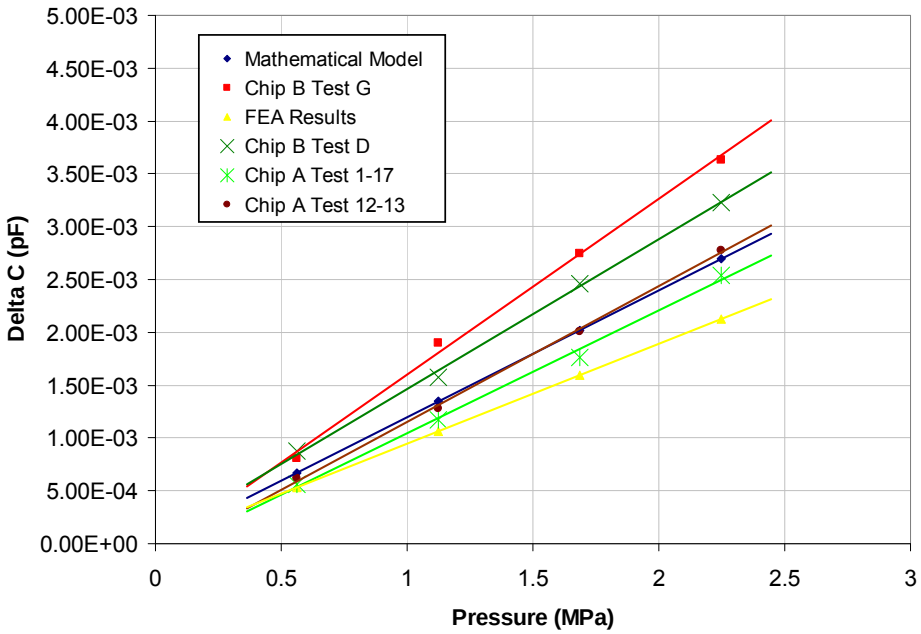

Figure 6.5: Comparison of sensor testing results with FEA and math model.

Table 6-1: Comparison of predicted sensitivity of sensors and test results.

Test	**Sensitivity (pF/MPa)**
Analytical Results	1.17 (10^{-3})
Finite Element Analysis	9.47 (10^{-4})
Chip B Test G	1.66 (10^{-3})
Chip Test D	1.41 (10^{-3})
Chip A Test 1-17	1.16 (10^{-3})
Chip A Test 12-13	1.28 (10^{-3})

The most important parameter is the slope of the capacitance-stress curve which indicates the sensitivity of the device. The slopes of the four different measurements, the mathematical model, and the finite element analysis are shown in Table 6-1. The finite element results for sensitivity correspond the closest with the results of Chip A, Test 1-17 with a difference in sensitivity values of 18% and least with the results of Chip B, Test G where they were 43% lower. The mathematical modeling results agree well with the results of Chip A Test, 12-13 with a difference of 3.3%, and in the worst case the analytical results were 27% lower. The differences between the experimental values and the analysis values were not unexpected due to variations in material properties, residual stresses, and the ability to model the exact geometry. Also, this problem is one of multiple scales. None of the finite element models had dimensions larger than 1.0 mm, and did not include the FR-4 or polycarbonate materials.

6.2 Shear Sensor Testing and Results

A test was developed to allow a state of shear stress to be applied to a region of epoxy encapsulating the shear sensor elements. This test is similar to a lap shear test, but is modified to produce a balanced loading with no induced bending moments at the bond joint. In order to connect to the sensors electrically, they were attached to an FR-4 printed circuit board with cyanoacrylate adhesive. The sensors were electrically connected to the traces on the circuit board by wire bonding and then encapsulated in a layer of Master Bond EP-30 medical epoxy approximately 3 mm thick. In a subsequent step, this layer was machined flat and parallel to the back side of the circuit board to a thickness of 2

mm. Similar pads of epoxy were made on two strips of polycarbonate material that was 5.79 mm thick by 25.4 mm wide by 100 mm long. These were assembled with epoxy into the test samples illustrated in Figure 6.6 and Figure 6.7.

The area of the epoxy encapsulating the sensors was 25 mm by 25 mm. During testing with the MTS system used for the normal strain sensor, loads of 445, 889, and 1334 N (100, 200, and 300 pounds) were applied to the test apparatus. The loading conditions result in a state of shear of 0.345, 0.689, and 1.034 MPa applied to the test sensor. Loads were applied at a rate of 6.67 N/s (1.5 pounds/s). Data was recorded using the same instrumentation setup as the normal strain sensor consisting of an Agilent 4285A LCR meter interfaced with a laptop using a HP-IB to USB adapter and Labview software to record the data.

The shear sensor is a differential sensor that consists of two capacitors in series as shown in Figure 3.7. During the application of pure shear, the capacitance of one of these should increase while the other decreases. This differential approach is required because this sensor will also be sensitive to normal strain. In the presence of a multiaxial strain, the common mode strain may be rejected by taking the difference of the two capacitance values. This sensor is intended to function with a signal conditioning circuit that subtracts the values of the two legs of the sensor in real time. This circuit was not available at the time these measurements were made, so two individual runs were made recording the change in capacitance between one electrode and the reference followed by recording the results between the other electrode and the reference. These values were subsequently subtracted during the data analysis step.

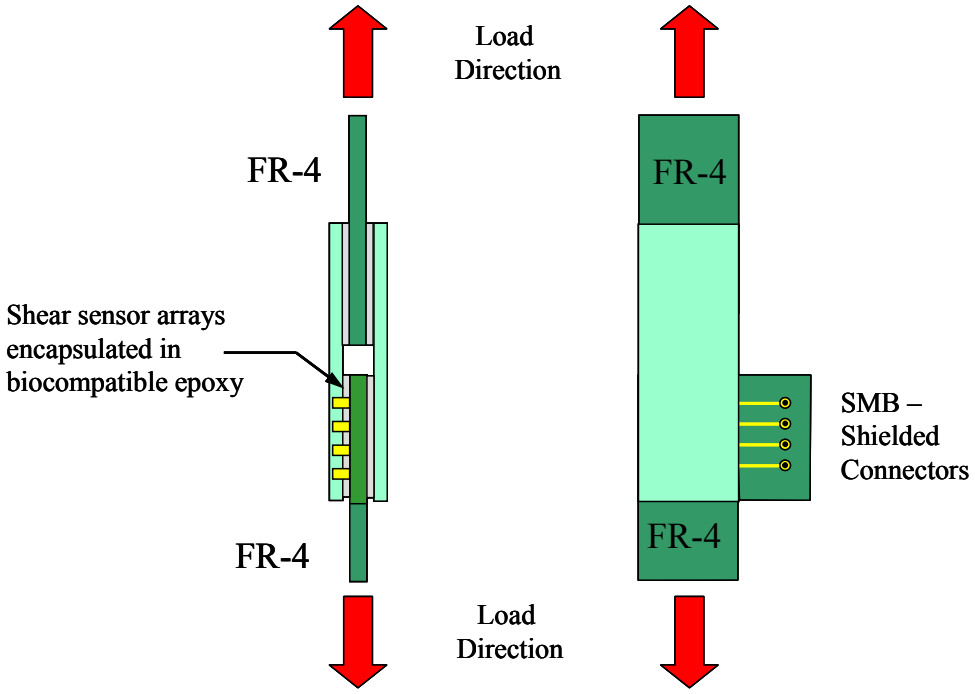

Figure 6.6: Illustration of testing scenario for shear sensors.

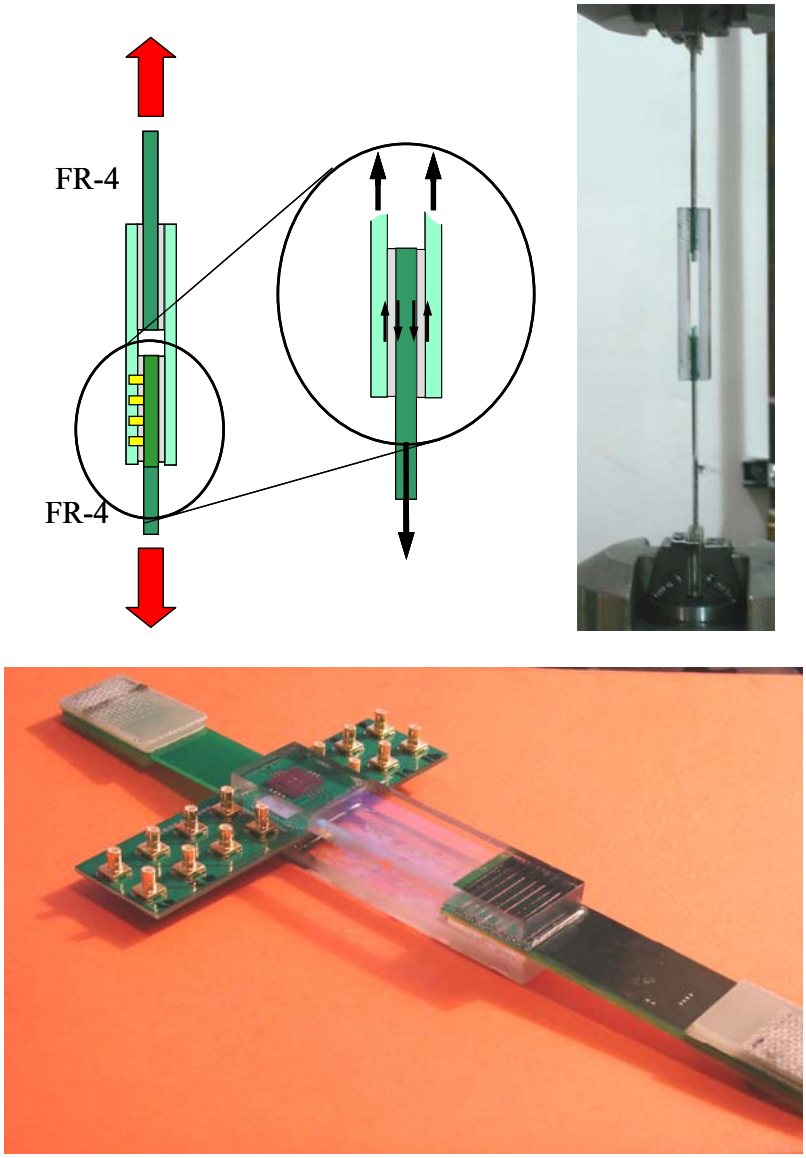

Figure 6.7: Upper left is illustration of transfer of shear load to epoxy connecting polycarbonate and FR-4 material. Upper right is image of test sample in MTS machine, and lower image is of sample used for shear testing.

Figure 6.8 shows the data recorded from the two loadings of the shear sensors, and the difference between the capacitance data for the two experiments. The data for the first run is illustrated in dark blue and the data from second run is illustrated in yellow. The subtracted signal representing the shear loading is represented in light blue. The loading data for both runs is also plotted to illustrate the consistency in the loading conditions between the runs. It is interesting to note that both portions of the sensor increased in capacitance during this test. This is because the area of the sensor is not only in shear, but it is also in tension. A transverse compressive strain occurs during this loading condition which resulted in the increase in capacitance of both sensors. The shear signal in Figure 6.8 is the difference between the two test signals and is shown in light blue. The results of this experiment illustrate this sensors ability to cancel out these effects and measure only the shear strain in the material. Loading data for both test runs is presented and overlaps in Figure 6.8 to show similarity in testing conditions.

A comparison between the shear sensor data, analytical methods, and finite element analysis was performed. A representative volume of the shear sensor containing the prototype materials Si, SiO_2, Au, Parylene, and EP-30 epoxy was generated for this comparison. These results are plotted in Figure 6.9. There appears to be a bias or offset in the magnitude of the experimental data. A linear least squares analysis was performed to determine the slope of the results in Figure 6.9 and the indicated sensitivity. These results are listed in Table 6-2. The sensitivity value predicted by the finite element analysis differs from the experimental value by 60.1%, and the sensitivity value predicted by the mathematical model differs by 9.3%.

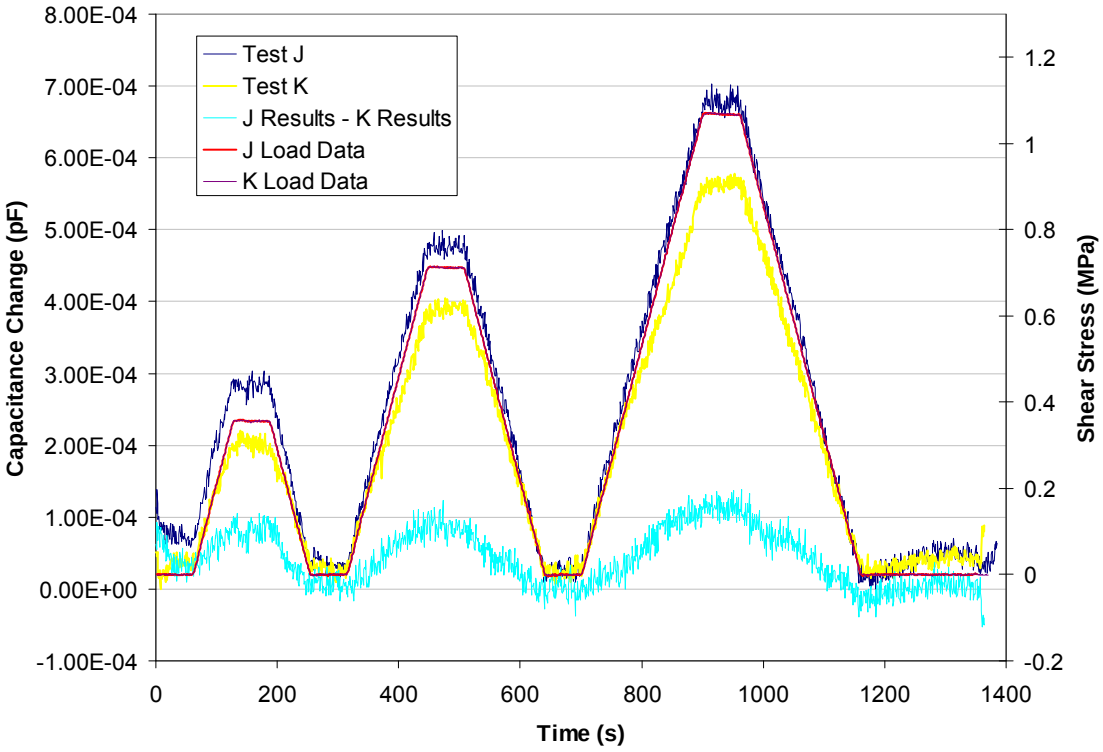

Figure 6.8: Results of shear sensor testing for 0.344, 0.689, and 1.034 MPa shear loads.

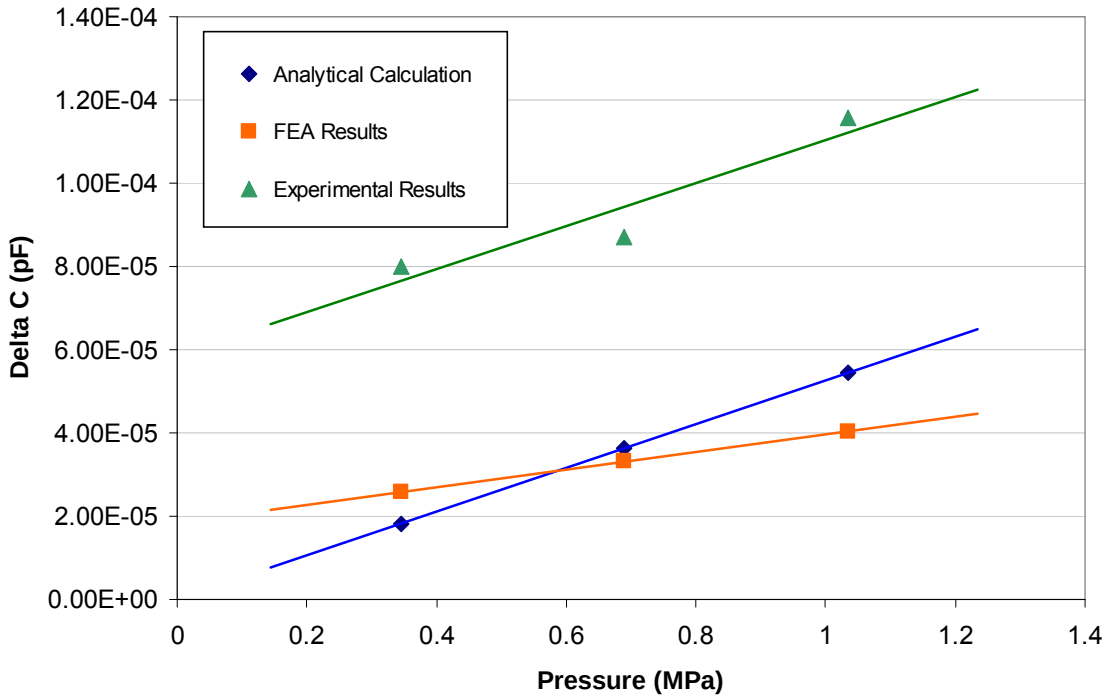

Figure 6.9: Comparison of experimental results and results predicted by analytical techniques and finite element analysis.

Table 6-2: Comparison of predicted sensitivity of the shear sensor and test results.

Test	Sensitivity (pF/MPa)
Analytical Results	5.26 (10^{-5})
Finite Element Analysis	2.10 (10^{-5})
Experimental	4.77 (10^{-5})

The total change in the differential capacitance from this experiment was 1.24×10-4 pF. This is a very small change in capacitance and may present a measurement challenge. It should be noted that this was a single shear sensor, and in future designs it is possible to fabricate a compact array of these in series as previously discussed. The output of the array can be increased proportional to the number of sensors in the array. Using this method the size and sensitivity of the shear sensor may be scaled to match the signal conditioning electronics.

6.3 IDT Sensor Test System and Data

In order to create an in plane strain for measuring the output of the interdigitated electrodes. A test chip containing the IDT structure was adhered to the surface of a printed circuit (PC) board using cyanoacrylate adhesive. Electrical connections between the sensors and the PC were made using wire bond connections, and SMB shielded connectors were used to make connections to the PC board. The configuration of the sensor during loading is illustrated in Figure 6.10. An image of the PC board is shown in Figure 6.11.

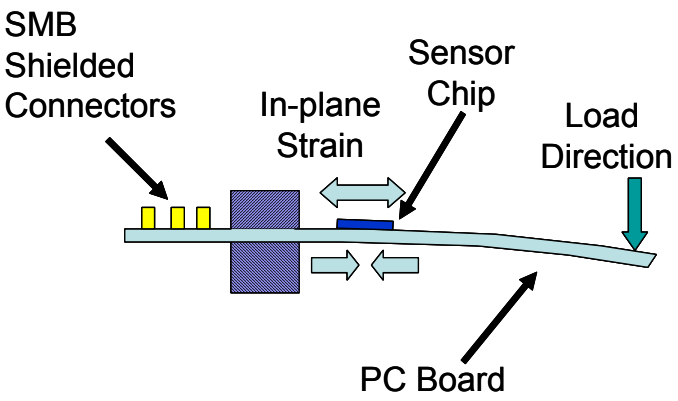

Figure 6.10 Loading and mounting diagram for testing of IDT in plane strain sensors.

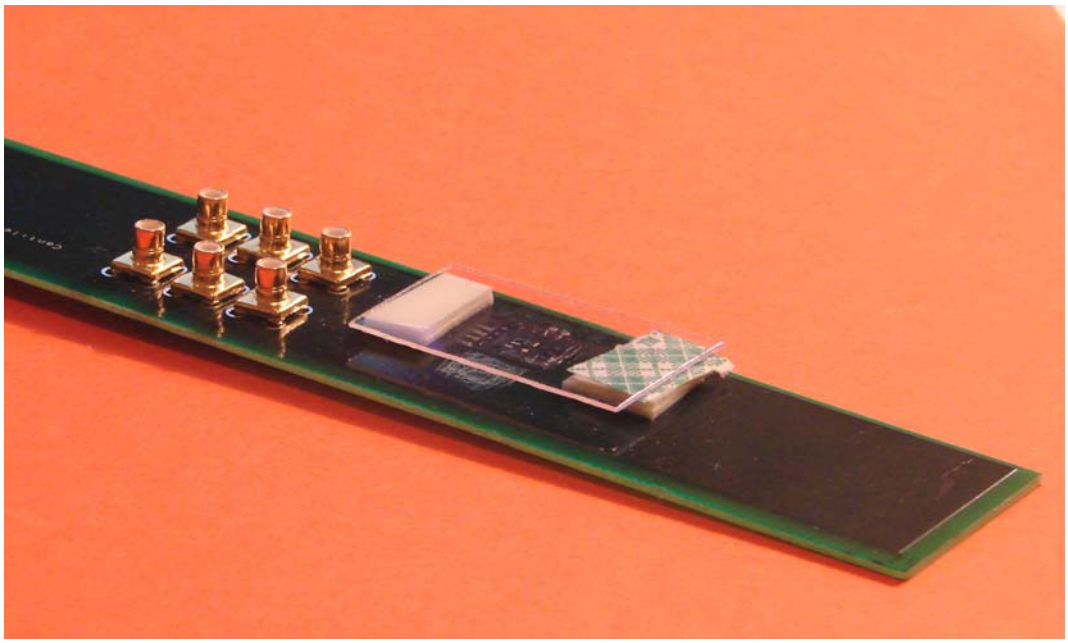

Figure 6.11: Image of PC board with sensor array mounted for cantilever testing.

Capacitance was measured with an Agilent (Santa Clara, CA) 4285A LCR meter. A 1MHz frequency was used with 1 volt peak-to-peak excitation. Foil shielding connected to the LCR meter instrument ground was used to reduce noise and the effects of stray fields. As in previous experiments, particular care was taken not to induce ground loops which affect the gain of the auto balancing bridge circuit of the LCR meter. The base capacitance of the sensor along with cabling and other fixture capacitances was calibrated out, such that the meter recorded the change in capacitance with applied load.

As illustrated in Figure 6.10, test measurements of the IDT response to in plane strains were made by applying loads to the end of the PC board causing it to bend. Loads of 20, 50, 70, 100, 120, and 150 grams were applied to the end of the PC board. Data was acquired over time with the LCR meter. Raw data from testing of the IDT strain sensor is shown in Figure 6.12. Care was taken when applying the loads to the end of the PC board, however the process of applying and removing the test masses resulted in some spikes in the data. Data from the periods of constant load were averaged and a linear least squares fit applied to the data. Results of the cantilever loading were linear with at coefficient of determination, r^2, value of 0.97. These results are shown in Figure 6.13.

6.4 Uncertainty Analysis of Testing Methods

An Agilent 4285A Precision LCR meter was used to make measurements during mechanical testing. This instrument operates on the basis of impedance or admittance measurement and uses an auto balancing bridge method. This method incorporates a four point probe technique in which current is supplied through one set of independent probes

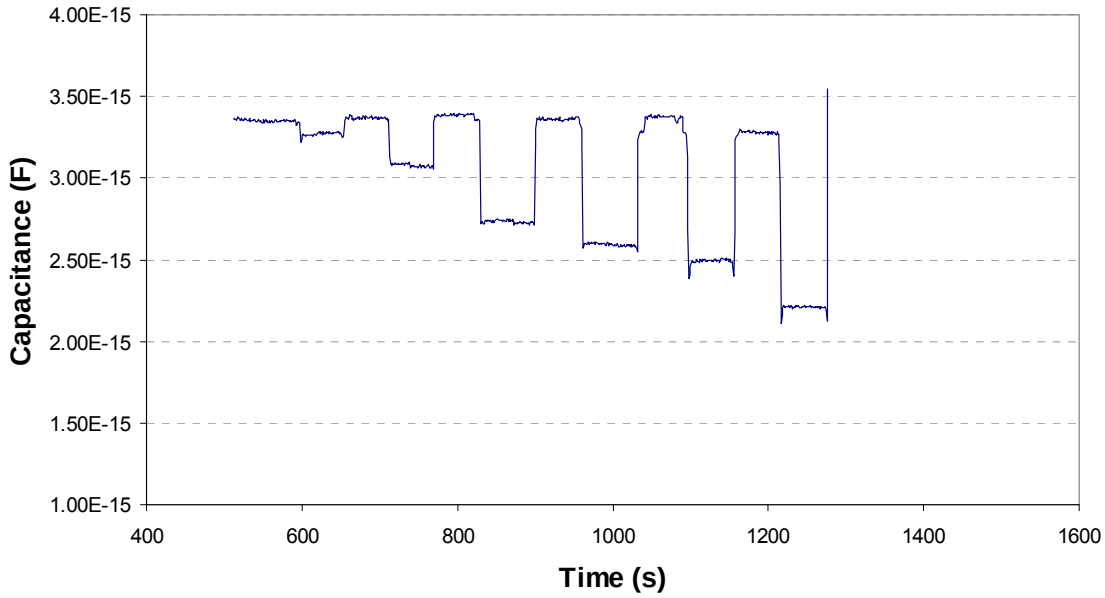

Figure 6.12: Raw data from in strain sensor test.

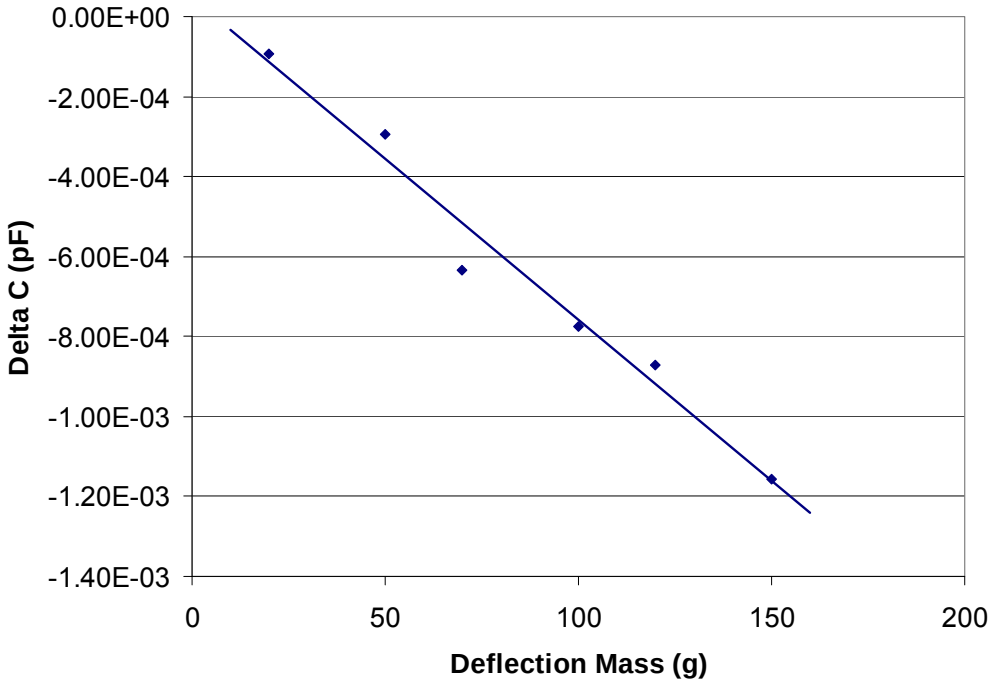

Figure 6.13: Data from constant loading averaged and plotted with linear least squares fit.

and voltage is measured through a different independent set of probes. It has a test signal frequency range of 75 kHz to 30 MHz with 100 Hz resolution and an accuracy of 0.01%. The manual for this instrument states that its display has a resolution of 0.00001 pF – 999.999 μF. The accuracy of the impedance measurement value must be calculated based on actual test conditions including temperature, cable length, test device impedance, measurement frequency, and voltage. The measurement accuracy was calculated to be ±0.3% of the displayed value using the conditions for our test.

Initial errors in measurements were caused by ground loops or stray inductances in the shielding. Shielding proved to be very important for making measurements with little noise or drift. However if the shielding techniques resulted in multiple paths to ground, instability in the auto balancing circuit bridge resulted in sudden offsets in data.

During testing, the calibration procedure for removing parasitic capacitances was used to subtract the base capacitance of the sensor such that the LCR meter reported the change in capacitance over the test instead of the actual capacitance value. This allowed operation of the instrument at resolutions intended for the measurement of smaller capacitance values. The LCR meter was carefully calibrated in the test fixture just prior to testing. Interfacing from a laptop computer to the instruments microprocessor using HP-IB connections to processor the instrument reported capacitance values to the laptop with a resolution of 1×10^{-10} pF. The root mean squared (RMS) error of the test setup was recorded with a dummy board containing all components and tracks, and with a set of sensors with broken wire bonds at $\pm7.34\times10^{-6}$ pF. The MTS mechanical testing system and data acquisition system were operating during this test. The RMS error of the MTS

load actuator was measured to be 1.21 N (0.27 pounds) during this evaluation which would result in an error of 6.11 kPa in the applied pressure. Figure 6.14 is an enlargement of the 2 minute, 50 pound constant load interval for the 5 pF sensor. This data shows some overshoot and noise in the hydraulic control system of the MTS mechanical testing machine.

6.5 Summary of Strain Sensor Testing Methods and Results

In this research, three unique sensors have been developed. These sensors are capable of being embedded inside other materials with minimal influence on the properties and stress in that material. Testing methods for these sensors have been developed and the fundamental response of these sensors has been demonstrated. Refinements in the fabrication techniques and metrology during fabrication may be required to ensure that the sensors have repeatable characteristics. Refinements in design to improve sensitivity may be desired to improve the magnitude of the output signal. Some of these require modifications in dimensions of the sensors, and can be made at the expense of increasing the size of the sensor.

Response linearity was a concern in the initial stages of this research, however results of sensor testing show that these sensors respond linearly to applied load. It has also been demonstrated that the macroscopic forces applied to these structures may be measured by the microscopic devices designed and fabricated during this research. It has also been demonstrated that the sensors can measure strain through an encapsulating material. Methods for measuring the small changes in capacitance in a laboratory

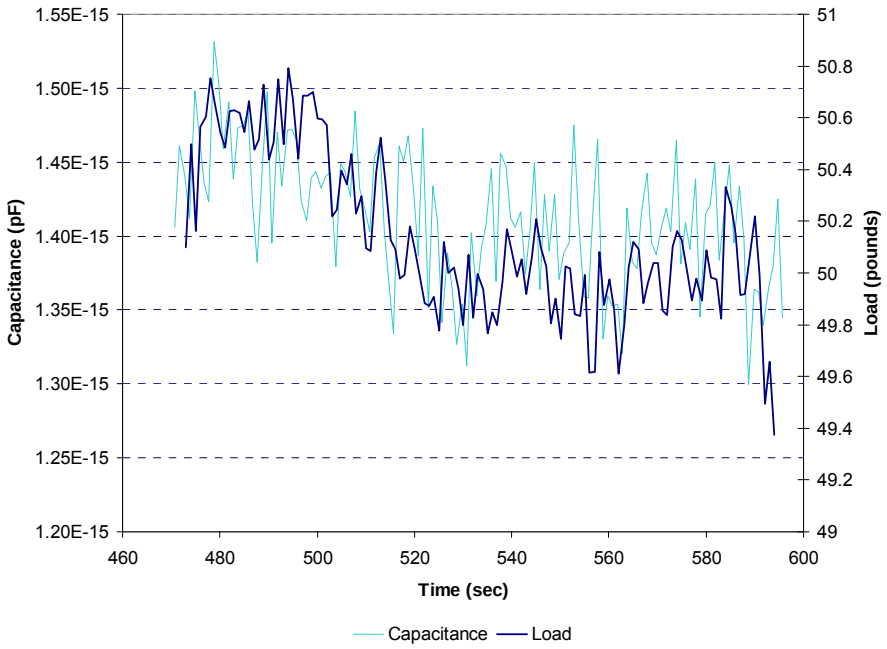

Figure 6.14: Enlarged view of MTS load data and capacitance data for 222.4 N (50 pound) load.

environment have been developed and validated. When possible to compare testing results with analytical results, the results of testing agree with results predicted by analytical techniques and finite element analysis within a factor of two. This variation is expected due to changes in material properties with fabrication technique, residual stress resulting from microfabrication techniques, and the ability of modeling techniques to incorporate macroscopic and microscopic geometries in an accurate way. The methods for testing the multiaxial strain sensors presented in this section and the testing results represent fundamental contributions of this investigation.

Chapter 7
Conclusions and Summary of Sensor Research

In this research a class of sensors was investigated which may be embedded in the load-bearing materials used in orthopedic components for the monitoring the state of strain and stress in that component. Sensors have been developed which can monitor the state of stress and stain in three dimensions at a single location. The challenge of developing sensors which can monitor pressure or strain in soft materials while having good response and a minimal effect on the state of stress in that material is significant. In this research, the background material necessary to design sensors for orthopedic components has been determined, and a set of capacitive sensors for the monitoring of pressure has been designed. These sensors may be grouped in an array to characterize the state of strain in three dimensions.

7.1 Conclusions of Microfabricated Strain Sensor Research

A novel set of capacitive sensors has been developed for this research which is capable of fully characterizing the three dimensional state of stress and strain at a single location. These sensors incorporate materials approved for biomedical use, and include a

parallel plate capacitive sensor for normal strain, a differential capacitor for the measurement of shear, and an interdigitated capacitor for monitoring in plane strain.

Analytical solutions have been developed to predict the performance the sensors and determine the sensitivity of the design parameters. These solutions indicate that the base capacitance of the micrometer-scale devices is in the pF range, and that the response of the sensors is in the 10^{-3} pF range. The analytical solutions indicate that the normal strain sensor may be optimized by reducing the gap between the electrodes and by increasing the electrode area, and that increasing the width of the shear sensor or using multiple sensors in parallel increases the sensitivity of this sensor to shear strains. These solutions indicate that increasing the IDT sensor thickness and decreasing the gap between electrodes improves the IDT sensor directional sensitivity. The analytical solutions for the capacitive strain sensors aid in the understanding of the mechanical and electrical response of the sensors. The analytical techniques also allowed for rapid investigation of multiple parameters on device sensitivity. Analytical methods were used throughout this research in conjunction with experimental techniques and finite element modeling.

Finite element methods were also used to examine the sensor structure. This research was performed in conjunction with the development of analytical techniques. Establishing boundary conditions and understanding the changes in capacitance with deformation was important for these techniques. Difficulties due to multi-scale effects were encountered during this portion of the research. To accurately model the small changes in capacitance and the micrometer-scale features of the sensors, fine resolution

finite element mesh models were constructed. These resulted in only a small portion of the problem being analyzed. The finite element results contributed to the understanding of the sensor response and confirmation of the assumptions used in analytical techniques. Parameter studies from finite element analysis also predicted improved response from the parallel plate sensor with increasing electrode area. Finite element results showed improvements in shear sensor response with the compact, parallel electrode geometry and with increasing electrode width. These results also predict improved response from IDT electrodes with increased electrode thickness or decreased gap.

Several portions of this research were investigated simultaneously. One of the immediate goals of this research was to investigate potential fabrication techniques. Investigating microfabrication techniques was an initial step in this investigation in order to develop the techniques for fabricating the sensors and to develop design rules and potential materials. Fabrication techniques for these sensors have been developed which primarily rely on currently used biomedical materials. Fundamental prototypes of sensors were fabricated using silicon wafers with a thermal oxide layer grown on them for insulating the sensors from the substrate. Fabrication techniques on polyethylene surfaces were investigated and a plasma surface treatment process was developed that allowed features with 2.0 micrometer critical dimensions to be fabricated. Patterning techniques for the biocompatible polymer parylene were also developed as part of this research.

An invention disclosure encompassing several aspects of integrated measurement techniques was submitted during this research. This invention disclosure contains 31

claims related to orthopedic sensing and was awarded U.S. Patent Number 7,097,662. This patent is presented in the Appendix and illustrates the contributions of this research.

Test methods for applying loads to the sensors and for accurately measuring the changes in capacitance were developed as part of this research. An array of six sensors was fabricated with a critical dimension of 2.25 micrometers. This array consisted of a parallel plate capacitor for measuring normal strain, two differential elements for sensing shear strain normal to the plane of the array, and three interdigitated transducer (IDT) elements for characterizing strain in the plane of the sensor. The normal strain sensor exhibited a sensitivity of 1.54×10^{-3} picofarads per megapascal, and the shear sensor had a sensitivity of 4.77×10^{-5} picofarads per megapascal. The results demonstrated that the sensors respond with good linearity to applied loads, and that the strain inside the encapsulating material could be measured with the embedded sensor. The experimental results also demonstrated that the macroscopic forces applied to these structures can be measured by the microscopic devices designed and fabricated during this research. Results from finite element modeling and analytical solutions were crucial as the measurement techniques were validated. Results from experimental testing had good agreement with analytical and numerical results, although they demonstrated that better verification of sensor dimensions and material properties is necessary. The changes in capacitance measured were in the femptofarad (1×10^{-15} F) range and sometimes lower. This result indicates the need for accurate measurement techniques and signal conditioning, or development of optimized sensor geometries based on signal conditioning circuit sensitivity.

7.2 Future Research in the Area of Embedded Strain Sensors

The results of this investigation may be expanded in several areas. Results of this research indicated the need to better characterize the properties of the sensor materials on the micrometer scale. The expansion of the use of biocompatible substrates and flexible or nonplanar substrates is one of the next challenges to be faced by this research. Substrates meeting the mechanical and biocompatibility requirements of this project while being suitable for microfabrication were not available at the time of this research. As part of future research in biocompatible substrates, the investigation of signal connections from the embedded sensor to the signal conditioning electronics should be included. Potential directions for this research are in the development of better techniques for molding polyethylene substrates and the use of other polymer substrates which could be laminated into the final bearing materials. Conducting polymer electrodes would also improve the response of the system due to better compliance matching.

The integration of power and signal conditioning electronics into the substrate is another area for further research. The capacitance changes measured with these devices was generally on the order of 10^{-2} pF, and the signal conditioning systems for use in implanted devices will need to be compact and of low power consumption yet sensitive enough to measure these effects. The design tools for integrated, capacitive strain sensors have been developed during this research which will allow the optimization of sensor response and the matching of sensor base capacitance and sensitivity with signal conditioning electronics.

Fundamental sensor prototypes have been tested and their function verified. Testing scenarios included the use of encapsulation materials. Several areas for sensor testing will be required as this research continues. Much of this should make use of the integrated signal conditioning circuit such that the ruggedness of the complete system can be verified. Future testing requirements should include cyclic load testing, testing of larger arrays of sensors,

The challenges in implementing these sensors on a large scale for implantable components is significant, however these challenges can be met using the techniques developed in this research and those to be developed through future research in this area. The ability to measure loads, contact position and area, axial rotation, roll back and other implant motions in real time and *in vivo* will have enormous impact on patient outcomes. The ability of clinicians to easily see the impacts of improper load balancing and lift-off has the potential to revolutionize the orthopedic industry. Also, the ability to monitor shear stresses in real time has tremendous implications for the understanding of wear of orthopedic components. The future research potential resulting from the implementation of these sensing techniques in orthopedic components is without limit.

BIBLIOGRAPHY

[1] Ranawat CS. History of Total Knee Replacement. J. Southern Orthopaedic Association. 11(4): 218-226. 2002.

[2] Charnley J. Arthroplasty of the Hip A New Operation. The Lancet. 1(7187). 1129-1132. May 27, 1961.

[3] National Hospital Discharge Summary 2001. National Center for Health Statistics. http://www.cdc.gov/nchs/data/series/sr_13/sr13_156.pdf

[4] Nationwide Inpatient Survey 1997. National Center for Health Statistics. http://www.cdc.gov/nis

[5] Buechel Sr, FF. Long-Term Followup After Mobile-Bearing Total Knee Replacement. *Clin Orthop Relat Res.* 404: 40-50, 2002.

[6] Pavone V, Boettner F, Fickert S, Sculco TP. Total Condylar Knee Arthroplasty: A Long-Term Followup. *Clin Orthop Relat Res.* 368: 18-25, 2001.

[7] Rodriguez JA, Bhende H, Ranawat CS. Total Condylar Knee Replacement A 20-Year Followup Study. *Clin Orthop Relat Res.* 388: 10-17, 2001.

[8] Sharkey PF: Why are total knee arthroplasties failing today? *Clin Orthop Relat Res.* 404: 7-13, 2002.

[9] Bush JL, Wilson JB, Vail TP. Management of bone loss in revision total knee arthroplasty. Clin Orthop Relat Res. 452:186-92. 2006.

[10] Diduch DR, Insal JN, Scott WN, Scuderi GR, Font-Rodriguez D. Total Knee Replacement in Young, Active Patients. Long-Term Follow-up and Functional Outcome. *J Bone Joint Surg Am.* 79:575-582, 1997.

[11] Saleh K, Rand J, McQueen D. Current status of revision total knee arthroplasty: how do we assess results? *J Bone Joint Surg Am*. 85:S18–S20. 2003.

[12] American Academy of Orthopedic Surgeons Fact sheets http://orthoinfo.aaos.org/fact/thr_report.cfm?Thread_ID=275&topcategory=Knee

[13] Sharkey PF: Why are total knee arthroplasties failing today? *Clin Orthop Relat Res.* 404: 7-13, 2002.

[14] Fehring TK: Early Failures in Total Knee Arthroplasty. *Clin Orthop Relat Res.* 382: 315-318, 2001.

[15] Mulhall KJ, Ghomrawi HM, Scully S, Callaghan JJ, Saleh KN. Current etiologies and modes of failure in total knee arthroplasty revision. *Clin Orthop Relat Res*. 446:45-50. 2006.

[16] Walldius B. Arthroplasty of the knee using an endoprosthesis. Acta Orthop Scand 30: 137. 1960.

[17] Walldius B. The classic: arthroplasty of the knee using an endoprosthesis. *Clin Orthop Relat Res.* 331: 4-10. 1996.

[18] Morrison JB. The mechanics of the knee joint in relation to normal walking. *J Biomech*. 3(1):51-61. 1970.

[19] Warwick R and Williams P.L. editors. Gray's Anatomy. 35th British Edition. W.B. Saunders Company. Philadelphia. 1973.

[20] Fukubayashi T, Torzilli PA, Sherman MF, Warren RF. An in vitro biomechanical evaluation of anterior-posterior motion of the knee. Tibial displacement, rotation, and torque. *J Bone Joint Surg Am.* 64(2):258-64. 1982.

[21] Hsieh HH, Walker PS. Stabilizing mechanisms of the loaded and unloaded knee joint. *J Bone Joint Surg Am*. 58(1):87-93. 1976.

[22] Girgis FG, Marshall JL, Monajem A. The cruciate ligaments of the knee joint. Anatomical, functional and experimental analysis. *Clin Orthop Relat Res.* 106:216-31. 1975.

[23] Andriacchi TP, Stanwyck TS, Galante JO. Knee biomechanics and total knee replacement. *J Arthroplasty*. 1:200-219. 1986.

[24] Andriacchi TP. Biomechanics and gait analysis in total knee replacement. Orthop Rev. 1988 May;17(5):470-3.

[25] Andriacchi TP, Dyrby CO. Interactions between kinematics and loading during walking for the normal and ACL deficient knee. J Biomech. 38(2):293-8. 2005.

[26] Nilsson KG, Karrlholm J, Ekelund L. Knee motion in total knee arthroplasty.: A roentgen stereophotogrammetric analysis of the kinematics of the Tricon-M knee prosthesis. *Clin Orthop Relat Res.*256:147-161. 1990.

[27] Nilsson KG, Karrlholm J, Gadegaard P. Abnormal kinematics of the artificial knee: Roentgen stereophotogrammetric analysis of 10 Miller-Galante and five New Jersey LCS knees. *Acta Orthop Scand*. 62: 440-446. 1991.

[28] Argenson JN, Scuderi GR, Komistek RD, Scott WN, Kelly MA, Aubaniac JM. In vivo kinematic evaluation and design considerations related to high flexion in total knee arthroplasty. *J Biomech.* Feb;38(2):277-84. 2005.

[29] Komistek RD, Dennis DA, Mahfouz MR. In Vivo Fluoroscopic analysis of the Normal Human Knee. *Clin Orthop Relat Res.* 410:69-81. 2003

[30] Dennis DA, Komistek RD, Cheal EJ, Stiehl JB. Femoral condylar lift-off in vivo in total knee arthroplasty. *J Bone Joint Surgery (BR)*. 83-B:33-39. 2001.

[31] Warwick R, Williams PL. Gray's Anatomy 35th British Edition. WB Saunders Co. Philadelphia. 1973.

[32] Blunn GW, Walker PS, Joshi A, Hardinge K. The dominance of cyclic sliding in producing wear in total knee replacements. Clin Orthop Relat Res. 273:253-60. 1991

[33] Blunn GW, Joshi AB, Lilley PA, Engelbrecht E, Ryd L, Lidgren L, Hardinge K, Nieder E, Walker PS. Polyethylene wear in unicondylar knee prostheses. 106 retrieved Marmor, PCA, and St Georg tibial components compared. Acta Orthop Scand. 63(3):247-55. 1992.

[34] Blunn GW, Joshi AB, Minns RJ, Lidgren L, Lilley P, Ryd L, Engelbrecht E, Walker PS. Wear in retrieved condylar knee arthroplasties. A comparison of wear in different designs of 280 retrieved condylar knee prostheses. J Arthroplasty. 12(3):281-90. 1997.

[35] Hood RW, Wright TM, Burstein AH. Retrieval analysis of total knee prostheses: a method and its application to 48 total condylar prostheses. J Biomed Mater Res. 17(5):829-42 1983.

[36] Hood RW, Wright TM, Burstein AH. Retrieval analysis of total knee prostheses. J Biomed Mat Res. 17: 829. 1983.

[37] Dennis DA, Komistek RD. Mobile-bearing Total Knee Arthroplasty, Design Factors in Minimizing Wear. *Clin Orthop Relat Res.* 452:70-77. 2006.

[38] Banks S, Bellemans J, Nozaki H, Whiteside LA, Harman M, Hodge Wa. Knee motion during maximum flexion in fixed and mobile-bearing arthroplasties. *Clin Orthop Relat Res.* 410: 131-138. 2002.

[39] Dennis DA, Komistek RD, Colwell CE Jr, Ranawat CS, Scott RD, Thornhill TS, Lapp MA. In vivo anteroposterior femorotibial translation of total knee arthroplasty: a multicenter analysis. *Clin Orthop Relat Res.* 410: 114-130. 2003.

[40] Dennis DA, Komistek RD, Mahfouz MR, Walker SA, Tucker A. A multicenter analysis of axial femorotibial rotation after total knee arthroplasty. *Clin Orthop Relat Res*. 428: 180-189. 2004.

[41] D'Lima DD, Trice M, Urquhart AG, Colwell CW Jr. Tibiofemoral conformality and kinematics of rotating-bearing knee prostheses. *Clin Orthop Relat Res.* 386: 235-242. 2001.

[42] Dennis DA, Komistek RD, Mahfouz MR, Outten JT, Sharma A. Mobile-bearing total knee arthroplasty: do the polyethylene bearings rotate? *Clin Orthop Relat Res.* 440: 88-95. 2005.

[43] Dennis DA, Komistek RD, Walker SA, Cheal EJ, Stiehl JB. Femoral condylar lift-of in total knee arthroplasty. *J Bone Joint Surg Br*. 83:33-39. 2001.

[44] Scuderi GR, Komistek RD, Dennis DA, Insall JN. The impact of femoral component rotational alignment on condylar lift-off. *Clin Orthop Relat Res.*

[45] Stiehl JB, Dennis DA, Komistek RD, Crane HS. In vivo determination of condylar lift-off and screw-home in a mobile-bearing total knee arthroplasty. *J Arthroplasty*. 14:293-299. 1999.

[46] Bartel DL, Burstein AH, Toda MD, Edwards DL. The effect of conformity and plastic thickness on contact stress in metal backed plastic implants. *J Bone Joint Surg Am.* 68:1041-1051. 1986.

[47] Blunn GW, Walker PS, Joshi A., Hardinge K. the dominance of cyclic sliding in producing wear in total knee replacements. *Clin Orthop Relat Res.* 273: 253-260. 1991.

[48] Blunn GW, Joshi AB, Minns RJ, Lidgren L. Lilley P. Ryd L, Engrelbrecht E, Walker PS. Wear in retrieved Condylar Knee Arthroplasties, A comparison of wear in different designs of 280 retrieved condylar knee prostheses. *J Arthroplasty*. 12(3): 281-291.

[49] Rawlinson JJ, Furman BD, Li S, Wright TM, Bartel DL. Retrieval, experimental, and computational assessment of the performance of total knee replacements. *J Ortho Res*. Jul; 24(7):1384-94. 2006.

[50] Edidin AA, Jewett CW, Kalinowski A, Kwarteng K, Kurtz SM. Degradation of mechanical behavior in UHMWPE after natural and accelerated aging. *Biomaterials*. 21: 1451-1460. 2000.

[51] Walker PS, Blunn GW, Broome DR. A knee simulating machine for performance evaluation of total knee replacements. *J Biomechanics*. 30: 83-389. 1997.

[52] Burgess IC, Kolar M, Cunningham JL, Unsworth A. Development of a six station knee wear simulator and preliminary wear results. *Proc Inst Mech Eng[H]*. 211:1451-1460. 1997.

[53] Fregly BJ, Sawyer WG, Harman MK, Banks SA. Computational wear prediction of a total knee replacement from in vivo kinematics. *J Biomechanics.* 38:305-314. 2005.

[54] Hoshino A, Fukuoka Y, Ishida A. Accurate in vivo measurement of polyethylene wear in total knee arthroplasty. J Arthroplasty. 17(4):490-6. 2002.

[55] Sanzen L, Sahlstrom A, Gentz CF, Johnell IR. Radiographic wear assessment in a total knee prosthesis. 5- to 9-year follow-up study of 158 knees. *J Arthroplasty.* 11(6):738-42. 1996.

[56] Kellett CF, Short A, Price A, Gill HS, Murray DW. In vivo measurement of total knee wear. *The Knee*. 11: 183-187. 2004.

[57] Gill HS, Waite JC, Short A, Kellett CF, Price AJ, Murray DW. In vivo measurement of volumetric wear of a total knee replacement. Knee. 13(4):312-7. 2006

[58] Price AJ, Short A, Kellett C, Beard D, Gill H, Pandit H, Dodd CA, Murray DW. Ten-year in vivo wear measurement of a fully congruent mobile bearing unicompartmental knee arthroplasty. J Bone Joint Surg Br. 87(11):1493-7. 2005.

[59] Mahfouz MR, Merkl BC, Kuhn MJ, Stiehl JB, Komistek RD. Method to measure implanted hip separation from two dimensional x-ray fluoroscopy images using novel gradient-based Hough transform. Scientific Exibit SE16. 2006 AAOS Annual Meeting, San Diego, CA.

[60] Delport HP, Banks SA, De Schepper J, Bellemans J. A kinematic comparison of fixed- and mobile-bearing knee replacements. *J Bone Joint Surg Br.* 88(8):1016-21. 2006.

[61] Fehring TK, Murphy JA, Hayes TD, Roberts DW, Pomeroy DL, Griffin WL. Factors Influencing Wear and Osteolysis in Press-Fit Condylar Modular Total Knee Replacements. *Clin Orthop Relat Res*. 428:40-50. 2004.

[62] Horowitz SM, Gonzales JB. Inflammatory response to implant particulates in a macrophage/osteoblast coculture model. *Calcified Tissue Int*. 59:392-396. 1996.

[63] Hirashima Y, Ishiguro N, Kondo S, Iwata H. Osteoclast induction from bone marrow cells is due to pro-inflammatory mediators from macrophages exposed to polyethylene particles: a possible mechanism of osteolysis in failed THA. *J Biomed Mater Res.* 56(2):177-83. 2001.

[64] Stewart T, Jin ZM, Shaw D, Auger DD, Stone M, Fisher J. Experimental and theoretical study of the contact mechanics of five total knee joint replacements. Proc Inst Mech Engr. Vol. 209: 225-231, 1995.

[65] Jin ZM, Stewart T, Auger DD, Dowson D, Fisher J. Contact pressure prediction in total knee replacements Part 2: application to the design of total knee replacements. Proc Inst Mech Engr. Vol. 209: 9-15, 1995.

[66] D'Lima DD, Chen PC, Colwell CW. Polyethylene Contact Stresses, Articular Congruity, and Knee Alignment. Clin Orthop. 393:232-238, 2001.

[67] Bristol RE, Fitzpatrick DC, Brown TD, Callaghan JJ. Non-uniformity of contact stress on polyethylene inserts in total knee arthroplasty. Clinical Biomechanics. Vol 11, No 2: 75-80; 1996.

[68] Buechel FF, Pappas MJ, Makris G. Evaluation of Contact Stress in Metal-Backed Patellar Replacements A Predictor of Survivorship. Clin Orthop. 273:190-197, 1991.

[69] Rostoker W, Galante JO. Contact Pressure Dependence of Wear Rates of Ultra High Molecular Weight Polyethylene. Journal of Biomedical Materials Research. 13: 957-964, 1979.

[70] Komistek RD, Kane TR, Mahfouz MR, Ochoa JA, Dennis DA. Knee mechanics: a review of past and present techniques to determine in vivo loads. *J Biomechanics*. 38: 215-228. (2005).

[71] Rydell NW. Forces acting on the femoral head-prosthesis. A study on strain gauge supplied prostheses in living persons. Acta Orthop Scand. 1966;37:Suppl 88:1-132.

[72] English TA, Kilvington M. In vivo records of hip loads using a femoral implant with telemetric output (a preliminary report). *J Biomed Eng*. 1(2):111-115. 1979.

[73] Bergmann G. Graichen F. Rohlmann A. Instrumentation of a hip joint prosthesis. In: Bergmann G, Graichen F, Rohlmann A (Eds.). Implantable Telemetry in Orthopaedics. Forshungsvermittlung der Freien universitat, Berlin, 35-63.

[74] Graichen F, Bergmann G, Rohlmann A. Inductively powered telemetry system for in vivo measurement with orthopedic implants. In: Cristalli, Amlaner, Neuman (Eds.), Thirteenth International Symposium on Biotelemetry, Williamsburg, Vol. XIII: 75-80.

[75] Graichen F, Bergmann G. Four-channel telemetry system for in vivo measurement of hip joint forces. Journal of Biomedical Engineering 13, 370-374, 1991.

[76] Bergmann G, Graichen F, Rohlmann A, Verdonschot N, van Lenthe GH. Frictional heating of total hip implants. Part 1. measurements in patients. Journal of Biomechanics 34;421-428, 2001.

[77] Bergmann G. Hip Joint Loading During Walking and Running Measured in Two Patients, Journal of Biomechanics 26 (8): 969-990, 1993.

[78] Bergman G, Graichen F, Rohlmann, A, Verdonschot N, van Lenthe GH. Frictional heating of total hip implants. Part 1. measurements in patients. Journal of Biomechanics 34: 421-428, 2001.

[79] Kotzar GM, Davy DT, Goldberg VM, Heiple KG, Gerilla J, Heiple KG Jr, Brown RH, Burstein AH. Telemeterized In Vivo Hip Joint Force Data: A Report on Two Patients After Total Hip Surgery. Journal of Orthopaedic Research 9 (5): 621-633, 1989.

[80] Davy DT, Kotzar GM, Brown RH, Heiple KG, Goldberg VM, Heiple KG Jr., Berilla J, Burstein AH. Telemetric Force Measurements Across the Hip after Total Arthroplasty. Journal of Bone and Joint Surgery 70-A (1): 45-50, 1988.

[81] Bassey, EJ, Littlewood, JJ, Taylor, SJG, 1997. Relations between compressive axial forces in an instrumented massive femoral implant, ground reaction forces, and integrated electromyographs from vastus lateralis during various osteogenic exercises. J. Biomechanics 30, 213–223.

[82] Taylor, SJG., Walker, PS, 2001. Forces and moments telemetered from two distal femoral replacements during various activities. J. Biomechanics 839–848.

[83] Taylor, SJG., Walker, PS, Perry, JS, Cannon SR, Woledge, R, 1998. The forces in the distal femur and the knee during walking and other activities measured by telemetry. J. Arthroplasty 13, 428–437.

[84] Taylor, SJG., Walker, PS, 2001. Forces and moments telemetered from two distal femoral replacements during various activities. J. Biomechanics 839–848.

[85] Kaufman KR, Kovacevic N, Irby SE, Colwell CW. Instrumented Implant for Measuring Tibiofemoral Forces. J. Biomechanics Vol. 29. No 5: 667-671, 1996.

[86] Morris BA, D'Lima DD, Llamin J, Kovacevic N, Arms SW, Townsend CP, Colwell CW. e-Knee: Evolution of the Electronic Knee Prosthesis Telemetry Technology Development. J Bone Joint Surg Am. Vol. 83A. Supplement 2, Part 1. 62-66, 2001.

[87] D'Lima DD, Townsend CP, Arms SW, Morris BA, Colwell CW. An implantable telemetry device to measure intra-articular tibial forces. J Biomechanics (38) 299-304, 2005.

[88] D'Lima DD, Shantanu P, Steklov N, Slamin JE, Colwell CW. Tibial forces measured in vivo after total knee arthroplasty. *J Arthroplasty*. 21(2): 255-262. 2006.

[89] Pan T, Hyman D Mehregany M, Reshotko E, Garverick S. Microfabricated shear stress sensors, part 1: design and fabrication. AIAA Journal. 37(1):66-72. 1999.

[90] Hymand D, Pan T Reshotko E, Mehregany M. Microfabricated shear stress sensors, part 2: testing and calibration. AIAA Journal. 37(1):73-78. 1999.

[91] Zhe J, Modi V, Farmer KR. A microfabricated wall shear-stress sensor with capacitative sensing. Journal of Microelectromechanical Systems 14(1):167-175. 2005.

[92] Lofdahl L, Gad-el-Hak M. MEMS-based pressure and shear stress sensors for turbulent flows. Meas. Sci. Technol. 10:665-686. 1999.

[93] Krantz D, Belk J, Biermann PJ, Dubow J, Gause LW, Harjani R, Mantell S, Polla D, Troyk P. Project Update: Applied Research on Remotely-Queried Embedded Microsensors. http://www.mts.com/aesd/pdf/SSM99PAPER.pdf

[94] Hautamaki C, Zurn S, Mantell SC, Poll DL. Experimental Evaluation of MEMS Strain Sensors Embedded in Composites. Journal of Microelectromechanical Systems. Vol 8 No 3, 272-279, 1999.

[95] Cao L, Kim TS, Mantell SC, Polla DL. Simulation and fabrication of piezoresistive membrane type MEMS strain sensors. Sensors and Actuators. 80:273-279, 2000.

[96] Cao L, Kim TS, Ahou J, Mantell SC, Polla DL. Calibration technique for MEMS membrane type strain sensors. University/Government/Industry Microelectronics Symposium, 1999. Proceedings of the Thirteenth Biennial ,20-23 June 1999. 204–210.

[97] Hsieh MC, Fang YK, Ju M, Chen G, Ho J, Yang CH, Wu PM, Wu GS, Chen TY. A contact-type piezoresistive microshear stress sensor for above-knee prosthesis application. IEEE Journal of Microelectromechanical Systems. 10(1):121-127. 2001.

[98] Gagg, JE Jr. Silicon Pressure Sensor. United States Patent 4,317,126. 1982.

[99] Monk DJ, Kim SW, Jung K, Gogoi B, Bitko G, McDonald B, Maudie TA, Mahadevan D. Micro electro-mechanical system sensor with selective encapsulation and method therefore. United States Patent Number 6,401,545. 2002.

[100] Bitko G, Mcneil A, Frank R. Improving the MEMS Pressure Sensor. Sensors, Vol 17 No 7, 2000.

[101] Gogoi BP, Mladenovic, D. Integration Technology for MEMS Automotive Sensors. IECON 02 [Industrial Electronics Society, IEEE 2002 28th Annual Conference of the] , Volume: 4 , 5-8 Nov. 2002 Pages:2712 - 2717

[102] Leger TJ; Johnston DA; Wolff M, High spatial resolution MEMS surface pressure sensor array for transonic compressor IGV measurement. Instrumentation in Aerospace Simulation Facilities, 2001. 19th International Congress on ICIASF 2001 , 27-30 Aug. 2001, 231 – 239.

[103] Tanielian MH; Kim NP. Pressure belt: an integrated multisensor system. Sensors, 2002. Proceedings of IEEE , Volume: 2 , 12-14 June 2002 pp:1182 - 1187 vol.2.

[104] Lin L, Yun W. MEMS pressure sensors for aerospace applications. Aerospace Conference, 1998. Proceedings., IEEE , Volume: 1 , 21-28 March 1998 pp:429 - 436 vol.1.

[105] Mohan, A.; Malshe, A.P.; Aravamudhan, S.; Bhansali, S.; Piezoresistive MEMS pressure sensor and packaging for harsh oceanic environment. Electronic Components and Technology, 2004. ECTC '04. Proceedings , Volume: 1 , 1-4 June 2004 pp:948 - 950 Vol.1.

[106] Lin L, Pisano AP, Howe RT. A Micro Strain Gauge with Mechanical Amplifier. Journal Of Microelectromechanical Systems, Vol. 6, No. 4, December 1997, pp 313-321.

[107] Wojciechowski KE; Boser BE; Pisano AP. A MEMS resonant strain sensor with 33 nano-strain resolution in a 10 kHz bandwidth. Sensors, 2005 IEEE. 30 Oct.-3 Nov. 2005.

[108] Gianchandani YB. Khalil N. Bent-Beam Strain Sensors. J. Microelectromechanical Systems. 5(1):52-58. 1996.

[109] Chu LL, Que L, Gianchandani YB. Measurements of material properties using differential capacitive strain sensors. *J Microelectromechanical Systems*. 11(5):489-497. 2002.

[110] Kane BJ, Cutkosky MR, Kovacs GTA, A Traction Stress Sensor Array for Use in High-Resolution Robotic Tactile Imaging. Journal Of Microelectromechanical Systems, Vol. 9, N0. 4, Dec 2000. 425-433.

[111] Engel J, Chen J, Liu C. Development of polyimide flexible tactile sensor skin. Journal of Micromechanics and Microengineering. 13:359-366. 2003.

[112] Chu Z, Sarro PM, Middelhoek S. Silicon three-axial tactile sensor. Sens. Actuators A 54:505-510. 1996.

[113] Someya T, Kato Y, Sekitani T, Iba S, Noguchi Y, Murase Y, Kawaguchi, H, Sakurai T. Conformable, flexible, large-area networks of pressure and thermal sensors with organic transistor active matrixes. Proceedings National Academy of Sciences. 102(35):12321-12325. 2005.

[114] Kawaguchi H, Someya T, Sekitani T, Sakuarai T. Cut-and-paste customization of organic FET integrated circuit and its application to electronic artificial skin. IEEE Journal of Solid-State Circuits. 40(1):177-185. 2005.

[115] Troyk PR, DeMichele GA. Inductively-Coupled Power and Data Link for Neural Prostheses using a Class-E Oscillator and FSK Modulation. Proceedings of the 25th Annual International Conference of the IEEE EMBS, Cancun, Mexico September 17-21, 2003. 3376-3375.

[116] Wentworth SM. Fundamentals of Electromagnetics with Engineering Applications. Hoboken, NJ. John Wiley & Sons, Inc. 2005.

[117] Kasap SO. Principles of Electronic Materials and Devices, Third Edition. Boston. McGraw-Hill. 2006.

[118] Binns KJ, Lawrenson PJ. Analysis and Computation of Electric and Magnetic Field Problems. Oxford. Pergamon Press, Ltd. 1973.

[119] Schwarz HA. Über einige Abbildungsaufgaben. *J. Reine Angew. Math.* 70, 105. 1869.

[120] Christoffel EB. Sul Problema delle Temperature Stazionarie e la Rappresentazione di una Data Superficie. *Anna. Mat. Pura Appl.* 1, 95. 1867.

[121] Schinzinger R, Laura PAA. Conformal Mapping: Methods and Applications. Mineola, NY. Dover. 2003.

[122] Gibbs WJ Conformal Transformations in Electrical Engineering. London. Chapman and Hall, Ltd. 1958.

[123] Driscoll TA, Trefethen LN. Schwarz-Christoffel Mapping. Cambridge, U.K. Cambridge University Press. 2002.

[124] Maxwell JC. Treatise on Electricity and Magnetism. Dover Publications, Inc. New York. 1891.

[125] Harsanyi G. Polymer Films in Sensor Applications. CRC Press. Boca Raton, Fl. 1995.

[126] Halloran JP, Petrella AJ, Rullkoetter PJ. Explicit finite element modeling of total knee replacement mechanics. J. Biomechanics. vol. 28, pp. 323-331. 2005

[127] Ishikawa H, Fujiki H, Yasuda K. Contact Analysis of Ultrahigh molecular weight polyethylene articular plate in artificial knee joint during gait movement," J. Biomech. Eng. vol. 118, pp. 377-386. 1996.

[128] Coventor software reference manual. Coventor, Inc. Cary, NC.

[129] Specialty Coating Systems. Parylene Knowledge> Discovery/History. Retrieved September 16, 2007, from http://www.scscoatings.com/parylene_knowledge/history.aspx

APPENDIX

Appendix A



(12) **United States Patent**
Evans, III et al.

(10) **Patent No.: US 7,097,662 B2**
(45) **Date of Patent: Aug. 29, 2006**

(54) **IN-VIVO ORTHOPEDIC IMPLANT DIAGNOSTIC DEVICE FOR SENSING LOAD, WEAR, AND INFECTION**

(75) Inventors: **Boyd McCutchen Evans, III**, Oak Ridge, TN (US); **Thomas G. Thundat**, Knoxville, TN (US); **Richard D. Komistek**, Knoxville, TN (US); **Douglas A. Dennis**, Littleton, CO (US); **Mohamed Mahfouz**, Knoxville, TN (US)

(73) Assignees: **UT-Battelle, LLC**, Oak Ridge, TN (US); **University of Tennessee Research Foundation**, Knoxville, TN (US)

(*) Notice: Subject to any disclaimer, the term of this patent is extended or adjusted under 35 U.S.C. 154(b) by 148 days.

(21) Appl. No.: **10/926,216**

(22) Filed: **Aug. 25, 2004**

(65) **Prior Publication Data**

US 2006/0047283 A1 Mar. 2, 2006

(51) **Int. Cl.**
A61F 2/30 (2006.01)

(52) **U.S. Cl.** **623/18.11**; 623/914

(58) **Field of Classification Search** 623/18.11, 623/17.13, 912, 914, 20.21, 20.14, 20.32, 623/22.11
See application file for complete search history.

(56) **References Cited**

U.S. PATENT DOCUMENTS

3,915,015	A *	10/1975	Crane et al.	73/865.4
4,503,705	A *	3/1985	Polchaninoff	73/172
4,822,362	A	4/1989	Walker et al.	
5,197,488	A *	3/1993	Kovacevic	600/595
5,326,363	A *	7/1994	Aikins	623/18.11
5,360,016	A *	11/1994	Kovacevic	600/595
5,425,775	A *	6/1995	Kovacevic et al.	128/898
5,456,724	A *	10/1995	Yen et al.	623/23.49
5,470,354	A *	11/1995	Hershberger et al.	128/898
5,719,324	A	2/1998	Thundat et al.	
5,733,292	A *	3/1998	Gustilo et al.	606/88
5,777,467	A	7/1998	Arms et al.	
5,840,047	A *	11/1998	Stedham	600/587
6,034,296	A *	3/2000	Elvin et al.	623/16.11
6,143,035	A *	11/2000	McDowell	623/22.11
6,245,109	B1 *	6/2001	Mendes et al.	623/18.11
6,523,392	B1	2/2003	Porter et al.	
6,553,681	B1 *	4/2003	Ekholm et al.	33/551
6,567,703	B1 *	5/2003	Thompson et al.	607/60
6,573,706	B1	6/2003	Mendes et al.	
6,583,630	B1	6/2003	Mendes et al.	
6,610,096	B1 *	8/2003	MacDonald	623/18.11
6,706,005	B1 *	3/2004	Roy et al.	600/594
2002/0102743	A1	8/2002	Majumdar et al.	
2002/0130673	A1 *	9/2002	Pelrine et al.	324/727
2003/0069644	A1 *	4/2003	Kovacevic et al.	623/20.32
2004/0019384	A1 *	1/2004	Kirking et al.	623/20.14

(Continued)

OTHER PUBLICATIONS

P.F. Sharkey et al., "Why are Total Knee Anthroplasties Failing Today?," Clin Orthop, 2002, pp. 7-13, vol. 404.

(Continued)

Primary Examiner—Alvin J. Stewart
(74) *Attorney, Agent, or Firm*—Kirk A. Wilson

(57) **ABSTRACT**

A device for providing in vivo diagnostics of loads, wear, and infection in orthopedic implants having at least one load sensor associated with the implant, at least one temperature sensor associated with the implant, at least one vibration sensor associated with the implant, and at least one signal processing device operatively coupled with the sensors. The signal processing device is operable to receive the output signal from the sensors and transmit a signal corresponding with the output signal.

31 Claims, 6 Drawing Sheets

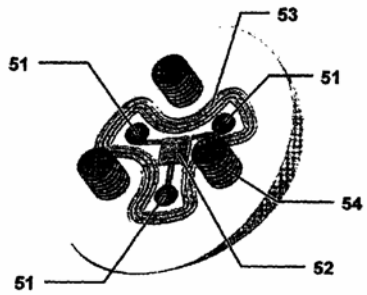

U.S. PATENT DOCUMENTS

2004/0080319	A1	4/2004	Merrill	
2005/0010302	A1*	1/2005	Dietz et al.	623/20.21
2005/0165317	A1*	7/2005	Turner et al.	600/486
2005/0273170	A1*	12/2005	Navarro et al.	623/17.13
2006/0004431	A1*	1/2006	Fuller et al.	607/116

OTHER PUBLICATIONS

T. K. Fehring, et al., "Early Failures in Total Knee Orthoplasty," Clin Orthop, 2001, pp. 315-318, vol. 382.

J. F. Brick, et al., The Patellofemoral Component of Total Knee Arthroplasty , Clin Orthop, 1988, pp. 163-178, vol. 231.

G. Bergmann, et al., "Hip Joint Loading During Walking and Running Measured in Two Patients," J of Biomechanics, 1993, pp. 969-990, vol. 26, Issue 8.

G. Bergman, et al., "Frictional Heating of Total Hip Implants, Part I Measurements in Patients" J of Biomechanics, 2001, pp. 421-428, vol. 34.

G. M. Kotzar, et al., "Telemeterized In Vivo Hip Joint Force Data: A Report on Two Patients After Total Hip Surgery," J of Ortho Research, 1989, pp. 621-633, vol. 9, Issue 5.

D. T. Davy, et al., "Telemetric Force Measurements Across the Hip after Total Arthroplasty," J of Bone and Joint Surgery, 1988, pp. 45-50, vol. 70-A, Issue 1.

K. R. Kaufman, et al., Instrumented Implant for Measuring Tibiofemoral Forces, J of Biomechanics, 1996, pp. 667-671, vol. 29, Issue 5.

S. J. G. Taylor, et al., "Forces and Moments Telemetered from Two Distal Femoral Replacement During Various Activities," J of Biomech, 2001, pp. 839-848, vol. 34.

* cited by examiner

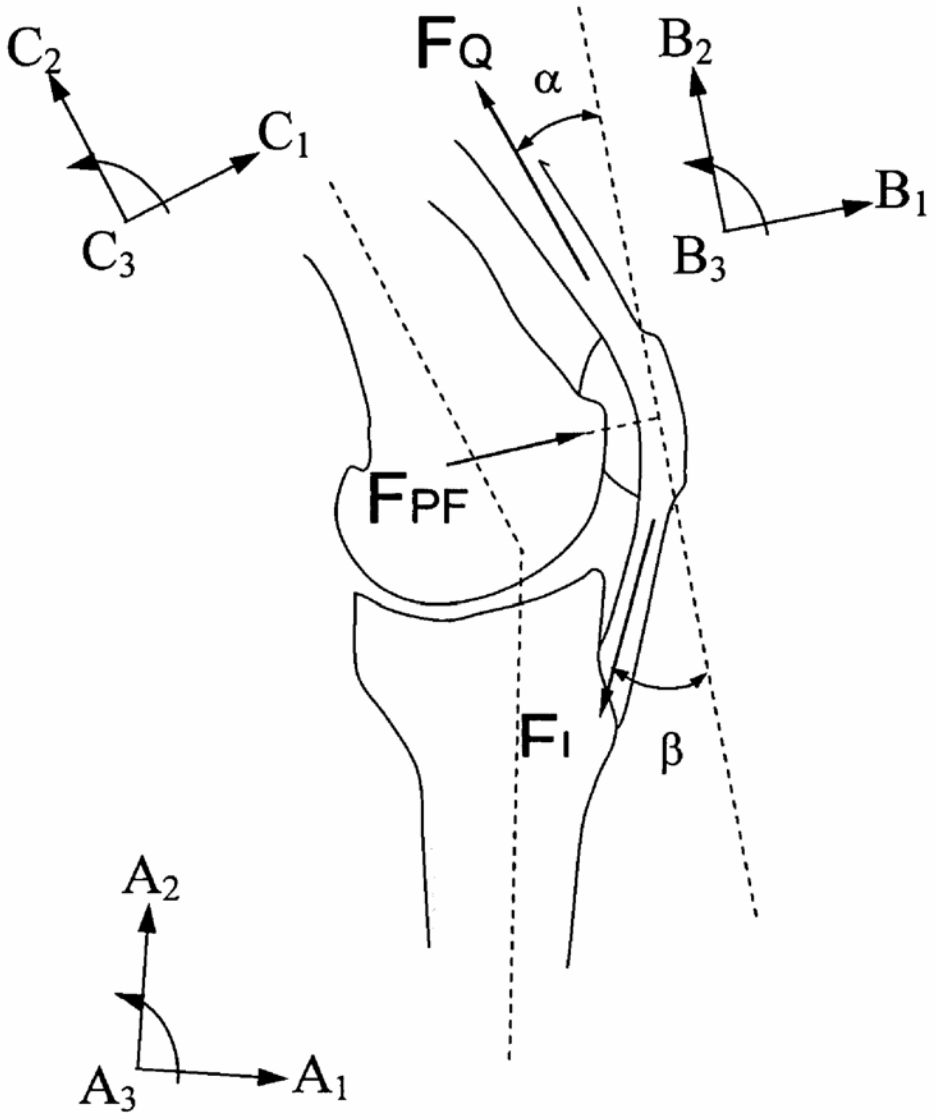

Fig. 1

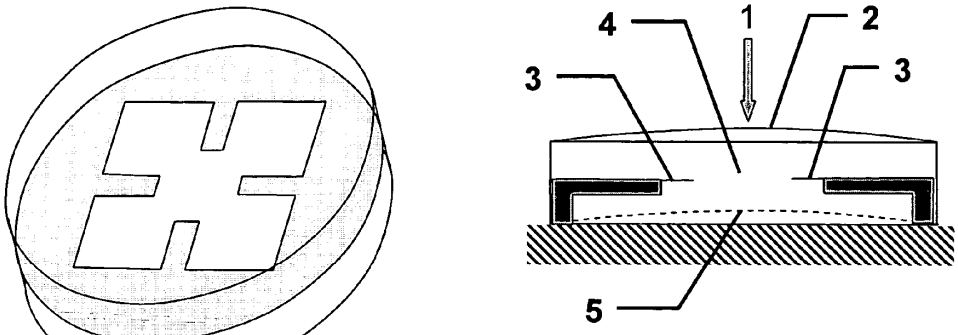

Fig. 2

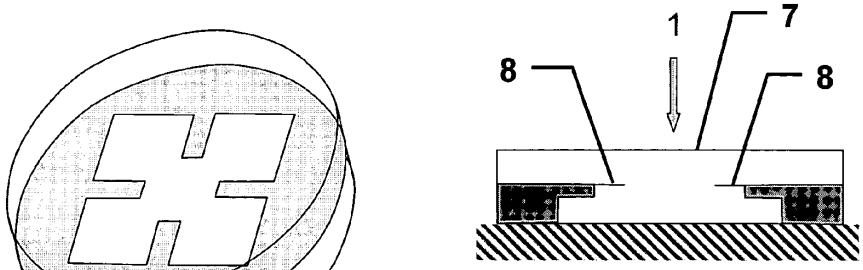

Fig. 3

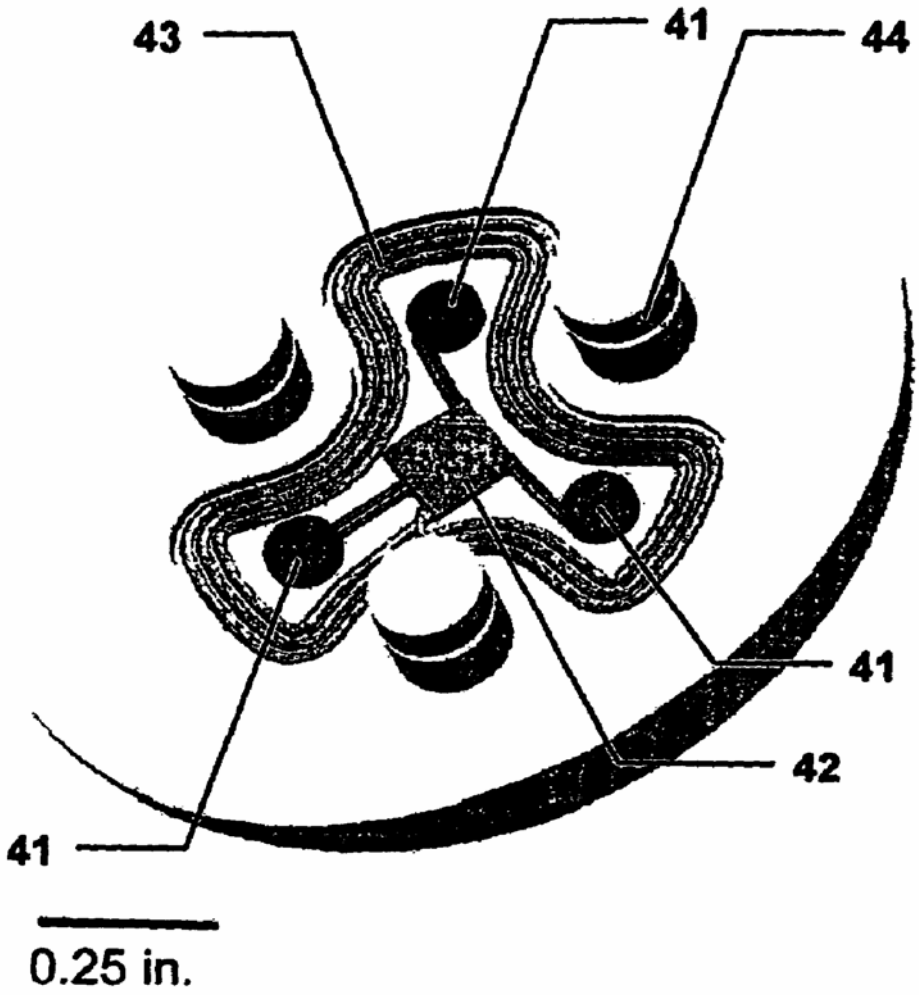

Fig. 4

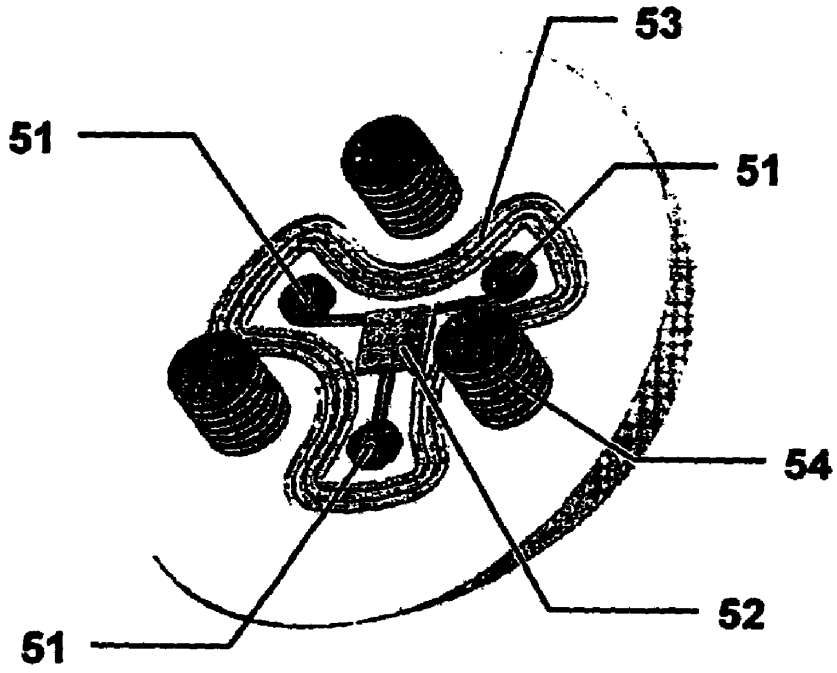

Fig. 5

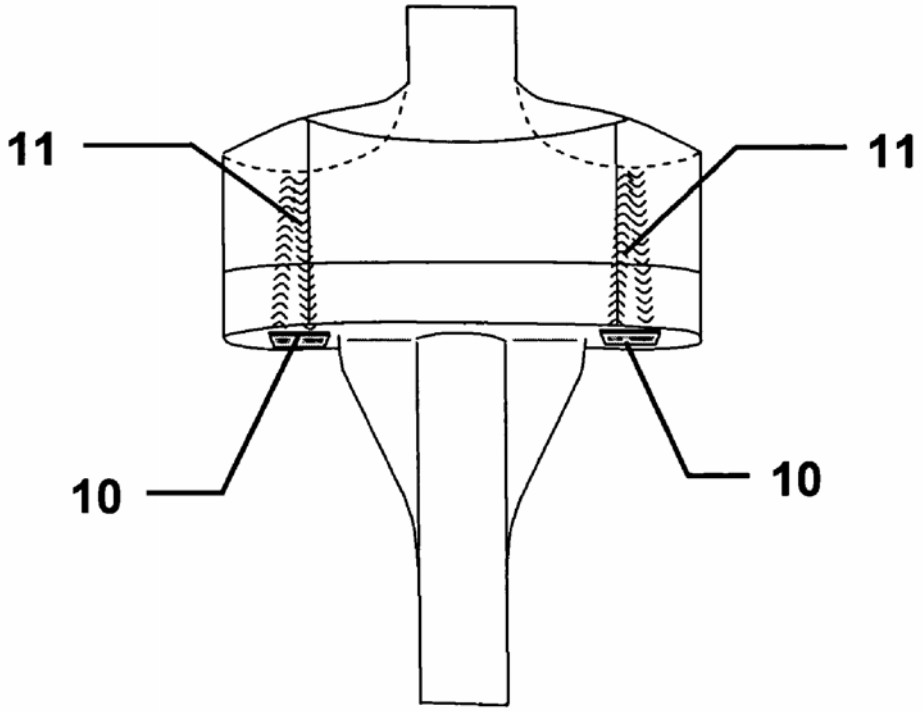

Fig. 6

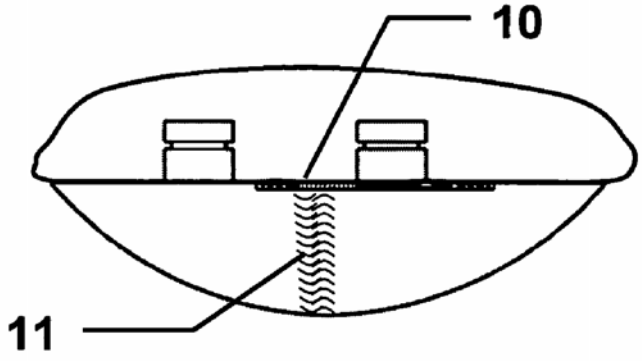

Fig. 7

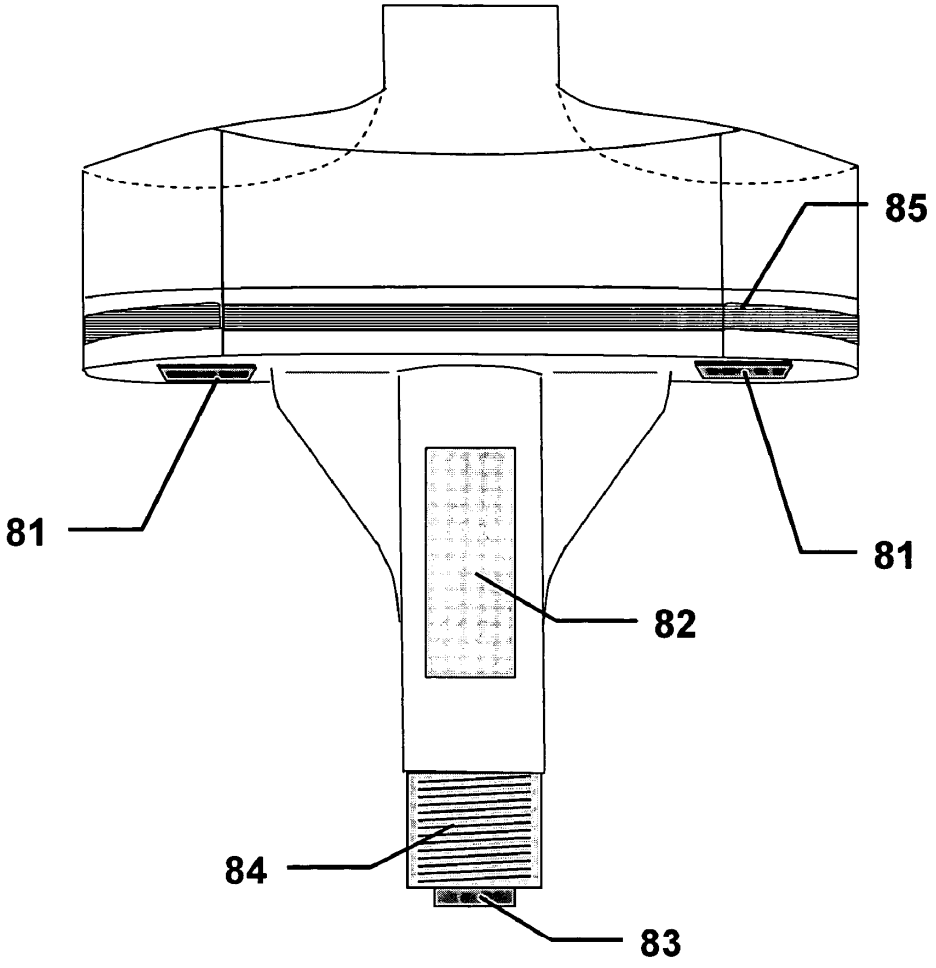

Fig. 8

IN-VIVO ORTHOPEDIC IMPLANT DIAGNOSTIC DEVICE FOR SENSING LOAD, WEAR, AND INFECTION

STATEMENT REGARDING FEDERALLY SPONSORED RESEARCH

This invention was made with Government support under Contract No. DE-AC05-00OR22725 awarded to UT-Battelle, LLC, by the U.S. Department of Energy. The Government has certain rights in this invention.

TECHNICAL FIELD

This invention relates to diagnostic medical instruments and procedures, and more particularly to implantable devices and methods for monitoring physiological parameters.

DESCRIPTION OF THE BACKGROUND ART

The procedure of replacing knee joints affected by osteoarthritis and other disease originated in the early 1960's. The success rate of this procedure improved tremendously in the following decades. However, there are an estimated 22,000 knee replacements revised yearly. Revision in other joint replacement surgery is common as well. There is still the need to improve the mechanical aspects and wear characteristics of the knee prosthesis, such that regardless of the age of the patient, any prosthesis will be expected to last a lifetime. The need also exists to improve the tools with which physicians can perform diagnostics on implanted devices in the general patient.

Much of the problem in designing prosthesis for the total knee arthroplasty (TKA) procedure lies in the fact that there is almost no in vivo data on the load conditions available. Much of the data that is available is derived from mathematical models or cadaver studies. A very limited amount of data is available using instrumented implants. There are concerns about the reliability of modeling data due to the inability to verify the modeling data with actual data and it is difficult to produce the forces and motions existing in a human using a cadaver. Most of the systems that have been used to collect data on living humans have been used on a small number of subjects and therefore the applicability of this data to a large population is questionable, and these systems have not been designed for use in a large number of devices over a long period of time, or to be manufactured on a commercial basis.

Complications resulting from patellofemoral resurfacing have been attributed as many as half of all revision total knee arthroplasties (TKA). Most complications are caused by errors in surgical technique, poor prosthetic design, or excessive patellofemoral loads of up to seven or eight times body weight during certain activities such as squatting. In many cases, however, poor knee kinematics and an inadequate understanding of the forces exerted on the prosthetic components play a key role in the wear, mal-alignment, or design flaws associated with the complications described below.

Patellofemoral complications are a prominent cause of failure in TKA. The most common TKA complication is patellofemoral subluxation (dislocation of the patella to either the medial or lateral side of the knee), which occurs in up to 29 percent of some series, resulting in patellofemoral pain and crepitus, component wear, failure, loosening and/or fracture. Other complications that lead to patellar component failure are malposition of the femoral, tibial or patellar components, poor implant design, patellar fracture, mal-alignment, inadequate patellar resection, avascular necrosis, and revision TKA.

Such complications induce many surgeons to avoid patellar resurfacing in patients with osteoarthritis and good remaining articular cartilage. However, several studies indicate increased patellofemoral problems without resurfacing, and secondary resurfacing after primary TKA with a failed nonresurfaced patella has proven inferior to resurfacing at the time of primary TKA.

In a 2002 review of all (212) revisions at one institution between 1997 and 2000, Sharkey et al. attributed early failures to infection (25.4%), loosening (16.9%), instability (21.2%), extensor mechanism deficiency (6.6%), avascular necrosis of the patella (4.2%), and isolated patella resurfacing (0.9%). The prevalent causes of overall failure were polyethylene wear (25%), aseptic loosening (24.1%), instability (21.2%), infection (17.5%), arthrofibrosis (14.6%), malalignment (11.8%), extensor mechanism deficiency (6.6%), patella necrosis (4.2%), periprosthetic fracture (2.8%), and the need to resurface the patella (0.9%). Malalignment was present in 11.8% of all implants requiring revision. Fehring, et al, in a survey of 440 patients, found similar results. These studies did not report patella-femoral complications individually, however revision of the patella-femoral component has been reported in as many as 50% of revisions.

Instrumentation of orthopedic implants has been performed by a few researchers on a small number of patients to measure the loads between the mating components. Most of this research has been performed on hip prosthesis instrumented with strain gages. G. Bergman has published research on hip loading using forces measured using strain gages. His instrumented prosthesis is powered using an inductive coil, and the measurements are sent to a personal computer using an RF telemetry system. The power for this system is generated using an inductive coil worn around the patient's leg during testing. Bergman reported loads from two patients. His data showed that joint loads range from 2.8 times body weight (BW) to 4.8 BW depending on walking speeds. These loads increased to 5.5 BW with jogging, and stumbling caused hip loads to go as high as 7.2 BW.

Similar research on hip implants has been performed by Davy and Kotzar. A similar hip prosthesis was implanted in two patients. Davy and Kotzar measured peak loads of 2.1–2.8 BW during gait and a maximum value of 5.5 BW during periods of instability during single leg stance.

K R Kaufman has reported on the design of an instrumented tibial component of TKA knee prosthesis. This device consists of a specially machined tibial tray. The tibial tray is hollowed out in Kaufman's research to form a diaphragm which is instrumented with strain gages. This device is used to determine the tibiofemoral loads. No reference as to power source or data collection method is given. We are unaware of any data collected or published using this device.

Taylor and Walker measured the forces in the distal femur in two subjects with an instrumented distal femoral replacement (DFR). The DFR was instrumented with strain gages and as in other devices inductive coupling was used to power the implant. The DFR is a large prosthesis which replaces the majority of the femur. The forces measured were as high as 3.6 BW for jogging. This device was capable of measuring the axial torque on the femur. Bending moments were greatest about the antero-posterior axis (varus-valgus) at 9.8 BW-cm.

Post-operative infection is a particularly serious threat occurring in total joint replacement and organ transplant procedures. In a survey of joint replacement surgeries performed at the Mayo Clinic in the years 1969–1996, deep wound infection (DWI) occurred in 2% of 16,035 primary total knee arthroplasty (TKA) and 1.3% of 23,519 total hip arthroplasty (THA) patients. Patients that develop DWI are at serious risk for loss of limb/organ or mortality. The estimated cost of treating post-surgical infections in orthopedic procedures alone is over $340,000,000 per year (Hansen 1999).

Recent drug-discovery research has focused on a new method of producing oligonucleotides called aptamers. These short (15–30 base) single-stranded, oligonucleotides are more stable than antibodies. Aptamers have protein recognition and binding characteristics similar to antibodies, and can be engineered to target virtually any molecule. Drug discovery researchers have examined using aptamers to aid the immune system in recognizing foreign invaders in a method similar to antibodies.

Research using instrumented implants has been fairly limited as shown in the preceding paragraphs. The research that has been done has been performed to gain an understanding of joint loading conditions has consisted of on a statistically small population. The number of patients and data gathered is given to illustrate the variation in data and statistically small population. The following paragraphs will discuss recent patents in this field.

U.S. Pat. No. 6,706,005 to Roy et al., issued on Mar. 16, 2004, teaches a device for measuring only loads incident on the device using microcantilevers. No teaching of load derivation, temperature measurement, or infection sensing is present.

U.S. Pat. No. 5,470,354 with inventors Hershberger; Troy W. (Warsaw, Ind.); Booth, Jr.; Robert E. assigned to Biomet, Inc. describes a device and a method for determining proper alignment and placement of implant components during joint reconstruction surgery. This patent is primarily aimed for use in the knee joint. Provisional components are often used in joint replacement surgery to determine the proper sizes and relationships of the final components used in joint arthroplasty. In this patent, provisional components are instrumented with force transducers. These transducers are used to determine the forces in the joint and to aid in determining the proper size component and how to balance the forces in the joint. Force transducers are connected to computers and provide readings of the location and magnitude of the forces generated in the joint when the joint is moved through its range of motion during surgery. Therefore, this system is utilized for Intraoperative assessment but is not of value in assessing in vivo, weight-bearing loads after total knee implantation.

U.S. Pat. Nos. 5,360,016 and 5,197,488 invented by Nebojsa Kovacevic is assigned to NK Biotechnical Engineering Company. This patent describes a force transducer for a joint prosthesis. The transducer in this patent is similar to the one described in the research paper published by Kaufman and Kovacevic in 1996. The transducer in this paper is a highly modified tibial tray TKA component. A series of cavities are machined on the superior side of the tibial tray such that they become flexible members. Strain gages are attached to each flexure member to provide a signal corresponding to the force applied to the flexure member. No mention is made of supply power, signal conditioning, or data collection.

U.S. Pat. No. 5,425,775 issued to Kovacevic; Nebojsa (Plymouth, Minn.) and assigned to NK Biotechnical Engineering Company Nov. 2, 1993 describes a method and apparatus for measuring the forces acting on a patella includes a patella sensor comprising a sensor, a sensor cover, and multiple strain gages. This sensor consists of a significantly modified patellar insert, similar to U.S. Pat. Nos. 5,360,016 and 5,197,488 by Kovacevic for a tibial tray force transducer. This system consists of a large metal diaphragm (sensor cover) or deformable member covering the entire diameter of the patellar implant. The sensor cover is attached to the sensor and has an outer surface that is in contact with a femoral insert. The sensor cover transmits the forces acting on its outer surface to the sensor. The sensor has a plurality of strain gages mounted thereon to measure the forces acting on the sensor cover. A requirement of this sensor is a metal-backed patellar prosthesis which has been shown in multiple studies in the orthopedic literature to have inferior long term clinical results and relatively high complication rates. It also seems a requirement that a larger amount of material be resected from the patient's patella than would be with a traditional patellar insert. No mention is made of how an entire measurement system from signal conditioning to operating power is derived for this sensor. No examples of use of this device or similar devices were found in the research literature.

U.S. Pat. No. 4,822,362 Walker; Peter S. (Weston, Mass.); Ewald; Frederick C. (Weston) A prosthesis and a surgical procedure (process) therefore are provided having a relatively thin plate fitted to a resected portion of the tibial plateau with the plate fitting uniformly around a major portion of the calcareous bone of the cortical wall. A pin on the under side of the plate aligned substantially with the axis of the intramedullary canal of the tibia fixes the plate against transverse relative motion between the plate and plateau, and blades or keels also on the under side of the plate are aligned maximum density (strength) of the cancellous bone of the plateau and fix the plate against rotation relative to the plateau. The surgical procedure of the invention employs a template to assure approximate positioning, and exact interrelationship between the plate and the fixing means.

References cited and herein incorporated by reference are:

1. Sharkey P F, Hozack W J, Rothman R H, Shastri S, Jacoby S M., "Why are total knee arthroplasties failing today?", *Clin Orthop* 404: 7–13, 2002.
2. Fehring T K, Odum S, Griffin G L, Mason J B, Nadaud M., "Early Failures in Total Knee Orthoplasty", *Clin Orthop* 382: 315–318, 2001.
3. Brick J F, Gutmann L., "The patellofemoral component of total knee arthroplasty", *Clin Orthop* 231: 163–178, 1988.
4. Bergmann G, Graichen F, Rohlmann A., "Hip Joint Loading During Walking and Running Measured in Two Patients", Journal of Biomechanics 26 (8): 969–990, 1993.
5. Bergman G, Graichen F, Rohlmann, A, Verdonschot N, van Lenthe G H. Frictional heating of total hip implants. Part 1. measurements in patients. Journal of Biomechanics 34: 421–428, 2001.
6. Kotzar G M, Davy D T, Goldberg V M, Heiple K G, Gerilla J, Heiple K G Jr, Brown R H, Burstein A H. Telemeterized In Vivo Hip Joint Force Data: A Report on Two Patients After Total Hip Surgery. Journal of Orthopaedic Research 9 (5): 621–633, 1989.
7. Davy D T, Kotzar G M, Brown R H, Heiple K G, Goldberg V M, Heiple K G Jr., Berilla J, Burstein A H. Telemetric Force Measurements Across the Hip after Total Arthroplasty. Journal of Bone and Joint Surgery 70-A (1): 45–50, 1988.

8. Kaufman K R, Kovacevic N, Irby S E, Colwell C W. Instrumented Implant for Measuring Tibiofemoral Forces. Journal of Biomechanics. 29 (5): 667–671, 1996.
9. Taylor S J G, Walker P S. Forces and Moments Telemetered from Two Distal Femoral Replacements During Various Activities. Journal of Biomechanics 34: 839–848, 2001.
10. U.S. Pat. No. 5,470,354. Force sensing apparatus and method for orthopaedic joint reconstruction. Inventors: Hershberger; Troy W. (Warsaw, Ind.); Booth, Jr.; Robert E. Assignee: Biomet, Inc.
11. U.S. Pat. No. 5,360,016 Force transducer for a joint prosthesis. Inventor: Nebojsa Kovacevic Assignee: NK Biotechnical Engineering Company. Nov. 1, 1994.
12. U.S. Pat. No. 5,197,488 Knee joint load measuring instrument and joint prosthesis Inventor: Nebojsa Kovacevic Assignee: NK Biotechnical Engineering Company. Mar. 30, 1993.
13. U.S. Pat. No. 5,425,775. Method for measuring patellofemoral forces. Inventor: Nebojsa Kovacevic Assignee: NK Biotechnical Engineering Company. Mar. 30, 1993.
14. U.S. Pat. No. 4,822,362 Process and apparatus for tibial plateau compenent Inventors: Walker; Peter S. (Weston, Mass.) and Ewald; Frederick C. (Weston, Mass.).
15. U.S. Pat. No. 6,706,005 Apparatus and method for assessing loads on adjacent bones; issued Mar. 16, 2004 to Roy et al.

SUMMARY OF THE INVENTION

This invention is a sensor system for use in orthopedic devices. The sensor suite allows the external monitoring of the forces between the orthopedic or other medical devices and the patient, the force or pressure between a joint replacement component and the underlying bone, the forces internal to the medical device, the amount of wear of the orthopedic device, the vibrational characteristics of the medical device, frictional heating, and internal infection. Examples of medical devices with which this invention can be used consist of, but are not limited to the following: the tibial, femoral, or patellar components used in total knee replacement, the femoral or acetabular components used in total hip implants, the scapular or humeral components in shoulder replacement, the tibia and talus in ankle replacement, and between the vertebral bodies in the lumbar and cervical spine disk replacements. Monitoring the forces in the joint will allow the manufacturers of implants to better understand the kinematics of the joint and develop more reliable implants. Data from in vivo sensing elements will provide accurate boundary conditions for mathematical models the affected joint. Also, this invention will allow the clinician to perform in vivo monitoring and diagnostics of orthopedic and other implants for the general patient in order to understand the effects of load magnitude, load imbalance, wear, and the presence of infection.

The invention consists of a series of a microscopic sensing element or elements fabricated using semiconductor or MEMS (microelectromechanical systems) fabrication technology. One embodiment of these sensors is an array of microcantilevers sensing elements. The sensor is self-powered using piezoelectric elements or externally powered by either electromagnetic induction, radio frequency (RF) induction or batteries. The sensor uses RF technology or other means to remotely transmit data. A passive version exists in which RFID technology is used to passively power the device and transmit the data. In the most robust embodiment of this sensor, the sensor package also incorporates a vibration sensing element, a temperature sensing element, a chemical sensing element, and an ultrasonic transmitter-receiver in the electronics package. These elements allow for the determination of the presence of infection and the determination of the thickness of the bearing surface of the implant. Other embodiments of the sensor elements are available for sensing different loads including piezoelectric sensing elements and double supported microbeam technology.

One embodiment of the device provides in vivo diagnostics of loads, wear, and infection in orthopedic implants. The device has at least one load sensor associated with the implant for generating an output signal in response to and indicative of normal and transverse loads being applied to the implant; and at least one temperature sensor associated with the implant for generating an output signal in response to and indicative of a temperature proximate said implant; and at least one vibration sensor associated with the implant for generating an output signal in response to and indicative of a vibration proximate the implant; and at least one signal processing device operatively coupled with at least one load, temperature, and vibration sensor and being operable to receive output signals from at least one load, temperature, and vibration sensor and to transmit a signal corresponding with the output signal.

BRIEF DESCRIPTION OF THE DRAWINGS

FIG. **1** is a force diagram showing the three force system acting on the patella.

FIG. **2** is an illustration of a curved embodiment of the micro load cell using encapsulant stiffness for tuning.

FIG. **3** is an illustration of a non-curved embodiment of the micro load cell using packaging stiffness for tuning.

FIG. **4** is a schematic diagram of an externally powered load cell.

FIG. **5** is a schematic diagram of a self-powered load cell.

FIG. **6** is an illustration of an ultrasonic device in patellar prosthesis.

FIG. **7** is an illustration of an ultrasonic device in a tibial prosthesis.

FIG. **8** is an illustration of a self-powered diagnostic device in a tibial prosthesis.

DETAILED DESCRIPTION OF THE PREFERRED EMBODIMENTS

This invention measures the forces and pressures existing between the human body or limb and prosthetic implants. A further advantage is to measure the patellofemoral bearing surface forces including forces in the coronal and saggital planes of the limb. Another advantage of this invention is to measure the wear in orthopedic prosthesis. A further advantage of this invention is to measure indicators of infection in orthopedic implants. Yet another advantage of this invention is to measure the vibration characteristics of orthopedic implants. Another advantage of this invention is to measure frictional heating in orthopedic implants. The advantages of this invention are accomplished by the novel application of micromachined cantilever or "simply-supported" beams. These beams have been shown to provide response to each of the previously mentioned advantages. Microcantilever beams are uniquely applicable to these measurement scenarios due to their small size, ease of determining measured quantity, and low power consumption. The patellar resurfacing prosthesis is used to illustrate this invention, however the concepts set forth in the patellar prosthesis are easily

8. Kaufman K R, Kovacevic N, Irby S E, Colwell C W. Instrumented Implant for Measuring Tibiofemoral Forces. Journal of Biomechanics. 29 (5): 667–671, 1996.
9. Taylor S J G, Walker P S. Forces and Moments Telemetered from Two Distal Femoral Replacements During Various Activities. Journal of Biomechanics 34: 839–848, 2001.
10. U.S. Pat. No. 5,470,354. Force sensing apparatus and method for orthopaedic joint reconstruction. Inventors: Hershberger; Troy W. (Warsaw, Ind.); Booth, Jr.; Robert E. Assignee: Biomet, Inc.
11. U.S. Pat. No. 5,360,016 Force transducer for a joint prosthesis. Inventor: Nebojsa Kovacevic Assignee: NK Biotechnical Engineering Company. Nov. 1, 1994.
12. U.S. Pat. No. 5,197,488 Knee joint load measuring instrument and joint prosthesis Inventor: Nebojsa Kovacevic Assignee: NK Biotechnical Engineering Company. Mar. 30, 1993.
13. U.S. Pat. No. 5,425,775. Method for measuring patellofemoral forces. Inventor: Nebojsa Kovacevic Assignee: NK Biotechnical Engineering Company. Mar. 30, 1993.
14. U.S. Pat. No. 4,822,362 Process and apparatus for tibial plateau compenent Inventors: Walker; Peter S. (Weston, Mass.) and Ewald; Frederick C. (Weston, Mass.).
15. U.S. Pat. No. 6,706,005 Apparatus and method for assessing loads on adjacent bones; issued Mar. 16, 2004 to Roy et al.

SUMMARY OF THE INVENTION

This invention is a sensor system for use in orthopedic devices. The sensor suite allows the external monitoring of the forces between the orthopedic or other medical devices and the patient, the force or pressure between a joint replacement component and the underlying bone, the forces internal to the medical device, the amount of wear of the orthopedic device, the vibrational characteristics of the medical device, frictional heating, and internal infection. Examples of medical devices with which this invention can be used consist of, but are not limited to the following: the tibial, femoral, or patellar components used in total knee replacement, the femoral or acetabular components used in total hip implants, the scapular or humeral components in shoulder replacement, the tibia and talus in ankle replacement, and between the vertebral bodies in the lumbar and cervical spine disk replacements. Monitoring the forces in the joint will allow the manufacturers of implants to better understand the kinematics of the joint and develop more reliable implants. Data from in vivo sensing elements will provide accurate boundary conditions for mathematical models the affected joint. Also, this invention will allow the clinician to perform in vivo monitoring and diagnostics of orthopedic and other implants for the general patient in order to understand the effects of load magnitude, load imbalance, wear, and the presence of infection.

The invention consists of a series of a microscopic sensing element or elements fabricated using semiconductor or MEMS (microelectromechanical systems) fabrication technology. One embodiment of these sensors is an array of microcantilevers sensing elements. The sensor is self-powered using piezoelectric elements or externally powered by either electromagnetic induction, radio frequency (RF) induction or batteries. The sensor uses RF technology or other means to remotely transmit data. A passive version exists in which RFID technology is used to passively power the device and transmit the data. In the most robust embodiment of this sensor, the sensor package also incorporates a vibration sensing element, a temperature sensing element, a chemical sensing element, and an ultrasonic transmitter-receiver in the electronics package. These elements allow for the determination of the presence of infection and the determination of the thickness of the bearing surface of the implant. Other embodiments of the sensor elements are available for sensing different loads including piezoelectric sensing elements and double supported microbeam technology.

One embodiment of the device provides in vivo diagnostics of loads, wear, and infection in orthopedic implants. The device has at least one load sensor associated with the implant for generating an output signal in response to and indicative of normal and transverse loads being applied to the implant; and at least one temperature sensor associated with the implant for generating an output signal in response to and indicative of a temperature proximate said implant; and at least one vibration sensor associated with the implant for generating an output signal in response to and indicative of a vibration proximate the implant; and at least one signal processing device operatively coupled with at least one load, temperature, and vibration sensor and being operable to receive output signals from at least one load, temperature, and vibration sensor and to transmit a signal corresponding with the output signal.

BRIEF DESCRIPTION OF THE DRAWINGS

FIG. **1** is a force diagram showing the three force system acting on the patella.

FIG. **2** is an illustration of a curved embodiment of the micro load cell using encapsulant stiffness for tuning.

FIG. **3** is an illustration of a non-curved embodiment of the micro load cell using packaging stiffness for tuning.

FIG. **4** is a schematic diagram of an externally powered load cell.

FIG. **5** is a schematic diagram of a self-powered load cell.

FIG. **6** is an illustration of an ultrasonic device in patellar prosthesis.

FIG. **7** is an illustration of an ultrasonic device in a tibial prosthesis.

FIG. **8** is an illustration of a self-powered diagnostic device in a tibial prosthesis.

DETAILED DESCRIPTION OF THE PREFERRED EMBODIMENTS

This invention measures the forces and pressures existing between the human body or limb and prosthetic implants. A further advantage is to measure the patellofemoral bearing surface forces including forces in the coronal and saggital planes of the limb. Another advantage of this invention is to measure the wear in orthopedic prosthesis. A further advantage of this invention is to measure indicators of infection in orthopedic implants. Yet another advantage of this invention is to measure the vibration characteristics of orthopedic implants. Another advantage of this invention is to measure frictional heating in orthopedic implants. The advantages of this invention are accomplished by the novel application of micromachined cantilever or "simply-supported" beams. These beams have been shown to provide response to each of the previously mentioned advantages. Microcantilever beams are uniquely applicable to these measurement scenarios due to their small size, ease of determining measured quantity, and low power consumption. The patellar resurfacing prosthesis is used to illustrate this invention, however the concepts set forth in the patellar prosthesis are easily

utilized in a hip, shoulder, tibial or femoral components of the TKA prosthesis, or other orthopedic devices and prosthesis.

In the manner in which this sensor is applied to the patellar prosthesis, not only will the forces between the prosthesis and the underlying patellar bone be measured, but tibiofemoral forces can be deduced as well as the muscle forces from the quadriceps and the force in the patellar tendon will be determined as well. This is because the patella has a system of three forces acting on it. These forces are the force supplied by the quadriceps, the reaction force supplied by the patellar tendon, and the bearing surface interaction force between the patella and the femur. Measurement of one of these forces allows solution of the other two forces. The ability to measure muscle forces in the human body has eluded the researcher for centuries. The three force system of forces in the patella and the equations for solving those forces are illustrated in FIG. **1**.

The equations for solving the forces are:

$$F_{PF} = F_Q \sin(\alpha) + F_L \sin(\beta)$$

$$F_Q \cos(\alpha) = F_L \cos(\beta)$$

$$F_Q = \frac{F_{PF}}{\sin(\alpha) + \cos(\beta)\tan(\alpha)}$$

$$F_L = \frac{F_{PF}}{\sin(\beta) + \cos(\alpha)\tan(\beta)}$$

where F_Q represents the quadriceps force, F_L represents the patellar ligament force, and F_{PF} represents the patellofemoral contact force. Frames A, B, and C are reference frames commonly used in dynamical modeling. The A frame represents the orientation of the tibia, the B frame represents the orientation of the patella, and the C frame represents the orientation of the femur. α represents the angle between the B_2 axis and the quadriceps tendon and specifies the direction of the quadriceps force. β represents the angle between the patellar ligament and the B_2 axis and specifies the direction of the force between the tibia and the patella. The patellofemoral joint reaction force is assumed to be along the B_1 axis.

The load measuring device in this invention is configured not only to measure the normal patello-femoral bearing surface loads, i.e. the normal pressure internal to the implant, but also measures the transverse load (or pressure) which in the case of the patella is indicative of muscle imbalance, malalignment, and potential subluxation. This invention feature is distinct from prior load measuring devices that incorporate only a single sensor capable of measuring the forces in a single direction. In the case of an instrumented tibial tray, the variation of the load over the sensor is indicative of the alignment, muscle/ligament imbalance, improper mechanics, etc. Even in the spine, it is beneficial to measure the load in multiple directions or locations.

Several methods are available for detecting the motion of the microcantilever beam. Common methods of measuring this motion are based on the application of specific coatings to the surface of the cantilever beams. These can be piezoresistive coatings whose resistance changes as a function of bending or piezoelectric coatings which emit charge when the beam undergoes a dynamic load. Another common method of determining the beam bending is to use the cantilever beam itself as one of the plates in a parallel plate capacitor and correlating the change in capacitance with deflection. Other methods are available for measuring this deflection, such as optical methods, but the previously mentioned methods are the most suited to this application at this time.

For measuring the forces in the patella, the beams may be encapsulated in an intermediate package, or otherwise attached to the surface of the prosthesis. In the preferred embodiment, the beams are encapsulated in a polymer or elastomeric material. This intermediate material can be used to "tune" the response of the device such that the optimum response range of the microcantilever device corresponds to the load range expected in the experimental conditions. The polymer material has a slight convex side and a slight concave side to improve the transmittal of forces through the package. This package is mounted between the surface of the prosthesis and the naturally occurring bone. FIG. **2** shows a diagram of this embodiment. A load **1** imposed on the concave surface **2** of a load cell is sensed by a microcantilever sensor **3** disposed in an encapsulant **4**. The load cell also has a concave surface **5**. The load cell uses at least one microcantilever sensor in the sensor suite. A single array or multiple arrays of sensors can also be used.

Another embodiment shown in FIG. **3** illustrates a micro load cell package using no convex or concave surfaces, but relies on the use of a stiffer packaging material **7** to support the cantilevers around the outside, such that there is a differential strain towards the center of the device. A load **1** imposed on the packaging material **7** disposed around a microcantilever sensor **8** is sensed by the load cell. The Young's modulus (stiffness) E of the packaging material **7** is used to tune the response of the micro load cell and is greater than the stiffness E of the internal components. This packaging scheme would possibly be preferred in environments where the package itself might be surrounded with cement or other adhesive in an uncontrolled manner, thereby negating the effects of the concave and convex surfaces. This package is on the order of three millimeters in diameter and a millimeter or less in height, and amounts to the equivalent of a micro load cell.

Another advantage of this invention is to measure the wear existing in orthopedic implants. This invention performs this task by incorporating an ultrasonic transmitter and receiver in its signal processing chip as shown in FIGS. **6** and **7**. The ultrasonic transmitter/receiver is in the form of a piezoelectric material incorporated in the ultrasonic transceiver element **10**. A burst of ultrasonic energy **11** is emitted and received allowing the thickness of the wear surface to be measured by measuring the time for the energy to reflect off of the back surface or surfaces of the material. In the preferred embodiment a single element is utilized as the transmitter and the receiver, another embodiment is to use different elements. Also in the preferred embodiment, the transducer/receiver is fabricated from piezoelectric material using surface micromachining techniques, and an alternative embodiment is to use surface micromachined capacitive structures as resonant cavities to produce and receive the ultrasonic energy. The principles of ultrasonic thickness measurement rely on knowing the speed of sound in a material. Equation 1 shows the relationship between the thickness of the material of interest, d, the bulk modulus of the material of interest, B, the density of the material, ρ_0, and the time between the emission and reception of the pulse of acoustic energy.

utilized in a hip, shoulder, tibial or femoral components of the TKA prosthesis, or other orthopedic devices and prosthesis.

In the manner in which this sensor is applied to the patellar prosthesis, not only will the forces between the prosthesis and the underlying patellar bone be measured, but tibiofemoral forces can be deduced as well as the muscle forces from the quadriceps and the force in the patellar tendon will be determined as well. This is because the patella has a system of three forces acting on it. These forces are the force supplied by the quadriceps, the reaction force supplied by the patellar tendon, and the bearing surface interaction force between the patella and the femur. Measurement of one of these forces allows solution of the other two forces. The ability to measure muscle forces in the human body has eluded the researcher for centuries. The three force system of forces in the patella and the equations for solving those forces are illustrated in FIG. **1**.

The equations for solving the forces are:

$$F_{PF} = F_Q \sin(\alpha) + F_L \sin(\beta)$$

$$F_Q \cos(\alpha) = F_L \cos(\beta)$$

$$F_Q = \frac{F_{PF}}{\sin(\alpha) + \cos(\beta)\tan(\alpha)}$$

$$F_L = \frac{F_{PF}}{\sin(\beta) + \cos(\alpha)\tan(\beta)}$$

where F_Q represents the quadriceps force, F_L represents the patellar ligament force, and F_{PF} represents the patellofemoral contact force. Frames A, B, and C are reference frames commonly used in dynamical modeling. The A frame represents the orientation of the tibia, the B frame represents the orientation of the patella, and the C frame represents the orientation of the femur. α represents the angle between the B_2 axis and the quadriceps tendon and specifies the direction of the quadriceps force. β represents the angle between the patellar ligament and the B_2 axis and specifies the direction of the force between the tibia and the patella. The patellofemoral joint reaction force is assumed to be along the B_1 axis.

The load measuring device in this invention is configured not only to measure the normal patello-femoral bearing surface loads, i.e. the normal pressure internal to the implant, but also measures the transverse load (or pressure) which in the case of the patella is indicative of muscle imbalance, malalignment, and potential subluxation. This invention feature is distinct from prior load measuring devices that incorporate only a single sensor capable of measuring the forces in a single direction. In the case of an instrumented tibial tray, the variation of the load over the sensor is indicative of the alignment, muscle/ligament imbalance, improper mechanics, etc. Even in the spine, it is beneficial to measure the load in multiple directions or locations.

Several methods are available for detecting the motion of the microcantilever beam. Common methods of measuring this motion are based on the application of specific coatings to the surface of the cantilever beams. These can be piezoresistive coatings whose resistance changes as a function of bending or piezoelectric coatings which emit charge when the beam undergoes a dynamic load. Another common method of determining the beam bending is to use the cantilever beam itself as one of the plates in a parallel plate capacitor and correlating the change in capacitance with deflection. Other methods are available for measuring this deflection, such as optical methods, but the previously mentioned methods are the most suited to this application at this time.

For measuring the forces in the patella, the beams may be encapsulated in an intermediate package, or otherwise attached to the surface of the prosthesis. In the preferred embodiment, the beams are encapsulated in a polymer or elastomeric material. This intermediate material can be used to "tune" the response of the device such that the optimum response range of the microcantilever device corresponds to the load range expected in the experimental conditions. The polymer material has a slight convex side and a slight concave side to improve the transmittal of forces through the package. This package is mounted between the surface of the prosthesis and the naturally occurring bone. FIG. **2** shows a diagram of this embodiment. A load **1** imposed on the concave surface **2** of a load cell is sensed by a microcantilever sensor **3** disposed in an encapsulant **4**. The load cell also has a concave surface **5**. The load cell uses at least one microcantilever sensor in the sensor suite. A single array or multiple arrays of sensors can also be used.

Another embodiment shown in FIG. **3** illustrates a micro load cell package using no convex or concave surfaces, but relies on the use of a stiffer packaging material **7** to support the cantilevers around the outside, such that there is a differential strain towards the center of the device. A load **1** imposed on the packaging material **7** disposed around a microcantilever sensor **8** is sensed by the load cell. The Young's modulus (stiffness) E of the packaging material **7** is used to tune the response of the micro load cell and is greater than the stiffness E of the internal components. This packaging scheme would possibly be preferred in environments where the package itself might be surrounded with cement or other adhesive in an uncontrolled manner, thereby negating the effects of the concave and convex surfaces. This package is on the order of three millimeters in diameter and a millimeter or less in height, and amounts to the equivalent of a micro load cell.

Another advantage of this invention is to measure the wear existing in orthopedic implants. This invention performs this task by incorporating an ultrasonic transmitter and receiver in its signal processing chip as shown in FIGS. **6** and **7**. The ultrasonic transmitter/receiver is in the form of a piezoelectric material incorporated in the ultrasonic transceiver element **10**. A burst of ultrasonic energy **11** is emitted and received allowing the thickness of the wear surface to be measured by measuring the time for the energy to reflect off of the back surface or surfaces of the material. In the preferred embodiment a single element is utilized as the transmitter and the receiver, another embodiment is to use different elements. Also in the preferred embodiment, the transducer/receiver is fabricated from piezoelectric material using surface micromachining techniques, and an alternative embodiment is to use surface micromachined capacitive structures as resonant cavities to produce and receive the ultrasonic energy. The principles of ultrasonic thickness measurement rely on knowing the speed of sound in a material. Equation 1 shows the relationship between the thickness of the material of interest, d, the bulk modulus of the material of interest, B, the density of the material, ρ_0, and the time between the emission and reception of the pulse of acoustic energy.

$$d = \frac{1}{2} t \sqrt{\frac{B}{\rho_0}}$$

This aspect of the invention is illustrated in a tibial TKA component and a patellar prosthesis component as shown in FIGS. **6** and **7** respectively. In the application of the tibial tray, the preferred embodiment places the sensor package underneath the tibial tray, such that it does not interfere with the polyethylene insert of mobile bearing prosthesis. The sensor package could easily be located underneath the bearing surface in fixed bearing components, or molded into the polyethylene component as well.

Microcantilevers have been used to measure very precise changes in temperature. Often these cantilevers are coated with a material, such as gold, which causes the microcantilever to undergo bimaterial bending. A temperature sensing cantilever will be included in the prosthesis diagnostic sensor suite. Measurement of temperature of the prosthesis will give indication of the presence of conditions such as infection or noninfectious inflammatory syndromes causing joint synovitis such as rheumatoid arthritis, soft tissue impingement or friction syndromes, etc. if the patient is not currently in an active mode. The measurement of temperature can also be used to measure frictional heating of the prosthesis component. Frictional heating is another indication of wear and has been suggested as a cause in prosthesis failure.

Infection is one of the most clinically devastating complications of any major surgical procedure. Post-operative infection, clinically referred to as deep wound infection (DWI), is a particularly serious threat occurring in procedures such as total joint replacement, organ transplant, and other surgical procedures in which a foreign material is implanted into the body. The presence of the foreign material allows bacterial proliferation which is more difficult to eradicate with traditional antibiotic treatment regimens than in infections in which foreign materials are not present. Subsequently, an infected total joint replacement requires implant removal in order to eradicate the infection in a substantial percentage of cases. One of the keys of infection eradication without implant removal is early recognition of the infection. While certain bacteria grow rapidly, creating clinical signs of infection early after inoculation, others create less clinical signs making early diagnosis difficult. Any sensing device which would provide an early signal to the physician of the presence of infection would result in higher infection cure rates and less patient morbidity. Cellular signaling responses to infection are represented by changes in electrical charge caused by increases in calcium and other ions and increases in concentrations of chemical and biological attractants of macrophages, T-lymphocytes, and neutrophils. These attractants include: c-reactive proteins, activated factor XII, serotonin, and epinephrine. During the immune response to infection, macrophages produce cytokines which in turn signal the production of proteins that participate in inflammation and immune response. Four families of cytokines produced early in the immune response are tumor necrosis factor-α, interleukin-1, interleukin-6, and interferon. Other families of cytokines are also present in the immune response.

Cellular signaling is determined by incorporating microcantilevers coated with antibodies specific to biological attractant molecules and microcantilevers coated with aptameric receptors (synthetic RNA molecules or single-stranded DNA molecules) specific to cytokines (cellular signaling proteins) in tissue culture or a representative sample in which endothelial, mast, neutrofil, macrophage, and osteoblast cells are stressed by infectious agents. This invention advances the state of the art in biological sensing on several fronts through detection of multiple mechanisms of cellular signaling, increasing in the understanding of the response to infection, and the incorporation of microcantilever technology for in vivo sensing applications.

One embodiment of the invention positions the infection sensor to monitor for infection markers in the drainage tube effluent from implants and other surgical procedures. This embodiment will detect specific bacteria indicative of infection.

This invention is also beneficial in the detection of sepsis and septic shock, the leading cause of death in intensive care units. The early detection of infection and the identification of the infectious process will lead to more effective treatment of infectious processes.

FIG. **8** is an embodiment schematic of a self-powered instrumented tibia wherein a tray sensor package **81** for loads, vibrations, temperature, and infections is disposed underneath the tibial tray. A signal processor **82** is disposed in the post of the device with an intramedulary sensor package **83** disposed on the tip of the antennae **84**. The intramedulary package **83** comprises sensors for infection, temperature, and vibrations. A piezoelectric layer **85** is used to power the device.

FIG. **4** is a patellar sensor package embodiment having microcantilever sensors **41** in communication with a signal processor **42** that is powered from an induction coil **43**. Patellar studs **44** are used for mounting. The power source could be external electromagnetic induction (not shown), external radio frequency induction (not shown) or rechargeable batteries (not shown).

FIG. **5** is a patellar self-powered sensor package embodiment having microcantilever sensors **51** in communication with a signal processor **52** that is powered from an induction coil **53**. The power source could be piezoelectric stacks **54**, external electromagnetic induction (not shown), external radio frequency induction (not shown) or rechargeable batteries (not shown).

The infection sensing portion of the invention represents a significant advancement in the understanding of cellular signaling processes, and the maturation of technology for investigation of interactions between micro-electromechanical devices and organic tissue. Drug-discovery experiments have been performed using aptamers and fluorescent labeling to detect cancer cells, HIV, and indicators of other diseases, and aptamers have been suggested for the investigation of other inflammatory diseases such as rheumatoid arthritis and osteoarthritis. This invention has general application to the investigation of drug delivery and the general treatment of disease.

In order to detect the presence of infection, this invention detects the body's earliest response mechanisms to infection rather than attempting to detect specific bacterial or viral elements. An array of sensing elements determines the presence of several indicators of infection in order to have redundancy in the detection scheme. The cytokine response spectrum, or other inflammatory chemicals typically associated with infection, is measured and used to determine information about the type of infection present. The primary method of detection is using microcantilevers functionalized with aptamers or antibodies specific to several cytokine proteins or other inflammatory chemicals. These elements will detect changes in the in vivo environment, and the

presence of proteins used in cellular communications. Part of this approach is based on microcantilever sensing technologies and use microcantilever arrays coated with cytokine receptors to detect the concentration of cytokines.

This invention uses aptamer nucleotides and antibodies with affinities to cytokines. In the case of aptamers, functional groups may be added to these aptamers to promote binding to microcantilever substrates, and a series of nucleotides combined with linking elements are used. C-reactive protein antibodies may also be used as a general indicator of pro-inflammatory cytokines. An array of microcantilevers is functionalized with the c-reactive protein antibodies and DNA aptamer materials. The response of these arrays is characterized and calibrated using known quantities of cytokine proteins.

These arrays of microcantilevers are utilized for in vitro tissue culture experiments in which endothelial, mast, neutrofil, macrophage, osteoblast, and osteoclast cells are stressed by common bacterial and viral infectious agents (*Staphylococcus epidermidis, Staphylococcus aureus, Peptostreptococcus* sp., *Proteus* sp., *Escherechia coli, Enerococcus,* Hepatitis B and C virus, etc.). The cytokine response of the various cellular signaling agents is determined under the controlled in vitro conditions. This invention also provides information on the compatibility of the sensors with biological materials.

Effective packaging and communication of biological information to processing elements is necessary; however these requirements are not as strict as they would be for longer term implantation. The packaging contains the sensing elements, provides physical protection, controls the diffusion of analytes, and protects the sensing elements from attack by the immune system. For this latter task, a suitable membrane is used to reduce the degradation of sensor performance by contaminants (e.g., immunoglobins) over short periods of time. Furthermore, the entire package is biocompatible.

Transmitting biosensor information to a suitable processing element is another requisite for in vivo sensing. Telemetry is a preferred mechanism for data transmission. It can be miniaturized to greatly increase user convenience. Percutaneous wires are another method for transmitting of cellular signaling information, and would be adequate for short-term testing.

A set of uncoated cantilevers is included in the sensor suite to measure vibrational forces and dynamic accelerations. The measurement of internal vibrations is used to determine if joint loosening has occurred. Early diagnosis of implant loosening is often difficult to determine from use of routine radiographs. The longer the delay in diagnosis of implant loosening, the greater the bone loss created from frictional abrasion of bone from motion of the loose components. Therefore, any sensing device which would signal early prosthetic loosening would result in bone preservation, and theoretically, higher success rates of revision total joint arthroplasty because more bone is available for revision implant fixation. The impacting of the joint components will cause large jumps in the vibration frequencies measured by this system. If the natural frequency of the prosthesis is similar to the frequencies encountered during ordinary activities, this can cause loosening of the prosthetic joint, excessive wear of the prosthetic joint and eventual failure of the prosthesis.

Several methods are available to power the sensor remotely. Remote power can be used to power the system for operation in a totally passive mode (the system only operates when a remote power source is available), or remote power coupling can be used to recharge internal batteries. In the preferred embodiment, the sensor is powered remotely using magnetic or RF induction. The analog data from the sensor will be converted to frequency and will be transmitted using a low-power RF transmitter.

A self-powered version of this system, as shown in FIG. **5**, uses a self-power generating system comprising substituting stacks **54** of piezoelectric material for the mounting studs of the patella. Layers of piezoelectric materials can also be incorporated in other orthopedic devices for self-powered applications, such as incorporating thin layers of piezoelectric material underneath the polyethylene portion of the tibial tray, as shown in FIG. **8**, or in the mounting locations of the femoral component. The forces from everyday activities are sufficient to charge a small battery or a capacitive storage system.

While there has been shown and described what are at present considered the preferred embodiments of the invention, it will be obvious to those skilled in the art that various changes and modifications can be made therein without departing from the scope.

We claim:

1. A device for providing in vivo diagnostics of loads, wear, and infection in orthopedic implants, said device comprising:

at least one load sensor associated with said implant, said at least one load sensor for generating an output signal in response to and indicative of normal and transverse loads being applied to said implant; and

at least one temperature sensor associated with said implant, said at least one temperature sensor for generating an output signal in response to and indicative of a temperature proximate said implant; and

at least one vibration sensor associated with said implant, said at least one vibration sensor for generating an output signal in response to and indicative of a vibration proximate said implant; and

at least one signal processing device operatively coupled with said at least one load, temperature, and vibration sensor, said at least one signal processing device being operable to receive said output signal from said at least one load, temperature, and vibration sensor and to transmit a signal corresponding with said output signal.

2. The device of claim **1** wherein said at least one load, temperature, and vibration sensor further comprises a microelectromechanical system.

3. The device of claim **2** wherein said microelectromechanical system further comprises at least one element selected from the group consisting of piezoelectric material, double supported microbeam, piezoresistive coating, piezoelectric coating, and parallel plate capacitor.

4. The device of claim **1** wherein said device is powered by a power supply comprising at least one device selected from the group consisting of piezoelectric elements, piezoelectric stacks, electromagnetic induction, radio frequency induction and rechargeable batteries.

5. The device of claim **1** wherein said at least one load, temperature, and vibration sensor further comprises at least one encapsulant selected from the group consisting of polymer and elastomeric material.

6. The device of claim **5** wherein said encapsulant further comprises a convex surface and a concave surface.

7. The device of claim **1** wherein said device is disposed in at least one component selected from the group consisting of tibia, fibia, femora, patella, acetabula, scapula, humera, talus, and intervertebral space.

8. The device of claim 1 wherein said signal processing device further comprises at least one transmission device selected from the group consisting of wireless telemetry and percutaneous wiring.

9. A device for providing in vivo diagnostics of loads, wear, and infection in orthopedic implants, said device comprising:

at least one load sensor associated with said implant, said at least one load sensor for generating an output signal in response to and indicative of a normal and transverse loads being applied to said implant;

at least one temperature sensor associated with said implant, said at least one temperature sensor for generating an output signal in response to and indicative of a temperature proximate said implant;

at least one vibration sensor associated with said implant, said at least one vibration sensor for generating an output signal in response to and indicative of a vibration proximate said implant;

at least one ultrasonic device associated with said implant, said at least one ultrasonic device for generating an output signal in response to and indicative of wear being imposed on said implant; and

at least one signal processing device operatively coupled with said at least one load sensor, temperature sensor, vibration sensor, and ultrasonic device, said at least one signal processing device being operable to receive said output signal from said at least one load sensor, temperature sensor, vibration sensor, and ultrasonic device and to transmit a signal corresponding with said output signal.

10. The device of claim 9 wherein said at least one load sensor, temperature sensor, vibration sensor, and ultrasonic device further comprises a microelectromechanical system.

11. The device of claim 10 wherein said microelectromechanical system further comprises at least one element selected from the group consisting of piezoelectric material, double supported microbeam, piezoresistive coating, piezoelectric coating, and parallel plate capacitor.

12. The device of claim 9 wherein said device is powered by a power supply comprising at least one device selected from the group consisting of piezoelectric elements, piezoelectric stacks, electromagnetic induction, radio frequency induction and rechargeable batteries.

13. The device of claim 9 wherein said at least one load sensor, temperature sensor, vibration sensor, and ultrasonic device further comprises at least one encapsulant selected from the group consisting of polymer and elastomeric material.

14. The device of claim 13 wherein said encapsulant further comprises a convex surface and a concave surface.

15. The device of claim 9 wherein said device is disposed in at least one component selected from the group consisting of tibia, fibia, femora, patella, acetabula, scapula, humera, talus, and intervertebral space.

16. The device of claim 9 wherein said signal processing device further comprises at least one transmission device selected from the group consisting of wireless telemetry and percutaneous wiring.

17. A device for providing in vivo diagnostics of loads, wear, and infection in orthopedic implants, said device comprising:

at least one load sensor associated with said implant, said at least one load sensor for generating an output signal in response to and indicative of a normal and transverse loads being applied to said implant; and

at least one temperature sensor associated with said implant, said at least one temperature sensor for generating an output signal in response to and indicative of a temperature proximate said implant;

at least one vibration sensor associated with said implant, said at least one vibration sensor for generating an output signal in response to and indicative of a vibration proximate said implant; and

at least one ultrasonic device associated with said implant, said at least one ultrasonic device for generating an output signal in response to and indicative of wear being imposed on said implant;

at least one chemical sensor associated with said implant, said at least one chemical sensor for generating an output signal in response to and indicative of infection proximate said implant; and

at least one signal processing device operatively coupled with said at least one load sensor, temperature sensor, vibration sensor, ultrasonic device, and chemical sensor said at least one signal processing device being operable to receive said output signal from said at least one load sensor, temperature sensor, vibration sensor, ultrasonic device, and chemical sensor and to transmit a signal corresponding with said output signal.

18. The device of claim 17 wherein said at least one load sensor, temperature sensor, vibration sensor, ultrasonic device, and chemical sensor further comprises a microelectromechanical system.

19. The device of claim 18 wherein said microelectromechanical system further comprises at least one element selected from the group consisting of piezoelectric material, double supported microbeam, piezoresistive coating, piezoelectric coating, parallel plate capacitor, antibody coating, and aptameric receptor coating.

20. The device of claim 19 wherein said antibody coating is specific to at least one attractant selected from the group consisting of c-reactive proteins, activated factor XII, serotonin, and epinephrine.

21. The device of claim 19 wherein said aptameric receptor coating is specific to at least one cytokine selected from the group consisting of tumor necrosis factor-•, interleukin-1, interleukin-6, and interferon.

22. The device of claim 17 wherein said device is powered by a power supply comprising at least one device selected from the group consisting of piezoelectric elements, piezoelectric stacks, electromagnetic induction, radio frequency induction and rechargeable batteries.

23. The device of claim 17 wherein said at least one load sensor, temperature sensor, vibration sensor, ultrasonic device, and chemical sensor further comprises at least one encapsulant selected from the group consisting of polymer and elastomeric material.

24. The device of claim 23 wherein said encapsulant further comprises a convex surface and a concave surface.

25. The device of claim 17 wherein said device is disposed in at least one component selected from the group consisting of tibia, fibia, femora, patella, acetabula, scapula, humera, talus, intervertebral space, and tissue.

26. The device of claim 17 wherein said signal processing device further comprises at least one transmission device selected from the group consisting of wireless telemetry and percutaneous wiring.

27. The device of claim 17 wherein said chemical sensor further comprises at least one bacteria sensor disposed in drainage tube effluent.

28. A method for providing in vivo diagnostics of loads, wear, and infection in orthopedic implants comprising the steps of:

positioning a sensor suite proximate an orthopedic implant, said sensor suite further comprising at least one device selected from the group consisting of load sensor, temperature sensor, vibration sensor, ultrasonic device, and chemical sensor,

powering said sensor suite for collecting and transmitting data,

analyzing said data to determine loads, wear, and infection in said orthopedic implant.

29. The method of claim 28 wherein said at least one load sensor, temperature sensor, vibration sensor, ultrasonic device, and chemical sensor further comprises a microelectromechanical system.

30. The method of claim 29 wherein said microelectromechanical system further comprises at least one element selected from the group consisting of piezoelectric material, double supported microbeam, piezoresistive coating, piezoelectric coating, parallel plate capacitor, antibody coating, and aptameric receptor coating.

31. The method of claim 30 wherein said antibody coating is specific to at least one attractant selected from the group consisting of c-reactive proteins, activated factor XII, serotonin, and epinephrine.

* * * * *

Appendix B

Computational Modeling

```
% This MATLAB m-file examines the complex mapping of a rectangular grid
% in the right hand quadrant to the exterior of a unit circle
% using the exponential transformation.
%

clear all

% Define the x-y domain:
a=3
u1=0
u2=1
v1=0
v2=pi;

% Make a grid of MxN points (x,y)
M=16
N=16
M
uv=linspace(u1,u2,M);
vv=linspace(v1,v2,N);
[u,v]=meshgrid(uv,vv);

% Create an array of colors for use plotting contours
C=colormap(jet(M));

% Plot W field
figure(1)
for R=1:M
    plot(u(R,:),v(R,:),'--','color',C(R,:),'linewidth',1.3); hold on;
    plot(u(:,R),v(:,R),'color',C(R,:),'linewidth',1.3);
end

grid on
axis([-.5 1.5 -.5 3.5])
hold off

% Define the complex variable w(z)=u+jv
w=u+j*v;

% Define the conformal mapping z=x+jy
z=exp(w);
x=real(z);
```

```
y=imag(z);

% PLOTS IN THE Z=X+JY PLANE
figure(2)
for R=1:M
    plot(x(R,:),y(R,:),'--','color',C(R,:),'linewidth',1.3); hold on;
    plot(x(:,R),y(:,R),'color',C(R,:),'linewidth',1.3);
end
axis equal
axis([-3 3 -2 4])
hold off
```

```
% This MATLAB examines the use of  conformal mapping to model the
% fringe capacitance from two infinite parallel plates. A non-fringing
% grid or field in the w plane (w=u+jv=w) is mapped
% to two non-infinite plates with fringing effects(z=x+jy).
% by considering first a rectangular domain [u1,u2,v1,v2]
% in the w=u+jv plane. The mapping function must be
% derived in a prior step.

clear all

% Define the x-y domain:
u1=-50;
u2=50;
v1=0;
v2=pi;

% Make a grid of MxN points (x,y)
M=600;
N=25;
uv=linspace(u1,u2,M);
vv=linspace(v1,v2,N);
[u,v]=meshgrid(uv,vv);

% Create an array of colors for use plotting contours
C=colormap(jet(M));

% Plot W field
figure(1)
for R=1:N
    plot(u(R,:),v(R,:),'color',C(R,:));
    hold on;
end

for R=1:M
plot(u(:,R),v(:,R),'--','color',C(R,:));
end

axis([-20 20 -1 5])
hold off

% Define the complex variable w(z)=u+jv
w=u+j*v;

% Define the conformal mapping z=x+jy
d=10; % Distance between plates
z=-d*((3*i*pi+1)/6+exp(2*w)-w)/(1*pi);
x=real(z);
y=imag(z);

% PLOTS IN THE Z=X+JY PLANE
figure(2)
for R=1:N
    plot(x(R,:),y(R,:),'color',C(R,:));
```

```
    hold on;
end

for R=1:M
    plot(x(:,R),y(:,R),'--r')%'color',C(R,:));
end

hold off
axis([-100 100 -30 30])
grid on
%axis equal

a=3.1415967
```

```
% This MATLAB examines the fringing field two semi-infinite
% parallel plates of nonequal lengths. An expression was derived
% previously using the Schwarz-Christoffel techniqe to map a
rectangular
% (w=u+jv=w)grid to the outside of two semi-infinite plates of
% non-equal length(z=x+jy).
%

clear all

% Define the x-y domain:
u1=-20*pi;
u2=20*pi;
v1=0;
v2=pi;

% Make a grid of MxN points (x,y)
M=500;
N=25;
uv=linspace(u1,u2,M);
vv=linspace(v1,v2,N);
[u,v]=meshgrid(uv,vv);

% Create an array of colors for use plotting contours
C=colormap(jet(M));

% Plot W field
figure(1)
for R=1:N
    plot(u(R,:),v(R,:),'color',C(R,:));
    hold on;
end

for R=1:M
plot(u(:,R),v(:,R),'--','color',C(R,:));
end

axis([-20 20 -1 5])
hold off

% Define the complex variable w(z)=u+jv
w=u+j*v;

% Define the conformal mapping z=x+jy
d=2; % Distance between plates
del=3.75*d/4 % Offset of lower plate
C1=(i*d-del)/(4.5+log(4)-2*i*pi);
C2=i*d/2-C1*(2.5-2*pi*i);

% PRIOR DERIVED MAPPING FUNCTION
z=C1*(.5*exp(2*w)-2*exp(w)-2*w)+C2;
%z=d*((3*i*pi+1)/6+exp(2*w)-w)/(1*pi);
x=real(z);
```

```
y=imag(z);

% PLOTS IN THE z=x+jy PLANE
figure(2)
for R=1:N
    plot(x(R,:),y(R,:),'color',C(R,:));
    hold on;
end

for R=1:M
    plot(x(:,R),y(:,R),'--r')%'color',C(R,:));
end

hold off
axis([-4 4 -4 4])
grid on
%axis equal

a=3.1415967
```

```
% This MATLAB examines the conformal mapping from electrodes in the
% same plane, and plots the fringing field. This is accomplished by
% mapping a rectangular grid to the electrodes.
%
%
clear all

% Define the conformal mapping z=x+jy

gap=200;
width=100;
a=gap/2;
b=width;

ratio=(a)./(b);
k=a/(a+b);
kp=(1-k^2)^0.5;
K=1;Kp=1;fract=1/2;
for m=0:60;
    Kold=K;
    K=K+fract^2*k.^(2*m+2);
    Kp=Kp+fract^2*kp.^(2*m+2);
    fract=fract*(2*(m+1)+1)/(2*(m+1)+2);
    check=K-Kold;
end

K=K*pi/2;
Kp=Kp*pi/2;
q=exp(-pi*Kp/K);
phi0=Kp/(2*K);

% Define the x-y domain:
u1=-K;
u2=K;
v1=-Kp;
v2=Kp;

% Make a grid of MxN points (x,y)
M=40;
N=40;
uv=linspace(u1,u2,M);
vv=linspace(v1,v2,N);
[u,v]=meshgrid(uv,vv);

% Create an array of colors for use plotting contours
C=colormap(jet(M));
D=colormap(jet(N));

% Plot W field
figure(1)
for R=1:N
    plot(u(R,:),v(R,:),'color',D(R,:));
    hold on;
```

```
end

for R=1:M
plot(u(:,R),v(:,R),'--','color',C(R,:));
end

%axis([-2 2 -1 1])
hold off

% Define the complex variable w(z)=u+jv
w=u+j*v;

snw=0;

for m=0:180
    snold=snw;
    % Function performs sn(w), Jacobian Elliptic Function
    snw=snw+q^(m+0.5)/(1-q^(2*m+1))*sin((2*m+1)*pi*w/(2*K));
    check=snw-snold;
end
check;

x=real(snw)*b/Kp;
y=imag(snw)*b/Kp;

% PLOTS IN THE z=x+jy PLANE
figure(2)
for R=1:N
    plot(x(R,:),y(R,:),'color','b')%D(R,:));
    hold on;
end

for Col=1:M
    plot(x(:,Col),y(:,Col),'--','color','r')
end

hold off
axis([-15 15 -25 25])
axis equal
```

```
% This is a Matlab m file to calculate changes in the capacitance
% between the legs of an interdigitated transducer (IDT). This
% algorithm examines the effect of changes in the electrode geometry
% due to applied loading conditions and plots the results.
% This algorithm calls the subroutine C_IDT which calculates
% the capacitance of the geometry sent.

clear all

% Define initial properties and base parameters
Gap=2.25;        % Distance between fingers (micrometers)
L=150;           % Length of fingers (micrometers)
Wth=4.75;        % Width of fingers (micrometers)
t_Au=.3;         % Thickness of fingers (micrometers)
t_par=2;         % Thickness of Parylene layer (micrometers)
t_PE=40;         % Effective Thickness of UHMW PE Layer
Ngap=58;         % Number of gaps between fingers (~# fingers * 2)
e0=8.8542e-6;    % Permeability Constant (pF/um)
ePE=2.3;         % Effective Dielectric Constant
ePar=2.95;       % Parylene Dielectric Constant
EPE=690;         % Young's Modulus Poly(MPa)
Epar=2757.9;     % Young's Modulus Parylene (MPa)
E_Au=57000;      % Young's Modulus Gold (MPa)
nu_Au=0.35; nu_PE=0.46; nu_Par=0.4; % Poisson's ratios for misc mat'ls.

% Calculation of Composite Material Properties
% Total area of representative cross section
Atotal=(Wth+Gap)*(t_Au+t_par+t_PE);

% E normal to IDT legs
Ex=(EPE*t_PE*(Wth+Gap)+Epar*(t_par-t_Au)*(Wth+Gap)+(E_Au*Epar)/...
    (Epar*Wth/(Wth+Gap)+E_Au*Gap/(Wth+Gap))*t_Au*(Wth+Gap))/Atotal;
% E parallel to IDT legs
Ey=(t_PE.*(Wth+Gap)*EPE+(t_par-t_Au).*(Wth+Gap)...
    *Epar+t_Au.*Gap.*Epar+t_Au.*Wth.*E_Au)./Atotal;

Eze=(Wth*E_Au+Gap*Epar)/(Wth+Gap);

% Composite Poisson's Ratio
nu=(nu_PE*t_PE*(Wth+Gap)+nu_Par*(t_par-t_Au)*(Wth+Gap)...
    +nu_Par*t_par*Gap+nu_Au*Wth*t_Au)/Atotal;

% Leg Length Parameter Study
P1=-1; % Load (Tension is positive, compression is negative)
L1=100:50:1000;
C1=C_IDT(Ngap,ePE,ePar,ePE,L1,t_Au,Gap,Wth);

% Change in capacitance due to y Direction Loading
epsy=P1/Ey; % Long strain

% Calculate secondary stress in electrode layer
sigy=nu*(P1/Ex)*Epar*E_Au/(Epar*Wth/(Wth+Gap)+E_Au*Gap/(Wth+Gap));
```

```
% C2_long = y direction
C2_long=C_IDT(Ngap,ePE,ePar,ePE,(L1+L1*epsy),...
    (t_Au-nu*t_Au*sigy/Eze),(Gap-Gap*sigy/Epar),(Wth-Wth*sigy/Eze));

% Change in capacitance due to x Direction Loading
sigx=(P1/Ex)*Epar*E_Au/(Epar*Wth/(Wth+Gap)+E_Au*Gap/(Wth+Gap));
C2_lat=C_IDT(Ngap,ePE,ePar,ePE,(L1-L1*nu*P1/Ey),...
    (t_Au-t_Au*nu*sigx/Eze),(Gap+Gap*sigx/Epar),...
    (Wth+Wth*sigx/Eze)); % Lat = x direction

Del_C_Long1=C1-C2_long;
Del_C_Lat1=C2_lat-C1;
nuC1=(Del_C_Lat1./Del_C_Long1).^-1;

figure(1)
subplot(2,1,1)
plot(L1,Del_C_Long1,L1,Del_C_Lat1); grid on;
%xlabel('Electrode Length (Micrometers)');
ylabel('Delta C, pF');
legend('1 MPa y Load','1 MPa x Load')
title({'Delta C vs. Electrode Length'})
subplot(2,1,2)
plot(L1,nuC1); grid on;
xlabel('Electrode Length (Micrometers)');
ylabel('Directional Sensitivity');

% Number of Gaps Parameter Study
P2=-1;
NGap2=10:1:400;
L2=500;
C2=C_IDT(NGap2,ePE,ePar,ePE,L2,t_Au,Gap,Wth);

% Calculate secondary stress in electrode layer
epsy=P1/Ey; % Long (y direction) strain
sigy=nu*(P1/Ex)*Epar*E_Au/(Epar*Wth/(Wth+Gap)+E_Au*Gap/(Wth+Gap));
C2_long=C_IDT(NGap2,ePE,ePar,ePE,(L2+L2*epsy),...
    (t_Au-t_Au*nu*sigy/Eze),(Gap-Gap*sigy/Epar),...
    (Wth-Wth*sigy/E_Au));    % Long = y direction

sigx=(P1/Ex)*Epar*E_Au/(Epar*Wth/(Wth+Gap)+E_Au*Gap/(Wth+Gap));
C2_lat=C_IDT(NGap2,ePE,ePar,ePE,(L2-L2*nu*P1/Ey),...
    (t_Au-t_Au*nu*sigx/Eze),(Gap+Gap*sigx/Epar),...
    (Wth+Wth*sigx/E_Au)); % Lat = x direction

Del_C_Long2=C2-C2_long;
Del_C_Lat2=C2_lat-C2;
nuNGap2=(Del_C_Lat2./Del_C_Long2).^-1;

figure(2)
subplot(2,1,1);plot(NGap2/2,Del_C_Long2,'b',NGap2/2,Del_C_Lat2,'g-');
%xlabel('Number of IDT Electrodes');
ylabel('Delta C, pF'); grid on;
title({'Number of IDT Electrodes vs. Delta C'});
```

```
legend('1 MPa y Load','1 MPa x Load');
subplot(2,1,2);plot(NGap2/2,nuNGap2);grid on;
xlabel('Number of IDT Electrodes');
ylabel('Directional Sensitivity');


% Pressure Parameter Study
P3a=logspace(-2,1,20);
P3=-2*P3a;
L3=500; Ngap3=30;
C3=C_IDT(Ngap3,ePE,ePar,ePE,L3,t_Au,Gap,Wth);

epsy=P3/Ey; % Long strain
% Calculate secondary stress in electrode layer
sigy=nu*(P3/Ex)*Epar*E_Au/(Epar*Wth/(Wth+Gap)+E_Au*Gap/(Wth+Gap));
C3_long=C_IDT(Ngap3,ePE,ePar,ePE,(L3+L3*epsy),...
    (t_Au-t_Au*nu*sigy/E_Au),(Gap-Gap*sigy/Epar),...
    (Wth-Wth*sigy/E_Au));    % Long = y direction

sigx=(P3/Ex)*Epar*E_Au/(Epar*Wth/(Wth+Gap)+E_Au*Gap/(Wth+Gap));
C3_lat=C_IDT(Ngap3,ePE,ePar,ePE,(L3-L3*nu*P3/Ey),...
    (t_Au-t_Au*nu*sigx/E_Au),(Gap+Gap*sigx/Epar),...
    (Wth+Wth*sigx/E_Au)); % Lat = x direction

Del_C_Long3=C3-C3_long;
Del_C_Lat3=C3_lat-C3;
nuP=(Del_C_Lat3./Del_C_Long3).^-1;

figure(3);subplot(2,1,1);
loglog(P3a,Del_C_Long3,P3a,Del_C_Lat3);grid on;
%xlabel('Applied Pressure');
ylabel('Delta C, pF');
legend('y Loading','x Loading')
title({'Applied Pressure vs. Delta C'})
subplot(2,1,2);plot(P3a,nuP);grid on;
xlabel('Applied Pressure (MPa)');ylabel('Directional Sensitivity');

% Gap Distance Parameter Study
P4=-1;
L4=L;
Gap4=0.25:0.1:8;

% Calculation of Composite Material Properties
% Total area of representative cross section
Atotal=(Wth+Gap4).*(t_Au+t_par+t_PE);

% E normal to IDT legs
Ex=(EPE.*t_PE.*(Wth+Gap4)+Epar.*(t_par-t_Au).*(Wth+Gap4)...
    +(E_Au.*Epar)./(Epar*Wth./(Wth+Gap4)+...
    E_Au*Gap4./((Wth+Gap4))).*t_Au.*(Wth+Gap4))./Atotal;

% E parallel to IDT legs
Ey=(t_PE.*(Wth+Gap4)*EPE+(t_par-t_Au).*(Wth+Gap4)*Epar+...
```

```
    t_Au.*Gap4.*Epar+t_Au.*Wth.*E_Au)./Atotal;
Eze=(Wth*E_Au+Gap4*Epar)/(Wth+Gap4);

% Composite Poisson's Ratio
nu=(nu_PE*t_PE.*(Wth+Gap4)+nu_Par.*(t_par-t_Au).*(Wth+Gap4)+...
    nu_Par.*t_par.*Gap4+nu_Au.*Wth.*t_Au)./Atotal;

C4=C_IDT(Ngap,ePE,ePar,ePE,L4,t_Au,Gap4,Wth);

epsy=P4./Ey; % y direction strain

% Calculate secondary stress in electrode layer
sigy=nu.*(P4./Ex).*Epar.*E_Au./(Epar*Wth./(Wth+Gap4)+...
    E_Au.*Gap4./(Wth+Gap4));
C4_long=C_IDT(Ngap,ePE,ePar,ePE,(L4+L4.*epsy),...
    (t_Au-t_Au.*nu.*sigy/E_Au),(Gap4-Gap4.*sigy./Epar),...
    (Wth-Wth.*sigy./E_Au));

sigx=(P4./Ex).*Epar*E_Au./(Epar*Wth./(Wth+Gap4)+E_Au*Gap4./(Wth+Gap4));
C4_lat=C_IDT(Ngap,ePE,ePar,ePE,(L4-L4.*nu.*P4./Ey),...
    (t_Au-t_Au.*nu.*sigx/E_Au),(Gap4+Gap4.*sigx./Epar),...
    (Wth+Wth*sigx/E_Au)); % Lat = x direction

Del_C_Long4=abs(C4-C4_long);
Del_C_Lat4=abs(C4_lat-C4);
nuGap=Del_C_Long4./Del_C_Lat4;


figure(4);subplot(2,1,1)
plot(Gap4,Del_C_Long4,Gap4,Del_C_Lat4);
%xlabel('Electrode Gap (micrometers)');
ylabel('Delta C, pF'); grid on;
legend('1MPa y Load','1 MPa x Load');
title({'Electrode Gap vs. Delta C'});
subplot(2,1,2); plot(Gap4,nuGap);grid on;
xlabel('Electrode Gap (micrometers)');ylabel('Directional
Sensitivity');

% Leg Width Parameter Study % [Cap] =
C_IDT(Ngap,ePE,ePar,ePE,L,th,GAP,WTH)
t_Au5=t_Au;
P5=-1;
L5=L;
Gap5=Gap;
Wth5=.1:.1:10;

% Total area of representative cross section
Atotal=(Wth5+Gap5).*(t_Au5+t_par+t_PE);
% E normal to IDT legs
Ex=(EPE.*t_PE.*(Wth5+Gap5)+Epar.*(t_par-t_Au5).*(Wth5+Gap5)+...
    (E_Au.*Epar)./(Epar.*Wth5./(Wth5+Gap5)+...
    E_Au.*Gap5./(Wth5+Gap5)).*t_Au.*(Wth5+Gap5))./Atotal;
% E parallel to IDT legs
```

```
Ey=(t_PE.*(Wth5+Gap5).*EPE+(t_par-t_Au).*(Wth5+Gap5).*Epar+...
    t_Au.*Gap5.*Epar+t_Au.*Wth5.*E_Au)./Atotal;
Eze=(Wth5.*E_Au+Gap5.*Epar)./(Wth5+Gap5);
% Composite Poisson's Ratio
nu=(nu_PE.*t_PE.*(Wth5+Gap5)+nu_Par.*(t_par-t_Au5).*(Wth5+Gap5)...
    +nu_Par.*t_par.*Gap5+nu_Au.*Wth5.*t_Au5)./Atotal;


C5=C_IDT(Ngap,ePE,ePar,ePE,L5,t_Au5,Gap5,Wth5);

epsy=P5./Ey; % Y strain
 % Calculate secondary stress in electrode layer
sigy=nu.*(P5./Ex).*Epar.*E_Au./(Epar.*Wth5./(Wth5+Gap5)+...
    E_Au.*Gap5./(Wth5+Gap5));
C5_long=C_IDT(Ngap,ePE,ePar,ePE,(L5+L5.*epsy),...
    (t_Au5-t_Au5.*nu.*sigy/E_Au),(Gap5-Gap5.*sigy./Epar),...
    (Wth5-Wth5.*sigy./E_Au));

sigx=(P5./Ex).*Epar.*E_Au./(Epar.*Wth5./(Wth5+Gap5)+E_Au.*Gap5./(Wth5+G
ap5));
C5_lat=C_IDT(Ngap,ePE,ePar,ePE,(L5-L5.*nu.*P5./Ey),...
    (t_Au5-t_Au5.*nu.*sigx/E_Au),(Gap5+Gap5.*sigx./Epar),...
    (Wth5+Wth5.*sigx./E_Au)); % Lat = x direction


Del_C_Long5=abs(C5_long-C5);
Del_C_Lat5=abs(C5_lat-C5);
nuWth5=Del_C_Long5./Del_C_Lat5;

figure(5);subplot(2,1,1)
plot(Wth5,Del_C_Long5,Wth5,Del_C_Lat5)
%xlabel('Electrode Width (micrometers)')
ylabel('Delta C, pF'); grid on;
legend('1 MPa y Load','1 MPa x Load')
title({'Delta C vs. Electrode Width'})
subplot(2,1,2); plot(Wth5,nuWth5);grid on;
xlabel('Electrode Width (micrometers)');ylabel('Directional
Sensitivity');

% Thickness Study    [Cap] = C_IDT(Ngap,ePE,ePar,ePE,L,th,GAP,WTH)
P6=-1;
L6=L;Wth6=Wth;Gap6=Gap;
t_Au6=0.1:0.25:6; t_par6=t_Au6+2;

% Calculation of Composite Material Properties
 % Total area of representative cross section
Atotal=(Wth6+Gap6).*(t_Au6+t_par6+t_PE);
% Ex = E normal to IDT legs
Ex=(EPE.*t_PE.*(Wth6+Gap6)+Epar.*(t_par6-t_Au6).*(Wth6+Gap6)+...
    (E_Au.*Epar)./(Epar.*Wth6./(Wth6+Gap6)+...
    E_Au.*Gap6./(Wth6+Gap6)).*t_Au.*(Wth6+Gap6))./Atotal;
% E parallel to IDT legs
Ey=(t_PE.*(Wth6+Gap6).*EPE+(t_par6-t_Au6).*(Wth6+Gap6).*Epar+...
```

```
    t_Au6.*Gap6.*Epar+t_Au6.*Wth6.*E_Au)./Atotal;  % E parallel to IDT
legs
Eze=(Wth6.*E_Au+Gap6.*Epar)./(Wth6+Gap6);

% Composite Poisson's Ratio
nu=(nu_PE.*t_PE.*(Wth6+Gap6)+nu_Par.*(t_par6-t_Au6).*(Wth6+Gap6)+...
    nu_Par.*t_par6.*Gap6+nu_Au.*Wth6.*t_Au6)./Atotal;

C6=C_IDT(Ngap,ePE,ePar,ePE,L6,t_Au6,Gap6,Wth6);

% Change in Capacitance Due to Longitudinal Loading
epsy=P6./Ey; % Long strain
sigy=nu.*(P6./Ex).*Epar.*E_Au./(Epar.*Wth6./(Wth6+Gap6)+...
    E_Au.*Gap6./(Wth6+Gap6)); % Calculate secondary stress in electrode
layer
C6_long=C_IDT(Ngap,ePE,ePar,ePE,(L6+L6.*epsy),...
    (t_Au6-t_Au6.*nu.*sigy./Eze),...
    (Gap6-Gap6.*sigy./Epar),(Wth6-Wth6.*sigy./Eze)); % Long = y
direction

% Change in Capacitance Due to Lateral Loading
sigx=(P6./Ex).*Epar.*E_Au./(Epar.*Wth6./(Wth6+Gap6)+E_Au.*Gap6./(Wth6+G
ap6));
C6_lat=C_IDT(Ngap,ePE,ePar,ePE,(L6-L6.*nu.*P6./Ey),...
    (t_Au6-t_Au6.*nu.*sigx./Eze),(Gap6+Gap6.*sigx./Epar),...
    (Wth6+Wth6.*sigx./Eze)); % Lat = x direction

Del_C_Long6=C6-C6_long;
Del_C_Lat6=C6_lat-C6;
nuC6=(Del_C_Lat6./Del_C_Long6).^-1;

figure(6)
subplot(2,1,1)
plot(t_Au6,Del_C_Long6,t_Au6,Del_C_Lat6); grid on;
%xlabel('Electrode Thickness (Micrometers)');
ylabel('Delta C, pF');
legend('1 MPa y Load','1 MPa x Load')
title({'Delta C vs. Electrode Thickness'})
subplot(2,1,2)
plot(t_Au6,nuC6); grid on;
xlabel('Electrode Thickness (Micrometers)');ylabel('Directional
Selectivity');
```

```
% Matlab function for calculating IDT Capacitance

function [Cap] = C_IDT(n,e1,e2,e3,L,th,a,b)
%a=gap
%b=width

e0=8.8542e-6; % pF/micrometer

ratio=(a)./(b);
k=a./(a+b);
kp=(1-k.^2).^0.5;
K=1;Kp=1;fract=1/2;
for m=0:60;
    Kold=K;
    K=fract^2*k.^(2*m+2)+K;
    Kp=fract^2*kp.^(2*m+2)+Kp;
    fract=fract*(2*(m+1)+1)/(2*(m+1)+2);
    fract_2=fract^2;
    check=K-Kold;
end

K=K*pi/2;
Kp=Kp*pi/2;
cap1=e0*((e1+e3)/2)*Kp./(K)+e0*e2*th./a;
Cap=cap1.*L.*n;
```

Vita

Boyd M. Evans III was born in the mountains of the western portion of Virginia in the late 1960's. He graduated from Cookeville High School in 1984 and attended college at Tennessee Technological University in Cookeville, Tennessee from 1984-1991 where he studied Mechanical Engineering and received both the Bachelor of Science and Master of Science degrees. During his time at Tennessee Tech, he was awarded a Society of Plastic Engineers Scholarship and was a member of Tau Beta Pi and Pi Tau Sigma engineering honor societies.

Boyd joined the staff of the Oak Ridge National Laboratory (ORNL) in June of 1991 where he initially worked in the Plastics and Adhesives Group before joining the Optics Manufacturing Operations Development and Integration Laboratory (MODIL) in 1992 to work on optomechanical design. During the late 1990s, the Optics MODIL project ended and the group's research transitioned into the MEMS sensor area. During this time he provided precision design and manufacturing assistance to several medical device projects which spurned his interest in the application of precision fabrication and sensing technologies to medical devices and surgical tools. Boyd currently works jointly as a Research Associate at the University of Tennessee's Center for Musculoskeletal Research and as a staff member in ORNL's Monolithic Systems and Devices group. He also manages and coordinates research for ORNL's Nanoscale Science and Technology Laboratory. Boyd received his PhD from the University of Tennessee in Biomedical Engineering in December of 2006.